A STUDY OF SOME PARAMETERS WHICH INFLUENCE THE STATIC AND DYNAMIC CHARACTERISTICS OF INTERFERENCE SHRINK-FITTED JOINTS

by

IBRAHIM MOHAMED ELEWA
BSc, MSc

A Thesis submitted for the Degree of
DOCTOR OF PHILOSOPHY

THE UNIVERSITY OF ASTON IN BIRMINGHAM

Faculty of Engineering

Department of
Production Technology and Production Management

April 1982

The University of Aston in Birmingham

A STUDY OF SOME PARAMETERS WHICH INFLUENCE THE STATIC AND DYNAMIC CHARACTERISTICS OF INTERFERENCE SHRINK-FITTED JOINTS

A Thesis Submitted For The Degree Of PhD

by

IBRAHIM MOHAMED ELEWA

S U M M A R Y

The main objective of the work presented in this Thesis is to investigate the static and dynamic characteristics of interference shrink-fitted joints using both experimental and theoretical approaches. The experimental investigation covers the main parameters affecting the static and dynamic holding load, joint stiffness and damping characteristics.

The investigated joints were made from bars of (EN1A) mild steel with various sizes (10, 15, 20 mm). Different manufacturing processes (turning and grinding) were used to achieve various degrees of surface roughness and surface characteristics. The joints interference levels were chosen so as to cover the I. S. O. range. A number of characteristic measurements were performed on every joint, namely: size, height, CLA, bearing area, peak to valley height, spot count, roundness and straightness.

The Thesis includes the design of a special test rig produced to satisfy the requirements of the testing programme for both static and dynamic loading conditions. The theoretical analysis leads to three different methods of evaluating the joint holding load. The first method made use of the measured bearing area curve of the joint surface profile; the second adds the assumption that the surface profile is a gaussian distribution; the last method relies on measuring the static coefficient of friction μs. A theoretical model was also derived to describe the joint damping characteristics by evaluating the energy dissipation between the joint surfaces.

The results showed that the joint holding load under static and dynamic loading increased as the mean value of interference (δm) increased and decreased with increasing the surface roughness. A significant influence is attributed to joint size on the joint holding load, stiffness and damping. The results showed that the dynamic holding load is approximately 50% of the static holding load. Under both static and dynamic loading conditions, it was found that a shrink-fitted holding load is between 1.5 to 3 times the press-fitted holding load.

The results present some empirical equations to describe the influence of surface roughness, size and interference value on the static and dynamic holding load. The effects of the induced stresses due to the applied load on the interference value were also taken into consideration. The theoretical results showed good correlation with the experimentally obtained data points.

KEY WORDS: Shrink-fitted joints;
Machine Tool Joints;
Machine Tool Structures.

April, 1982

LIST OF CONTENTS

LIST OF TABLES

LIST OF FIGURES

Figure Number

A C K N O W L E D G E M E N T S

The Author wishes to thank:

Professor R H Thornley, MSc Tech, PhD, DSc, AMCT, CEng, FIMechE, FIProdE, Mem JSME, for permitting this work to be carried out in the Department of Production Technology and Production Management of the University of Aston in Birmingham. Also, for his help, guidance and encouragement as Supervisor throughout the whole project.

The Egyptian Government for providing the financial support.

Mr G Yardley for his assistance and enthusiasm in the building of the test rig and manufacturing of the test specimens. Mr E R Langton for his assistance with the electronic instrumentations. Also, the many other colleagues who are too numerous to list, but to whom one is nevertheless very much indebted.

Dr N N Gindy for his assistance and for the active support in a good presentation of the work. Also, Miss L Harris for typing the script.

Finally, his wife for her assistance, patience and understanding throughout a sometimes arduous project.

D E C L A R A T I O N

No part of the work described in this thesis has been submitted in support of an application for another degree or qualification of this or any other University or Institution of learning.

NOMENCLATURE

K	Tangential Stiffness
P_m	Mean Interface pressure
d	Joint nominal size
D	Outside diameter of the ring
L	Length of fit
μs	Static coefficient of friction
σt	Tangential pressure
σr	Radial pressure
σy	Axial pressure
σe	Equivalent pressure
E	Young's Modulus of Elasticity
G	Young's Modulus of Elasticity in shear
δ	Interference on the radius
δm	Mean value of interference on the diameter
Ua	Actual interference on diameter
δma	Macro-Interference on diameter
δmi	Micro-Interference on diameter
δin	Ineffective interference value
H	Material hardness
ν	Poisson's ratio
T (max.)	Maximum shearing stress
P	Pressure due to fit
ε_r	Radial strain
ε_t	Tangential strain
P_a	Actual interface pressure
W	Applied Load

W'	Preload
A_t	True area of contact
N	Normal load
F	Friction force
Y_c	Yield pressure of a material as measured by a Vickers Hardness Indentor
CLA	Centre line average of the surface profile
H_t	Peak to valley height of the surface profile
H_{ts}	Peak to valley height of the shaft surface profile
H_{tr}	Peak to valley height of the ring surface profile
μ	Coefficient of friction due to adhesion at the interface
ζs	The ratio of the normal load supported by the junctions at which adhesion only takes place to the total normal loads
μy	Coefficient of friction between the mating surface within the elastic limit of shear deformation
P_{sy}	The limit shear pressure for elastic deformation
P_s	Tangential load
$\lambda_s = \delta_t$	Tangential displacement
δe	Elastic displacement in the tangential direction
δr	The Micro sliding
W_d	Energy dissipation at the joint interface
n	Number of asperities in contact at the contacting surface
a	Mean radius of the asperities in contact
τ	Loss factor
H. L.	Joint holding load
SH.F.	Shrink-fit
P.F.	Press-fit

CHAPTER 1

INTRODUCTION

Power transmission by elements with cylindrical mating surfaces has for a long time been utilised successfully as machine members. Mechanical methods of fixing the mating surfaces, involving e.g. keys or splines, have long been used to transmit torque through shaft coupling. However, the space and weight limitations of such methods make it more desirable to utilise an assembly which relies on the material elastic properties to produce the same action. Such an assembly would require the shaft diameter to be slightly larger than the diameter of the ring. This kind of fit is known as interference fit.

In the many theoretical and experimental studies concerning shrink and press-fitted joints, two principal methods were followed to evaluate the joint holding load. The first is based on assuming a fixed range for the static coefficient of friction μs and then using Lame' equation to arrive at the value of the joint holding load, with the additional assumption that the mean interference value is equivalent to the joint's macro-interference. The results obtained by using this method have provided poor agreement with the experimental data. The second method estimates the joint strength by using the bearing area diagram of the joint surface to evaluate the percentage bearing area at the desired interference value. The calculated holding load using this method proved to be always much

higher than the experimental data points, especially at high values of interference. This can be attributed to the accompanied assumption that the mean interference value is equivalent to the micro-interference. Both basic methods have a major drawback in not including the actual relationship between the micro- and macro-interference in their calculations of the joint holding load. This drawback can lead to a very wide gap between the theoretical and experimental data.

The traditional recommendation is to produce a joint with surfaces as smooth as possible, but this method is limited by the economy of the manufacture of such parts. The sacrifice in economy for uncalculated and indefinite gain in the joint holding load is not an acceptable engineering practice. Consequently, it has been substituted by increasing the joint interference value, which has resulted in the limited use of such fits due to the large stresses induced in the mating parts. In addition, a large value of interference can have an adverse effect on the holding load if the stresses exceed the material yield stress.

In spite of the importance of joints in general, it is rather difficult to make an accurate theoretical prediction of their behaviour. A joint, whether intended to be fixed or movable, is the product of contact of two machined surfaces. The region of metallic contact between the two surfaces makes it difficult to form a correct idea about the true area of contact, while the very high transmissibility of joints creates problems in measuring the stiffness and, in particular, the damping of the interface. The randomness of surface

topography complicates the attempts of deriving much needed theoretical expressions which can accommodate a wide range of topography of the joint surfaces.

Most of the previous research has concentrated on the joints holding load under static conditions without any consideration given to many of the applications in which the joints are exposed to dynamic loading. The dynamic performance of a machine tool is greatly affected by the collective response of its joints. Hence, studying the joints damping and stiffness characteristics is of great importance.

In many applications in which shrink-fitted joints are used, such as engines and machine tools, their dynamic characteristics can be an important factor in deciding the overall performance of the machine.

From the previous comments, it becomes clear that there is a great need for a better understanding of the parameters and interactions that affect the performance of a shrink-fitted joint. The joint design process must be greatly simplified if theoretical analysis or empirical equations are to be deduced and successfully describe the joint characteristics. A successful investigation into the static and dynamic characteristics of shrink-fitted joints should include the effects of varying the main joint parameters, such as surface roughness, size and value interference on the holding load as well as the joint stiffness and damping.

CHAPTER 2

DEFINITION OF THE PROBLEM

2.1 Introduction

For the purpose of this thesis, the word "joint" refers to the two parts mating to form a joint. The male (shaft) and the female (ring) are matched, after which they are fitted together at a predetermined interference level.

The word "interference" means the discrepancy in free size between the mating diameters of the shaft and ring, where the lower limit of the shaft is always larger than the ring's upper limit.

The joints formed by interference fits are permanent or semi-permanent in nature and fall within two basic categories: press-fitted joints and shrink-fitted joints.

A press-fitted joint can be achieved by forcing the two mating parts to deform when pushed together under pressure. On the other hand, shrink-fitted joints are formed by only heating the ring or cooling the shaft and, if necessary, by simultaneously heating the ring and cooling the shaft.

The press-fitted joints are best formed by means of a hydraulic press, as the pressure can be easily controlled. However,

many operators may prefer lever or screw presses for delicate work, as the insertion pressure can be felt and there is less likelihood of damaging the components. Great care has to be taken to keep the components square with each other and properly aligned at the start of the pressing operation.

In shrink-fitted joints a sufficient clearance must be achieved to permit the two parts to be joined together without effort. Many methods can be used for heating the female part, such as immersion in boiling water or hot oil, or placing it in a furnace, depending on the value of interference. The male member contracts as it cools when immersed in liquid nitrogen. During assembly of a shrink-fitted joint, a special jig and fixture should be used to ensure the best possible alignment between the mating parts.

2.2 Uses

An interference fit is used in a variety of applications, perhaps the most common being: bushings in machine housings; bearings; fastening of axles to the wheels of railway rolling stock and their rims; worm gear rims to wheel centres in machine tools; pump shafts; fractional horsepower motors; the component cylinders of gun barrels; built-up crankshafts for oil or marine engines; and in construction of automotive vehicles.

Interference-fit constructions are well-suited to different design situations, such as replaceable liners in pressure vessels or strengthening of a liner by a shrunk-on shell that helps retard crack propagation. Its versatility can also be demonstrated in assemblies composed of materials having different properties or degrees of corrosion resistance, such as a shrunk-on steel shell over a copper or aluminium liner. The process is particularly useful where space, weight or design limitations make it impractical to use standard fasteners.

Shrink-fitted joints are about two to three times stronger than press-fitted joints, in which abrasion takes place during assembly, reducing the value of interference. One of the main disadvantages of press-fitted joints is the difficulty of controlling their dependability during assembly, in addition to the difficulty of obtaining the high level of accuracy required of the mating sizes. Shrink-fitted joints are one of the most effective means of assembling parts whose materials have different properties or corrosion resistance.

2.3 Previous Research into the Subject

As early as 1899, Wilmore (1) carried out an experimental investigation in which he compared the characteristics of shrink and press-fitted joints under tension and torsion loading. The results indicated that a shrink-fitted joint holding load was about three times the holding load of the press-fitted joint. The early research records of 1913 for press-fitted assemblies performed by

McGill (2) show that the value of the coefficient of friction in many assemblies, calculated on the basis of the two-dimensional thick cylinder theory, varied widely depending on the manufacturing processes. The damping characteristics of shrink-fitted joints have been shown to be dependent on the value of the friction coefficient of the mating surfaces (3).

Russell and Shannon (4) have noticed a permanent enlargement of bore and outside diameter of the ring when the value of interference increases beyond a certain value with the shaft dimensions remaining unaffected. The holding load also shows an increase when the elastic limit of the material is increased. The later works of Russell (5, 6, 7) show a non-linear relationship between the axial load and the length of grip for both pressing-on and pressing-off. The pressing-off operation frequently gives a higher holding force after the shaft has started to slip from the ring.

Baugher (8) concludes that the maximum equivalent tensile stress at the ring bore increases in the case of an increase in the value of interference with the possibility of estimating the maximum value at which all the deformations are still elastic. The holding load of the fit can be increased by increasing the maximum tensile strength of the material (9). Trock (10) and Conway (11) come to the conclusion that the two fundamental factors which affect the holding load between two shrink-fitted components are the elastic limit of the material and the magnitude of the modulus of elasticity. The elastic break-down in thick-cylinders occurs at an internal pressure approximately mid-way between the pressure

estimated when the maximum strain criterion is used, and that calculated when the maximum shear stress criterion is applied (12).

Recently, several research workers, Sawin (13), El Khatib (14),Tsukizoe et al (15) and Elewa (16) have carried out research work to investigate the effects of surface roughness on the holding load of the shrink-fitted joints. Most of them come to the general conclusion that the finer the finish of the mating surfaces is, the greater the holding load for a given value of interference would be (details to be discussed later).

CHAPTER 3

FACTORS AFFECTING THE HOLDING LOAD OF THE JOINT

The different factors that may influence the holding ability of shrink-fitted joints can be summarised as follows:

(1) Values of interference in the joint.

(2) Frictional conditions between the mating parts.

(3) Form errors such as roundness, straightness or taperness, etc.

(4) The nominal size of the parts.

(5) End effect.

(6) Ageing.

(7) Type of loading (static or dynamic).

3.1 Value of Interference

In many structural and machine elements, it is not permissible to stress the material beyond the yield point. In shrink and press-fits, however, it is no longer unusual to have stresses beyond the yield point. According to the maximum shear theory (17) which is generally applicable to ductile materials, such as mild steel, the

deformation of the ring will remain elastic until the maximum equivalent tensile stress (equals to twice the maximum shearing stress at the bore of the ring) becomes greater than the yield strength of the ring material in tension.

The experimental research carried out by Russell and Shannon (4) on force-fits indicates that the maximum grip occurs at a value of interference corresponding to the point of elastic failure based on the thick cylinder theory.

Baugher (8) has produced useful experimental curves showing the relationship between the maximum equivalent tensile stress at the hub bore and the value of interference, as shown in Figure 1. From these curves, it is possible to determine the maximum value of interference at which all deformations are still elastic. Plastic deformation is observed to occur in the ring before the shaft unless the shaft is hollow with a thin wall thickness. Werth (18) has shown that for plain carbon steels both the value of pressure, and the holding load continue to increase up to a limiting fit value (0.003 inch/inch of the shaft diameter), beyond which the holding load starts to decrease.

The use of large interference values would normally lead to problems in assembling the joint and this has been observed by Trock (10) in assembling steel rings on solid shafts of large diameters. These observations can be summarised as follows:

(1) When the value of interference is increased beyond 0.003 "/ inch of the shaft diameter, the observed increase in the holding load corresponding to a unit increase in interference is greatly reduced.

(2) This suggests the existence of an optimum value of unit interference to achieve the joints maximum holding load.

The same trend of results showing an increase in the joints strength corresponding to an increase in the mean value of interference has been observed when the value of surface finish is held constant (14, 16).

It has been observed that the zone of plastic strain in the fitted parts of the joint occurs at values of the contact stresses, which are 20 to 30% below the conditional yield point. In calculating the amount of clearance needed for fitting through heating, the possible variations in the physio-mechanical material properties under the combined effect of the simultaneous action of temperature and plastic deformation should be taken into consideration (19).

In the case of assembling joints made of steels inclined to ageing when the thermal method is applied, it has been found that the value of the joints contact pressure is higher than that of a press-fitted joint of the same value of interference, while the residual stresses are lower.

3.2 Effect of Frictional Conditions

Friction between the parts is one of the main parameters that affects the holding load of press and shrink-fitted joints. That is why an adequate listing of the research results on surface friction effects is necessarily lengthy, due to the diverse efforts of many investigators particularly during the last few decades. Indeed, most of the work has been confined to rigid-rigid interacting surfaces (i.e. metal to metal), either with or without the presence of lubrication.

The significant effect of surface texture on friction has been appreciated by researchers for a long time, and it can be said that texture is perhaps the single, most important variable that determines the magnitude of the frictional coupling between surfaces. Other factors that affect the frictional conditions between the interacting surfaces are the actual area of contact, the type of joint material and the kind of heat treatment to which the surface has been exposed. The following Section is a modest attempt to summarise the research findings regarding the effect of the previously mentioned factors on the frictional conditions.

3.2.1 Effect of Material and Heat Treatment

The experimental results show that the holding load of a force-fitted joint can be increased by increasing the elastic limit of the material through cold-working (4). Conway's (11) attempt to

verify Lame's formula equation (3.1)

$$P = \frac{E\delta m}{2d} \left(1 - \frac{d^2}{D^2}\right) \qquad 3.1$$

has shown that the two fundamental factors affecting the grip between the two shrink-fitted components are the elastic limit and the magnitude of the modulus of elasticity. It has also been shown that the interference required to give a specific radial pressure is inversely proportional to the Young's modulus. From a comparison between several different materials it becomes obvious when using Lame's formula that an increase in the modulus of elasticity is followed by a proportional increase in the holding load. For example, the holding load of a joint made of steel is three times greater than the same joint manufactured from duralumin ($E = 10 \times 10^6$ Psi).

The experimental results have shown that, when materials with comparable tensile strengths need to be selected, it is preferable to choose a material with high toughness and high yield points, because it is on these features that the fatigue strength mainly depends (9).

Kestel'man (20) has carried out an experimental investigation in which carbon bushings were press-fitted to metal parts. The results have shown that the load which must be applied to form the joint is dependent on the surface roughness and the heat treatment method. The bushings that are heat treated using oil, require 50% higher force than those treated using water. Oil is a more preferable heat treatment medium due to the improvement in reliability

and strength that accompany its use. The strength of the permanent joints increases with increasing the value of interference, of joint length and of bushing wall thickness, as well as of the metal part surface roughness and heat treatment. The tests have also shown that heat treatment of carbon bushings in oil can be used to improve the reliability and strength of the permanent joints (carbon bushing-metal part).

3.2.2 Effect of Surface Roughness

The surface roughness of the mating surfaces of an interference fit joint plays an important role in deciding the joint's strength.

Many investigators have discussed the influence of the surface roughness on the strength of the joint. Their treatment of the subject has been based on considering the strength of the shrink-fitted joint as a function of pure friction between the mating surfaces governed by equation (3.2):

$$H.L. = \pi \cdot d \cdot L \cdot P \cdot \mu s \qquad 3.2$$

where:

H.L. = holding load in KN

L. = length of fit, i.e. length of contact between the two members of the joint in mm.

Their utmost endeavour has been focussed on the effect of surface roughness on the value of the coefficient of friction μs. In one study by Sawin (13) an experiment was performed to determine the effect of surface finish on the joint grip strength. The tests have shown that the finer the finish is, the higher the grip strength would be. Baugher (8) disagrees with this view, stating that in more than 100 press-fits in which the surfaces vary from ground to rough turned, practically no difference has been observed in their strength. He does, however, advocate using ground finishes to obtain closer machining tolerances. The experiments carried out by Russell (6, 7) show that using a lubricant during assembling a force-fit joint can cause a difference of over 300% in the grip strength.

Trock (10) comes to the conclusion that the holding load of the fits is related not only to radial pressure, but also to the surface finish of mating parts, and that the finer the finish on the mating surfaces is, the greater the holding load would be for a given interference value. The observed increase is of the order of 15 to 25%.

More recently, Tsukizoe (15), El-Khatib (14), Elewa (16) have carried out extensive experimental investigations to study the effects of the surface roughness on the holding load of the shrink-fitted joints. Most of their research has led to similar conclusions to those of Trock.

3.3 Effect of Form Errors

Some of the form errors of the surface profile, such as out-of-roundness and out of straightness, have a great effect on the strength of the shrink-fitted joints, and should be eliminated or minimised.

Russell (5) has carried out some experiments to investigate the effect of out-of-roundness on the joint strength. The out-of-roundness measurements are made at different planes along the shaft and wheel. The results show that the wheel seat and shaft are not truly circular at same planes with the maximum out-of-roundness estimated at 3.5 and 2.5 thousandths of an inch respectively. The deviation in the roundness causes a variation in the intensity of the radial pressure at the interface, which in turn influences the pressing-on load.

In the theoretical and experimental work executed by Hisakado et al (21), the assumption has been that the contact pressure and interference value in the cross-section perpendicular to the axis of the shaft and the ring can be expressed by a series of trigonometrical functions from which the relationship between the average contact pressure and average interference can be deduced. The results obtained using strain gauges to measure the contact pressure between the mating surfaces of a ring and a shaft with poor roundness demonstrate that the coefficient of friction between the fitted parts is not influenced by the out-of-roundness. Another investigator (14, 16) has concluded that a taper on the shaft or hub or both will in

some cases lead to a shearing action along the length of joint if the value of the taper is less than the value of the interference. In this case, the tension required to release the fit is not the force due to friction between shaft and hub, but it is a shearing force which is not affected by either the value of interference sum or the surface finish. This situation can give misleading results if it is not avoided. The out-of-roundness of the shaft, hub, or both, due to ovality or lobedness may also influence the results, especially in the case of torsion loading. In the case of joints under tension, the area of contact and the actual value of interference will change along the circumference of the mating parts, which can result in misleading conclusions if the out-of-roundness is not minimised or accounted for.

3.4 Effect of the Nominal Size of the Parts

The shrink-fitted joint parameters, such as shaft diameter, ring wall thickness and the mean value of interference, can be quickly and successfully arranged as a nomogram to ease the amount of calculations to determine the contact pressure (10). The results obtained for shrink-fitted crankshafts have demonstrated that the joints shape and size have an influence on the joints endurance limits of large crankshafts (22). Another experimental investigation relating to the holding load and joint size, if it is either under tension or under torsion, suggests that the variation in the holding load is mainly due to the joint diameter for a constant joint area (16).

3.5 End Effect

The end effect has been investigated by Barton (23), and later, using a slightly different mathematical approach, by Rankin (24). Assuming an infinitely long shaft with a finite band of pressure of uniform intensity over the breadth of the band, Rankin has calculated the stress components and the shaft deformation adjacent to the pressure band. The maximum deformation of the shaft occurs at the middle of the pressure band, while the stresses and deformations are relieved when the shaft returns to its free diameter after a short distance from the pressure band. Assuming that the interface pressure in a shrink-fit is constant over the axial length of grip, the shaft deformation is analogous to the case where a thin ring is shrunk over a relatively long shaft. If the decrease in diameter of the shaft is assumed to follow the Lame's plane stress equations, the interface pressure of such an assembly when calculated involves some error. Making calculations on the basis of plane stress assumptions, Rankin has compared the decrease in diameter of the shaft with the average decrease under the pressure band on a long shaft and related the two values by factor K, in such a way that:

$$K = \frac{\text{radial deformation on plane stress assumption}}{\text{average radial deformation under pressure band}}$$

The values of K have been plotted for varying band widths. It would appear that for widths in excess of about 0.3 times the shaft diameter, no appreciable error is introduced by the simplified calculations.

If the dimensions of the bands are used and it is assumed that there is no coupling between adjacent bands, the increase in the radial pressures with the above correction amount to about 25%, whereas the increase in actual grip is 95% (5). In this case, however, the ring bore is subjected to the same pressure band conditions and the average radial deformation of the bore must be smaller than that calculated by the plane stress theory. Pressure bands on infinite cylinders have been considered by McGregor and Coffin (25). By making certain approximations with regard to the stress systems induced by the deformation of the cylinder wall, the resulting solution is in agreement with the plane stress solution. According to McGregor and Coffin's analysis, the radial deformation under a circumferential line pressure load, which is equal to the bearing band load, can be compared with the corresponding deformation calculated by Lame's equations. The deformation under the line pressure is less than 0.02 of the Lame deformation, and therefore, for a given value of interference, the pressure is much higher. The comparison is, admittedly, highly approximate, since the ring used in Russell's tests is not infinite, nor even long. Moreover, the calculated deformation should be modified to account for additional deformation due to the other closely adjacent bearing bands.

It should be noted, however, that the radial deformation evaluated by Rankin is not compatible with the assumption on which it is based. The mating surfaces of the plug and ring must be deformed by the boundary tractions in such a way that the profiles and dimensions are identical. The tractions are equal and opposite at every point on the mating surfaces. These are the only two

conditions imposed on the boundaries, and a solution on this basis has not been attempted. The accuracy of an assumed stress distribution must be judged by the compatibility of the deformations of the two parts on which the stress is acting. It is clear that the interface pressure in an interference assembly, where the two parts are unequal in length, must be a maximum at the ends of the grip and a minimum in the middle. The actual value of the maximum pressure is important in view of the pressure required to overstrain the ring bore, as well as on account of the deleterious effect of radial pressure on the fatigue strength of the shaft.

One of the attempts to calculate the actual pressure distribution in a shrink-fit has been executed by Okubo (26). Okubo has used varying combinations of both the finite-length sleeve and infinite-length shaft and has applied elasticity theory to describe the behaviour of both components. However, with an application of the finite-length sleeve analysis it is very difficult to arrive at an exact solution and it has proved impossible to meet the condition of zero normal stress on the end faces of the sleeve. Thus the behaviour of the contact stresses near the end of the sleeve is open to questioning.

A significant contribution to the study of shrink-fit has been made by Eubanks (27) who has obtained an exact closed-form solution of the problem of a finite-length sleeve shrunk onto a cylindrical shell of infinite length. Friction in the contact area is ignored, and the classical, thin-shell theory is utilised for both the sleeve and shell. Within the framework of the classical,

thin-shell theory, concentrated forces and couples are found to act at points in the infinite-length shell adjacent to the ends of the sleeve, which correspond to the abrupt jumps in the moment and the shear at these points.

Conway and Farnham (28) have used numerical methods to find out the distribution of contact stresses and displacements induced by shrinking a flexible sleeve onto a flexible shaft. The classical theory of thin shells is applied to calculate the displacements of the sleeve, while the elasticity theory is used to calculate those for the shaft. Distributions of the contact stresses and displacements are worked out for various sleeve length/sleeve thickness and sleeve length/shaft radius parameters. The sleeve is considered to be rigid, and the infinite-length shaft is treated as an axisymmetrical elasticity problem. However, if the effect of friction is to be included in the analysis, friction would have a slight influence on the magnitudes of the normal contact stresses and displacements.

In a later study, Conway (29) has used a method of analysis which is essentially similar to that adopted in his previous articles (28, 30, 31). The normal contact stress distributions are replaced by a series of pressure bands over large numbers of incremental lengths. The displacements of the sleeve and shaft at the centres of each increment are then computed in terms of the incremental pressure. It has been shown by comparison with some known exact solutions (28) that this technique is capable of producing very accurate distributions. These theoretically infinite values pertain only to an

elasticity theory and a sleeve having absolutely sharp corners. Any slight rounding of the corners which occurs in practice, will reduce both the stresses at the extreme ends and any plastic action.

3.6 Effect of the Ageing

The effect of time on the grip strength in the interference shrink-fitted joints has been investigated by Russell (7) in test series of up to 32 months duration. The grip of force fits increase in the first eight months and then become erratic. Shrink and press-fits show no definite tendency. The increase in grip strength of force-fits with time has been noted by Baugher (8), who states that the force required to press-off is 25% lower immediately after assembly than after two days time. Thomson explains this observation by relating its origin to the lubricating film at the contacting surfaces (7).

Trock (10) also shows that the holding load of shrink-fitted joints is affected by time. The specimens used are made of steel quenched and tempered to a hardness of 32 to 36 Rc. The mating surfaces are ground to a finish of 10 to 20 micro inches. The tests show that ageing is responsible for the decrease in load required to cause failure in some samples. The samples, which originally withstand 400,000 lb, fail at much lower loads when they are retested approximately eight months later (180,000 lb in the case of some samples). These results suggest that time is another factor to be considered when designing shrink-fits with high radial pressure.

3.7 Effect of Type of Loading

Horger et al (32) has carried out an investigation on the fatigue strength of shafts, and shown that a press-fitted collar on a shaft seriously diminishes its fatigue strength. Fractures occur just inside the end of the collar at which the bending moment in the shaft is greatest. In cases where a large number of reversals have taken place before fracture, the collar becomes loose, and fracture occurs in the middle of the grip.

This indicates that the cyclic bending of the shaft progressively overstrains the fitted ring, with a consequent progressive reduction of the interface pressure and destruction of the grip strength. It appears that the loss of fit depends on the number of cycles and corresponds to a creep of the overstrain through the ring material. This is of utmost importance in the case of the built crankshaft where cyclic bending and torsion actions are imposed on the grip. The strength of the assembly under superimposed cyclic loading should not be inferred from the initial grip strength. In Russell's work involving static axial loading, he concludes that the damage occurs with the plug either entering or leaving the ring during force fitting or stripping. It is possible that similar damage can occur in stripping a shrink-fit by axial displacement.

CHAPTER 4

ANALYSIS OF THE STRESSES INDUCED IN THE MATING PAIR DUE TO SHRINK-FITTING

4.1 Introduction

In almost every practical application of shrink-fitted joints, the grip force is developed between two cylindrical surfaces. In a plane perpendicular to the cylinder axis the theoretical profile of the mating surfaces is circular. The stress system in that plane can be radically simplified, if the other boundaries of the elements are considered to be concentric circles, and if the boundaries and stress system are assumed to be invariant in the direction of the cylinder axis.

Previous investigations have assumed that the stress system can be calculated without appreciable error if the Lamé equations are applied. These well-known equations are applicable to conditions of either plane stress or plane strain, the former being assumed for the stress analysis of shrink-fits. This is, at best, a fair approximation, as shrinkage in the axial direction induces axial shearing stresses in the joint's cross-section. The boundary loading and deformation in the joint are interdependent, and the only necessary conditions to solve the stress system are the continuity of stress and deformation at the mating surfaces.

The axial shrinkage is assumed to be entirely prevented by the fact that the consequent stress system for this deformation is a uniformly distributed axial tension and compression in the ring and shaft respectively. This is equivalent to Goddier's (33) assumption of a long cylinder, in which the friction preventing the axial shrinkage is confined to the ends, as a consequence of which the bending and shearing stresses in any section of the cylinder wall near the middle of the grip are of a low magnitude.

A Lame stress system for the cross-section of the grip is not incompatible with the assumption that there is uniform tension or compression in the axial direction, since a condition of plane strain exists.

4.2 Stress Distribution in Cylindrical Fitted Parts

4.2.1 Previous Work

The equations used to estimate the radial and circumferential stresses in an elastic thick cylinder, according to Lame, are well-known, and univerally used for shrink-fitted joint calculations. In addition to the usual assumption of elasticity, isotropy and homogeneity, the assumption is made that a condition of plane stress or plane strain exists on planes normal to the cylinder axis and that body forces are zero or constant. The stress distribution in the radial and circumferential directions is unaffected by axial stresses, provided that these are uniformly distributed over the cross-section giving a condition of plane strain.

The radial and cirumferential stresses are greatest at the bore of the cylinder and it is at this radius that elastic breakdown occurs under increasing bore pressure.

Many investigators have conducted experiments to study the criterion of elastic failure of thick cylinders. Cook and Robertson (34) have carried out experiments on closed mild steel cylinders with a view to ascertaining the correct failure criterion and have shown that breakdown of the elastic condition, as indicated by the outside diameter measurements, occurs at a pressure mid-way between the pressure calculated from the maximum strain theory (of St Vensant) and the maximum shear stress theory (of Guest). Later, these experimental results have been used by Haigh (36) to substantiate his strain energy criterion of failure for thick cylinders.

Cook (36, 37) indicates in his work that the upper yield point which can be observed in tensile tests of annealed mild steel specimens, has a counterpart in non-uniform stress systems. Cook's experiments on small steel cylinders with closed ends demonstrates that the upper yield point is not a constant, nor equal to the tensile test value, but varies as overstrains advance through the wall of the cylinders. In their theoretical analysis, Nadai (38) and McGregor, Coffin and Fisher (39) have used the Von-Mises shear strain energy criterion of failure. The analysis maintains that the failure of gun steel is more closely in accordance with this criterion, but its adoption leads to mathematical complexities in the analysis.

Macrae (40) has carried out experimental and theoretical work dealing with the manufacture of gun barrels using the shear stress criterion. There is a substantial amount of experimental evidence in this work to show that the behaviour of overstrained cylinders, within the limits of accuracy of measurement, can be calculated from the shear stress theory without appreciable error. Sopwith (41) has used this theory of failure in his theoretical work in order to take into account the compressibility of the overstrained material, which is usually neglected when the plastic strain is large in comparison with the elastic strain. In thick cylinders the inelastic material is bounded by elastic material which limits the amount of plastic strain to values of the same order as those occurring in the elastic region.

The problem of determining the stress distribution in a long shaft caused by shrinking a ring with a short axial length onto the shaft, has been discussed by Rankin (24), Tranter (42), Graggs (43) and Conway (29), but no quantitative value of its influence on joint design is available.

4.2.2 Elastic Failure Criterion

In the case of thick cylinders under internal pressure, two criteria are normally selected to correlate their behaviour with the observed behaviour of tensile test specimens of the same material.

$$P_t - P_r = P_e \qquad 4.1$$

and $(P_t - P_r)^2 + (P_r - P_z)^2 + (P_z - P_t)^2 = 2 P_e^2$ 4.2

where:

P_t = Tangential pressure

P_r = Radial pressure

P_z = Axial pressure

P_e = Equivalent pressure

The first equation is the criterion of maximum shear stress, while the second, the shear strain energy criterion, is usually associated with Tresca and Von-Mises respectively.

The shear stress criterion enables the radial depth of over-strain to be calculated from equilibrium considerations, independently of axial stress condition and, therefore, of end condition. For this reason, in mild steel cylinders, no great discrepancy occurs between calculated and measured external diametral extensions, as is shown by Cook, Macrae and Sopwith in their treatments of the subject.

Cook's analysis takes account of the possible difference of yield stress between the initial elastic breakdown and subsequent plastic deformation. Nadai and McGregor, Coffin and Fisher, have analysed the problem, using the Von-Mises criterion, which is claimed to be representative of behaviour of gun steel. Hill, Lee and Tupper

have also used this criterion, which they allege to be more satisfactory than the maximum shear stress criterion if the maximum energy dissipation during plastic deformation is considered.

The analysis made by Baugher (8) shows how the maximum equivalent tensile stress at the ring bore increases with increasing the value of interference (δma). From Figure 1 it is possible to determine the maximum fit at which all deformations are still elastic.

4.3 Stresses Due to Shrink-Fit

4.3.1 Pressure in the Joint

From the point of view of stress, the shrink-fitted assembly can be regarded as being composed of a ring subjected to internal pressure (P_1) caused by interference, and of a shaft subjected to the same value of pressure from its outside.

It is assumed, for example, that the external radius of the internally hollow cylinder in the unstressed condition is larger than the internal radius of an outer cylinder by an amount "δ", as is shown in Figure 2. After assembling the cylinders a pressure (P) is produced between them. The magnitude of the pressure can be found from the condition that the increase in the inner radius of the outer cylinder plus the decrease in the outer radius of the inner cylinder must be equal to "δ".

Hence from equations (7 and 8) in Appendix (I) it follows:

$$\delta = \frac{d.P}{2E}\left(\frac{d^2 + D^2}{D^2 - d^2} + \nu\right) + \frac{d.P}{2E}\left(\frac{a^2 + d^2}{d^2 - a^2} - \nu\right) \qquad 4.3$$

from which it can be derived that:

$$P = \frac{E\delta}{d/2} \quad \frac{(d^2 - a^2)\ (D^2 - d^2)}{2d^2\ (D^2 - a^2)} \qquad 4.4$$

In the particular case of a solid shaft and a ring, (a) is equal to zero, which reduces the equations to:

$$P = \frac{E\delta^*}{dD^2}\ (D^2 - d^2) \qquad 4.5$$

i.e. $$P = \frac{E\delta^*}{d}\ \left(1 - \frac{d^2}{D^2}\right) \qquad 4.6$$

4.3.2 Stresses in the Joint

The general method of calculating the stresses in the joint is given in Appendix I. From the Appendix, the stresses on the inner surface of the cylinder are given by:

$$\sigma_t = P\,\frac{(d^2 + D^2)}{(D^2 + d^2)} \quad ; \quad \sigma_r = -P \qquad 4.7$$

where:

σ_t = The tangential stress

σ_r = The radial stress

---

*$\delta = \delta_{Ma} = \delta_{Measured} - \delta_{mi}$, as discussed in Chapter 6.

The maximum shearing stress at this surface is T max.

where:

$$T \text{ (max.)} = \frac{PD^2}{(D^2 - d^2)}$$

Substituting in equation 4.4 then,

$$T \text{ (max.)} = \frac{E\delta D^2 (d^2 - a^2)}{d^3 (D^2 - a^2)} \qquad 4.8$$

In the case of (a), equal zero for solid shaft equation 4.8 becomes:

$$T \text{ (max.)} = \frac{E\delta}{d} \qquad 4.9$$

The maximum equivalent tensile stress at radius (r) in the ring bore is given by:

$$\sigma_e \text{ (max.)} = \frac{E\delta}{d} \qquad 4.10$$

4.3.3 Strain in the Joint

The strain in the ring can be estimated as described in Appendix I. The radial and tangential strains can be written as follows:

(1) Radial strain $\varepsilon_r = \frac{1}{E} (\sigma_r - \nu \sigma_t)$

i.e. $$\varepsilon_r = \frac{Pd^2}{E (D^2 - d^2)} \left[(\nu - 1) + \frac{D^2}{4r^2} (1 - \nu)\right] \qquad 4.11$$

(2) Tangential strain $\varepsilon_t = \frac{1}{E} (\sigma_t - \nu \sigma_r)$

i.e. $$\varepsilon_t = \frac{Pd^2}{E (D^2 - d^2)} \left((1 - \nu) + \frac{D^2}{4r^2} (1 + \nu) \right) \qquad 4.12$$

The longitudinal stress is neglected

Strain on shaft $$\varepsilon_r = \varepsilon_t = \frac{-P}{E} (1 - \nu) \qquad 4.13$$

4.4 Effect of the Loading Conditions on the Stresses Induced during the Test

4.4.1 Static Test

The stress system due to the static loading of the joint is shown in Figure 3. While the shaft is compressed, the ring is subjected to an axial pressure at the contacting face. The effect of this stress system is an increase or decrease in the effective value of interference depending on the loading direction (tension or compression). This effect can be taken into account through using the following treatments (1) and (2):

(1) Considering the equilibrium of the circular element in Figure 3, we get:

$$\sigma_y \cdot \frac{\pi}{4} (D^2 - d^2) = W \pi d \delta_y + (\sigma_y + \delta \sigma_y) \frac{\pi}{4} (D^2 - d^2) \qquad 4.14$$

The axial stress σ_y will influence the radial strain ε_r according to the relationship:

$$\Delta \varepsilon_r = \frac{\nu}{E} \cdot \sigma_y \qquad 4.15$$

The value of the corrected contact pressure, which includes the axial load effect, becomes:

$$P_a = \frac{E\ Ua}{2d} \left(1 - \frac{d^2}{D^2}\right) = K\ Ua = K \left(\delta_m + \frac{\nu d}{E} \sigma_y\right) \qquad 4.16$$

Solving the equilibrium equation we get:

$$\sigma_y = \left(S + \frac{A}{B}\right) e^{-cy} - \frac{A}{B} \qquad 4.17$$

Substituting equation 4.17 in equation 4.16 we get:

$$P_a = (K' W + K \delta_m)\ e^{-cy} \qquad 4.18$$

Equation 4.18 is an exponential relationship which describes the pressure distribution along the contact surface of the ring.

The pressure distribution after applying the load on the inner surface of the ring, is a max. at the face which makes contact with the base, while it is a minimum at the free end. This relation is shown in Figures 4 to 6. It is possible now to estimate the effect of the applied load on the interference value δ_m, for the various joint sizes, as is shown in Appendix 1.

(2) Referring to a circular element of the shaft at a distance Y from the upper face of the ring and a thickness (δ_y), as shown in Figure 3, the equilibrium of the element is given as:

$$\sigma_y \cdot \frac{\pi}{4} \cdot d^2 = P. \mu_s \cdot \pi. d \cdot \delta_y + (\sigma_y + \delta \sigma_y) \frac{\pi}{4} d^2 \qquad 4.19$$

The value of the corrected contact pressure becomes:

$$P_a = K U_a = K (\delta_m + \frac{\nu .d}{E} \sigma_y) \qquad 4.20$$

Solving the equilibrium equation for (σ_y) and substituting in equation 4.20 we get:

$$P_a = (K' W + K \delta_m) e^{-cy} \qquad 4.21$$

The relationship between pressure distribution and shaft length for the various shaft sizes used are shown in Figures 4 to Figure 6. It is clear from these Figures that the pressure is maximum at the end which makes contact with the upper end of the ring, and minimum at the lower end.

4.4.2 Dynamic Tests

4.4.2.1 The Effect of Pre-Load on the Value of Interference

In the case of the dynamic tests, it has proved to be necessary to apply a preload on the ring to prevent any slipping or shocks between the

base and the ring. The pre-load value is kept constant for all joint sizes. The induced stresses in the ring due to the pre-load will in turn affect the value of interference, as is shown in the following analysis.

(a) The ring is subjected to a normal compressive stress which can be calculated from equation 4.22.

$$\sigma_y = \frac{4W'}{\pi\ (D^2 - d^2)} = K_1\ W \qquad 4.22$$

where:

W' = pre-load = 20 KN

K_1 = constant depends on the joint size

(b) The radial strain corresponding to σ_y is given as:

$$\Delta\ \varepsilon_r = \frac{\nu}{E}\ \sigma_y = \frac{\nu}{E}\ .K_1\ .\ W' \qquad 4.23$$

(c) The diametral displacement $= \dfrac{d.\ \nu.\ K_1.\ W'}{E}$ 4.24

The diametral displacement for the different sizes can be estimated by using the above equation and the necessary correction is made in relation to the value of interference in a manner similar to that for the static load.

4.4.2.2 The Effect of Cyclic Loading on the Value of Interference

The cyclic loading will increase or decrease the value of interference depending on the load direction, i.e. compression or tension. For design purposes the calculations should be based on tension loading, i.e. the load effect is decreasing the value of interference.

The same equations deduced for the case of static loading are used to calculate the diametral displacement of the shaft. The preload and cyclic loading effects have been estimated for all sizes, while the correction to the interference value is made as shown in Appendix 1.

CHAPTER 5

THE AREA OF CONTACT AND FRICTION BETWEEN TWO METAL SURFACES IN CONTACT

5.1 Introduction

As early as 1699, Amonton (44) stated that, "the resistance caused by the friction between surfaces rubbing together increases or diminishes according to the value of pressure, not according to the nature of the contacting surfaces". This statement forms the basis of what are now known as the laws of friction.

The friction of the metal surfaces is dependent on the surface film, adhesion and wear within the contacting surfaces. The junction growth under unlubricated conditions occurs not only in the static contact before gross sliding, but also in dynamic contact (45). Bowden and Tabor (46) suggest that the friction of metals is due to local adhesion. In addition, there may be an appreciable penetration and ploughing of grooves in the surface, which must be considered. Bowden et al also notices that the effect of the ploughing term is small and the main friction resistance is the force required to shear the welded junctions formed by adhesion at the contact areas. In this model the junctions are assumed to be parallel to the sliding direction, while the normal and shear stresses acting on them are taken to be independent of each other. The shear and normal stresses at the junctions are related to the indentation yield stress and shear flow stress of the contacting

materials. It follows that the friction force is proportional to the load normal to the surfaces and independent of their area. However, the coefficient of friction estimated in this way is normally of the order of .2 and this is significantly less than the values normally obtained for unlubricated metals. At a later stage, the theory has been modified to take account of the interdependence of the normal and shear stresses, which should be related to a yield criterion (47). The concept of an interfacial film separating the surfaces in the contact region, with the film having strengths ranging from zero (perfect lubrication) to the shear strength of the asperities (strong adhesion), has also been introduced. With this model the resolved shear stress at the junctions, resulting from an applied tangential force, will only cause relative sliding of the surfaces, if it is equal to the shear strength of the interfacial film (48). For lower values of tangential force the deformation of the asperities occurs under the combined action of the normal and shear stresses increasing the area of contact from its initial value, with this process continuing until the tangential force is increased sufficiently to shear the interfacial film. The predictions made in this way regarding the increase in the real area of contact are shown to be in good agreement with experimental results and theoretical analysis.

5.2 Friction at very small Displacement

Some understanding may be gained from studying the deformation in the contact region by measuring the tangential force

when the displacement between the two surfaces is very small (micro-sliding).

Many investigators have carried out experimental work to study the asperities deformation and the change in their shape before gross slip occurs. Courtney-pratt and Eisner (45) have investigated the effect of small displacements on a single region of contact. The experiments show that both the relative displacement, between the two surfaces, and the area of contact increase in a regular and smooth manner as the tangential force is increased.

Green (49, 50) has applied plasticity theory to estimate the forces involved in asperity deformation and obtained a slip-line field solution for both strong and weak junctions. The results were used to show how the coefficient of friction could be extremely high in the case of strong junctions. Green points out that during the initial junction growth period the two surfaces move closer together; however, under steady state sliding conditions they must move parallel to each other. He shows that the necessary imposition of this condition on each individual junction determines both its manner of deformation and the forces exerted through it. In his investigation of the influence of the strength of adhesion on the value of the coefficient of friction, Green argues that if there are many junctions at different stages of development, then the coefficient of friction for the surface as a whole can be estimated by taking the ratio of the average tangential and normal forces that cover the life cycle of a typical junction, which he said consisted of formation, deformation and fracture.

Lacking a method for predicting the change in shape of an asperity and the corresponding forces during a life cycle, Green has carried out experiments using scaled-up asperities made from plasticine to give some indication of the type of deformation that might be expected. The results show that the change in shape of the plasticine asperities can be roughly characterised by an increase in the angle ζ and a decrease in the angle α. In the case of one asperity being harder than the other, α will not change (see Figure 7). The slip-line field solutions have proved to be successful for values ζ in the range of 0 to $\frac{\pi}{4}$. However, no theoretical solution exists for ζ between $\frac{\pi}{4}$ and $\frac{\pi}{2}$. An interesting result of this type of analysis is the way it predicts that the normal stress could become tensile towards the end of the life cycle and, hence, cause fracture of the junction.

It has not been possible to reach an accurate quantitative estimate for the coefficient of friction, due to the fact that neither the forces over the life cycle, nor the point of fracture are known with sufficient accuracy. However, Green has been able to show in a general way how this might be expected to vary with such factors as the strength of adhesion and the ductility and hardness of the contacting surfaces. The resulting trends are in good agreement with experiments.

Edwards and Halling (51) have followed Green's approach for estimating the coefficient of friction by considering the life cycle of a typical junction. They have been able to estimate forces beyond the range covered by Green's slip-line field solution. They

have studied the relevant effect of the plastic interaction of surface asperities on the coefficient of friction μs. The results show that it is a function of the shear strength of the junctions and the angles defining the initial asperity geometry; however, no quantitative analysis has been introduced.

Kraghelsky (52, 53) shows that for most interacting asperities of intermediate value, tangential displacement results for both the relative sliding over the contact surface of the two bodies, and the relative displacement within each of them. This tangential displacement is reversible in the case of elastic deformation and irreversible in the case of plastic deformation. The latter is more typical of friction, since the actual contact pressures are always larger.

5.3 Area of Contact and Friction Area

5.3.1 Introduction

Engineering surfaces are rough on a microscale, so that when two surfaces come into contact, the tips of their asperities interact and the load is carried by the load-bearing area created by the plastic deformation of these tips. The sum of these areas is normally much smaller than the apparent area of the surfaces. The friction force is related to the contact area, since friction arises at the real contact area between the two surfaces.

Epifanov and Sanzharovskii (54) assume that the true area of contact between two rubbing surfaces is equivalent to the true area of friction. This concept serves as a basis for a number of theories of friction. However, the mechanism of interaction between hard friction surfaces and the extensive experimental materials, which have been accumulated in the study of friction between highly smooth and even lubricated surfaces, testify to the fact that the true area of friction and the contact area are not identical.

Holm (55) emphasises the crucial fact that when two bodies are placed together the true area of contact is small. Bowden and Tabor (46) argue that because the surfaces contain asperities of small radii of curvature, plastic flow occurs at the true areas of contact even under very small loads. They continue to assume that the true area of contact, A_t, arises from the plastic deformation, while the major force of friction arises from shearing the junctions thus formed. Thus the relationship between the friction force F, the normal load N and the coefficient of friction μs is as follows:

$$N = A_t \cdot H, \quad F = T. A_t \quad , \quad \mu s = \frac{F}{N} \qquad 5.1$$

$$\therefore \quad \mu s = T./H \qquad 5.2$$

where:

H : is the hardness of the softer of the contacting materials.

5.3.2 The Factors Affecting the Area of Contact and Friction Area

5.3.2.1 The Physical and Mechanical Properties of Metals

Rabinowicz and Sikorski (56, 57, 58) suggest that the surface energy of adhesion is the main contributory factor in frictional resistance. They report that the ratio of the surface energy to the material hardness varies approximately as $H^{-.75}$, being smaller for harder metals. High values of surface energy to hardness correspond to large adhesion and a high coefficient of friction. Surface energy can be greatly increased by heat treatment, alloying or peening in order to produce increased hardness and a lower coefficient of friction.

The effects of crystal structure, modulus of elasticity, hardness, and surface energy on friction have also been studied by Buckley (59, 60), who concludes that cold welding readily occurs in metals having cubic crystalline structure, but does not occur with those of hexagonal structure. Moreover, friction attains its lowest values with slip planes of greatest atomic density. Sikorski (58) has shown experimentally that metals having large values of elastic moduli, hardness, surface energy, recrystallisation temperature, and resistance to plastic flow, are characterised by low values for the coefficient of friction. Mokhtar et al (61; 62) have investigated the effect of mechanical properties on frictional behaviour of metals. They conclude that the strength of the interatomic bonds, which may be held responsible for the mechanical properties of metals, is thought to play a significant role in dictating the

material's frictional behaviour. Soft metals show high frictional resistance, while hard metals, which are characterised by high yield and tensile strength, high hardness and low surface energy to hardness ratio, exhibit low friction values. The results also show that for unlike metals the coefficient of friction is lower than that obtained for similar metals interacting together; the behaviour is usually analogous to that of the softer metal.

5.3.2.2 The Effect of the Applied Load on the Contacting Surfaces

The relationship between the area of contact and the applied load is complicated and depends on the shape of the contact region and on the elastic deformation of the region around the plastic zone. An essential requirement of any theory of friction is that it should satisfactorily explain the experimentally observed proportionality between the friction force F and the normal load N. This observation leads to the definition of the coefficient of friction as $\mu s = F/N$.

Most theories of friction obtain this relationship by assuming that the tangential force F is proportional to the real area of contact and, if the mechanics of contact are considered, that the real area of contact A_t is proportional to the normal load N. In the past these proportionalities have been assumed to hold for individual asperity interactions and, hence, for the microscopic measurements. Greenwood (63) has contributed greatly to the development of more general theories of friction by demonstrating that the distribution of contact sizes is almost independent of load for surfaces with micro-

scopic roughness. Thus the proportionality between normal load and the real area of contact is a consequence of the inherent roughness of real surfaces and is independent of the deformation characteristics of individual asperities. The principle underlying this general result has been recognised by Archard (64), although he has only demonstrated it for the elastic contact of a model surface having asperities of an unlikely geometry.

Kraghelsky and Sablenikov (65) have carried out experiments to obtain the area of contact between transparent surfaces, and observed that the true area of contact increases with the load W. Archard (66) has pointed out that it is very difficult to envisage any deformation process which will give an index of W outside the range of 0.67 to 1.

The observance of asperity persistence and the failure of Moore (67) to show how the plastic deformation could be sustained between surfaces where rubbing takes places, have led Blok (68) and Halliday (69) to consider the shape of surface asperities which could be pressed into the general surface level without incurring plastic deformation. It has been shown that the criterion that satisfies certain conditions under which surfaces could make elastic contact can be described as:

$$m = \frac{H_t}{\ell} = \frac{d_1}{2R} = \left(\frac{H_t}{2R}\right)^{\frac{1}{2}} < \frac{KH}{E} \qquad 5.3$$

where:

m : is the average surface slope

r : is the radius of curvature

ℓ : is the asperities spacing

K : is a constant with value between 0.8 and 1.7 depending upon the assumed shape of asperity

Halliday (70) has examined the surface slopes using electron microscopy to justify equation (5.3). He shows that the surfaces which have been subjected to gross plastic flow and have asperities which conform to this criterion, even those subjected to relatively severe wear, contain asperities which deform according to equation (5.3) and thus may not be plastically deformed.

Archard's model (Figure 8) shows that the relation between the area δA_t and load W is very close to direct proportionality, while the apparent area of contact has a negligible influence. The relationships between the area A_t and the load δ W at a single asperity contact with a smooth flat and the deformation of the asperity at depth u, are:

$$\delta A_t = \pi . R . u \qquad 5.4$$

$$W = \frac{4}{3} E R^{\frac{1}{2}} u^{3/2} \qquad 5.5$$

The surface model assumed is a gaussian distribution, so that the probability of finding an asperity between heights Y and (Y + d Y) is ϕ (Y) dY. In this case the total contact area A_t and the total load W are:

$$A_t = \Sigma \delta A_t = \zeta \int_a^{\infty} R (Y - a) \phi (Y) dY \qquad 5.6$$

$$W = \Sigma \delta W = \int_a^{\infty} \frac{4}{3} E R^{\frac{1}{2}} (Y - a)^{3/2} \phi (Y) dY \qquad 5.7$$

where:

ζ : is the density of asperities per unit area

a : is the separation between two surfaces

The results also show that the true area of contact under a certain load is proportional to the number of contacts.

5.3.2.3 The Effect of the Surface Texture on the Contacting Surfaces

The elastic theory of contact, though successful in explaining some of the observed behaviour during wear tests, fails to confirm the proportionality between load and true area of contact, which is important for the explanation of the friction laws.

Kraghelsky (52), who has studied the interaction of two rough surfaces, comes to the conclusion that the heights of the asperities and their configuration on the contact surfaces are so vastly different that a compression of the surfaces will inevitably result in mechanical friction due to deep mutual penetration of the surfaces involving a voluminal destruction of the two bodies. Archard (64) points out that, although plastic flow may be expected to occur on the first few passes of two contacting surfaces in relative motion, it will not continue indefinitely. Some equilibrium state would occur when the asperities could support the load elastically. He adds that, even if the deformation is entirely elastic, the area of contact is nearly proportional to the load, the crucial point being the consideration of multiple contact condition.

Archard (64) shows that, as the model contains more small scale size of asperities, the relation between the area of contact and load becomes near to direct proportionality. The basic argument is that, because the topography of real surfaces is complex, the relationship between the area of contact and load must be so close to direct proportionality that the laws of friction can be accepted for multiple contact conditions, even if the deformation is entirely elastic.

Kraghelsky and Demkin (71) have estimated the true area of contact by using a model that consists of a regular spherical or cylindrical waviness. There are conical protrusions which are considerably less than their own height. They assume that the growth of the contact area is mainly due to the increase in the number of contacting protrusions, while they neglect the diameter of the contact spot, i.e consider it to be constant, after it has reached a certain pressure. The results obtained by using this model show that the relative real area of contact is a function of the approximation and is determined with sufficient precision by a parabolic function, consisting of two parts; the area of plastic contact and the elastic part, which is dependent on the bearing area curve of the surface waviness and elastic properties of the material.

Archard and Hirst (72) come to the same conclusion about the slight change of the area of contact spots when the load is increased.

CHAPTER 6

THE EFFECT OF SURFACE ROUGHNESS ON THE HOLDING LOAD OF SHRINK-FITTED JOINTS

6.1 Introduction

The control of surface texture of a work piece has become increasingly important during the last few decades. It has become obvious that surface texture is a determining factor with respect to the cost, wear, fatigue strength, load carrying capacity, heat transfer, noise, appearance and life of any manufactured part.

All manufactured surfaces depart to some extent from perfect smoothness and perfect geometrical form. These deviations take the form of a succession of peaks and valleys which vary in amplitude, spacing and form. The surface texture represents a combination of irregularities of various kinds and magnitudes, whose presence is due to several different causes, i.e. machining or finishing processes, machine vibration, tool wear, etc.

Surface texture measurement is important in the control of manufacturing processes and determining the functional behaviour of components. Surface finish control involves additional cost and should be restricted only to functionally important surfaces. That is why a set of roughness parameters which describe the main characteristics of the surface with respect to the function of interest should be found. For example, in the case of static contact

between surfaces, it is clear that the functional behaviour of a surface under static loading is dependent on the true area of contact. Many investigators (73 to 78) have shown that the area of contact is influenced by the surface characteristics, such as the density of peaks, the mean peak heights, the variance of peak heights, the mean slope of the surface profile, the mean and the variance of curvatures. The main concern of other researchers concentrates on the relationship between surface roughness and functional behaviour. They attribute the influence of parameters, like elastic contact, wear, lubrication, friction, sealing capacity, etc., to similar characteristics. The results of recent research show that for any reliable study of contact problems, the classical parameters, like the CLA or peak to valley height, are not enough for the establishment of a coherent contact theory.

6.2 Surface Roughness Assessment

The machined surfaces are generally characterised using the value of the ordinates of a profile obtained from a specified section through the surface referred to as a specified length (sampling length). It is always considered that the roughness average value, CLA, represents only a specific parameter of the surface roughness. In fact, however, the performance of the mechanical parts depends not only on the centre line average value, but also on the form of the roughness profile, which constitutes the so-called "typology" of the roughness profile itself.

The stylus profilemeter has for many years been the major technique used to measure the different parameters of surface texture. It is still being used now with the addition of analogue to digital conversion techniques, which allows the full power of the digital computers to be hardnessed in surface texture analysis.

The impact of the introduction of the digital techniques for measuring machined surfaces appears in the work of Greenwood and Williamson (73), who were among the first researchers to use this technique. By examining the distribution of the peak height for many machined surfaces, they conclude that even surfaces which do not have Gaussian distribution of heights appear to display Gaussian distribution of peak heights. Pesante (79) proposes an assessment of surface roughness using the amplitude density function and the bearing area curves. He continues to show how the shape of the bearing area curve and the amplitude density function change with the various machining operations. While Reason (80) shows that the crest spacing should be taken into account by drawing the consolidated profile with a crest spacing nominally equal to that of the original profile. Reason's ideas have proved to be particularly useful when both theoretical and experimental investigations are applied to machine tool joints as performed by Schofield and Thornley (81, 82).

Whitehouse and Archard (74) suggest that the sampling interval will affect the computed mean radius of the asperity curvature. They propose that the surface profile could be treated as a random signal. The profile is then assumed to have a Gaussian

distribution of height in an exponentially decaying auto correlation function. The sampling interval at which the auto correlation function decays to 0.1 of its original values is defined as the interval at which the ordinates of the digitised profile are statistically independent. Thus, curvature measured using this interval should reveal the main structure of the profile, while shorter sampling intervals could reveal only the fine scale structure. Onions and Archard (83) extend the above approach to a theory of contact and come to results similar to those of Greenwood and Williamson.

Recently, Thomas and Sayles (84) have shown that, since shorter wavelengths on the surfaces of joints may suffer plastic deformations, the surface profile should be filtered to eliminate these wavelengths. They also suggest that the surface should be filtered to eliminate any wavelengths that are longer than twice the longest dimension on the joint surface. The remaining part of the profile is then assumed to have an exponentially decaying auto correlation function. The basic objection to the above method of treatment is that this part of roughness, which is filtered, is the major source for studying the elastic behaviour of joints (85, 86, 87). Furthermore, very small roughness asperities could persist, and resist plastic deformation (88), and thus, instead of being crushed, they can display elastic behaviour which cannot be ignored.

Thomas and Sayles (89) argue about the effect of the sampling intervals on the surface parameters. They come to the conclusion that some parameters, such as asperity curvature and slopes are not intrinsic properties of a surface or surface profile, but are functions of the sampling interval. They show that rough surfaces are produced by non-stationary random processes, and that, as a consequence of this, such parameters as r.m.s. or CLA roughness and correlation length are also non-intrinsic properties of a profile, and must be defined in terms of a band width of wavelengths.

Stout (90) suggests that the skewness and kurtosis of the height distribution are useful in predicting the functional behaviour of the surface, while Whitehouse (91) argues that those parameters are non-discriminant between widely different machining operations.

6.3 Effect of the Surface Roughness on the Static Coefficient of Friction

The effect of surface roughness on friction has been known to early investigators, e.g. Amontons, Coulumb, Rennie and Hirn (all of whom investigated the problem in the period from 1699 to 1854). Explanations to that effect have been given either as lifting the load from one position of interlocking surface irregularities to another, or by bending and fracture of the asperities. The friction between metallic surfaces is no longer regarded purely as a surface effect, since during sliding metallic junctions are formed and then sheared.

Bowden et al (92) have found that mutual contact between individual asperities result in plastic deformation and that friction could be attributed to the successive and continuous forming and shearing of the welded junctions. McFarlane and Tabor (47) have first analysed the deformation process experimentally for the contact of steel on vanidium, and have introduced a relation between μs and the shear strength of the junction. The results show that the relation between the coefficient of friction and other parameters is as follows:

$$1 + \alpha \mu_s^2 = \sigma^2 \qquad 6.1$$

where σ is the coefficient of adhesion and α is a constant.

They show that with certain assumptions, equation (6.1) is considered to be equivalent to the relation:

$$P^2 + \alpha S^2 = K^2 \qquad 6.2$$

where P is the nominal normal stress, S is the nominal shear stress and K is the initial contact pressure.

Bowden and Rowe (93) have examined the above relation for other metals and confirm that it is applicable to gold, platinum, silver and copper, and that the value of α is about 3. Because of the variations in the value of α, Bowden and Tabor (46) emphasise the inadequacy of the experimental techniques for contact area measurement. A ploughing term is also postulated as an unknown

factor in the determination of α. They consider the shear strength only at the interface and neglect the importance of α in determining the friction force. In dry friction the shear strength cannot be taken as the only factor controlling the friction conditions. The shear strength is considered to have a value far from the ideal case, where the coefficient of friction is sensitive to the shear strength. In such cases, α plays an important part in determining the friction. Tabor (48) suggests that fracture takes place at the interface when the shear stress exceeds the shear strength at the interface. Consequently, the theory could relate the interfacial shear strength directly to the static coefficient of friction. It is therefore suggested that low friction would result from low shear strength at the interface. Rubenstein (94) modifies Tabor's theory by assuming a linear relationship between the shear strength and the normal pressure, although the relation has not been examined experimentally. Furey (95) states that surface topography is an important factor in dry friction, but no attempt has been made to evaluate that assumption theoretically.

The interaction of surface asperities during sliding has been studied in several investigations made using macroscopic models made of plasticine, aluminium, copper and lead (8, 96, 97, 98). Edwards and Halling (51, 99) have studied the effect of the plastic interaction of surface asperities on μs and found that it is a function of the shear strength of the junctions and the angles defining the initial asperity geometry. However, no quantitative relations have been introduced.

Hisakado (100, 101) has investigated the effect of surface roughness on dry friction between two metals, assuming that the asperities are cones of slopes which depend on the surface roughness. A theoretical expression is derived which includes ploughing and adhesion in determining the friction coefficients for cones, spheres and square pyramids ploughing along a soft metal surface. A comparision of calculated values based on this theory with experimental data shows good agreement. Hisakado suggests that the theoretical estimation of the coefficient of friction between two metal surfaces can be determined using the relations between the surface roughness, the slope of the asperities and the coefficient of friction due to the adhesion at the interface. The relationship between the coefficient of friction μs, slope $\tan \theta$ and the coefficient of friction due to adhesion at the interface μ, can be written as:

$$\mu s = \zeta s \, \mu + (1 - \zeta s) \frac{\frac{2}{\pi} \tan \theta + .5 \, \mu \, (\frac{1}{\cos \theta} + 1)}{(1 - \frac{2}{\pi} \mu \tan \theta)} \qquad 6.3$$

where:

μ : is the coefficient of friction due to adhesion at the interface.

ζs : is the ratio of the normal load supported by the junctions at which adhesion only takes place to the total normal load.

Tuskizoe and Hisakado (102) have found experimentally that the relation between the mean slope and the maximum height of the

irregularities in the direction normal to the surface lay can be described as:

$$(\tan \theta)_{Ht} \text{ mean} = \frac{Ht}{3.48\ Ht + 23.46} \qquad 6.4$$

Greenwood and Williamson (73) consider that the contact of nominally flat surfaces may be explained by the shapes of the peaks and their distribution through the upper decile of texture. Ghabrial and Zaghlool (103) have carried out an experimental investigation to examine the comparative effect of various surface finish parameters on μs for steel surfaces prepared by different machining processes. The results show that the most significant surface roughness parameters affecting μs are the initial asperity angle θ and a specific process parameter, (the product of the standard deviation of peaks distribution (σp) and the smoothness index or peaks shape factor, which is the ratio of the depth of smoothness G, and CLA values).

Empirically, the relation between μs and surface finish parameters for a wide range of surface roughness has been found to have the following general form:

$$\mu s = 0.12 + 10^{-4} (18\ \theta + 60 \log (\sigma\ p.G/CLA) + 0.8\ \varepsilon \qquad 6.5$$

where:

ε : is the mutual approach.

The relation between the slope and CLA has been found to be:

$$(\tan \theta)_{CLA} = \frac{CLA}{3.1\ CLA + 3.35} \qquad 6.6$$

Recently, Koura (104) has investigated the effect of surface texture on the ploughing and shearing components of friction using a theoretical model based on experimental data, and arrived at the following conclusions:

(1) The theoretical estimation of the coefficient of friction based on the fact that the surface texture has an idealised conical asperity shape is basically incorrect. The cylindrical and hemispherical asperity models do give a qualitative and not a quantitative assessment. For the correct evaluation of the friction components, both the number of asperities and the interaction depth should be considered in addition to the actual area of contact, as has been done in the model.

(2) The maximum value of the coefficient of friction is found to occur at a roughness CLA = 1.5 μ.mm with the two components being almost equal (shearing and ploughing). If CLA increases, the shearing component becomes dominant, as it increases linearly with CLA, while the ploughing component remains almost constant with a slight decrease at relatively high roughness. For smooth surfaces both the ploughing and shearing

components change sharply, at first decreasing, until it approaches zero and, subsequently, increasing until it is affected by the depth of interaction between the mating asperities.

(3) The adhesion theory of welding and shearing of asperities with plastic deformation and junction growth appears to be feasible for smooth surfaces. However, for rough surfaces only continuous shearing of asperities has been detected.

6.4 Estimation of the Value of the Static Coefficient of Friction μs

Tsukizoe et al (15) have investigated the effects of surface roughness on the holding load of shrink-fitted joints. For the purpose of comparing the theoretical and experimental values of the holding load, the static coefficient of friction is estimated by substituting a value of $\zeta_s = 0.7$ and $\mu = 0.4$ in equation 6.3. This technique has proved very successful in representing the experimental data. One of the drawbacks of equation 6.3 is that it uses only one method of determining the value of the mean slope ($\tan \theta$), which cannot be fully representative of all types of surface variations.

In the present investigation a similar approach has been adopted for the evaluation of the friction coefficient μs. It is considered that an average value of the mean slope depending on the different parameters that characterise the surface, namely, CLA, H_t and the average wave length represent a better estimation of the mean slope. The equation used to calculate the mean slope is as follows:

$$\tan(\theta)_{av} = \frac{\tan(\theta)_{Ht} + \tan(\theta)_{CLA} + \tan(\theta)_{\lambda}}{3} \qquad 6.7$$

where:

$$(\tan\theta)_{\lambda} = \frac{2\pi(CLA)}{\lambda_{av}} \qquad \text{(Whitehouse 105, 106)} \qquad 6.8$$

The average mean slope calculated from equation 6.7 is substituted in equation 6.3 to evaluate μs. The average wave length (λ_{av}) is determined using the high spot count on the talysurf (4) and taken as the average of ten traces taken at the mean line.

6.5 Calculation of the Sheared Area During Releasing the Fit

6.5.1 Introduction

When two nominally flat metal surfaces are brought into contact, they begin to touch at the tips of the higher asperities. After the beginning of contact the penetration of the one surface into the other surface follows. The total real area of contact resulting from the penetration depth is determined by the deformation of the metal occurring at the contact surfaces under the applied load.

The penetration depth, i.e. the distance through which the one surface moves into the other, is therefore dependent on the applied load.

It is generally accepted that the real contact area under the applied load is a small fraction of the apparent area of contact. The average distance between the opposite surfaces under an applied load is also dependent on its value. At every contact point in the mating surfaces, even an infinitesimal load will deform the tips of the contacting asperities beyond its elastic limit (107) and a condition of full plasticity will readily be established. After reaching a stage of full plasticity, the flow pressure P_f is found to be almost independent of the load. In this case, the real area of contact A_t under the applied load W can be written as:

$$A_t = \frac{1}{P_f} .W \qquad 6.9$$

Assuming that the surface profile can be represented using a normal distribution, the true area of contact between the two surfaces under the applied load can be deduced. These theoretical implications will be discussed later.

6.5.2 The Relationship between Macro and Micro Interference

The discrepancy between the shaft and ring diameters is donated as the actual interference U_a after fitting. The actual interference value can be divided into three as follows:

(1) A macro-interference δma due to the elastic or plastic deformation of a shaft and a ring.

(2) A microscopic interference δmi due to the plastic deformation at the tips of the contacting asperities.

(3) An ineffective interference δin due to the difference between the measured interference and the interference at the beginning of contact of the asperities in the shrink-fits.

Hence, the actual interference U_a can be written as follows:

$$U_a = \delta ma + \delta mi + \delta in \qquad 6.10$$

6.5.2.1 Macroscopic Interference

The macro-interference is basically due to the elastic deformation of the bulk of the material. This value can be readily established according to Lame's formula as follows:

$$\delta ma = d \left[(1 - \nu_1) \frac{1}{E_1} + \left(\frac{D^2 + d^2}{D^2 - d^2}\right) \frac{1}{E_2}\right] P_m \qquad 6.11$$

When the shaft and ring are of the same material, equation 6.11 can be simplified as:

$$\delta ma = \frac{2d}{E} \left(\frac{D^2}{D^2 - d^2}\right) P_m \qquad 6.12$$

The contribution of the macro-interference in the total value of interference in a shrink-fitted joint can be calculated by substituting equation 6.9 in equation 6.12 to arrive at the relationship between the macro-interference and the bearing area curve %.

$$\text{Where:} \qquad P_m = \frac{At}{A} \; P_f = (B.A)\,\%\; P_f \qquad 6.13$$

The material flow pressure (P_f) is assumed to be equal to the Vickers Hardness value (Yc), as suggested by Schofield (87).

For calculating the macro-interference, equation 6.12 can be written as:

$$\delta\, ma = K_1 \,.(B.A.)\,\% \qquad 6.14$$

where K_1 = constant depending on joint size, flow pressure and modulus of elasticity.

6.5.2.2 Microscopic Interference

When an ideal flat surface is brought close to a rough surface, the true area of contact as resulting from the movement of the ideal flat surface over a distance $U = m\,\sigma - u$ under an applied load, A_t is the summation of the individual areas of asperities crossed by the ideal flat surface at given separation distance u.

For a normally distributed rough surface, A_t is given statistically as follows:

$$A_t = A. \frac{F\ (U)}{f\ (-m\sigma)} = A.\ (B.A.)\ \% \qquad 6.15$$

where:

$$F\ (U) = \int_{u}^{m} \frac{1}{\sqrt{2\pi\sigma}} e^{-\frac{1}{2}\left(\frac{u}{\sigma}\right)^2}$$

σ : standard deviation

m : a constant depending on the surface roughness and type of finish. (m is the peak to valley height of curve profile.)

$m\sigma$: is a distance between the tip of the highest asperity and the median line of curve profile.

δ mi represents the micro-interference value between the shaft and the ring. By analogy, the separation distance U can be given as $(\frac{\delta\ mi}{4})$. It is possible to find the relationship between the macroscopic and microscopic interference by using the measured bearing area curve or assuming that the surface profile has a normal distribution, as the following paragraphs show.

6.5.2.2.a The Measured Bearing Area Curve Method

The bearing area curve is measured using two traces taken across the lay for every specimen. The B.A.C. is then drawn representing the relationship between the penetration depth and the percentage area of contact. If δ mi is the micro-interference between the shaft and ring diameters, then the value of micro-interference on the joint radius is $\frac{\delta \text{ mi}}{2}$, i.e. the micro-interference for one surface is $\frac{\delta \text{ mi}}{4}$ µmm.

At different value of $\frac{\delta \text{ mi}}{4}$, the corresponding percentage of the bearing area % can be calculated for the shaft and ring. The average value of (B.A.) % of the shaft and ring is calculated, and by substituting in the equation 6.14 the value of the macro-interference corresponding to every value of micro-interference is estimated. Hence, the relationship between actual, macro and micro-interference for every joint can be found, as shown in Figures 9 to 12.

6.5.2.2.b The Normal Distribution Method

Assuming the distribution curve of the surface profile is a Gaussian distribution (Figure 13), the bearing area diagram of the surface can be described by the following equation:

$$Y = \frac{1}{\sqrt{2\pi\sigma}} \int_{o}^{x} e^{-\frac{1}{2}\left(\frac{x}{\sigma}\right)^2} dx \qquad 6.16$$

The curve representing the aforementioned equation for different values of Y can be drawn using the statistical probability tables. The previous curve can be drawn as to represent the relationship between (B. A.)% of the joint and the value of micro-interference, as shown in Figure 14.

In performing this conversion, the following remarks should be taken into account:

(1) The ordinate of the curve (Y) represents the percentage area sheared during releasing the fit.

(2) The abscissa of the curve represents 12 σ which is equal to the maximum height H_t of the surface profile, where ($H_t = H_{ts} + H_{tr}$) and can be taken as a measure of micro-interference.

In this formula:

H_{ts} = Peak to valley height of the shaft surface profile.

H_{tr} = Peak to valley height of the ring surface profile.

6.5.3 Estimation of the Sheared Area using the Bearing Area Diagram

The sheared area at different values of interferences and surface finish (H_t) can be found using the curve represented by equation 6.16 as follows:

(1) The number of divisions representing the full scale of H_t = 12 divisions.

$\therefore$ Number of divisions representing a given value of micro-interference (X) is,

$$X = \frac{12}{H_t} \cdot \frac{\delta mi}{2} = \frac{6.\ \delta mi}{H_t} \qquad 6.17$$

where:

$\frac{\delta mi}{4}$ is the value representing the distance between the actual contact line and the peaks of the surface profile.

(2) δmi and H_t are known hence by substituting equation 6.17, we get (X) and from the curve in Figure 4, we can obtain the corresponding value of Y, which is equal to the percentage contact area for the given δmi and H_t.

(3) The sheared area for the definite values of δmi and H_t becomes:

$$S.\ A. = Y \times A = (B.\ A.)\% \times \pi\ dL \qquad 6.18$$

where:

L = The length of the joint, (length of contact).

6.6 Estimation of the Holding Load using the Static Coefficient of Friction

In many of the previous investigations the holding load for shrink-fitted joints has been based on the assumption that the joint is subjected to pure friction (14, 15, 108). The friction between the mating surfaces can be given as:

$$H.\ L. = \pi d.\ L.\ P_m\ \mu_s \qquad 6.19$$

The coefficient of friction μs is normally given values of between 0.2 and 0.6 for machined surfaces made of mild steel. The value of the mean pressure (P_m) is estimated using Lame's equation. The value of interference (δm) is considered to be equal to the macro-interference. The main drawbacks of using this approach is the over-estimation of the joint's holding load.

The method adopted in the present work is based on estimating the mean slope of the surface profile using three different methods, as previously mentioned, and taking the average value, which overcomes the basic deficiency of over-estimating the holding load, which can lead to the joint prematurely failing under loading. By substituting in equation 6.3, which has been predicted by the theory of dry friction between rough surfaces (101), the value of μs can be calculated.

The value of the coefficient of friction (μs) is calculated from equation 6.3. The method of calculation and the values of the mean slope are shown in Tables (1, 2). As described previously, the value of (P_m) can be calculated for every level of macro-interference. The value of the holding load can then be calculated using the coefficient of friction and the mean pressure (P_m), as in equation 6.19.

6.7 Estimation of the Holding Load using the Sheared Area

6.7.1 Based on the Measured B. A. C.

The contribution that the macro-interference makes to the total interference value can be obtained, as discussed in (10.5.2.2.a). The value of the mean interference δm is corrected to give the actual value of interference (U_a), as previously mentioned in Section (6.5.2). Then equation 6.14 is used to obtain the (B. A.)% corresponding the macro-interference value. The holding load can be estimated using the following equation:

$$H.\ L. = A.(B.\ A.)\%\ .T \qquad 6.20$$

6.7.2 Based on the Normal Distribution Curve Method

The sheared area can be estimated using the same steps described in Section (6.5.3) and equation 6.18. The holding load can be evaluated using the same procedure as above.

CHAPTER 7

THE STIFFNESS OF THE MACHINE TOOL JOINTS

7.1 Introduction

Joints are an essential part of machine tools. They are required for assembling, manufacturing, transportation and as a functional component of the machine structure. Joints can be divided into two main types, e.g. fixed and sliding joints. Fixed joints are those which hold together the parts of a machine structure, so that there is no relative movement between the parts, e.g. the joint between the base and column of a radial drilling machine, between the pulley and rim of large gears or between shafts and bearings. They are usually held together under pressure by studs, bolts, or by using interference fits.

In practice, joints are in most cases subjected to a system of loads such that normal and shear forces are transmitted by the joint interface. The main requirements for machine tool joints are stiffness and wear resistance. In machining operations the accuracy is affected by the normal and shear displacements in the different machine joints, like dead stops, rotary tables, slides, cutter-heads and also the turrets in precision machine tools. In high precision machine tools operating with very low cutting forces, the machining accuracy is also affected by the shear deformations in a contact joint due to dynamic forces developed during the operation. The

conditions in which such joints operate should ensure that any deformation must be limited to the elastic range. In the case of fixed joints, the static and dynamic stiffness and the damping capacity are especially important factors, as they determine the dynamic behaviour of the machine tool.

A great deal of work in the past four decades has been directed towards investigating the mechanisms in action within the joint interfaces. The early investigations date as far back as 1699 to Amontom's laws of friction, their verification by Couloumb and their later development by Bowden and Tabor (46).

7.2 Joint Stiffness in the Normal Direction

Most of the previous research in the past four decades has been concerned with the joint stiffness in the normal direction. The earliest known investigation into the deflection of joint faces under normal loads within the elastic condition has been made by Votinov (109), who proposes that the joint elastic deformation can be described by the following equation:

$$\lambda_J = C\, P^{\alpha} + K \qquad 7.1$$

where:

C, α and K are constants to be estimated experimentally. This work has been followed by Levina, Reshetov and Ostrovskii (110, 111), whose analysis has followed similar approaches.

The most extensive work on the subject, however, is attributed to Thornley, Connolly and Schofield (81, 85, 86, 112, 113, 114), who have investigated the deflection of machine tool joints formed from relatively large areas. The experimental results show that, as the applied load increases, the plastic deformation progresses, and if the load is removed, the joint recovers elastically. The non-linear behaviour of contacting surfaces in the normal direction is attributed to the changes which take place during loading and unloading in the joint dimensions, condition and the number of the asperities carrying the load. The general characteristics of joints are shown in Figure 15. The relationship between the mean interface pressure and the joint deflection proposed is as follows:

$$\ln P = m \lambda_J + C \qquad 7.2$$

where m and C are constants depending on material properties and surface roughness.

Greenwood (63) arrives at the conclusion that the joint stiffness is dependent on the applied load and not the apparent pressure. He has been able to show that theoretically by using an exponential approximation of the upper tail of a Gaussian distribution to represent the asperities peaks, the joints elastic deformation can be estimated using the following equation:

$$\ln P = C - \frac{U}{\sigma} \qquad 7.3$$

where C is a constant, σ is the standard deviation of peak heights and u is the separation between the mean planes of the two surfaces. The results also show that the surface stiffness increases with decreasing the surface roughness. Schofield (81, 82, 87) shows that the surface roughness using asperity shapes based on the shape of the bearing area diagram (115) could be realised by a mathematical expression. The elastic recovery of the joint would be obtained from:

$$\lambda_J = C \sqrt{P} \quad F \qquad 7.4$$

where C is a constant which depends on material properties and the shape given to the asperities where F is the cutting tool feed rate.

7.2.1 Effect of Lubrication on the Joint Stiffness

The effect of lubrication upon the joint stiffness has been investigated by Connolly (116), who has found that the presence of grease or oil has no significant effect on the elastic recovery of rough machined surfaces, while it has an effect on fine surfaces. Levina (117) reports a slight increase (15 to 20%) in the static stiffness when rough joints are lubricated. It has also been shown (118 to 128) that the energy dissipation increases as the quantity and viscosity of the lubricant increases, and that it decreases by increasing the applied load. The dynamic stiffness of non-lubricated joints does not differ from their measured static stiffness, while an increase in the joint preload increases its dynamic stiffness and

reduces the loss factor (129). Within the frequency range of 20 to 300 Hz, the joint stiffness under dry clean conditions is found to be frequency independent, whilst the loss factor increases linearly with frequency. The amplitude of vibration is found to have no effect on either the dynamic stiffness or the loss factor.

7.3 The Horizontal Stiffness of the Joint

In many practical configurations the joints are subjected to tangential loading. The information on stiffness characteristics of machine tool joints in the tangential direction is limited when compared to that of the normal direction. The reason may be attributed to the difficulty in arriving at reliable predictions due to the constant deterioration caused by fretting, corrosion and its irreversible behaviour. However, the calculations for the joints failure in the tangential direction are normally carried out on the basis of the coefficient of friction, but this may prove unsatisfactory in some cases, because the loads may exceed the elastic limit causing irreversible displacements to occur before the joint fails. It is necessary to design the joint in such a way that the shear deformations remain below the plastic limit.

Kirsanova (130) has been one of the early investigators to study the characteristics of joint surfaces loaded in the tangential direction. The test specimens are made of grey cast iron with large contact areas (225 cm^2). The results show that for repeated loads which do not exceed the first loading limit, the displacements are

also limited to the elastic range, as shown in Figures 16, 17. It has also been observed that at the elastic limit, the ratio between the shear stress (T) and the normal stress (Pn) has a constant value over the measured pressure range (1 to 15 kg/cm^2). This ratio is approximately half the static coefficient of friction, as represented by equation 7.5:

$$\mu_y = P_{sy} \; / \; P_n \qquad 7.5$$

where P_{sy} is the limit shear pressure for elastic deformation and P_n is the normal pressure. The value of μ_y in equation 7.5 has been found experimentally for several values of interface pressures, and proves to be independent from P_n.

In the case where the initial relative position of the components is of prime importance, the joints should be designed so as not to exceed the material elastic limit in the first loading. In this case the shear pressure must be limited by the following value:

$$P_S \text{ max.} = \mu_y \cdot P_n \qquad 7.6$$

If the initial relative position of the components is not so important, the pressure can be limited by the static friction force and the shear pressure with deflection related linearly by the following equation:

$$\lambda_s = K_t \cdot P_s \qquad 7.7$$

Figure 18 shows the value of K_t as a function of the pressure and surface finish for cast iron. As can be seen from the Figure, the shear stiffness increases with decreasing the surface roughness.

Masuko et al (131) have also investigated the shear stiffness of bolted joints using steel and cast iron specimens and interface pressures of 100 and 200 kg/cm^2. They report that the horizontal displacements of the joint surfaces are larger than for the equivalent solid specimen and that it is due to the sum of the elastic displacement and the micro-sliding between the joint surfaces. The results show that the joint stiffness has a value of about 70 to 90% compared to the stiffness of the equivalent solid in spite of the very high preload. The horizontal displacement of the joint surfaces is almost linear with the applied tangential load during the loading and unloading process under high normal preload, while under low normal preload the relationship is non-linear due to the hysteresis. They report on two types of hysteresis loops, one having a repeatable loop (ground mild steel and brass), and the other a progressive loop having a gradually decreasing width (ground cast iron).

Back et al (132, 133, 134) have carried out experimental work to investigate the normal and shear stiffness characteristics of joint interfaces formed from cast iron surfaces. The results show that, after the initial application of the shear pressure, a large amount of permanent deformation is observed. They consider this deformation to represent the plastic shear deflection of the asperities, as shown in Figure 19. After the first loading, the

subsequent unloading and loading show good repeatability if the shear pressure is kept equal to or below the first maximum loading. Therefore, they conclude the following:

(1) The shear compliance can be determined as a function of the normal pressure according to equation 7.8:

$$K_s = \frac{R}{(P_n)\ S} \qquad 7.8$$

where R and S are constants depending upon the materials and surface finishes of the contacting parts.

(2) For higher interface pressure the shear stiffness becomes independent of the machining process.

(3) The relationship between the normal and shear stiffness of the machined surfaces can be estimated using the following equation:

$$\frac{d\,P_m}{d\,\lambda_n} \;/\; \frac{d\,P_s}{d\,\lambda_s} = \frac{E}{G} = 2\,(1 + \nu) \qquad 7.9$$

(4) It is not necessary to test the shear stiffness of machined surfaces, because all parameters can be defined from the parameters of the normal stiffness for both simultaneous and non-simultaneous loading.

Later, Shoukry and Thornley (135) have carried out theoretical estimations for normal and tangential stiffness of machined surfaces using a mathematical model. The conditions of the surface roughness and flatness deviations on the joint surface are included in the model. Their results are in agreement with the Back results. However, they come to the following conclusions:

(1) The normal stiffness of machine tool joints is dependent on the applied normal load, the root mean square value of the flatness errors on the joint surface and the level of the elastic deformation of the joint surface.

(2) The tangential stiffness of machine tool joints is dependent on Poisson's ratio and the ratio of the applied tangential load to the limiting friction force.

(3) The ratio between the normal and shear stiffness of the machined surfaces at zero applied tangential load is constant and only dependent on Poisson's ratio for the joints having similar materials. The constant also includes the moduli of elasticity and rigidity of the joints made of different materials.

7.3.1 The Elastic Deformation and Micro-Slip

When the joint surfaces are subjected to a tangential load even smaller than the frictional forces (determined using macroscopic coefficient of friction), a micro-slip can be sensed on the joint. From the standpoint of a structural design of a machine tool this micro-slip is as important as the tangential stiffness (136).

Goodman et al (137) have reported that, when a sphere is held between parallel flat surfaces by means of a constant clamping pressure and then subjected to a cyclic tangential displacement parallel to the flats, energy is dissipated at the contact. This occurs even when the maximum tangential force is less than the friction forces (μ_s N). Goodman suggests that, during the application of the normal load, there is no relative slip of the points in contact. The relative tangential displacement of the points in the two bodies at the interface is given by the equation:

$$\delta = \frac{3\ (2 - \nu)\ \mu_s \cdot N}{8\ G\ a} \left| 1 - \left(1 - \frac{P_s}{\mu_s\ N}\right)^{2/3} \right| \qquad 7.10$$

Masuko et al (138) suggest that the residual displacement is due to the micro-slip between the joint surfaces or the micro-plastic deformation on the joint surface asperities. The micro-slip value can be estimated using the following equation:

$$\delta_r = \delta_t - \delta_e \qquad 7.11$$

where:

δ_r : is the micro-sliding

δ_e : is the elastic shear deformation

δ_t : is the total tangential deformation

The surface roughness of the joint has significant effect on the tangential stiffness and micro-sliding. The micro-sliding gradually decreases with the roughening of the surface, while the tangential stiffness increases with decreasing the surface roughness (138).

The elastic displacement in the tangential direction can be determined by the elastic shearing deformation. Masuko et al (138) assume that, if the real contact area has (n) junctions and each junction is an identical circle having a radius (a), then the elastic shear deformation can be estimated by considering this as an elasticity problem (139). Equation 7.12 is utilised to determine the shear deformation and the results represent a good qualitative assessment with the Masuko's results.

$$\delta_e = \frac{P_s / n}{G \pi a} (2 - \nu) \qquad 7.12$$

where:

P_s : is the tangential force

G : modulus of elasticity in shear

ν : Poisson's ratio

7.3.2 The Effects of the Machined Lay Orientations and the Material on Joint Stiffness

The experimental results show that the machined lay orientation has no significant effects on the tangential stiffness and micro-sliding for joint surfaces made of mild steel. However, it affects them slightly when the joints' surfaces are made of either cast iron, brass or aluminium alloys. The tangential stiffness of the joints in which the machined lays are at right-angles to each other are larger than those with lays that are in parallel. The tangential stiffness of the joints is also affected by the micro-contact between the joint surfaces in addition to the effects of the machined lay orientation and the material (138).

7.3.3 The Effects of Dynamic Loading on the Horizontal Stiffness and the Micro-Slip

It has been shown (131) that for joint surfaces made of materials having a low flow pressure, the micro-seizure points do not break, but slip only within a contact point when the tangential load is applied. On the other hand, for joint surfaces made of materials having a high flow pressure, some micro-seizure points are observed to tear while the rest of the points deform plastically within a contact point. For joint surfaces made of mild steel, the contact area increases due to the tangential displacement, to reach a sufficient value to support the tangential load only after one loading cycle, after which the slip becomes small. However, for the joint surfaces made of cast iron, a large slip occurs and the tangential displacement is considered not to be

in a stable condition, even after a few loading cycles. The horizontal contact stiffness and micro-slip under a large preload are independent of the number of loading cycles, but for joint materials having a high flow pressure, such as cast iron, the number of loading cycles has an influence on the micro-slip especially under the low preload condition.

CHAPTER 8

DAMPING IN DRY CLEAN JOINTS SUBJECTED TO DYNAMIC LOADS TANGENTIAL TO THE JOINT INTERFACE

8.1 Introduction

Recently the demand for machine tool structures having a high dynamic stiffness and large damping capacity has increased. It is also, in most cases, desirable that a machine tool should have high static stiffness combined with light weight. At the design stage of a mechanism or structure, sufficient damping should be built-in the system, so that under all conceivable working conditions stress or amplitude levels may never cause failure or impair the required functioning of the structure. Dynamic stiffness is dependent on the properties of the structural elements and on the methods of joining them. The inherent damping of all fabricated structures is usually dominated by the damping that occurs in joints due to interfacial slip, the contribution from the structure material being small.

The friction damping mechanism is non-linear and difficult to analyse, because the relative interfacial slip in a joint can give rise to fretting corrosion and fatigue failure. Also it may be influenced by time effects and several environmental factors, such as temperature and humidity.

In practice, it is generally found that the frictional damping is kept to a minimum by increasing the tightening force in an endeavour to prohibit slip and minimise fretting corrosion. However, even if fretting does take place in a joint, it may be preferable to the occurrence of large resonant stress amplitudes, which may happen if the joints are rigidly fixed to prevent slipping. The surface treatments show (140, 141, 142) that it can reduce the undesirable effects of fretting between contacting slipping surfaces, and thus it would appear practical to consider the purposeful introduction of frictional damping into vibrating structures as a means of increasing the inherent damping. An improvement in fretting fatigue behaviour can be achieved by shot-peening or blasting the surfaces of the joints, since the cracks produced by fretting are unable to propagate through the sub-surface layer of compressive stresses induced. Case hardening is also known to produce a hard surface layer with high compressive stress, leading to a greatly increased fatigue life.

The frictional damping has usually been concerned with maximising the energy dissipated by interfacial slip in a joint and the conditions under which this can be achieved. Since the maximum energy dissipated by slip in a joint is independent of coefficient of friction μs, the joint interfaces and their surface preparation can be chosen to minimise the damaging effects of fretting corrosion (143, 144).

8.2 Sources of Damping

The damping sources in machine tool joints can be divided into two basic groups, namely, external and internal. The external sources comprise the friction of a vibrating system against the medium in which the vibration is produced, such as air, gas, water, oil, etc. The internal sources consist of the incomplete elasticity of the material forming the elastic element of the vibrating system, friction in the joints and linkage. The present work is mainly concerned with the second group. The energy dissipation or damping has been classified as material damping and system damping (145).

Excluding pure absorbers and viscous dampers designed and tuned to particular structures, the sources of damping in a machine tool are friction damping in sliding contacts and bearings; material damping; and damping from friction in bolted joints.

8.3 Energy Dissipation in Dry Joints

It has been known that the damping in structures having joints is several times larger than the material energy dissipation. Andrew (122) reports that, if a structure is formed by one component of cast iron, the dynamic magnitude factor is in the order of 100 to 150, and if joints are introduced, this factor decreases to about 10 to 30. The exact mechanism of this large amount of damping that arises from the joints is not known in detail, but several works explain qualitatively the influence of some parameters.

In general, the damping in joints has been studied under three operating conditions: dry surfaces, lubricated surfaces and adhesively bonded surfaces. For dry surfaces, the interface shear effects, i.e. relative motions of mating surfaces in the plane of the interface, would appear to offer greater potential for energy dissipation. Dry surfaces can also suffer deterioration due to fretting. To reduce the latter effect it is preferable to add oil or viscoelastic layers, which can be dimensioned to avoid any slip at the interface, then the general system is analysed again in terms of material damping.

The case of dry interfaces has been investigated by Lazan (145), using coulomb friction mechanism for estimating the dissipating energy under cyclic shear displacement. Goodman (146) shows that a joint is capable of dissipating very large amounts of energy if it is properly designed and optimised, as explained by the mechanism of coulomb friction. However, fretting corrosion may sometimes develop in a joint which has been optimised for maximum dry slip damping, particularly in regions subjected to large cyclic slip.

8.3.1 Damping in Dry and Lubricated Surfaces

In an investigation of the damping of dry and lubricated surfaces, Andrew (122) uses small contacting surfaces to define the inphase damping. The quadrature stiffness is measured as a function of preload, surface finish, frequency of vibration and viscosity of

the lubricants. For the case of dry surfaces, the quadrature component is not measurable and the inphase stiffness is independent of the frequency; this means there is no damping in dry surfaces actuated normally. When oil is introduced at the interface, the previous parameters have such effects as a superposition of the characteristics of dry contact and oil film. The results show that, after the addition of oil, the quadrature and inphase stiffness components rise with the increase of the frequency of the applied load. Also the energy dissipation increases as the quantity and viscosity of lubricant increase. Corbach (120), Thornley and Lee (147) have carried out similar work and their results follow the same trends.

Thornley (124, 125) shows that the damping ratio decreases with increasing preload and increases with an increase in lubricant viscosity. Khoyi (127) reports that the main parameters which influence the loss factor of a joint, are the joint's apparent area, its surface roughness and the applied load. An increase in joint preload reduces the loss factor. The frequency and amplitude of vibration are found to have no significant effect on the loss factor. Later, similar results have been obtained by Shoukry (129).

8.3.2 The Energy Dissipation in Simple Joints

Hanks (148) has carried out tests to investigate the effect of the vibration amplitude, joint clamping pressure, model scale and lubricant at the interface on the damping capacity of the joint. He uses the logarithmic decrement method to estimate the damping for dry

interfaces and the results show that the loss due to air and material could be considered independent from the amplitude, but the total damping of the joint increases linearly with the amplitude of vibration and decreases with the increase of the clamping pressure. It has also been observed that the total damping increases by decreasing the scale factor. When oil is added to the interface, the damping is affected in the same way as dry joints, but the logarithmic decrement is always larger.

An experimental analysis of the damping on a clamped cantilever has been carried out by Ito et al (136). Apart from factors such as surface finish and bolt size, the main parameters that have been analysed are the clamping pressure, beam thickness and the distance between the bolts. It has been observed that an increase in the interface pressure increases the damping capacity to a certain maximum, whereafter it decreases, which means that an optimum interface pressure exists. When the thickness of the beam increases, the damping also increases. It has been observed that there is also an optimum value regarding the damping capacity.

Earles (149) has carried out an experimental and theoretical study to assess the energy dissipation using a joint made of stainless steel, with its surfaces finely ground. For the purpose of the theoretical analysis of the energy dissipation, it is assumed that the surface is stiff in shear and that the slip at the contact occurs when the friction force is reached. It has been observed that a partial slip occurs at low levels of tensile load, while the gross slip occurs when the level of load reaches a value larger than

the friction force. In both cases, theoretically and experimentally, the hysteresis loops are closed and the agreement between theoretical and experimental results is good mainly for partial slip. It has also been observed that for the partial slip the friction conditions are nearly constant with time, while for the gross slip this is not true due to the fretting of the surfaces.

8.4 Calculation of Energy Dissipation in the Shrink-Fitted Joints Due to Friction

The following assumptions have been adopted for the determination of the energy losses in the shrink-fitted joints:

(1) The coefficient of friction is assumed to be constant over the entire area of the contacting surfaces and independent of time. The independence of time is a precise assumption as long as the shear deformations of the surfaces are elastic, whereas if the shear slip is large, fretting will arise, as is reported by Earles (149). The fretting changes the friction conditions and with the passing of time the joint will not follow the predicted behaviour.

(2) The energy dissipation is independent of the frequency, but dependent upon the amplitude of the tangential load.

(3) A symmetric cycle is assumed and the energy dissipation for the complete cycle will be estimated from the loading half cycle.

(4) For the case of shrink-fitted joints, it is assumed that the tangential load should not exceed the friction holding load, i.e. the joints are designed in order not to exceed the elastic limit.

Basically, the general method used is the same for any loading type, but here it will be distinguished as the case of shrink-fitted joints, where the shear slip is elastic and the normal interface pressure does not change when the tangential load is applied to the surface.

The procedure for the calculation of the energy dissipation at the joint interface due to a certain value of interference consists of the following steps:

(1) Depending upon the value of interference between the two mating parts and considering the shear deformations are elastic, equation 8.1 can be used to estimate the value of the shear deformation where:

$$\delta_e = \lambda_s = \frac{P_s / n}{G \pi a} (2 - \nu) \qquad 8.1$$

The values of n and a can be estimated from the relationship between the micro and macro-interference, at a known actual interference value, as described in Chapter 6.

(2) The friction force transmitted by the area Ai* (πa^2) is given by:

$$P_{si} = \mu_d \cdot P_{ni} \cdot A_i \qquad 8.2$$

where:

μ_d = coefficient of friction between the mating surfaces within the elastic limit of shear deformation [equal to 0.5 μ_s (130)].

P_{ni} = normal pressure between the two asperities = P_f.

(3) If the tangential force and the shear deformations of the surfaces are known, the energy dissipated at the area A_i is given by:

$$W_i = 0.5\ \mu_s \cdot P_f \cdot A_i \cdot \lambda_{si} \qquad 8.3$$

(4) The total energy dissipated at the joint interface due to a certain value of interference and tangential load is obtained from:

$$W_d = \sum_{i=1}^{i=n} 0.5\ _s \cdot P_f \cdot A_i \cdot \lambda_{si}$$

$$= 0.5\ \mu s \cdot P_f \cdot A_t \cdot \lambda_s \qquad 8.4$$

where: n is the number of asperities in contact at the contacting surface.

---

* The calculations have been based on one pair of asperities and then generalised for the whole surface.

(5) Substituting in the aforementioned equation (8.4), where:

$P_f \cdot A_t = P_m \cdot A$ and $P_m = \frac{E\ \delta ma}{2d} (1 - \frac{d^2}{D^2})$,

equation 8.4 becomes:

$$W_d = 0.5\ \mu s \cdot A \cdot \lambda_s \left[\frac{E\ \delta ma}{2d} (1 - \frac{d^2}{D^2}) \right]$$

$$= 0.5\ \mu s \cdot A \cdot \frac{P_s / n}{G\ \pi\ a} (2 - \nu) \left[\frac{E\ \delta ma}{2d} (1 - \frac{d^2}{D^2}) \right] \quad 8.5$$

A sample of calculations is shown in Appendix II and Figures 134 and 135.

8.5 Relationship between the Various Measures of Damping

Most of the measures used to describe damping are often related to the damping capacity of a single degree of freedom system with the frequency as the independent parameter.

The damping capacity of any structure can be expressed in several ways. According to Podnicks and Lazen (150), some of the more commonly used energy units are shown below.

(1) Logarithmic decrement (δ)

$$\delta = \frac{Do}{2W_o} = \psi/2 = \pi/A_r = \pi b$$

(2) Damping capacity (ψ)

$$\psi = \frac{Do}{Wo} = 2\delta = \frac{2\pi}{A_r} = 2\pi b$$

(3) Resonance amplification factor

$$A_r = 2\pi \frac{Wo}{Do} = \frac{\pi}{\delta} = \frac{2\pi}{\psi} = \frac{1}{b}$$

(4) Bluntness of the resonance curve

$$b = \frac{1}{2\pi} \frac{Do}{Wo} = \frac{\delta}{\pi} + \frac{\psi}{2\pi} = \frac{1}{A_r}$$

where:

Do = Total internal damping energy of a specimen or element.

Wo = Total elastic strain energy in an element.

The above units are all dependent upon the total damping energy unit Do. The total damping energy for any specimen not only depends on the material, but also on the size and shape of the element, as well as on stress distribution brought about by the loading method. It is clear that to define the damping properties of a material in terms of Do without specifying the details and methods of carrying out the test, can be rather misleading.

Plunkett (151) has discussed various methods of damping measurements, which can be summarised as follows:

(1) Logarithmic decrement (δ)

(2) Amplification factor (A_r)

(3) Equivalent dashpot constant (Ce)

(4) Quality factor $Q = \frac{1}{2\zeta}$

(5) Complex modulus $E' + j\,E''$

(6) Bandwidth $(\Delta f/f)$

where:

ζ = Damping ratio = $\frac{c}{Cc}$

The definition of the different measures of damping are shown in Appendix III.

8.6 Comparison of Results

It is fairly common for the researchers in the field to quote results for the same material and stress levels of similar specimens which are quite different. One has then the task of determining which result, if any, is the correct one. Plunkett suggests that under these circumstances the lowest reported value is most likely to be the correct answer, since any variation either in the testing condition or in the specimen, or any fault in the

measuring apparatus tends to increase the apparent value of damping. Furthermore, since most of the methods of determining damping are based upon the single degree of freedom system with linear viscous damping, if under excitation more than one normal mode is excited, the value of damping so measured is apt to be larger than the true value of the system.

Therefore, if other investigators are to be able to compare results of tests, the size, frequency and stress level of the specimen should be clearly stated. In using any particular method of determining damping, the basic assumptions of the method should not be violated heavily.

CHAPTER 9

EXPERIMENTAL PROCEDURE

9.1 Introduction

This Chapter describes the overall experimental plan, methods adopted for specimen preparation, measurement and joint fitting.

The experimental investigation has been designed to study the effects of surface finish, size and the value of interference on the joint's holding load, damping and stiffness under dynamic loading, as well as the stiffness and holding load under static loading. The shrink-fitted joints used are formed from a shaft and ring with the interference values for the various joints chosen according to I. S. O. standards (International Standardisation Organisation).

The specimens are divided into individual groups, with each group having the same roughness parameter CLA, and varying values of interference (δm). For each specimen a number of characteristic measurements are performed, namely, specimen size and height, CLA, bearing area, peak to valley height, spot count, average wave length, roundness, and straightness. These characteristic values are used later in the experimental and theoretical analysis.

The method adopted to produce a shrink-fitted joint consists of heating the ring in an induction oven and cooling the shaft using liquid nitrogen. The shaft and ring are then fitted together using a special fixture on a bench drilling machine. Half the specimens are tested statically and half of them dynamically.

9.2 Specimen Preparation

The specimens used are manufactured from mild steel bar (ENIA). (Specifications in Table 3.)

The design of the shafts and rings constituting the joints are shown in Figures 20a, 20b and 20c respectively. The manufacturing process has a significant influence on the type of surface finish obtained. Hence, it is necessary to change the process type and process parameters to obtain various levels and types of finish on the specimens used. The manufacturing processes and process parameters used in this investigation are shown in Table 4.

To ease the process of fitting the shafts to the rings, it is necessary to produce a small chamfer on the inside diameter of the rings. However, care is to be taken to ensure that the specimen's nominal contact area is kept constant. This is achieved using a special fixutre on a centre lathe. Each specimen is then checked using an optical microscope, to ensure a constant specimen contact area.

9.3 Measurement Techniques

9.3.1 Dimensional Measurements

The outer diameter of the shaft and the inner diameter of the ring are measured using a Universal Measuring Machine model (Mu 214B) shown in Figure 21. Six readings are taken axially for each shaft or ring with the average value taken as the effective diameter. (Machine sensitivity ± 1 μ mm). A spherical-ended feeler of 6 mm diameter is used for diameter measurement to avoid including the specimen roughness in the measurement.

The straightness of the shafts and rings is measured using a Taylor Hobson Talylin 1 shown in Figure 23, by taking different traces along the length of the specimen, as shown in Figures 24 and 25. The specimen's out-of-roundness is assessed using Taylor Hobson Talyrond Model (1) shown in Figure 26. A number of traces are recorded for each diameter at constant intervals along the specimen's height, as shown in Figures 27 and 28.

9.3.2 Surface Finish Measurement

The centre line average CLA of the specimens is determined using Taylor Hobson Talysurf 4, shown in Figure 22. The stylus is positioned to move along the specimens which are held in a vee-block to obtain the (CLA) value across the lay. The mean value of (CLA) is taken as the average of ten readings. A mean value of the peak to valley height (H_t) is calculated from a trace taken across the lay for every specimen.

The talysurf level potentiometer is set above and below the mean line to measure the percentage of the bearing area at different roughness levels. Two traces across the lay are taken to accurately evaluate the B.A., with the high spot count recorded at each potentiometer level. For each specimen ten traces are taken at the mean line from which the average wave length is calculated as the quotient of dividing the stroke length by the number of spots. A sample calculation is shown in Tables 1 and 2.

9.4 Joint Assembly

A pair consisting of a shaft and ring of almost the same surface finish (CLA) are assembled as joints of different values of interference, fulfilling the following conditions:

(a) To provide adequate interference to ensure satisfactory strength for the finished assembly.

(b) To keep the stresses resulting from the fit below the level of the material's allowable stress.

(c) To ensure that the amount of heating and cooling to the rings and shafts would provide an adequate clearance for fitting.

9.4.1 Specimens Heating/Cooling

For small values of interference the shafts are cooled using liquid nitrogen to - 196°C without heating the rings. However, for large interference values it is necessary to cool the shafts and heat the rings in an induction oven. The temperatures required to provide the adequate clearance for fitting are calculated on the basis of equation 9.1.

$$d_2 = d_1 + \alpha\ (T_2 - T_1)\ d_1$$

or $$\delta_{max.} = \alpha\ (T_2 - T_1)\ d_1 \qquad 9.1$$

where:

α = coefficient of linear thermal expansion.

T_1 = ampient temperature °C.

T_2 = final temperature °C.

d_1 = inside diameter of ring at temperature T_1.

d_2 = inside diameter of ring at temperature T_2.

$\delta_{max.}$ = interference value plus clearance value.

9.4.1.1 Cooling using Liquid Nitrogen

Once the value of interference required for a specific application is determined, it is then possible to decide whether it can be achieved by cooling the shaft alone or whether heating the ring becomes necessary.

The amount of L. N. needed to carry out specimen cooling can be obtained from equation 9.2.

$$Q_t = Q_H + Q_L \qquad 9.2$$

where:

Q_t = total amount of L. N.

Q_L = process losses.

Q_H = $(T_1 - T_2)\ W_i\ s\ /\ H_i$ 9.3

s = average specific heat J/kg^{o}C.

W_i = weight of metal to be cooled.

H_i = latent heat of vaporisation per unit weight of the component.

The special fixture designed to lower eight specimens into the L. N. bath is shown in Figure 29. The fixture ensures a fixed distance of 75 mm between the component and bath wall to ensure consistent submersion.

9.5 Shrink-Fitted Procedure

The specimens are first degreased and dried, after which the shafts are loaded into the fixture and lowered into the L. N. bath. The rings are placed inside an induction oven for a predetermined time and temperature. A jig is specially designed to ensure the best

possible alignment during assembling the joint. The shafts are clamped inside a jig and fitted to the spindle of an accurate bench drill. The heated rings are placed on a floating table (Figure 30), located on the drill base. The axial movement of the machine spindle is used to position the shaft inside the ring to a pre-determined depth. The assembly is left in this position for a few seconds to form the joint. The joint is then left to cool at room temperature.

9.6 Experimental Investigation

A special purpose rig for the static and dynamic testing of specimens needs to be designed and manufactured (refer to Chapter 10).

9.6.1 Static Testing

The objectives of the static series of tests are the evaluation of the joint's stiffness and its holding load.

As shown in Figure 31, the shaft is connected to the hydraulic vibrator through a mounting fixture. In the meantime, the ring is in contact with a load cell (Kistler 9051) placed on the rig base.

The joint is loaded with predetermined loading increment. At that loading level the shear compliance is measured using an electronic comparator (Model 1) before removing the load and measuring the amount of micro-slip.

The process is repeated by adding loading increments until the loading level is sufficiently high to cause gross-slip, which is considered to be the joint's static holding load.

A block diagram of the static test is shown in Figure 32.

9.6.2 Dynamic Testing

This series of tests are performed in order to study the effect of the dynamic loading on the holding load, stiffness and damping of a shrink-fitted joint.

The joint is held in the experimental rig in the same way as for static testing. The only exceptions are in preloading the ring with a constant load of 20 KN., as well as in using the vibrator to induce varying levels of amplitude of vibration to the shaft (constant frequency of 25 Hz).

The joint is loaded incrementally and the amplitude of shear compliance measured at each loading level. The exciting force from the vibrator may be measured using an impedence head (Kistler Z 11280), while the joint's deformation can be measured using a displacement transducer (Wynne-Kerr B731B).

At every load the amplitude of the exciting force and its phase angle (ϕ) between the force signal and slip signal are recorded using a frequency response analyser (Solartron 1170).

A block diagram of the dynamic test is shown in Figure 32.

9.7 Experimental Plan

The joints are manufactured according to the basic shaft system of fit. A large number of rings are manufactured to provide enough specimens for the matching process.

The joints are divided into two equal groups according to the method of manufacture, the one being produced by turning, the other half by grinding. The process parameters are changed to produce two different types of finish, course and fine. Each sub-group includes three different sizes, namely, 10, 15 and 20 mm. For each five to six joints of the same value of (CLA), varying interference values were tested statically and dynamically. An overall block diagram representing specimen classification is shown in Figure 33. Table 5 describes the method of matching the shafts to the rings, and Table 6 explains the coding system used.

CHAPTER 10

DESIGN OF THE TESTING SYSTEM

10.1 Consideration in the Design of the Testing System

The main requirements of a suitable system for testing the static and dynamic characteristics of shrink-fitted joints can be summarised by the following points:

(1) To be able to deliver a variable static loading of a magnitude high enough to release the joints fitted with the maximum interference value.

(2) To be designed for maximum rigidity to minimise the deflections that may exist at the high loading levels; also to ensure the best possible alignment between the loading and direction and the specimen axis.

(3) To have the provision of accurate incremental loading and unloading of the force to calculate the micro-slip in the joint.

(4) To include a provision for the application of a high level dynamic exciting force at different amplitudes within a wide range of exciting frequences.

(5) To be isolated from the floor to prevent any damage that may occur to the building at high amplitude and frequency levels.

(6) To have a natural frequency of the system high enough to avoid the que range of frequencies intended for the experimental investigation.

(7) To include a method of preloading in the system to firmly hold the specimen during the dynamic testing, which involves the reversal of the loading direction.

(8) To include a provision to prevent any lateral movement in testing in order to keep the best alignment for the test specimen.

(9) To be flexible enough to allow easy specimen change and fixing of measuring instrumentation.

10.2 Test Rig Structure

Figure 34 shows the general arrangement of the testing system, which can be divided into the following main groups:

(1) Concrete base.

(2) Floating bed.

(3) Supporting structure.

(4) Specimen locating frame.

(1) Concrete Base

It has proved to be extremely important to obtain a high level of accuracy of levelling the floor area of the test rig. This is achieved by digging a shallow area (6" deep) and positioning two side plates. The plates are levelled accurately using three height adjusting threaded bolts. The supporting height bolts for each plate are joined together using tie rods to ensure accurate levelling during the pouring of the concrete mix and during the setting period.

(2) Floating Bed

The floating bed of the rig is constructed from a large concrete block onto which a machined cast iron bed plate is attached. Sixteen anti-vibration rubber pads are situated between the concrete block and the concrete base. The floating bed has two horizontal holes with two tie rods passing through. Both tie rods are connected to a plain bearing, which is constrained, but free to move in the vertical direction. Where the tie rods pass through the concrete bed, they are supported with rubber sleeves.

(3) Supporting Structure

The supporting structure is manufactured from standard R.S.J.'s, universal beams and plates. It consists of four uprights with two mild steel plates welded into position. Each upright is fixed with the main plates using four bolts. Two cross beams are mounted on the four upright tops, on which a manufactured base is fixed to hold the vibrator head. An absorber is situated between the vibrator head and the frame, (see Figure 34).

(4) Specimen Locating Frames

The specimen holding assembly consists of two U shape frames. The cylindrical part of the specimen (ring) is held between the outer and inner frames using a sleeve and two nuts. The joint shaft passes through the sleeve and connects to the hydraulic vibrator through a ball and socket arrangement. The lower end of the shaft is connected to an extension rod with a ground flat face which is used as a reference for the displacement transducer. By means of the adjusting nuts, the specimens could be changed and provision is made for different specimen heights.

Extreme care must be taken when assembling the test rig to ensure that all mating faces are perfectly clean and free from burrs. Figure 35 and Figure 36 show the general arrangement of the testing system.

10.3 Principle of Operation and Equipment

The operation of the rig and its associated equipment may be divided into parts:

(1) Instrumentation for the loading and excitation of the specimens.

(2) Measuring instrumentation for the resulting displacements and damping coefficients.

10.3.1 Loading and Excitation Equipment

The basic principle of the testing system is based on loading the specimen using an electro-hydraulic vibrator and using piezo-electric load cells to measure the magnitude of the applied load. The vibrator is essentially a double acting hydraulic jack powered by oil under pressure (3000 lbf/in^2). The oil flow is controlled by two flow valves, operated by an electrical signal from a servo amplifier.

The controlling signal to the summing junction of the servo amplifier is supplied by a low freqency electronic oscillator. A displacement transducer mounted on the ram introduces a feed back signal to the servo amplifier summing junction in such a way as to cancel the controlling signal, thus providing closed loop servo control. The displacement transducer for the vibrator's feed back system is a linear differential transformer having d.c. input and output.

The output of the servo amplifier is passed through a constant current circuit, prior to the servo valves, thus providing an enhanced frequency response for the unit. The servo amplifier also contains a rotary gain control with variable resistors for setting the magnitude of the controlling signal, thus providing a variable amplitude at the vibrator. A second potentiometer provides a variable d.c. bias at the summing junction of the servo amplifier, enabling the mean position of the ram to be adjusted.

In the case of the static test the vibrator ram is moved incrementally, using the second potentiometer to a certain level of static loading. A signal from the load cell is first fed through a charge amplifier, which after tuning to the sensitivity of the particular load cell, gives a calibrated output voltage signal. A digital voltameter is arranged in the circuit to measure the magnitude of the signal from the charge amplifier and, hence, the level of the static load is transmitted to the joint.

Under dynamic loading it is essential that a dynamic force transducer be situated between the vibration source and the test specimen. The signal from the load cell is first fed through the charge amplifier. A Solarton wave analyser is arranged in the circuit to measure the amplitude of the signal from the charge amplifier, and hence the magnitude of the dynamic load is transmitted to the joint. The same signal could also be displayed on one channel of a double beam oscilloscope. A block diagram of the system is shown in Figure 32.

10.3.2 Displacement and Damping Measuring System

The whole system of measurements for stiffness, damping, etc. hinges on the effective measurements of the displacement between the two mating surfaces in the tangential direction.

A_M. Metronic comparator, which is held in a special fixture underneath the shaft, is used to measure the displacement during loading and unloading for the static test. The signal from the comparator is passed through a charge amplifier, selecting the appropriate magnification on the recording unit.

Under dynamic testing conditions the displacements are measured using capacitive type pickups, provided with variable sensitivity ranges. The displacement probe is situated underneath the shaft and connected to the distance meter and power supply. The instrument displays the actual gap setting on a graduated scale and its output terminal is connected to the frequency analyser. The mains frequency noise is eliminated using a special tunable filter connected between the instrument and the frequency analyser. Provision is also made to monitor the output signal of the probe on an oscilloscope. The phase angle shift between the force signal and displacement signal due to the effect of the filter has been found to be negligible.

The assessment of the joint damping is calculated from measuring the phase difference between the force and displacement signals using the frequency analyser.

10.3.3 Setting up the Probes

The displacement measurement for both static and dynamic tests is performed using a probe situated in a special fixture which connects with the upper plate of the specimen locating frames. Extreme care ought to be taken in the positioning of the fixture in order to ensure that the probe axis is parallel to the joint axis and that, therefore, the gap between the probe and measuring face is kept constant. A precision ground measuring face is connected to the shaft using a special extension rod.

The displacement probes are used to measure the deformation of the reference solid specimens in exactly the same way and in the same relative position. Deformation of the equivalent solid material could be calculated and subtracted from the overall displacement of the joints in order to determine the true joint displacements.

Various ranges of the distance probes are available, ranging from 0.001 in. to 0.5 in. gap setting. The probe with range of 0.005 in. is used for all the dynamic tests. To obtain repeatable setting positions a micrometer (60 T. P. I.) adjustment is fitted to hold and adjust these probes.

10.4 Calibration of the Instrumentation

The Solartron frequency response analyser used is almost a substandard measuring instrument. A standard circuit supplied by the manufacturer is used to check that the tolerances on the measured

response are maintained within the limits specified (± 0.1° for phase and ± 0.1 db for amplitude). It is then possible to make use of the analyser in calibrating the high quality transducers used in this investigation.

10.4.1 Calibration of the Charge Amplifiers

The "Kistler" charge amplifiers are calibrated using a capacitor (1000 ± 1% PF) shunted across the input. The function of this arrangement is to enable an input of a known voltage to the capacitor, which transforms every 1 mv into 1 pc input to the charge amplifier. The charge amplifier is set to the sensitivity of the actual transducer used during the tests. The input voltage at the required frequency (25 Hz) is obtained by programming the F.R.A., while the output of the charge amplifier is measured by the analyser with respect to the input signal. The calibration arrangement is shown in Figure 39.

The results of the calibration of the charge amplifiers indicate that they are functioning properly within the limits specified by the manufacturers.

10.4.2 Calibration of the Load Cell

The piezo-electric load cell is calibrated both statically and dynamically. The static calibration of the cell is performed on a "Denison" testing machine and the results are shown in Figures 37

fed to the vibrator at a known frequency (25 Hz), while simultaneously the outputs of the Wynne Kerr and the accelerometer are fed to the F.R.A. The calibration is carried out by increasing the signal amplitude by a certain value until the reading covers the range of the probe. At every level of amplitude, the meter and F.R.S. readings are recorded. From the accelerometer and meter readings the calibration chart, Figure 41, is obtained.

10.4.4 Calibration of Micro Metronic Comparator

The static displacement is measured using the M.M.C., which is connected with the talysurf tracer unit through a charge amplifier. The calibration of this probe is carried out in the metrology laboratory using slip gauges. The probe is mounted in the holder bracket of a comparator stand. A slip gauge of known value is positioned on the table of the comparator and the probe is brought into contact with it, as shown in Figure 42. The bracket of the comparator is then locked in position. The meter reading and the talysurf trace are taken at this setting, after which the slip gauges are incremented at steps of 0.001 mm. The procedure is repeated over the range of the probe. The whole procedure is then repeated, with the probe mounted in the test rig in the actual working position. This time the slip gauges are positioned between the probe and the measuring face. This method of carrying out the probe calibration in situ is repeated several times throughout the actual tests. The calibration chart for the probe is shown in Figure 43.

CHAPTER 11

RESULTS AND DISCUSSION

11.1 Introduction

This Chapter presents the experimental programme results and deals with the effects of size, surface roughness and the value of interference on the static and dynamic characteristics of interference shrink-fitted joints.

11.2 The Holding Load

11.2.1 The Effect of Interference Value

Figures 44 to 46 show the relationships between the holding load and the mean interference value (δm) for the different joint sizes investigated (10, 15, 20 mm). Every plot represents one joint size and four values of surface roughness.

As can be seen from the Figures, the general trend can be represented by a linear relationship for the same value of interference. After a certain interference value the relationship starts to show a non-linear trend. This non-linearity can be directly related to the material elastic behaviour. The low levels of interference are not enough to induce stresses beyond the material elastic limit, while at high interference levels the stresses may reach the material plastic range. The deviation from linearity for

each curve has proved to be size-dependent. The increase in the joint holding load with the increase in the mean interference value (δm) is due to the pressure increase induced between the mating surfaces. Hence, the increase in the total sheared area of asperities occurs, as shown from their characteristic B. A. C., Figure 14. For the joints loaded dynamically, similar general trends can be observed, Figures 47 to 49. The same linear trend exists, but the rate of increase in the holding load with increasing (δm) is considerably lower by 30 to 60%, for all sizes investigated. For design purposes the "only" permissible interference values are those which must ensure that the stresses induced are lower than the material yield stress.

11.2.2 The Effect of Surface Roughness

The effects of varying surface roughness on the static and dynamic holding load for the different joint sizes investigated are shown in Figures 50 to 55. The solid lines in each Figure represent different values of surface roughness. For all joint sizes the holding load decreases with increasing the surface roughness (C.L.A.). The rate of increase in the holding load with decreasing the surface roughness is much greater for the dynamically loaded joints, when compared with statically loaded joints of the same characteristics. From the Figures it can be seen that the influence of the surface roughness on the holding load almost diminishes at higher values of surface roughness.

From Figure 14 it can be seen that for the same value of interference, the sheared area of the asperities forming the joint is considerably smaller for rough surfaces than smooth surfaces. This is reflected in the level of loading which the joint is able to sustain. The surface roughness influence on the holding load proved to be not only dependent on the absolute value of surface roughness, but also on the value of interference. For example a decrease in the joint surface roughness from 4.27 to 0.33 μ mm was accompanied with an 85% increase in the holding load at an interference level of 10 mm. When the interference level is increased by a factor of four, this % increase drops to 35%, for joint size 20 mm. Dynamically loaded joints prove to be more sensitive to the changes in the interference level than the statically loaded joints.

11.2.3 The Effect of Joint Size on the Holding Load

For both statically and dynamically loaded joints, the joint size has a significant influence on the value of holding load which the joint is able to sustain, as shown in Figures 56 to 59. For the same value of interference, surface roughness, the holding load increases with decreasing joint size, while keeping the contact area constant at the same time. Together with the experimental points, Lame' equation (4.6) is also plotted as the dashed line. The solid line in the Figures represent the theoretically calculated holding load obtained from equation (6.19), coefficient of friction and N. D. C. method (refer to Chapter 6). As can be seen from the Figures for the statically and dynamically loaded joints, the degree

of correlation of the holding load calculated from the Lame' equation with the experimental points varies widely depending on the machining process used to produce the joints. This is not surprising because Lame' equation totally ignores the effect of the surface roughness.

The theoretical solid line in the Figures represents a much better approximation to the experimental data, because it includes the effect of the surface roughness in calculating the joint holding load. However, a slight deviation can still be observed between the theoretical line and experimental data. This deviation is considered to be due to ignoring the effect of geometrical errors in the analysis. When comparing dynamically and statically loaded joints, it can be observed that the holding load ratio between each consequentive diameter is lower for dynamically loaded joints for the same sizes. It can also be observed that the holding load ratio increased also with the absolute increase in size. This trend may be due to the increase and decrease in the amount of deformation occurring in the shafts of a dynamically loaded joint depending on the loading direction. This change of shaft deformation causes a repeated change in the joints interference value and, hence, increases the amount of wear between the mating surfaces. The amount of changing deformation and the consequent increase in wear is also observed to be size-dependent, with a higher influence on the smaller the joint size. The experimental and theoretical holding load ratios for the joint sizes investigated are shown in Tables 7 and 8.

In order to simplify the design procedure of a shrink-fitted joint and still include the effect of surface roughness in the calculation, Lame' equation can be taken as a reference in calculating the holding load ratio between the desired joint size and tested size. This ratio can then be multiplied by the experimental holding load to obtain a corrected value of the holding load, which includes the effect of surface roughness and geometrical error under the same surface characteristics. (Refer to Table 9.)

11.3 Holding Load Determination (Theoretical Methods)

In the present work, three methods have been adopted to estimate the holding load of shrink-fitted joints, namely, B. A. C. method, N. D. C. method and Lame's theoretical method. Table 9 shows a comparison between the experimental values of the joints holding load and the corresponding theoretical values obtained using the above three methods.

(1) Bearing Area Curve Method

The detailed analysis of determining the holding load using the B. A. C. is previously outlined in Chapter 6. Figures 60 to 71 show the experimental results of the holding load as well as the predicted value using B. A. C. As can be seen from these Figures, the degree of correlation between the experimental and theoretical line varies depending on the surface roughness, joint size and the

value of interference (δm). For ground surfaces the % deviation between the experimental data points and the theoretically calculated points is observed to be more pronounced as the joint size becomes smaller. When the machining process is changed in order to produce a rougher surface and, at the same time, to make it less random in nature, the amount of deviation increases more than the observed deviation for ground surfaces. The theoretically estimated values for turned surfaces are lower than the experimental data points and also lower than the estimated values of ground surfaces.

The deviation in estimating the holding load is observed to be higher with decreasing the interference value. The deviations observed when estimating the holding load using the B. A. C. method are largely due to the effect of geometrical errors in the joint as well as to the nature of the surface produced by different manufacturing processes, as will be explained in Section 11.3.1. The percentage deviations in estimating the holding load are shown in Table 9.

(2) Normal Distribution Curve Method

The analysis adopted using the N. D. C. method for calculating the holding load is outlined in Chapter 6. As can be observed from Figures 60 to 71, the

surface roughness, joint size and the value of interference influenced the degree of correlation between the theoretical and experimental data points. The surface characteristics played an important role in determining the success of method in describing the experimental data. The deviation between the theoretical line and the experimental points is observed to be less for ground surface than turned surface. This is not surprising, because the ground surface is better described using the normal distribution than turned surface, due to its near random characteristic. The deviation between the experimental and theoretically determined values is more pronounced, the smaller the joint size becomes. An increase in the value of interference has an opposite effect to decreasing the joint size. The deviation has proved to be more pronounced for small interference values. The percentage deviations of the theoretically determined holding load from the experimental data are shown in Table 9 for the different joint sizes investigated.

(3) Coefficient of Friction Method

The details of the method used to include μs in calculating the theoretical joint holding load are outlined in Chapter 6. Figures 60 to 71 describe the predicted values of holding load for the experimental range investigated. The main joint parameters, viz. surface roughness, size and interference value, all play an important role in determining the degree of correlation between the theoretical line and the experimental data points.

For small joint size (10 mm) the percentage deviation between the theoretical and experimental values has proved to be more significant than in the case of medium and large joint sizes (15, 20 mm). For small value of joint interference a large percentage deviation can be observed. However, the % deviation is smaller for large interference levels. Although the overall maximum deviation between the theoretical line and experimental points has a constant range for all types of surfaces, the method has proved to be sensitive in calculating the holding load for the different surface characteristics and joint sizes.

The percentage deviations of the theoretically calculated holding load and experimental data are shown in Table 9 for the different joint sizes and surface roughness.

11.3.1 Comparison between the Theoretical Methods of Determining the Joint Holding Load

The results obtained using the theoretical methods outlined in the previous Section show that these methods are in general successful in describing the experimental data. The degree of correlation for each method depends upon the nature of the principle involved as the basis of determining the holding load.

The B. A. C. method is based on the calculated sheared area from which the shearing force only is estimated, without taking into account the ploughing component. Ignoring the ploughing component influences the accuracy of using this method in calculating the holding load, especially for rough surfaces. This is reflected in the results as an increase in the deviation between the theoretically calculated and experimental values for turned surfaces as compared to ground surfaces. The amount of plastic deformation in the surface asperities that accompany shrink-fitting, has the effect of increasing the physical contact area in comparison with the originally calculated bearing area for the asperities before the deformation for the same loading level. Hence, the calculated holding loads using this method are expected to be lower than the experimental values. This trend is also reflected in the experimental results. For large values of interference inducing high stress concentration, the asperities can start to persist. This phenomenon can cause a decrease in the rate of increase in the area of contact, which can partially cancel the effect of the increase in the contact area due to large interference value. Hence, there is a reduction in the difference between the real area of contact and the measured area from the B. A. C.

The N. D. C. method also relies in its determination of holding load on the bearing area curve, which is the same as the B. A. C. method, with the additional assumption that surface profile follows a gaussian distribution. The previous comments mentioned for the B. A. C. method can also be applied to the results of the normal distribution method. However, it assumes that a gaussian distribution to the surface profile would lead to an increase in the deviation between the theoretically calculated and experimental values for turned surfaces as compared with ground surface. This is due to the fact that the ground surfaces are much nearer to being normally distributed.

The theoretical method of determining the holding load using the coefficient of friction relied on using empirical equations which are based on measuring the physical parameters characterising the surface, such as the profile mean slope ($\tan \theta$). The average mean slope is also dependent on the average wave length, peak to valley height and centre line average and neglects the effect of the ploughing component in the analysis. The analysis of the experimental results indicates that the results obtained using this method give a better overall assessment of the experimental data. However, the method relies heavily on many surface parameters that can only be determined experimentally, while in a method like N. D. C. the only experimentally determined parameter is the surface peak to valley height.

An overall assessment of the theoretical methods of determining the joint holding load can show that they represent a reasonable correlation with the experimental results. The degree of correlation between each method and the experimental data depends primarily on the particular situation to which it is applied in the light of the previously mentioned comments. It must also be stressed that in all three methods the effects of the geometrical errors have been neglected, which can have a large influence on the value of the holding load, especially for small joint sizes.

11.4 Comparison between the Static and Dynamic Loading of Shrink-Fitted Joints

Figures 72 to 83 show the results of the dynamically tested joints as well as the theoretical holding loads obtained using the B. A. C., N. D. C. and μs methods. It can be observed from these Figures that the results show the same trends as those for the statically tested joints and agree with comments made in Section 11.3.1. The results show that the percentage deviation also depends on the joint surface roughness. The deviation increases with increasing the surface roughness.

The value of the percentage deviation between the static and dynamic holding load increases with decreasing the joint size and the interference value. However, the degree of correlation between the dynamic experimental data and the theoretical solutions is very poor. This is not surprising, because there is a wide difference between the static and dynamic testing results. For most joints the

dynamic holding load is between 30 and 60% lower than the static holding load. A closer analysis of the values of percentage deviations in Table 10 shows that the theoretically obtained results can be corrected to give better correlation with the dynamic testing results. This can be achieved by reducing the theoretical values by an average of 50% and then adding/subtracting the percentage deviation between the theoretical and static testing results. It can also be observed from the Figures that the most successful theoretical method in correlating the dynamic testing data is the N. D. C. method. This is due to the fact that the calculated area of contact using the N. D. C. method is smaller than the real contact area and, consequently, the theoretically calculated holding load is smaller, which brings the values closer to the dynamic testing results.

11.5 The Holding Load of Press-Fitted Joints

When gross slip occurs in a shrink-fitted joint, it can be considered equivalent in its characteristics to press-fitted joints. This has been confirmed experimentally because the holding load stayed constant after gross slip occurred. Figures 60 to 83 show the experimental results obtained for the statically and dynamically tested shrink-fitted joint after the occurrence of gross slip, i.e. press-fitted joints. The results show that the capacity of a shrink-fitted joint in sustaining an applied load is between 1.5 to 3 times that of a press-fitted joint of the same original interference value and surface roughness. The amount of deviation

between the shrink-fitted and press-fitted joints depends on the value of surface roughness. The smoother the surface is, the smaller the amount of deviation would be. The holding load of shrink-fitted joints is always higher than the press-fitted joints due to absence of abrasion between the mating surface of a shrink-fitted joint. After reaching the gross slip condition the true area of contact between the mating surface decreases and is accompanied by a decrease in the holding load.

11.6 Tangential Displacement

11.6.1 The Effect of Value of Interference

Figures 84 to 99 show the effect of the joint interference value on the amount of tangential displacement for both the statically and dynamically tested joints. The graphs are plotted for the total value of tangential displacement as the sum of the elastic displacement and the micro slip. The load-displacement relationship for the equivalent solid specimen is also included to provide a comparison with the tested joints.

The tangential displacement increases almost linearly with the applied tangential load during the loading cycles for the large interference values. From the Figures it can be seen that the value of interference plays an important role in determining the amount of tangential displacement between the joint making surfaces. A proportional decrease in the tangential displacement can be observed when increasing the joint interference value, until finally reaching

a value almost equal to the tangential displacement of the equivalent solid specimen for all joint sizes. When the tangential load reaches a magnitude equivalent to the joint holding load, gross slip or sliding occurs and the joint can no longer be considered a shrink-fitted joint. For small interference values the load-tangential displacement has proved to be non-linear. At the end of the unloading cycle in which the applied load is incrementally decreased until reaching zero load, a permanent tangential displacement is observed. This can be taken to represent the amount of plastic deformation and micro sliding that occurs in the joint mating surfaces.

The interference level has a significant effect in determining the amount of the joint micro slip. There is an inverse proportionality between the value of interference and the amount of micro slip, which proves to be almost insignificant at high value of interference, as can be seen from Figures 100 to 105. Subsequent loading and unloading cycles produces good repeatability. The same value of applied load has to be reached to achieve the original tangential displacement before the start of the unloading cycle.

The type of hystersis loops observed for the case of shrink-fitted joints can be divided into two types, as shown in Figures 100 to 105. In the first type the loop is characterised by a repeatable loop of small width at all loads below the joint holding load for joints with large values of interference. The other type also has a repeatable loop, but it has a much larger width and mostly occurs for joints with small interference levels. The area enclosed by both types of loops is considered to be small compared with the materials with different mechanical properties.

11.6.2 The Effect of Surface Roughness

When taken sequentially, Figures 84 to 99 can show the effect of the joint surface roughness on the amount of tangential displacement of the mating surfaces. To clarify the effects of the joint surfaces, the displacement of the equivalent solid specimen must be eliminated from the overall tangential displacement of the joints. It is also noticed that the elastic displacement of shrink-fitted joints during unloading is about 90% of the overall tangential displacement for large values of interference. Therefore, the elastic displacement can be taken to represent the tangential displacement of the shrink-fitted joint with large value of interference, if the tangential load is less than the joint holding load.

For all joint sizes an increase in the joint surface roughness leads to a proportional increase in the amount of tangential displacement and micro slip at the same loading level.

11.7 The Joint Tangential Stiffness Under Static and Dynamic Loading

The tangential stiffness for the shrink-fitted joints is estimated using the following equation:

$$K_s = \frac{F_s}{\delta_B \cdot A} \qquad N/\mu.mm \; \frac{1}{mm^2}$$

Figures 106 to 121 show the relationship between the tangential load and the value of static and dynamic stiffness. The stiffness of the equivalent solid specimen is also included for comparison. It is clear from these Figures that the value of interference plays an important role in determining the value of joint stiffness. At large joint interference value the tangential stiffness is between 75 to 93% of the equivalent solid specimen value. The relationship between the joint stiffness and the applied tangential load has proved to be almost linear for high interference values, while it deviates from linearity with decreasing the interference value. Some fluctuation in the joint stiffness is observed with increasing the tangential load. This can be explained by the occurrence of micro stick slip conditions between the contacting asperities. Under dynamic loading the amount of fluctuation in the tangential displacement is much more pronounced due to the repeated change in the loading direction, which can give rise to the amount of wear between the asperities.

The variation of the joint tangential stiffness is highly dependent on the surface roughness of the mating surface. It can be observed that under both static and dynamic loading the stiffness increased with decreasing the surface roughness for all joint sizes. The effect of changing the joint surface roughness is shown in Figures 106 to 121. The value of surface roughness plays an important part in determining the conditions and amount of the micro slip and, consequently, the joint tangential stiffness. The amount of micro stick slip increases with increasing the joint surface roughness.

11.8 Damping of Shrink-Fitted Joints

The relationships between the shrink-fitted joint damping characteristics represented by the loss factor and the applied dynamic load are shown in Figures 122 to 133. Several plots are indicated for the varying values of interference. The equivalent solid specimen loss factor is also indicated for comparison between the different tests.

From the Figures it can be shown that there is a close relation between the loss factor and the value of interference. The loss factor increases with decreasing the value of interference and increasing the surface roughness. The relationship between the loss factor with value of the applied load has proved to be non-linear. This can be attributed to the effect of the mirco stick slip conditions that accompany the dynamic loading of the joint. The loss factor varies from 0.05 to 0.08 for a decrease in the interference value from 36 to 7 μmm. However, it is observed that the loss factor reaches a maximum value as the applied load becomes closer to the joint holding load, i.e. before gross slip occurs.

The loss factor of a joint of size 20 increases by approximately 300% from its equivalent solid specimen value. For the same joint the loss factor shows a dependency on the value of surface roughness, increasing by 64% due to changing the method of production from grinding to turning. The loss factor is observed to increase depending on the joint size. This can be explained as the effect of the applied load on the amount of deformation is induced in the shaft, which increases with decreasing its size.

The damping characteristics are also assessed using the energy dissipation method based on the theoretical model developed in Chapter 8. When coulomb friction conditions are assumed to exist, the amount of energy dissipation is given by the following relationship:

$$W = \mu_d \cdot P_m \cdot A \cdot \delta_e$$

$$= 0.5\, \mu_s \cdot P_m \cdot A \cdot \delta_e \qquad 11.1$$

The damping tangential load relationships using the energy dissipation method are shown in Figures 134 and 135. From the Figures it can be observed that there is a large scatter in the experimental data. This is attributed to the variation of the joint damping according to the micro stick slip characteristics. However, a good correlation can be found between the theoretical model and the average line taken to represent the experimental data points for most of the joints investigated. The theoretical model preserves the same trends as the experimental data from the view point of the increase in the energy dissipation with increasing the tangential load and surface roughness, as well as from the point of its decrease with increasing the value of interference.

The parameters that generally increase the joint damping characteristics normally lead to a decrease in its holding load. Hence, it becomes obvious that a balance should be struck between the value of the joint holding load and its damping characteristics if both parameters are equally important. Under operating conditions,

where the holding load is of prime importance, the joint surface should be as fine as possible.

11.9 Summary of the Equations Governing the Effects of the Interference Value and Surface Roughness on the Joint Holding Load

The following relations between the joint holding load (H. L.), mean value of interference (δ_m) and the surface roughness (C. L. A.) have been deduced:

(1) For size d = 20 mm

(a) Static loading (for δ_m up to 45 μ.mm)

H. L. = .00366 + .00112 δ_m - .00211 (C. L. A.)

KN/mm^2 of the apparent contact area (π dL)

(b) Dynamic loading (for δ_m up to 45 μ.mm)

H. L. = .00456 + .000935 δ_m - .00268 (C. L. A.)

KN/mm^2 of the apparent contact area (π dL)

(2) For size d = 15 mm

(a) Static loading (for δ_m up to 35 μ.mm)

H. L. = .01804 + .00163 δ_m - .00592 (C. L. A.)

KN/mm^2 of the apparent contact area (π dL)

(b) Dynamic loading (for δ_m up to 35 μ.mm)

H. L. = .00926 + .00099 δ_m - .00458 (C. L. A.)

KN/mm^2 of the apparent contact area (π dL)

(3) For size d = 10 mm

(a) Static loading (for δ_m up to 25 μ.mm)

H. L. = .01696 + .00286 δ_m - .00999 (C. L. A.)

KN/mm^2 of the apparent contact area (π dL)

(b) Dynamic loading (for δ_m up to 25 μ.mm)

H. L. = .0092 + .00146 δ_m - .00593 (C. L. A.)

KN/mm^2 of the apparent contact area (π dL)

A comparison between the experimental results and the above empirical equations provides a good correlation which warrants its use for design purposes. The correlation coefficient (r) exceeds 0.975 for most joint sizes investigated.

CHAPTER 12

CONCLUSIONS AND FUTURE WORK

12.1 Conclusions

The conclusions mentioned in this Chapter are mainly concerned with the effects of some parameters on the static and dynamic characteristics of shrink-fitted joints, namely the surface roughness, interference value and joint size.

The main results and conclusions can be related as follows:

(1) The joint holding load of a shrink-fitted joint under both static and dynamic loading increases proportionally with the increase in the interference value (δm) for the same value of surface roughness.

(2) For the same joint surface roughness, the dynamic holding load is between 30 to 60% lower than the static holding load for all joint sizes.

(3) For a given value of mean interference (δm), the joint holding load increases with decreasing the joint surface roughness under both static and dynamic loading conditions.

(4) The joint surface roughness has a more pronounced effect on the holding load under dynamic conditions than under static loading.

(5) For the same mean interference value and surface roughness, the joint holding load increases with decreasing the joint size (at the same area of contact).

(6) Lame' equation can be used as a reference in calculating the holding load ratio between the desired joint sizes and the tested sizes. This ratio can then be multiplied by the experimental holding load to obtain a corrected value of the joint holding load, which includes the effect of surface roughness and geometrical error for the same surface characteristics.

(7) A shrink-fitted joint holding load is approximately twice its equivalent press-fitted joint under both static and dynamic loading conditions.

(8) The B. A. C. method of calculating the joint holding load gives a better correlation with the experimental values for ground than for turned surfaces. The calculated holding load using this method is expected in general to be lower than the experimental values.

(9) The N. D. C. method of calculating the joint holding load gives good representation of the experimental data points obtained for ground surface. The calculated holding load for joints with turned surfaces is generally expected to be lower than the experimentally obtained levels.

(10) The theoretical method of calculating the joint holding load using the coefficient of friction gives a better overall assessment of the experimental data. The calculated holding load using this method divided by a factor of 1.35 gives a realistic joint holding load that can be used for design purposes.

(11) The mean value of interference (δm) has a significant influence on the joint tangential displacement. The displacement decreases with increasing the interference value, reaching a constant value nearly equal to the displacement of the equivalent solid specimen.

(12) The relationship between the tangential displacement and the applied load proves to be linear for large interference values. However, it deviates from linearity for small values of interference.

(13) The value of the joint tangential displacement and micro slip increases with increasing the surface roughness at the same interference level.

(14) The elastic displacement of shrink-fitted joints after unloading is approximately 90% of the overall tangential displacement of the joints with large interference values. Hence, the elastic displacement can be considered equivalent to the tangential displacement up to the value of the joint holding load.

(15) The hysteresis loops observed for shrink-fitted joints prove to be repeatable at all loading levels, while their width depends on the value of interference.

(16) The tangential stiffness of shrink-fitted joints increases with increasing the interference value and surface roughness. It represents approximately 75 to 93% of the stiffness of the equivalent solid specimen for large interference values.

(17) Under dynamic loading the amount of fluctuations in the tangential displacement is considerably more pronounced than the fluctuation observed under static loading.

(18) The joint damping represented by the loss factor (τ) increases with decreasing the interference value and increasing the surface roughness. The loss factor increases by approximately 300% from its equivalent solid specimen.

(19) The amount of energy dissipation representing the joint damping characteristics increases with decreasing the interference value and increasing the surface roughness. Good correlation can be found between the theoretical model and an average line taken to represent the experimental data point.

(20) The empirical equations developed to describe the influence of the mean value of interference (δm) and the effect of surface roughness on the holding load under static and dynamic loading, give a good correlation with the experimentally obtained data. (Coefficient of correlation (r) exceeds 0.97 for most equations.)

12.2 Future Work

(1) The presented investigation concentrates on the study of the characteristics of shrink-fitted joints under axial loading only. The change of the type of loading is expected to influence its characteristics. Different loading modes, i.e. torsion, bending and combined loading conditions, should be studied to provide a wider understanding to the joint behaviour under complex loading systems.

(2) The obtained results show an important influence of the geometrical errors on the holding load, which has not been fully investigated in the present study. An investigation should be carried out to study the effects of the geometrical errors normally encountered in machining processes on the characteristics of the produced joints.

(3) The material used for this investigation is a commercially available mild steel (ENIA). Shrink-fitted joints are produced using a much wider material range which can include non-ferrous materials. The effects of changing material type and the use of differing material combinations should be investigated.

(4) The shrink-fitted joints used for the present study are of round cross-section. An investigation into the effects of changing the joint cross-section type (i.e. square, hexagonal) should also concern the feasibility of using dissimilar ring and shaft cross-sections.

(5) The area of contact has been kept constant for all the joints investigated. It is thought probable that a change in the contact area may have an influence on the joint characteristics. Hence, a further study should include joints with differing contact area.

(6) The joints investigated can be considered to be made from "dry clean surfaces". The effect of surface contamination by oxidation, oil, etc. should be included in future studies.

(7) In this study the joints, produced from mild steel bars, have been used in their received state. The effects of changing the material mechanical properties by heat treatment on the joint characteristics should be analysed.

(8) The time dependent characteristic of shrink-fitted joints can prove to be an important element for their practical applications. The effect of ageing on the joint characteristics should be studied. The suggested future investigation should also include the study of the fatigue characteristics of the joints under various loading systems.

(9) The validity of the proposed theoretical and empirical models should be investigated at a wider experimental range and with varying manufacturing processes.

(10) The dynamic characteristics of shrink-fitted joints should be studied at a wider frequency range at different loading levels, as well as at shock loading levels.

REFERENCES

1 WILMORE J J, Shrink and force fits. American Machinist, Vol 22, 1899, pp 126.

2 MC GILL, A record of press-fits. Trans., ASME, Nov, 1913, pp 1657.

3 ORBECK F, A study of shrink-fitted assemblies loaded in torsion with special reference to damping capacity. Proc. Instn. Mech. Engineers, Vol 173, No 34, 1959.

4 RUSSELL R and SHANNON J F, The limit of grip due to force fits and its increases by cold-working. Jour. R. T. C., Vol 2, Pt 2, 1930.

5 RUSSELL R, Factors affecting the grip in force, shrink and expansion fits. Proc. Instn. Mech. Engineers, Vol 125, 1933.

6 RUSSELL R, Contact film resistance in rail wheel force fits. Jour. R. T. C., Vol 3, 1935.

7 RUSSELL R, Influence of film and time on force and shrink fits. Trans. I Eng. and Ship. Scotland, Vol 80, 1937.

8 BAUGHER J W, Transmission of torque by means of press and shrink-fits. Trans. ASME, Vol 53, 1931.

9 WILSON W K, The strength of large crankshafts. Gas and Oil Power, Vol 46, No 554, 1951, pp 261-4.

10 TROCK B, Shrink fits holding power can be increased. Iron Age, Vol 172, No 20, 1953, pp 175-7.

11 CONWAY H G, Engineering Tolerances. Pitman, London, 1966.

12 COOK G and ROBERTSON A, Strength of thick hollow cylinders under internal pressure. Engineering, Vol 92, 1911, pp 786.

13 SAWIN N N, Research on force fits. American Machinist, Vol 68, 1952.

14 EL-KHATIB A, Effect of surface finish degree on the strength of interference shrink-fits. MsC, Faculty of Eng. Alex. Univ., Sept 1966.

15 TSUKIZOE T, HISAKADO T and MIYOSHI K, Effects of surface roughness on shrinkage fits. Bull. of the JSME, Vol 17, No 105, 1974.

16 ELEWA I, Effect of surface texture on the loading of interference fits, MsC, Faculty of Eng., Helwan Univ, Cairo, 1976.

17 OSCAR J H and NELSON C W, Design of press and shrink-fitted assemblies. Applied Mech., Vol 4, No 4, 1937, pp 183 - 187.

18 WERTH S, As reported in paper published by OSCAR J H, Metal Eng. H. B., Part 2, 1937.

19 LYTHINA N K, The influence of the method of assembly on the stress condition of joints with large interference fits. Russian Eng. J., Vol 56, No 10, 1976, pp 29 - 32.

20 KESTEL'MAN N Y, KESTEL'MAN N V and MUKHA M S, Strength of non-moving joints formed between carbon bushings and metal parts. Chem. and Petroleum, No 3 - 4, 1969, pp 185 - 187.

21 HISAKADO T and MIYOSHI K, Effect of roundness on shrink-fits. Bull. JSME, Vol 16, No 102, 1973, pp 1977.

22 GOUGH H J, Engineering steels under combined cyclic and static stresses. Proc. Instn. Mech. Engineers, Vol 106, 1949, pp 417.

23 BARTON M V, Circular cylinder with a band of uniform pressure on a finite length of surface. Trans. ASME, Vol 63 (A), 1941, pp 97.

24 RANKIN A W, Shrink-fit stresses and deformations. Trans. ASME, Vol 66, 1944, pp 77 - 85.

25 MC GREGOR and COFFIN, Approximate solutions for symmetrically loaded thick-walled cylinders. Trans. ASME, Vol 14, No 4, 1947.

26 OKUBO H, The stress distribution in a shaft press-fitted with a collar. Quart. J. Mech. and Appl. Math., 1951, pp 178 - 186.

27 EUBANKS R A, Shrink-fit of arbitrary length sleeves on thin cylindrical shells. Proc. 8th Midwestern Mechs. Conf. 2, part 2, 1963, pp 84 - 101.

28 CONWAY H D and FARNHAM K A, Contact stresses between cylindrical shaft and sleeves, Int. J. Eng. Sci, Vol 5, 1967, pp 541 - 554.

29 CONWAY H D and FARNHAM K A, The shrink-fit of flexible sleeve on a shaft. Int. J. Mech. Sci., Vol 10, 1968, pp 757 - 764.

30 CONWAY H D and FARNHAM K A, The contact stress problem for indented strips and slabs under conditions of partial slipping. Int. J. Eng. Sci., Vol 5, 1967, pp 145 - 154.

31 CONWAY H D, VOGEL S M, FARNHAM K A and SO,S., Normal and shearing contact stresses in indented strips and slabs. Int. J. Eng. Sci., Vol 4, 1966, pp 343 - 359.

32 HORGER O J and MAULBETSCH S, Increasing the fatigue strength of press-fitted axle assemblies by surface rolling. Trans. ASME, Vol 58, 1936, pp 91.

33 GOODIER I, Frictional effects in shrink-fits. Stephen Timoshenko 60th Anniv. Vol , 1938, MacMillan, NY.

34 COOK and ROBERTSON, Transition from the elastic to the plastic state in mild steel. Proc. Roy. Soc. A., Vol 88, 1913.

35 HAIGH, The strain energy function and the elastic limit. B. A. Report 1919, (as reported by DAVIDSON W R, PhD Thesis, Glasgow Univ., 1951).

36 COOK G, Yield point and initial stages of plastic strain in mild steel subjected to uniform and non-uniform stress distributions. Phil. Trans. Roy. Soc. A., Vol 230, 1931.

37 COOK G, The stresses in thick-walled cylinders of mild steel overstrained by internal pressure. Proc. I. Mech. E., Vol 126, 1934.

38 NADAI, Plasticity, McGraw Hill, NY, 1931.

39 MC GREGOR, COFFIN and FISHER, Partially-plastic thick-walled tubes, Jour. Franklin Inst., Vol 245, 1948.

40 MACRAE, Overstrain of metal, as reported by DAVIDSON W R, PhD Thesis, Glasgow University, 1951.

41 SOPWITH, The stresses and strains in a party-plastic thick tube under internal pressure and end load. IX. Int. Conf. App. Mech., 1948.

42 TRANTER C J and GRAGGS J W, Stresses near the end of a long cylindrical shaft under non-uniform pressure loading. Phil. Mag. Vol 38, March 1947.

43 GRAGGS J W, ASME, Metal Engineering Design 1953.

44 AMONTON M, Histoire de l'Academie Royale des sciences avec les Memoires de Mathematique et de physique, P. 206, 1966. (As reported by WOOD K L and THOMAS T R wear, Vol 57, 1979, pp 357 - 363).

45 COURTNEY PRATT J S and EISNER E, The effect of a tangential force on the contact of metallic bodies. Proc. Roy. Soc. London, A. 238, 1957, pp 529.

46 BOWDEN F P and TABOR D, Friction and lubrication of solids. Oxford University Press, 1964.

47 MC FARLANE J S and TABOR D, Junction growth in metallic crystals. Proc. Roy. Soc. London, A 202, 1950, pp 244 - 253.

48 TABOR D, Junction growth in metallic friction: The role of combined stresses and surface contamination. Proc. Roy. Soc. London, A 251, 1959, pp 378 - 393.

49 GREEN A P, The plastic yielding of metal junction due to combined shear and pressure. J. Mech. Phys. Solids, Ser. 2, 1954, pp 197 - 211.

50 GREEN A P, Friction between unlubricated metals: a theoretical analysis of the junction model. Proc. Roy. Soc. London, A 228, 1955, pp 191 - 204.

51 EDWARDS C M and HALLING J, An analysis of the plastic interaction of surface asperities and its relevance to the value of the coefficient of friction. J. Mech. Eng. Sci., Vol 10, No 2, 1968, pp 101 - 110.

52 KRAGHELSKY I V, Second all-Soviet conference on friction and wear in machines. Part 3, 1949.

53 KRAGHELSKY I V, Friction and wear. Butterworths, 1965.

54 EPIFANOV G I and SANZHAROVSKII, Determining the true friction and wear. Machinery, Vol 15, 1962.

55 HOLM R, Electric contacts Handbook. Springer-verlag, 1958, Ch. 1, pp 8 - 10.

56 RABINOWICZ E, Influence of surface energy on friction and wear phenomena. J. Appl. Phys. Vol 32, No 8, 1961, pp 1440 - 1444.

57 RABINOWICZ E, Friction and wear of metals. Met. Eng. Q. Vol 7, No 7, 1967, pp 4 - 8.

58 SIKORSKI M E, Correlation of the coefficient of adhesion with various physical and mechanical properties of metals. J. Basic Eng. Vol 85, No 2, 1963, pp 279 - 285.

59 BUCKLEY D H, The influence of various physical properties of metals on their friction and wear behaviour in vacuum. Met. Eng. Q. Vol 7, No 2, 1967, pp 44 - 53.

60 BUCKLEY D H, Influence of atomic nature of crystalline materials on friction. ASLE Trans. Vol 11, No 2, 1968, pp 89 - 100.

61 MOKHTAR M, ZAKI M and SHAWKI G, Effect of mechanical properties on frictional behaviour of metals. Trib. Int., Dec. 1979, pp 265 - 267.

62 MOKHTAR M, ZAKI M and SHAWKI G, Correlation between the frictional behaviour and the physical properties of metals. Wear, Vol 65, 1980, pp 29 - 34.

63 GREENWOOD J A, The area of contact between rough surfaces and flats. Trans ASME, J. Lut. Tech., Vol 89, 1967.

64 ARCHARD J F, Elastic deformation and the laws of friction. Proc. Roy. Soc. London, Ser. A, No 243, 1957, pp 190.

65 KRAGHELSKY I V and SABLENIKOV, Experimental check of elementary law of boundary friction: Dry friction. Instn. Mech. Engrs., Proc. Conf. Lubrication and Wear, Oct 1957.

66 ARCHARD J F, Elastic deformation and the contact of surfaces. Nature, London, Vol 172, 1953, pp 1918.

67 MOORE A J W, Deformation of metals in static and sliding contact. Proc. Roy. Soc. London, A 195, 1948, pp 231.

68 BLOK H, Comments on the paper by Wilson, R., Proc. Roy. Soc. London, A 212, 1952, pp 480.

69 HALLIDAY J S, Surface examination by reflection electron microscopy. Proc. Inst. Mech. Engrs., Vol 169, 1955, pp 777.

70 HALLIDAY J S, Conference on lubrication and wear. Application of reflection electron microscopy to the study of wear. Proc. Inst. Mech. Engr, Vol 647, 1957, pp 868.

71 KRAGHELSKY I V and DEMKIN N B. Contact area of rough surfaces. Wear, Vol 3, 1960, pp 170 - 187.

72 ARCHARD J F and HIRST W, An examination of a mild wear process. Proc. Roy. Soc., London, A 238, 1957, pp 515.

73 GREENWOOD A J and WILLIAMSON J B, Contact of nominally flat surfaces. Proc. Roy. Soc. London, A 295, 1966, pp 300.

74 WHITEHOUSE D J and ARCHARD J F, The properties of random surfaces of significance in their contact. Proc. Roy. Soc. London, A 316, 1970, pp 97 - 121.

75 HISAKADO T, Surface roughness and deformation of contact asperities between a rough and a flat surface. Wear, Vol 35, 1975, pp 53 - 61.

76 YAMADA K, TAKEDA N, KAGAMI I and NAOI T, Mechanism of elastic contact and friction between rough surfaces, Wear, Vol 39, 1976, pp 15 - 34.

77 SURATHAR P I, PANDIT S M and WU S M, A statistical approach to the mode of deformation and contact between rough surfaces. Wear, Vol 40, 1976, pp 239 - 250.

78 FRANCIS H A, Application of spherical indentation mechanics to reversible and irreversible contact between rough surfaces. Wear, Vol 45, 1977, pp 221 - 269.

79 PESANTE M, Determination of surface roughness typology by means of amplitude density curves. Annals of the CIRP, Vol 12, No 2, 1963.

80 REASON R E, The bearing parameters of surface topography. Int. MTDR Conf. 1964.

81 SCHOFIELD R E and THORNLEY R H, Calculating the elastic and plastic components of deflection of plane joints formed from machined surfaces. Int. MTDR. Conf., 1971.

82 SCHOFIELD R E and THORNLEY R H, Calculating the elastic and plastic components of deflection of joints formed from machined surfaces with flatness errors. Int. MTDR., Conf., 1972.

83 ONIONS R A and ARCHARD J F, The contact of surfaces having a random structure. J. Phys. D., Vol 6, 1973.

84 THOMAS T R and SAYLES R S, Stiffness of machine tool joints: a random-process approach. Trans. ASME., J. Eng. Ind., Vol 99, 1977.

85 THORNLEY R H and CONNOLLY R, BARASH M M and KOENIGSBERGER F The effect of surface topography upon the static stiffness of machine tool joints. Int. J. Mach. Tool Des., Res., Vol 5, 1965.

86 CONNOLLY R and THORNLEY R J, The static stiffness of joints between machined surfaces, MTIRA, report No 13, 1966.

87 SCHOFIELD R E, An investigation into the fundamental problems of the static stiffness of bolted joints. PhD Thesis, UMIST, 1967.

88 PULLEN J and WILLIAMSON J B P, On the plastic contact of rough surfaces. Proc. Roy. Soc. London, A 327, 1972.

89 THOMAS T R and SAYLES R S, Some problems in the tribology of rough surfaces. Trib. Int., Vol 6, 1978, pp 163.

90 STOUT K, How smooth is smooth? The Prod. Eng., May 1980.

91 WHITEHOUSE D J, Beta functions for surface typologiez. Annals of the CIRP., Vol 27, 1978.

92 BOWDEN F P, MOORE A J W and TABOR D, The ploughing and adhesion of sliding metals. J. Appl. Phys, Vol 14, 1943, pp 80.

93 BOWDEN F P and ROWE W, The adhesion of clean metals. Proc. Roy. Soc. London, A 233, 1956, pp 429.

94 RUBENSTEIN C, The coefficient of friction of metals. Wear, Vol 2, 1958 - 59, pp 85.

95 FUREY M J, Surface roughness effects of metallic contact friction ASLE., Transactions, Vol 6, 1963, pp 49.

96 GREENWOOD J A and TABOR D, Deformation properties of friction junctions. Proc. Phys. Soc. Vol 66, 1955, pp 609.

97 GREENWOOD J A and TABOR D, The properties of model friction junctions. Proc. Conf. Lubrication and Wear, 1957, pp 314. Instn. Mech. Engrs, London.

98 LING F F and LUCER R C, On model studies of metallic surface asperities. J. Appl. Phys. Vol 30, 1959, pp 1559.

99 EDWARDS C M and HALLING J, Experimental study of the plastic interaction of model surface asperities during sliding. J. Mech. Eng. Sci., Vol 10, No 2, 1968, pp 121 - 132.

100 TSUKIZOE T and HISAKADO T, The influence of surface roughness on the mechanism of friction. Trans. Am. Soc. Mech. Engrs., Vol 92, Ser. F, 1970.

101 HISAKADO T, On the mechanism of contact solid surfaces, (4th report, surface roughness effect on dry friction), JSME, Vol 13, No 55, 1970, pp 129 - 139.

102 TSUKIZOE T and HISAKADO T, On the mechanism of contact between metal surfaces - The penetrating depth and the average clearance. Tran. of the ASME, Vol 9, 1965, pp 666 - 674.

103 GHABRIAL S R and ZAGHLOOL S A, The effect of surface roughness on static friction. Int. J. Mach. Tool. Des. Res., Vol 14, 1974, pp 299 - 309.

104 KOURA M M, The effect of surface texture on friction mechanism. Wear, Vol 63, 1980, pp 1 - 12.

105 SPRAGG R C and WHITEHOUSE D J, A new unified approach to surface metrology. Proc. Instn. Mech. Engrs. Vol 185, 1970 - 71.

106 TAYLOR - HOBSON, Talysurf 5: Operating instructions.

107 BOWDEN F P and LEBEN L, The nature of sliding and analysis of friction. Soc. London, A., Vol 169, 1939, pp 371.

108 ELEWA I M, KOURA M F and ABDOU A I, Effect of surface texture and interference on statically loaded shrink-fitted joints. Bulletin, Faculty of Engineering, Mansoura University, Egypt 1978.

109 VOTINOV K V, The rigidity of machine tools. Leningrad section machine Builders Union, Leningrad 1940. (As reported by THORNLEY R H 124).

110 LEVINA Z M and RESHETOV D N, Machine design for contact stiffness. Russian Engineering Journal, No 12, 1965.

111 OSTROVSKII V I, The influence of machining methods on slideway contact stiffness. Machine and Tooling, 36, 1965.

112 CONNOLLY R and THORNLEY R J, The significance of joints on the overall deflection of machine tool structures. Int. MTDR., Conf, 1965.

113 CONNOLLY R and THORNLEY R H, Determining the normal stiffness of joint faces. Trans. ASME., J. Eng. Ind., No 6, 1967.

114 THORNLEY R H, CONNOLLY R and KOENIGSBERGER F, The effect of flatness of joint faces upon the static stiffness of machine tool joints. Proc. Instn. Mech. Engrs, Vol 182, Pt 1, No 18, 1967.

115 SCHOFIELD R E and THORNLEY R H, Mathematical expression of surface-finish characteristics. Proc. Instn. Mech. Engrs., Vol 182, Pt 3K, 1967.

116 CONNOLLY R, The static stiffness of joint faces. MSc Thesis, UMIST, 1965.

117 LEVINA Z M, Research on the static stiffness of joints in machine tools. Int. MTDR. Conf., 1967.

118 RESHETOV D N and LEVINA Z M, Damping of oscillations in the couplings of components of machines. Vestnik Mashinostroyeniya, No 12, 1956. (Translated from Russian.)

119 BOLLINGER J G, Shock and vibration handbook. Edited by HARRIS C M and CREDE C E, McGraw Hill, 1976, Ch 40, pp 16 - 17.

120 CORBACH K, Die dynamische steifigheit ruhender und beweglicher verbindungen an werkzeugmaschinen. Machinenmarkt, Jg. 72, Nr. 79, 1966. (Translation UMIST 1969.)

121 ANDREW C, COCKBURN J A and WARING A E, Metal surfaces in contact under normal forces: some dynamic stiffness and damping characteristics. Proc. Instn. Mech. Engrs., Vol 182, Pt 3K, 1967.

122 ANDREW C, Damping in fixed joints. MTIRA Conf. on Damping in machine tool structures, 1969.

123 PERA Report 198, Machine Tool Joints, 1969.

124 THORNLEY R H, A study of some parameters which influence the static and dynamic stiffness of joints in machine tool structures. PhD Thesis, UMIST, 1969.

125 THORNLEY R H and KOENIGSBERGER F, Dynamic characteristics of machined joints loaded and excited normal to the joint face. Annals of the CIRP., Vol 19, 1971.

126 DEKONINCK C, Experimental investigation of the normal dynamic stiffness of metal joints. Int. J. Mach. Tool Des. Res., Vol 9, 1969.

127 KHOYI M R H, Some aspects of damping and dynamic characteristics of machine tool structural joints. PhD Thesis, Aston University, 1976

128 SCHOFIELD R E, The damping effect of joints formed from machine surfaces. Int. MTDR. Conf., 1972.

129 SHOUKRY S N, Some aspects of the dynamic performance of machine tool structural joints. PhD Thesis, Aston University, 1980.

130 KIRSANOVA V N, The shear compliance of flat joints. Machines and Tooling, 38, No 7, 1967.

131 MASUKO M, ITO Y, and KOIZUMI T, Horizontal stiffness and micro-slip on a bolted joint subjected to repeated tangential static loads. JSME., Vol 17, No 113, 1974.

132 BACK N, Deformation in machine tool joints. PhD Thesis, UMIST, 1972.

133 BACK N, BURDEKIN M and COWLEY A, Review of the research on fixed and sliding joints. Int. MTDR. Conf., 1972.

134 BURDEKIN M, COWLEY A and BACK N, Experimental study of normal and shear characteristics of machined surfaces in contact. J. Mech. Eng. Science, Vol 20, No 3, 1978.

135 SHOUKRY S N and THORNLEY R H, Theoretical expressions for the normal and tangential stiffness of machine tool joints. Proc. of 22nd Int. MTDR. Conf., UMIST, 1981.

136 ITO Y and MASUKO M, Experimental study on the optimum interface pressure on a bolted joint. 12th MTDR. Conf., 1971.

137 GOODMAN L E and BROWN C B, Energy dissipation in contact friction: contact normal and cyclic tangential loading. J. of applied Mech., 1962.

138 MASUKO M, ITO Y and FUJIMOTO C, Behaviour of the horizontal stiffness and the micro-sliding on the bolted joint under the normal preload. Int. MTDR. Conf., 1971.

139 MUKI R, Progress in solid Mechanics, Vol 1, North Holland, 1960.

140 EARLES S W and BEARDS C F, Some aspects of frictional damping as applied to vibrating beams. Int. J. Mach. Tool Des. Res., Vol 10, 1970.

141 EARLES S W and MOTT N, A response prediction and optimisation of a frictionally damped structure. Proc. MTDR., Vol 13, 1972.

142 EARLES S W and MANSOORI F S, Frictional damping applied to a cantilever-beam structure: A theoretical and experimental response comparison. Int. J. Mach. Tool Des. Res., Vol 14, 1974.

143 BOWERS J E, FINISH N J and GOREHAM A R, The prevention of fretting fatigue in aluminium alloys. Proc. Inst. Mech. Engrs., Vol 182, 1967 - 68, pp 703.

144 BISHOP R E D and JOHNSON D C, The mechanics of vibration. Cambridge University Press, 1960.

145 LAZAN B J, Energy dissipation mechanisms in structures, with particular reference to material damping. Colloquium on structural damping, ASME., 1959. Published by Pergamon Press Ltd, 1960.

146 GOODMAN L E, A review of progress in analysis of interfacial slip damping. Colloquium on structural damping, ASME, 1959.

147 THORNLEY R H and LEES K, Some static and dynamic characteristics of bonded, machine joint faces. Int. MTDR. Conf., 1972.

148 HANKS B R and STEPHENS D G, Mechanism and scaling of damping in a practical structural joint. NASA., Langley Research Centre, 1966.

149 EARLES S W and PHILPOT M G, Energy dissipation at plane surfaces in contact. J. of Mech. Eng. Science, Vol 9, No 2, 1967.

150 PODNICKS E R and LAZAN B J, Analytical methods for determining specific damping energy considering stress distribution. WADC., Technical Report 36 - 44 June, 1957, University of Minnesota.

151 PLUNKETT R, Measurement of damping. Colloquium on structural damping. ASME., 1959, published by Pergamon Press Ltd, 1960.

APPENDIX (I)

1. Stress Distribution In Cylindrical Fitted Parts

As shown in fig (2) if a cylinder of constant wall thickness is subjected to the action of uniformly distributed internal and external pressures, the deformation produced is symmetrical about the axis of the cylinder and does not change along its length.

Consider a ring cut from the cylinder by two planes perpendicular to the axis and at unit distance apart. From the condition of symmetry it follows that there are no shearing stresses on the sides of the element mn m_1n_1 of the ring.

The element is bounded by two axial planes and two concentric cylindrical surfaces. Let σ_t denote the tangential stress acting normal to the side mm_1 and nn_1 of the element and σ_r the radial stress normal to the side mn.

The radial stress varies with the radius r and changes by an amount $(d_{\sigma r}/d_r.d_r)$ in the distance d_r. The normal radial stress on the side m_1n_1 cosequintly is,

$$\sigma_r + \frac{d_{\sigma r}}{d_r}\, d_r \qquad (I.1)$$

Summing up the forces on the element in the direction of the bisector of the angle d ϕ gives the following equilibeium equation,

$$\sigma_r r d\phi + \sigma_t d_r d\phi - (\sigma_r + \frac{d_{\sigma r}}{d_r} d_r)(r + d_r)d\phi = 0$$

neglecting small quantities of higher order, then:

$$\sigma_t - \sigma_r - r \frac{d_{\sigma r}}{d_r} = 0 \qquad (I.2)$$

Equation (I.2) contains two unknowns, namely the stresses σ_t and σ_r. A second equation is necessary for the determination of these quantities which can be found by considering the deformation of the cylinder. The deformation of the cylinder is symmetrical with respect to the axis and consists of a radial displacement of all points on the wall of the cylinder. This displacement is constant in the circumferential direction but varies along the radius, ie it is a function of the radius only. If U denotes the radial displacement of a cylindrical surface of radius r, then the displacement for a surface of radius $r + d_r$ is,

$$U + \frac{du}{dr} d_r$$

Hence an element such as $mn\, m_1 n_1$ undergoes a total elongation in the radial direction equal to $(du/dr.d_r)$ and the unit elongation is therefore,

$$\varepsilon_r = \frac{du}{dr} = \text{radial strain}$$

The expressions for the stresses in terms of strains are:

$$\sigma_r = \frac{E}{1 - \nu^2} \left(\frac{du}{dr} + \nu \frac{u}{r}\right) \qquad (I.3)$$

$$\sigma_t = \frac{E}{1 - \nu^2} \left(\frac{u}{r} + \nu \frac{du}{dr}\right) \qquad (I.4)$$

The normal stresses σ_r and σ_t are evidently not independent, since they can be expressed in terms of one function u substituting equation (I.3), and (I.4) into equation (I.2) we obtain the following equation for determining u:

$$\frac{du^2}{dr^2} + \frac{1}{r}\frac{du}{dr} - \frac{u}{r^2} = 0 \qquad (I.5)$$

The general solution of this equation is:

$$U = C_1 r + \frac{c_2}{r} \qquad (I.6)$$

The constants c_1 and c_2 are determined from the condition at the inner and outer surfaces of the cylinder where the pressures, ie the normal stress σ_r, is known. Substituting from equation (I.6) into equations (I.3), (I.4) we obtain,

$$\sigma_r = \frac{E}{1 - \nu^2} \left| c_1 (1 + \nu) - c_2 \left(\frac{1 - \nu}{r^2}\right) \right| \qquad (I.7)$$

$$\sigma_t = \frac{E}{1 - \nu^2} \left| c_1 (1 + \nu) + c_2 \left(\frac{1 - \nu}{r^2}\right) \right. \qquad (I.8)$$

If P_i and P_o denote the internal and external pressures respectively, the conditions at the outer and inner surfaces of the cylinder are:

$$\sigma_r\left(r = \frac{D}{2}\right) = -P_o \quad \text{and} \quad \sigma_r\left(r = \frac{d}{2}\right) = -P_i \qquad (I.9)$$

The usual convention for stresses is used (positive = tensile). The sign on right-hand side of each equation is negative, because the normal stress is taken as positive for tension.

Substituting the expression for σ_r (equation (I.7)) in equation (I.9) gives two equations for determining the unknown constants c_1 and c_2 from which,

$$c_1 = \frac{1 - \nu}{E} \quad \frac{d^2Pi - D^2Po}{D^2 - d^2} \qquad (I.10)$$

$$c_2 = \frac{1 + \nu}{E} \quad \frac{d^2D^2(Pi - Po)}{4(D^2 - d^2)} \qquad (I.11)$$

Using the values of c_1 and c_2 in equations (I.7) and (I.8) the general expressions for the normal stresses σ_r and σ_t become:

$$\sigma_r = \frac{d^2Pi - D^2Po}{D^2 - d^2} - \frac{(Pi - Po)\, d^2D^2}{4r^2(D^2 - d^2)} \qquad (I.12)$$

$$\sigma_t = \frac{d^2Pi - D^2Po}{D^2 - d^2} + \frac{(Pi - Po)\, d^2D^2}{4r^2(D^2 - d^2)} \qquad (I.13)$$

It is important to note that the sum of these two stresses remains constant, so that the deformation of all elements in the direction of the axis of the cylinder is the same and the induced deformation in any element taken along the cylinder axis is identical.

Considering now the particular case when $p_o = 0$, ie the cylinder is subjected to internal pressure only. Then equations (I.12) and (I.13) become:

$$\sigma_r = \frac{d^2Pi}{D^2 - d^2}\left(1 - \frac{D^2}{4r^2}\right)$$

$$\sigma_t = \frac{d^2Pi}{D^2 - d^2}\left(1 + \frac{D^2}{4r^2}\right)$$

These equations show that σ_r is always a compressive stress and σ_t a tensile stress. The latter is maximum at the inner surface of the cylinder, where:

$$\sigma_t(max) = P_i \frac{(d^2 + D^2)}{(D^2 - d^2)}$$

This equation shows that σ_t maximum is always numerically greater than the internal pressure and approaches this quantity as d increases. The minimum value of σ_t is at the outer surface of the cylinder, the ratio:

$$\frac{\sigma_t(max)}{\sigma_t(min)} = \frac{d^2 + D^2}{d^2} \qquad (I.14)$$

Increases with the increase in the thickness of the cylinder wall. For a comparatively small thickness there is not a great difference between the maximum and minimum values of σ_t.

The shearing stress is maximum at the inner surface of the cylinder where:

$$T(max) = \frac{\sigma t - \sigma r}{2} = \tfrac{1}{2}\left| \frac{Pi(d^2 + D^2)}{D^2 - d^2} + \frac{Pi(D^2 + d^2)}{D^2 - d^2} \right| = \frac{PiD^2}{D^2 - d^2} \qquad (I.15)$$

Considering the deformation of the cylinder and substituting from equations (I.10), (I.11) for the arbitrary constants in equation (I.6) then;

$$U = \frac{1 - \nu}{E} \frac{d^2Pi - D^2Po}{D^2 - d^2} r + \frac{1 + \nu}{E} \frac{d^2D^2(Pi - Po)}{(D^2 - d^2)4r} \qquad (I.16)$$

This gives the radial displacement of any point in the wall of the cylinder. In the particular case of a cylinder subjected to internal pressure only ($P_o = 0$), the radial displacement at the inner surface from equation (I.16) is,

$$U(r = a) = \frac{dPi}{2E} \left(\frac{d^2 + D^2}{D^2 - d^2} + \nu\right)$$

When the cylinder is subjected to external pressure only ($P_i = 0$), the radial displacement at the outer surface is,

$$U(r = b) = -\frac{DPo}{2E} \left(\frac{d^2 + D^2}{D^2 - d^2} - \nu\right)$$

The minus sign indicates that the displacement is towards the axis of the cylinder.

In the case of a shrink-fitted joint, the totals for the ring and shaft = $U_1 + U_2$ interference/rad.

$$\delta = \frac{d.P}{2E}\left(\frac{d^2 + D^2}{D^2 - d^2} + \nu\right) + \frac{d.P}{2E}\left(\frac{d^2 + a^2}{d^2 - a^2} - \nu\right)$$

$$= \frac{d.P}{2E}\left(\frac{d^2 + D^2}{D^2 - d^2} + 1\right)$$

$$\delta = \frac{d.P}{2E} \cdot \frac{2D^2}{D^2 - d^2} = \frac{d.P}{E} \cdot \frac{D^2}{D^2 - d^2}$$

Where:

$\delta m = 2\delta$ interference/diam

The pressure between the mating parts becomes,

$$P = \frac{E\delta m}{2d}\left(1 - \frac{d^2}{D^2}\right) \qquad (I.17)$$

2. The Effect of Loading Conditions During The Test on The Stresses Induced

2.1 Static Test

For the static test case, a compressive load is applied to the shaft. The ring is also subjected to an axial pressure on the face which makes contact with the fixture as shown in fig (3). This pressure will have an effect on the previously calculated stresses induced in the ring and shaft and on the value of interference. This effect can be treated as follows:

1 - Referring to the element of the ring at distance y from the ring face and of thickness (δy) as shown in fig (3) and considering the equilibrium of the element we get,

$$\sigma_y \cdot \frac{\pi}{4} \cdot (D^2 - d^2) = W \cdot \pi \cdot d \cdot \delta_y + (\sigma_y + \delta\sigma y)\frac{\pi}{4}(D^2 - d^2)$$

$$W \cdot d \cdot \delta_y + \frac{\pi}{4}(D^2 - d^2)\delta\sigma_y = 0 \qquad (I.18)$$

$$\text{or } P_a \mu_s \cdot d \cdot \delta_y + \frac{\pi}{4}(D^2 - d^2)\delta\sigma_y = 0$$

The axial stress σ_y will affect the radial strain ε_r by a value given by:

$$\Delta\varepsilon_r = \frac{\nu}{E}\sigma_y \qquad (I.19)$$

This in turn will affect the value of interference (δ_m). If we put

$Uac = \delta_m + U_d$

Where:

Uac = actual interference on the diameter after applying the load

U_d = diameter displacement due to the axial load

$$Uac = \delta_m + d\Delta\varepsilon_r = \delta_m + \frac{d \cdot \nu}{E}\sigma_y \qquad (I.20)$$

The actual pressure at the contact surfaces for the geometry of the specimens used is:

$$P_a = \frac{EUa}{2d}\left(1 - \frac{d^2}{D^2}\right) = K\left(\delta_m + \frac{\nu d}{E}\sigma_y\right)$$

$$P_a = K\delta_m + B\sigma_y$$

$$\text{or } P_a = A + B\sigma_y \qquad (I.21)$$

Where:

$A = K\delta_m$

$B = K \cdot \frac{\nu d}{E}$

$$K = \frac{E}{2D}\left(1 - \frac{d^2}{D^2}\right)$$

By substituting from equation (I.21) into equation (I.18) we get:

$$\mu_s(A + B\sigma_y).d.\delta_y + \frac{\pi}{4}(D^2 - d^2)\delta\sigma_y = 0$$

The above equation is a differential equation in Y and σ_y, by separating the variables and integrating we get:

$$\frac{4\mu s.B.d}{D^2 - d^2}\int_o^y d_y = -\int_s^y \frac{B.d.\sigma y}{A + B\sigma y}$$

$$e^{-cy} = \frac{A + B\sigma y}{A + B.S}, \quad c = \frac{4.\mu s.B.d}{D^2 - d^2}$$

$$\sigma_y = (S + \frac{A}{B})e^{-cy} - \frac{A}{B} \qquad (I.22)$$

Where:

S = axial stress at the ring face which makes contant with the base

$$S = \frac{4W}{(D^2 - d^2)\pi}$$

W = compressive load required to release the fit

$$P_a = A + B\left|\ (S + \frac{A}{B})e^{-cy} - \frac{A}{B}\ \right|$$

or $P_a = (BS + A)e^{-cy}$

$$P_a = (\frac{2\nu}{\pi D^2}W + K\delta_m)e^{-cy} \qquad (I.23)$$

K = .98437 for size 10 mm

= .60156 for size 15 mm

K = .39375 for size 20 mm

C = 1.5×10^{-3}, 2.23×10^{-3} and 3.0×10^{-3} for size 10, 15 and 20 mm respectively.

As an approximation the friction coefficient μ_s can be taken as 0.4 for the joint in the following equation:

$$W = P_a \pi . d . L . \mu_s$$

The maximum diameter displacement = $\frac{d.\nu}{E} . \sigma_y$

$$U_a(max) = \frac{d.\nu}{E} . S$$

$$\text{or } U_a(max) = \frac{d.\nu}{E} \cdot \frac{4}{\pi(D^2 - d^2)} . W \qquad \mu . mm$$

2 - Referring to the element of the shaft at distance Y from the upper face of the ring and of a thickness δ_y as shown in fig (3).

The equilibrium of the element will give:

$$\sigma_y . \frac{\pi}{4} d^2 = P_a . \mu_s . \pi . d . \delta_y + (\sigma_y + \delta\sigma_y)\frac{\pi}{4} d^2$$

$$P_a \mu_s . \delta_y + \frac{d}{4}\delta\sigma_y = 0 \qquad (I.24)$$

$$\text{But } P_a = A + B\sigma_y \qquad (I.25)$$

substituting equation (I.25) into equation (I.24)

$$\mu_s . (A + B\sigma_y)\delta_y + \frac{\pi}{4} . d . \delta\sigma_y = 0$$

The above equation is a differential equation in y and σy, separating the variables and integrating we get:

$$\frac{4.\mu s.B}{d} \int_{o}^{-y} d_y = -\int_{s}^{y} \frac{B.\sigma y}{A + B\sigma y}$$

$$e^{-cy} = \frac{A + B\sigma y}{A + B.S} \quad , \quad C = \frac{4.\mu s.B}{d}$$

But $y = (S + \frac{A}{B})e^{-cy} - \frac{A}{B}$;

$$P_a = (BS + A)e^{-cy}$$

Where:

$B = \frac{K.\nu.d}{E}$ = 0.1406, 0.1289 and 0.1125 for size 10, 15 and 20 mm respectively

$S = \frac{4W}{\pi d^2}$ Kg/mm^2

$A = K\delta m$

$C = \frac{4.\mu sB}{d}$ = 0.0225, 0.0137 and 0.009 for size 10, 15 and 20 mm respectively

The diameter displacement for the ring and shaft were calculated and its mean value used for correcting the interference value. Equation (I.26) is then used to find the actual pressure at different lengths along the ring and shaft for every size.

$$P_a = \frac{K\delta ma\ e^{-cy}}{1 - K_1\ e^{-cy}} \qquad (I.26)$$

Where:

K, K_1, C are constants depending on the joint size.

2.2 Dynamic Testing

2.2.1 The Effect Of The Cyclic Load On The Value Of Interference

The cyclic load will have an effect on the stresses induced in the shaft during the test. To calculate this effect, it was necessary to estimate the value of the load required to release the fit, as follows:

1 - Assume that the value of interference δm is equal to the actual value of interference Uac.

2 - From the relationship between the actual value of interference and mac-mic. interference, the macro-interference (δma) can be estimated.

3 - Using the following equation the value of (B.A)% can be found:

$$\delta ma = K(B.A)\%$$

Where:

K is a constant depending on the joint size

= 72.43, 118.525 and 181.079 for size 10, 15 and 20 mm respectively

4 - The load required to release the fit is,

$$W = A.(B.A)\% \qquad T. = K' \delta ma$$

Where:

T = Material shear stress

5 - The equation deduced for the case of static loading was used to calculate the diameter displacement of ths shaft using the average value of the diameter.

6 - The maximum value of the diameter displacement for the shaft was estimated from the following equation:

$$U_{ds}max = \frac{d.\nu}{E} \cdot \frac{4}{\pi d^2} \cdot W$$

The diameter displacement for the joint was calculated using the following equation:

$$U_d = U_{dr} - \frac{Uds}{2}$$

APPENDIX (II)

Example Of Calculation Of The Energy Dissipation Between Two Surfaces Consisting Shrink-Fitted Joints

The energy dissipation was estimated using a mathematical model as described in Chapter (8). The following sample calculations can be used as a guide to explain the overall method of treatment.

The equation has been deduced from the theoretical analysis and was as follows:

$$\text{Energy dissipation } (W) = 0.5\mu s.A.\lambda s \left| \frac{\delta ma.E}{2d}\left(1 - \frac{d^2}{D^2}\right) \right| \qquad (II.1)$$

Where:

$$\lambda s = \delta e = \frac{Ps/n}{\pi.a.G}(2 - \nu) \qquad (II.2)$$

$$G = \frac{E}{2(1 + \nu)} \qquad (II.3)$$

a = average asperities radius in mm

n = number of asperity per mm^2

From equations (II.2) and (II.3) λs can be found as follows:

$$\lambda s = \frac{0.011}{a.n} \cdot P_s \quad \mu mm$$

The values of a and n were estimated using the following equations:

$$a = \frac{\text{Stroke length x (B.A)\%}}{2\ \text{Nav}}$$

$$n = \left(\frac{Nav}{L}\right)^2 = \left(\frac{\text{Average number of asperities per stroke}}{\text{Stroke length}}\right)^2$$

(B.A)% estimated using the bearing area curve and the value of micro-interference for every joint.

μs was evaluated as described in Chapter (6)

$$\frac{\delta ma.E}{2d}\left(1 - \frac{d^2}{D^2}\right) = 0.39375\,\delta ma \quad \text{for the joint with d = 20 mm}$$

The different parameters for the group of D62 were calculated as shown in the following table:

Joint No	δm μmm	$\frac{\delta mi}{4}$ μmm	(B.A)%	Nav/mm	n/mm^2	a mm
7-40	7.3	0.50	2.5%	21.0	30.5	.0023
8-42	13.72	0.65	4.56%	30.75	65.48	.0028
18-34	24.62	0.70	8.37%	30.5	64	.0052
21-36	16.78	0.68	6.5%	35.5	87	.0035

The stroke length of the Talysurf (K) = 3.8 mm

The theoretical values of energy dissipation using the previous method and those measured experimentally for the different joints are shown in the following tables:

1 - J(7-40)

Ps KN	.579	.736	1.43	1.923	2.43	3.2	3.767	4.25
W theor. KNmm x 10^{-4}	2.087	2.68	5.216	7.02	8.87	11.69	13.75	15.53
W exp. KNmm x 10^{-4}	0.64	0.77	2.223	5.569	8.796	9.532	12.22	15.43

2-J(8-42)

Ps KN	1.304	2.737	3.65	4.64	5.925	6.465	7.3	8.8
W theor. KNmm x 10^{-4}	3.99	8.38	11.17	14.2	18.14	19.8	22.35	26.95
W exp. KNmm x 10^{-4}	6.89	11.94	10.77	24.18	31.99	28.83	33.68	38.73

3 - J(18-34)

Ps KN	2.81	4.42	6.89	8.0	9.015	10.15	11.96
W theor KNmm x 10^{-4}	9.26	14.57	22.72	26.37	29.72	33.77	39.43
W exp KNmm x 10^{-4}	18.97	24.17	29.25	20.98	18.38	17.89	18.98

4 - J(21-36)

Ps KN	3.16	7.913	9.87	11.026	11.38
W theor KNmm x 10^{-4}	7.49	18.74	23.4	26.15	27.0
W exp KNmm x 10^{-4}	11.66	17.11	19.44	14.58	35.63

APPENDIX (III)

Measurement Of Damping

The following damping measures are often used to describe the damping capacity for a single degree of freedom and their definition as follows:

1 - Logarithmic decrement δ

The logarithmic decrement is the natural logarithm of the ratio of any two successive amplitude of like sign in the decay curve; or to express the average for n cycles:

$$\delta = \frac{1}{n} \ln \frac{x1}{xn} = \frac{2\pi\xi}{\sqrt{1 - \xi^2}} \simeq 2\pi\xi$$

2 - Loss factor τ

The loss factor τ is a non-dimensional measure of damping defined as the ratio of the quadrature to the inphase stiffness components:

$\tau = \frac{h}{k} = \tan \theta$, where h is the coefficient of hysteretic damping.

3 - Viscous damping coefficient C

Viscous damping is the dissipation of energy that occurs when a particle in a vibrating system is resisted by a force that has a magnitude proportional to the velocity of the particle. The coefficient of proportionality C is called the damping coefficient and is the value of this force at unit velocity.

4 - Damping ratio

The damping ratio is the ratio of the damping coefficient C to the critical damping coefficient C_c, thus

$$\xi = \frac{C}{C_c} = \frac{C}{2Mw} = \frac{C}{2\sqrt{KM}}$$

5 - Specific damping capacity Ψ

The specific damping capacity is the ratio of the energy dissipated to the maximum available energy per cycle of vibrations.

$$\Psi = \frac{-Do}{Vo} = \frac{\pi\omega C\ X_o^2}{\frac{1}{2}K\ X_o^2} = 2\pi\frac{\omega C}{K} = 2\pi\tau = 4\pi\xi = 2\delta$$

TABLE 1

Shaft and Ring profile mean slope (Group ST62)

a - Shafts (Grinding)

Shaft No	HSC Mean	λav mm	CLA μmm	θ using eqn (6.8)	θ using eqn (6.4)	θ using eqn (6.6)	θ av
11	125.4	.03	.349	4.15	4.69	4.5	4.45
12	114	.033	.346	3.77	4.5	4.47	4.25
12	127	.030	.347	4.15	4.38	4.48	4.35
13	119	.032	.376	4.22	4.73	4.759	4.57
14	116	.033	.4	4.35	4.97	4.98	4.77
15	120	.032	.368	4.13	4.73	4.68	4.51
16	76.75	.05	.304	4.16	5.028	4.05	4.41

Talysurf stroke (K) = 3.8 mm

Table 1 continued

b - Rings (Grinding)

Ring No	HSC Mean	λav mm	CLA μmm	θ using eqn (6.8)	θ using eqn (6.4)	θ using eqn (6.6)	θ av
27	83.87	.0226	.284	4.5	4.3	3.84	4.2
37	78.37	.024	.29	4.34	4.76	3.9	4.33
28	81.25	.0233	.275	4.25	4.63	3.74	4.21
29	82.75	.023	.299	4.67	4.94	4.0	4.54
26	77.7	.024	.256	3.83	4.38	3.5	3.9
41	86.1	.022	.41	6.67	5.23	5.07	5.65
39	81.0	.023	.31	5.3	5.23	4.4	4.98

Talysurf stroke (J) = 1.9 mm

TABLE 2

Shaft and Ring profile mean slope (Group D11)

a - Shafts (Turning)

Shaft No	HSC Mean	λav mm	CLA μmm	θ using eqn (6.8)	θ using eqn (6.4)	θ using eqn (6.6)	θ av
2'	15.87	.239	3.19	4.8	12.05	13.55	10.13
3'	16.12	.235	3.21	4.9	11.97	13.57	10.15
4'	15.75	.241	3.09	4.63	11.9	13.44	9.99
5'	16.12	.235	3.04	4.63	11.32	13.39	9.78
6	26.37	.144	2.67	6.61	10.42	12.93	9.99

Talysurf stroke (K) = 3.8 mm

Table 2 continued

b - Rings (Turning)

Ring No	HSC Mean	λav mm	CLA μmm	θ using eqn (6.8)	θ using eqn (6.4)	θ using eqn (6.6)	θ av
28	11.125	.34	4.67	4.9	12.05	14.68	10.54
3	13.75	.276	2.65	3.4	10.5	12.91	9.94
2	13.6	.279	2.5	3.2	10.5	12.69	9.8
1	11.665	.325	3.65	4.06	11.63	13.97	9.89
6	13.625	.279	2.7	3.5	10.87	12.97	9.11

Talysurf stroke (K) = 3.8 mm

TABLE 3

Mechanical properties and chemical composition of (ENIA)

Mechanical Properties	Tensile strength (max)	Tensile strength (min)	Flow pressure Yc (HV)	Elongation %
	47.3 kg/mm^2	46.7 kg/mm^2	71.3 kg/mm^2	20%

Chemical Composition	C%	Si%	Mn%	S%	P%
	.07 - 0.15	0.1 max	0.8 - 1.2	0.2 - 0.3	.07 max

TABLE 4

Cutting conditions for the specimens

1 - Turning

Specimens	Speed rpm	Feed mm/rev	Depth of cut mm	Tool nose radius mm
ST	580	.0059	.002	.4
ST	580	.002	.002	.4
D	580	.0059	.002	.4
D	580	.002	.002	.4

2 - Grinding

Specimens	Wheel type	Depth of cut mm	Wheel speed rpm
ST	WA-46 K5V	.006	2850
ST	WA-180 K5V	.006	2850
D	WA-46 K5V	.006	2850
D	WA-180 K5V	.006	2850

TABLE 5

Example of the matching process

Joint size d = 20 mm, Group D61

a) The mean tolerance and surface roughness of the machined shafts and rings

Shaft No	CLA µmm	Mean tolerance µmm	Ring No	CLA µmm	Mean tolerance µmm
2	.88	-5.4	3	.81	-29.12
3	.87	-6.2	6	.88	-11.22
4	.93	-8.2	7	.84	-18.3
5	.71	-15.6	9	.82	-25.98
5'	.83	-16.2	16	.97	-28.9
			17	.99	-12.7
			18	.97	-9.88
			19	.86	-39.26
			22	.8	-52.32
			45	.93	-12.72

Table 5 continued

b) The mean interference value resulting from matching the above shafts and rings

Sh No \ R No	3	6	7	9	16	17	18	19	22	45
2	23.75*	5.82	12.9	20.58	23.5	7.3	4.48	33.86	46.92	7.32
3	22.92	5.02	12.1	19.78	22.7	6.5	3.68	33.06*	46.12	6.52
4	20.92	3.02	10.1	17.78	20.7	4.5	1.68	31.06	44.12*	4.52
5	13.52	-	2.7*	10.38	13.3	-	-	23.66	36.72	-
5'	12.92	-	2.1	9.78	12.7*	-	-	23.06	36.12	-

* The ring and shaft were chosen in such a way as to make the step increase/decrease in the interference level almost constant.

Table 5 continued

c) The chosen interference values* for the tested joints

Shaft number	2	3	4	5	5'
Ring number	3	19	22	7	16
Value of interference μmm	23.75	33.06	44.12	2.7	12.7

* The ring and shaft were chosen in such a way as to make the step increase/decrease in the interference level almost constant.

TABLE 6

Coding System

ST : Static Test
D : Dynamic Test

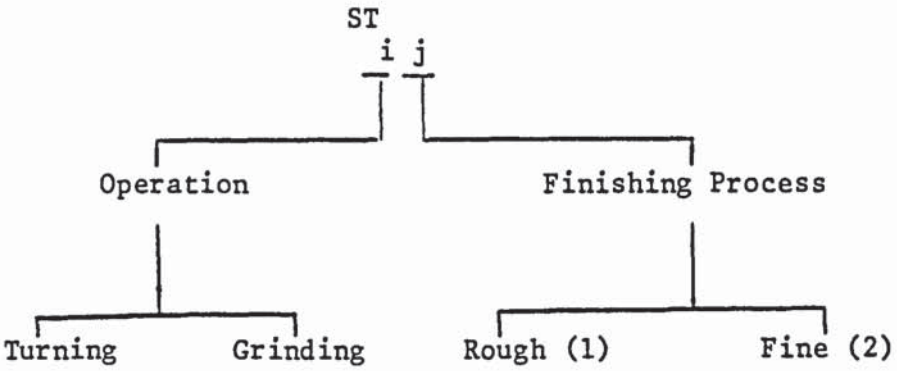

Size mm	Turning Code	Grinding Code
10	1	2
15	3	4
20	5	6

TABLE 7

The experimental holding load ratio

1 - Static loading

a) Grinding

δm µmm	CLA µmm	d10/d15 HL ratio	d10/d20 HL ratio	d15/d20 HL ratio	δm µmm	CLA µmm	d10/d15 HL ratio	d10/d20 HL ratio	d15/d20 HL ratio
10	.23-.33	1.506	3.413	2.266	20	.23-.33	1.466	2.75	1.878

b) Turning

δm µmm	CLA µmm	d10/d15 HL ratio	d10/d20 HL ratio	d15/d20 HL ratio	δm µmm	CLA µmm	d10/d15 HL ratio	d10/d20 HL ratio	d15/d20 HL ratio
10	1.05-1.5	1.1726	3.36	2.865	20	1.05-1.5	1.47	2.95	2.008

Table 7 continued

2 - Dynamic loading

a) Grinding

δm µmm	CLA µmm	d10/d15 HL ratio	d10/d20 HL ratio	d15/d20 HL ratio	δm µmm	CLA µmm	d10/d15 HL ratio	d10/d20 HL ratio	d15/d20 HL ratio
10	.31-.39	1.096	1.69	1.329	20	.31-.39	1.37	1.663	1.2138

b) Turning

δm µmm	CLA µmm	d10/d15 HL ratio	d10/d20 HL ratio	d15/d20 HL ratio	δm µmm	CLA µmm	d10/d15 HL ratio	d10/d20 HL ratio	d15/d20 HL ratio
10	.66-.73	1.184	1.81	1.529	20	.66-.73	1.272	1.59	1.248

TABLE 8

The theoretical holding load ratio

1 - Using equation (6.19), coefficient of friction and NDC method

a) Grinding

δm µmm	CLA µmm	d10/d15 HL ratio	d10/d20 HL ratio	d15/d20 HL ratio	δm µmm	CLA µmm	d10/d15 HL ratio	d10/d20 HL ratio	d15/d20 HL ratio
10	.23-.33	1.44	2.22	1.533	20	.23-.33	1.57	2.42	1.538

b) Turning

δm µmm	CLA µmm	d10/d15 HL ratio	d10/d20 HL ratio	d15/d20 HL ratio	δm µmm	CLA µmm	d10/d15 HL ratio	d10/d20 HL ratio	d15/d20 HL ratio
10	1.05-1.5	1.44	1.65	1.146	20	1.05-1.5	1.65	2.33	1.41

2 - Using Lame equation (4.6)

d10/d15 = 1.636 d10/d20 = 2.5 d15/d20 = 1.528

TABLE 9

The experimentally obtained holding load for shrink and press fitted joints and the equivalent HL obtained using the BAC, NDC and μs methods

I - Static Testing

1 - ST62 joints

CLA / δm μmm	0.33 μmm								
	Exp Sh F HL KN	Exp P F HL KN	% dev of PF HL	BAC HL KN	% dev of BAC HL	NDC HL KN	% dev of NDC HL	theor μs HL KN	% dev of theor μs HL
7.74	7.455	3.924	-47%	4.964	-33%	4.898	-34%	5.509	-26%
13.62	8.437	3.139	-63%	9.967	+18%	9.465	+12%	10.979	+30%
19.02	13.734	9.094	-34%	13.273	-3%	13.851	+0.8%	14.65	+6.7%
29.98	22.563	10.889	-52%	23.053	+2%	22.713	+6.6%	25.46	+12.8%
34.42	26.291	15.99	-39%	27.075	+3%	26.808	+2%	29.82	+13.4%
43.84	31.882	17.952	-44%	34.237	+7.3%	34.486	+8.2%	37.77	+18.5%
50.58	36.885	18.443	-50%	40.81	+10.6%	40.196	+8.9%	44.951	+21.8%

Table 9 continued

2 - ST61 joints

CLA / δm µmm	0.49 µmm								
	Exp Sh F HL KN	Exp P F HL KN	% dev of PF HL	BAC HL KN	% dev of BAC HL	NDC HL KN	% dev of NDC HL	theor µs HL KN	% dev of theor µs HL
4.6	4.993	2.953	-41%	2.158	-56%	1.944	-61%	2.408	-52%
14.0	9.594	5.15	-46%	9.192	-4.2%	8.622	-10%	10.224	+6.5%
20.82	14.999	8.093	-46%	14.558	-2.9%	13.727	-8.5%	16.144	+7.6%
26.42	18.001	9.908	-45%	19.002	+5.5%	18.385	+2.1%	21.15	+17.5%
34.52	23.053	12.459	-46%	23.338	+1.2%	24.955	+8.2%	26.013	+12.8%

Table 9 continued

3 - ST52 joints

CLA / δm µmm	1.5 µmm								
	Exp Sh F HL KN	Exp P F HL KN	% dev of PF HL	BAC HL KN	% dev of BAC HL	NDC HL KN	% dev of NDC HL	theor µs HL KN	% dev of theor µs HL
12.26	7.043	2.599	-63%	6.298	-10%	4.964	-29%	7.402	+5.1%
20.14	12.498	5.101	-59%	10.4	-17%	10.144	-19%	12.126	-3%
28.64	17.501	8.849	-49%	18.041	+3%	16.134	-7.8%	20.59	+17.6%
36.48	22.465	11.497	-49%	23.514	+4.6%	22.009	-2%	26.827	+19.4%
43.34	26.879	14.048	-48%	29.106	+8.3%	27.396	+1.9%	33.129	+23%

Table 9 continued

4 - ST51 joints

CLA / δm µmm	4.25 µmm								
	Exp Sh F HL KN	Exp P F HL KN	% dev of PF HL	BAC HL KN	% dev of BAC HL	NDC HL KN	% dev of NDC HL	theor µs HL KN	% dev of theor µs HL
9.33	4.199	1.55	-63%	4.513	+7.5%	1.539	-63%	5.39	+28%
19.84	9.398	3.051	-67%	10.33	+9.9%	5.411	-42%	12.25	+30%
29.84	14.999	4.453	-70%	14.646	-2.3%	10.657	-30%	17.302	+15%
36.52	19.375	6.298	-67%	21.583	+11.4%	14.907	-23%	25.704	+32%
46.54	25.624	7.603	-70%	29.136	+13.7%	21.116	-17.6%	34.62	+35%

Table 9 continued

5 - ST42 joints

CLA / δm µmm	0.23 µmm								
	Exp Sh F HL KN	Exp P F HL KN	% dev of PF HL	BAC HL KN	% dev of BAC HL	NDC HL KN	% dev of NDC HL	theor µs HL KN	% dev of theor µs HL
3.72	7.995	3.247	-59%	3.92	-51%	3.148	-60%	4.283	-46%
4.98	9.996	3.571	-64%	4.852	-51%	4.576	-54%	5.289	-47%
10.24	18.639	10.202	-45%	12.066	-35%	10.884	-41.6%	13.205	-29%
13.58	22.494	11.287	-50%	15.75	-30%	15.126	-33%	17.214	-23.5%
25.86	39.436	19.492	-50.5%	33.55	-15%	31.11	-21%	36.537	-7.3%
34.98	46.548	27.664	-41%	45.065	-3.2%	43.156	-7.3%	49.015	+5.3%
44.58	51.247	32.373	-37%	56.702	+10.6%	55.81	+8.9%	61.733	+20%

Table 9 continued

6 - ST41 joints

CLA / δm µmm	0.44 µmm								
	Exp Sh F HL KN	Exp P F HL KN	% dev of PF HL	BAC HL KN	% dev of BAC HL	NDC HL KN	% dev of NDC HL	theor µs HL KN	% dev of theor µs HL
9.26	12.822	4.581	-64%	8.839	-31%	8.014	-37%	9.806	-23.5%
25.58	36.101	16.245	-55%	30.509	-15%	28.063	-22%	33.849	-6.2%
32.62	41.692	21.248	-49%	38.85	-6.8	37.063	-11%	43.085	+3.3%
41.1	46.4	22.563	-51.4%	50.394	+8.6	48.036	+3.5%	56.025	+20.7%
50.94	51.012	25.506	-50%	61.312	+20%	60.664	+18.9%	68.47	+34%

Table 9 continued

7 - ST32 joints

CLA / δm µmm	1.37 µmm								
	Exp Sh F HL KN	Exp P F HL KN	% dev of PF HL	BAC HL KN	% dev of BAC HL	NDC HL KN	% dev of NDC HL	theor µs HL KN	% dev of theor µs HL
12.96	15.304	4.346	-71%	8.829	-42%	7.509	-51%	10.162	-33%
28.1	34.335	12.066	-65%	26.92	-21.5%	23.727	-31%	30.78	-10%
37.88	41.241	14.421	-65%	37.18	-9.8%	35.079	-15%	42.44	+2.9%
50.75	48.657	17.658	-64%	50.47	+3.7%	50.258	+3.3%	57.846	+18.9%
56.34	50.816	22.073	-56%	54.779	+7.8%	57.276	+12.7%	62.93	+24%

Table 9 continued

8 - ST31 joints

CLA / δm µmm	2.35 µmm								
	Exp Sh F HL KN	Exp P F HL KN	% dev of PF HL	BAC HL KN	% dev of BAC HL	NDC HL KN	% dev of NDC HL	theor µs HL KN	% dev of theor µs HL
11.24	11.242	3.581	-68%	8.25	-26.6%	4.424	-60%	9.6	-14.6%
17.56	18.609	5.425	-71%	14.744	-21%	9.278	-50%	17.556	-5.6%
26.9	28.449	13.734	-52%	20.797	-27%	18.431	-35%	24.788	-13%
37.2	37.494	14.224	-62%	28.85	-23%	29.1	-22%	33.98	-9.4%
46.84	42.477	16.245	-62%	40.221	-5.3%	39.566	-6.8%	47.407	+11.5%

Table 9 continued

9 - ST22 joints

CLA / δm µmm	0.27 µmm								
	Exp Sh F HL KN	Exp P F HL KN	% dev of PF HL	BAC HL KN	% dev of BAC HL	NDC HL KN	% dev of NDC HL	theor µs HL KN	% dev of theor µs HL
10.07	24.034	5.748	-76%	20.63	-14%	17.396	-27%	22.612	-5.9%
23.34	51.5	19.247	-62%	49.57	-3.7%	47.51	-7.7%	54.39	+5.6%
32.48	56.407	28.645	-49%	69.308	+22.8%	68.364	+21%	75.95	+34%
43.44									
48.84									

Table 9 continued

10 - ST21 joints

CLA / δm µmm	0.41 µmm								
	Exp Sh F HL KN	Exp P F HL KN	% dev of PF HL	BAC HL KN	% dev of BAC HL	NDC HL KN	% dev of NDC HL	theor µs HL KN	% dev of theor µs HL
7.12	17.167	4.748	-72%	9.663	-43.7%	8.832	-48%	10.813	-37%
11.42	22.494	10.752	-52%	20.71	-7.9%	17.417	-22.5%	22.918	+1.9%
24.42	47.5	19.247	-59%	49.079	+3.3%	45.569	-4%	54.296	+14%
39.38									
44.3									

Table 9 continued

11 - ST12 joints

CLA / δm µmm	1.05 µmm								
	Exp Sh F HL KN	Exp P F HL KN	% dev of PF HL	BAC HL KN	% dev of BAC HL	NDC HL KN	% dev of NDC HL	theor µs HL KN	% dev of theor µs HL
10.51	19.914	5.395	-73%	11.782	-41%	7.864	-60.5%	13.57	-31.8%
22.46	39.995	21.19	-47%	30.529	-23.6%	27.718	-30.7%	34.913	-12.7%
28.71	50.002	27.272	-45.5%	42.87	-14%	40.336	-19%	49.001	-2%
39.1									
50.1									

Table 9 continued

12 - ST11 joints

CLA / δm µmm	2.32 µmm								
	Exp Sh F HL KN	Exp P F HL KN	% dev of PF HL	BAC HL KN	% dev of BAC HL	NDC HL KN	% dev of NDC HL	theor µs HL KN	% dev of theor µs HL
10.55	13.881	4.248	-69%	7.976	-42.5%	3.916	-71.8%	9.263	-33%
20.35	30.744	16.059	-48%	21.592	-30%	14.893	-51%	25.199	-18%
30.73	45.499	26.88	-41%	35.02	-23%	30.89	-32%	41.05	-9.8%
34.01	49.894	27.958	-44%	40.633	-18.5%	37.11	-25.6%	47.21	-5.4%
42.68									

Table 9 continued

II - Dynamic Testing

13 - D62 joints

CLA / δm µmm	0.39 µmm								
	Exp Sh F HL KN	Exp P F HL KN	% dev of PF HL	BAC HL KN	% dev of BAC HL	NDC HL KN	% dev of NDC HL	theor µs HL KN	% dev of theor µs HL
2.86	1.324	.657	-50%	1.58	+19%	1.565	+18%	1.752	+32%
7.3	5.003	2.472	-50.6%	4.576	-8.5%	4.344	-13%	5.073	+1.4%
13.72	8.839	4.306	-51%	9.209	+4.2%	8.911	+0.8%	10.235	+15.8%
16.78	11.026	5.395	-51%	11.683	+5.9%	11.228	+1.8%	12.954	+17.5%
24.62	15.48	7.985	-48%	18.021	+16%	16.962	+9.5%	19.98	+29%
36.56	24.427	12.066	-50.6%	26.954	+10.3%	25.93	+6%	29.88	+22%
39.48	27.125	12.792	-53%	29.34	+8%	28.132	+3.7%	32.454	+19.6%

Table 9 continued

14 - D61 joints

CLA / δm µmm	0.73 µmm								
	Exp Sh F HL KN	Exp P F HL KN	% dev of PF HL	BAC HL KN	% dev of BAC HL	NDC HL KN	% dev of NDC HL	theor µs HL KN	% dev of theor µs HL
2.7	.883	.49	-44.5%	1.125	+27%	1.006	+14%	1.268	+43.6%
12.7	7.848	5.866	-25%	6.859	-12.6%	6.674	-15%	7.786	-0.8%
23.72	12.645	5.493	-56.5%	15.478	+22%	14.265	+12.8%	17.365	+37%
33.06	19.875	10.79	-46%	21.753	+9.4%	20.95	+5.4%	24.463	+23%
44.12	25.99	13.008	-50%	29.042	+11.7%	29.117	+12.1%	32.968	+27%

Table 9 continued

15 - D52 joints

CLA / δm µmm	3.5 µmm								
	Exp Sh F HL KN	Exp P F HL KN	% dev of PF HL	BAC HL KN	% dev of BAC HL	NDC HL KN	% dev of NDC HL	theor µs HL KN	% dev of theor µs HL
7.33	1.324	.638	-51.8%	2.921	+120%	1.32	-0.3%	3.452	+160%
24.56	9.545	4.169	-56%	13.925	+46%	8.646	-9.4%	16.47	+72.5%
33.16	14.813	7.21	-51%	17.299	+16.8%	13.735	-7.3%	20.55	+39%
39.2	16.579	8.064	-51%	23.846	+44%	17.839	+7.6%	28.2	+70%
45.86	19.512	8.976	-54%	27.834	+43%	22.125	+13.4%	33.066	+69%

Table 9 continued

16 - D51 joints

CLA / δm µmm	5.15 µmm								
	Exp Sh F HL KN	Exp P F HL KN	% dev of PF HL	BAC HL KN	% dev of BAC HL	NDC HL KN	% dev of NDC HL	theor µs HL KN	% dev of theor µs HL
6.5	1.471	.922	-37%	2.093	+42%	.858	-39%	2.487	+69%
16.9	3.708	2.815	-24%	8.249	+122%	3.514	-5.2%	9.865	+166%
29.76	8.839	4.591	-48%	15.597	+76%	9.23	-4.4%	18.529	+109%
36.54	11.664	6.011	-48%	19.254	+65%	12.502	+7.2%	22.873	+96%
42.7	13.587	7.177	-47%	20.25	+49%	16.21	+19.1%	23.98	+76%

Table 9 continued

17 - D42 joints

CLA / δm µmm	0.31 µmm								
	Exp Sh F HL KN	Exp P F HL KN	% dev of PF HL	BAC HL KN	% dev of BAC HL	NDC HL KN	% dev of NDC HL	theor µs HL KN	% dev of theor µs HL
3.46	4.012	2.541	-37%	2.905	-27%	2.465	-38%	3.213	-20%
10.18	10.595	6.19	-41.6%	10.467	-1.2%	9.215	-13%	11.439	+8%
14.14	10.894	5.082	-53%	13.837	+27%	13.36	+22%	15.27	+40%
26.62	20.012	12.37	-38%	28.177	+41%	27.039	+35%	30.87	+54%
34.72	26.87	12.9	-52%	36.937	+37%	35.99	+34%	40.66	+51%

Table 9 continued

18 - D41 joints

CLA / δm µmm	0.68 µmm								
	Exp Sh F HL KN	Exp P F HL KN	% dev of PF HL	BAC HL KN	% dev of BAC HL	NDC HL KN	% dev of NDC HL	theor µs HL KN	% dev of theor µs HL
2.55	4.248	2.207	-48%	.683	-84%	1.064	-75%	0.77	-82%
11.12	8.181	5.16	-37%	12.287	+50%	7.99	-2.3%	13.786	+68%
25.8	18.443	9.643	-48%	23.487	+27%	22.362	+21%	26.29	+42%
37.8	25.31	12.164	-52%	37.24	+47%	35.142	+39%	41.685	+65%
43.84	28.282	13.077	-54%	41.69	+47%	41.513	+46.7%	46.885	+66%

Table 9 continued

19 - D32 joints

CLA / δm µmm	1.61 µmm								
	Exp Sh F HL KN	Exp P F HL KN	% dev of PF HL	BAC HL KN	% dev of BAC HL	NDC HL KN	% dev of NDC HL	theor µs HL KN	% dev of theor µs HL
8.5	6.112	2.727	-55%	6.232	+2%	3.35	-45%	7.173	+17%
18.28	11.213	5.729	-49%	13.968	+24%	11.073	-1.2%	16.188	+44%
27.96	16.932	8.064	-52%	21.363	+26%	20.251	+19.6%	25.323	+49%
36.72	20.11	8.945	-55%	28.86	+43%	28.189	+40%	33.37	+66%
44.83	23.897	11.252	-53%	38.264	+60%	36.28	+52%	43.94	+84%

Table 9 continued

20 - D31 joints

CLA / δm µmm	2.64 µmm								
	Exp Sh F HL KN	Exp P F HL KN	% dev of PF HL	BAC HL KN	% dev of BAC HL	NDC HL KN	% dev of NDC HL	theor µs HL KN	% dev of theor µs HL
7.02	4.199	2.109	-50%	3.008	-28%	1.459	-65%	3.542	-15.6%
14.58	7.357	3.178	-57%	9.904	+35%	4.68	-36%	11.661	+58%
26.4	12.37	7.554	-39%	18.86	+52%	13.349	+7.9%	22.057	+78%
34.58	15.765	7.711	-51%	25.168	+59%	20.921	+32%	29.9	+90%
45.76	21.78	9.329	-57%	32.07	+47%	30.844	+41.6%	38.099	+75%

Table 9 continued

21 - D22 joints

CLA / δm µmm	0.36 µmm								
	Exp Sh F HL KN	Exp P F HL KN	% dev of PF HL	BAC HL KN	% dev of BAC HL	NDC HL KN	% dev of NDC HL	theor µs HL KN	% dev of theor µs HL
5.61	4.63	2.443	-47%	6.929	+50%	5.386	+16%	7.61	+64%
15.36	18.806	8.976	-52%	21.388	+13.7%	19.32	+2.7%	23.546	+25%
26.46	28.233	12.753	-55%	38.572	+36%	35.95	+27%	42.673	+51%
47.6									
54.04									

Table 9 continued

22 - D21 joints

CLA / δm µmm	0.66 µmm								
	Exp Sh F HL KN	Exp P F HL KN	% dev of PF HL	BAC HL KN	% dev of BAC HL	NDC HL KN	% dev of NDC HL	theor µs HL KN	% dev of theor µs HL
4.57	3.747	1.832	-51%	3.661	-2.3%	2.42	-35%	4.127	+10%
10.39	10.418	5.7	-45%	8.636	-17%	8.501	-18%	9.712	-6.8%
14.78	14.735	7.917	-46%	15.534	+5.4%	13.983	-5.1%	17.717	+20%
20.48	20.503	11.576	-43.5%	22.753	+11%	21.926	+6.9%	25.65	+25%
34.62	29.175	12.37	-58%	45.914	+57%	42.135	+44%	51.88	+78%
42.08									

Table 9 continued

23 - D12 joints

CLA / δm µmm	1.85 µmm								
	Exp Sh F HL KN	Exp P F HL KN	% dev of PF HL	BAC HL KN	% dev of BAC HL	NDC HL KN	% dev of NDC HL	theor µs HL KN	% dev of theor µs HL
9.65	7.357	2.933	-60%	8.253	+12%	3.378	-54%	9.565	+30%
19.98	14.744	6.011	-59%	18.368	+24%	12.349	-16%	21.482	+46%
30.38	24.751	9.614	-61%	28.932	+16.9%	24.057	-2.8%	33.837	+37%
41.96	29.587	13.793	-53%	37.059	+25%	39.425	+33%	43.733	+48%
50.65									

Table 9 continued

24 - D11 joints

CLA / δm µmm	3.07 µmm								
	Exp Sh F HL KN	Exp P F HL KN	% dev of PF HL	BAC HL KN	% dev of BAC HL	NDC HL KN	% dev of NDC HL	theor µs HL KN	% dev of theor µs HL
10.91	6.131	2.295	-62%	2.59	-58%	2.221	-64%	3.015	-51%
25.43	15.696	6.573	-58%	16.101	+2.6%	11.356	-27%	18.831	+20%
31.53	18.148	6.992	-61.5%	18.45	+1.7%	15.555	-14%	21.577	+19%
38.75	24.554	13.783	-44%	25.588	+4.2%	23.995	-2.3%	29.857	+21.6%
48.28	30.048	14.489	-52%	42.32	+41%	33.551	+11.6%	49.384	+64.1%

TABLE 10

The experimentally obtained holding load for static and dynamic tests

1 - Size d = 20 mm

CLA / δm µmm	0.33 - 0.39 µmm				0.49 - 0.73 µmm			
	ST62 HL KN	D62 HL KN	deviation KN	% age dev	ST61 HL KN	D61 HL KN	deviation KN	% age dev
10	7.664	6.32	1.344	-17.5%	7.939	5.46	2.479	-31.2%
20	14.91	13.188	1.722	-11.5%	14.083	11.485	2.598	-18.4%
30	22.152	20.051	2.101	-9.5%	20.226	17.508	2.718	-13.5%
40	29.396	26.914	2.482	-8.5%	26.369	23.53	2.839	-11%
45	33.018	30.346	2.672	-8.1%	29.44	26.543	2.897	-9.8%

Table 10 continued

1 - Size d = 20 mm

CLA / δm µmm	1.5 - 3.5 µmm				4.25 - 5.15 µmm			
	ST52 HL KN	D52 HL KN	deviation KN	% age dev	ST51 HL KN	D51 HL KN	deviation KN	% age dev
10	5.70	2.778	2.922	-51%	4.106	2.111	1.995	-48.6%
20	12.111	7.560	4.551	-37.6%	9.894	5.596	4.298	-43.4%
30	18.433	12.342	6.091	-33%	15.681	9.081	6.60	-42.1%
40	24.755	17.124	7.631	-31%	21.467	12.566	8.901	-41.5%
45	27.916	19.515	8.401	-30%	24.36	14.308	10.052	-41.3%

Table 10 continued

2 - Size d = 15 mm

CLA / δm µmm	0.23 - 0.31 µmm				0.44 - 0.68 µmm			
	ST42 HL KN	D42 HL KN	deviation KN	% age dev	ST41 HL KN	D41 HL KN	deviation KN	% age dev
10	17.368	8.97	8.398	-48.3%	17.685	8.348	9.337	-52.8%
20	28	16.008	11.992	-43%	26.781	14.34	12.441	-46.4%
30	39.378	23.046	16.332	-41.5%	35.876	20.332	15.544	-43.3%
35	44.881	26.565	18.316	-40.8%	40.423	23.328	17.095	-42.3%
40	50.383	30.084	20.299	-40.3%	44.971	26.324	18.647	-41.5%

Table 10 continued

2 - Size d = 15 mm

CLA / δm µmm	1.37 - 1.61 µmm				2.35 - 2.64 µmm			
	ST32 HL KN	D32 HL KN	deviation KN	% age dev	ST31 HL KN	D31 HL KN	deviation KN	% age dev
10	16.333	7.209	9.124	-55.9%	11.699	5.279	6.42	-55%
20	24.323	12.131	12.192	-50.1%	20.588	9.756	10.832	-52.6%
30	32.313	17.053	15.26	-47.2%	29.477	14.233	15.244	-51.7%
35	36.308	19.514	16.794	-46.2%	33.922	16.472	17.45	-51.4%
40	40.303	21.975	18.328	-45.5%	38.366	18.710	19.656	-51.2%

Table 10 continued

3 - Size d = 10 mm

CLA / δm µmm	0.27 - 0.36 µmm				0.41 - 0.66 µmm			
	ST22 HL KN	D22 HL KN	deviation KN	% age dev	ST21 HL KN	D21 HL KN	deviation KN	% age dev
5	18.712	5.055	13.657	-73%	12.344	5.703	6.641	-54%
10	26.16	10.683	15.477	-59%	21.308	9.886	11.422	-53.6%
15	33.607	16.311	17.296	-51.5%	30.273	14.068	16.205	-53.5%
20	41.055	21.938	19.117	-46.5%	39.237	18.251	20.986	-53.5%
25	48.502	27.565	20.937	-43.7%	48.202	22.433	25.769	-53.4%

Table 10 continued

3 - Size d = 10 mm

CLA / δm µmm	1.05 - 1.85 µmm				2.32 - 3.07 µmm			
	ST12 HL KN	D12 HL KN	deviation KN	% age dev	ST11 HL KN	D11 HL KN	deviation KN	% age dev
5	10.863	4.521	6.342	-58.4%	6.093	2.205	3.888	-63.8%
10	19.153	8.081	11.072	-57.8%	13.737	5.421	8.316	-60.5%
15	27.443	11.64	15.803	-57.6%	21.381	8.637	12.744	-59.6%
20	35.733	15.199	20.534	-57.5%	29.025	11.853	17.172	-59.2%
25	44.023	18.76	25.263	-57.4%	36.669	15.069	21.60	-58.9%

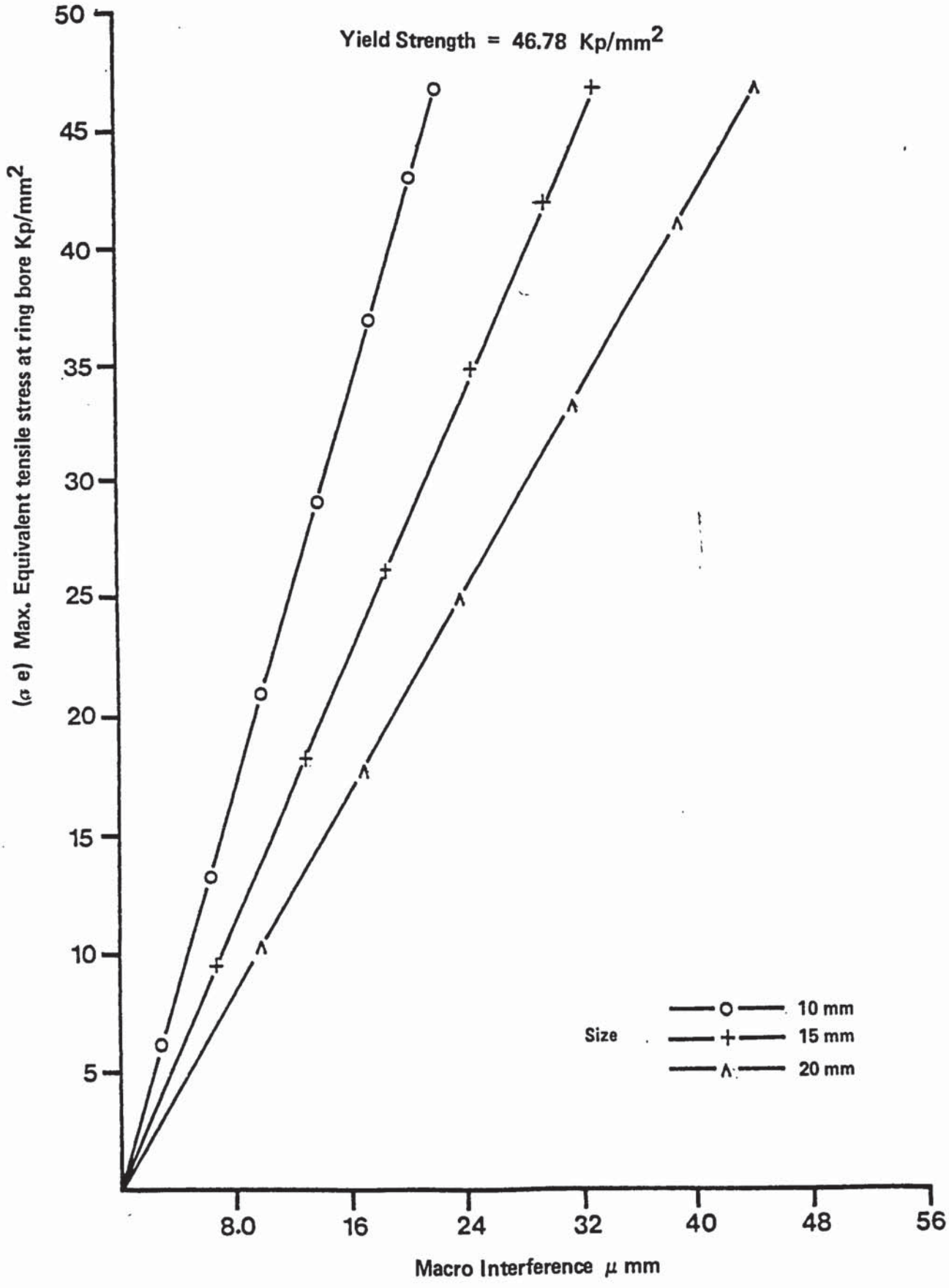

Fig 1 (σ e - δ ma) For the Shaft and Ring by Baugher

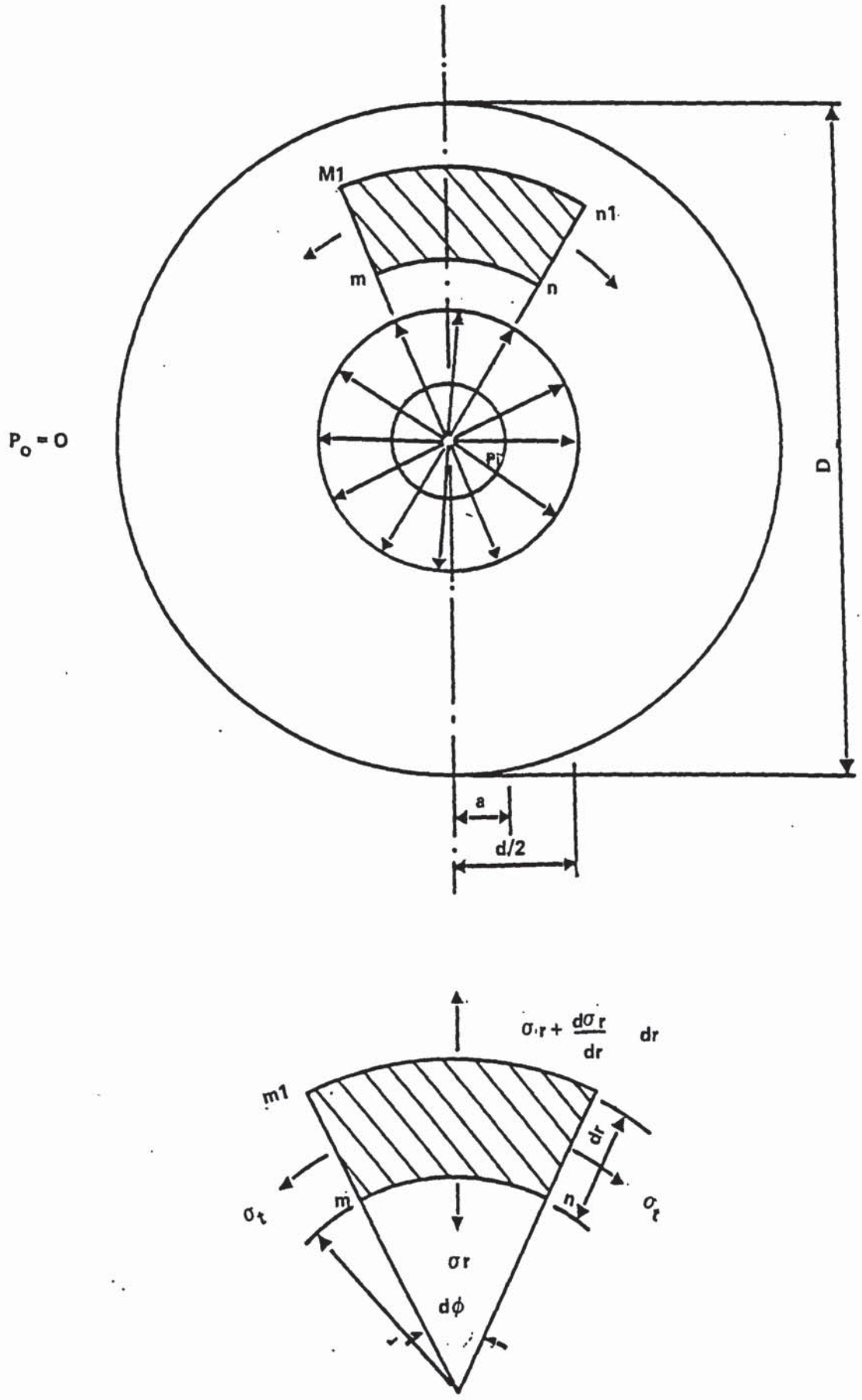

Fig 2 Stresses induced due to the fit

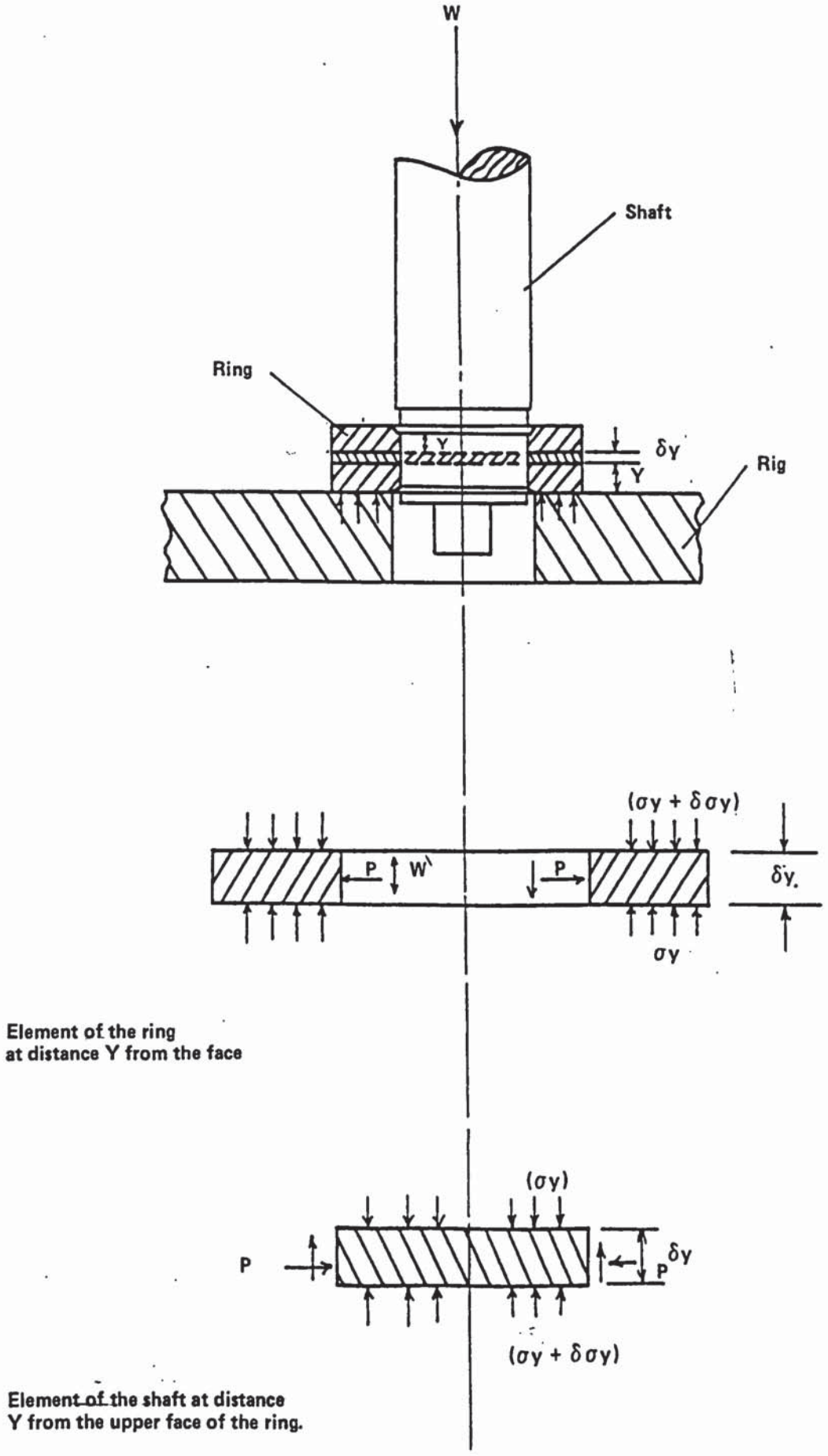

Fig 3 Stress distribution in the shaft and the ring due to the axial loading

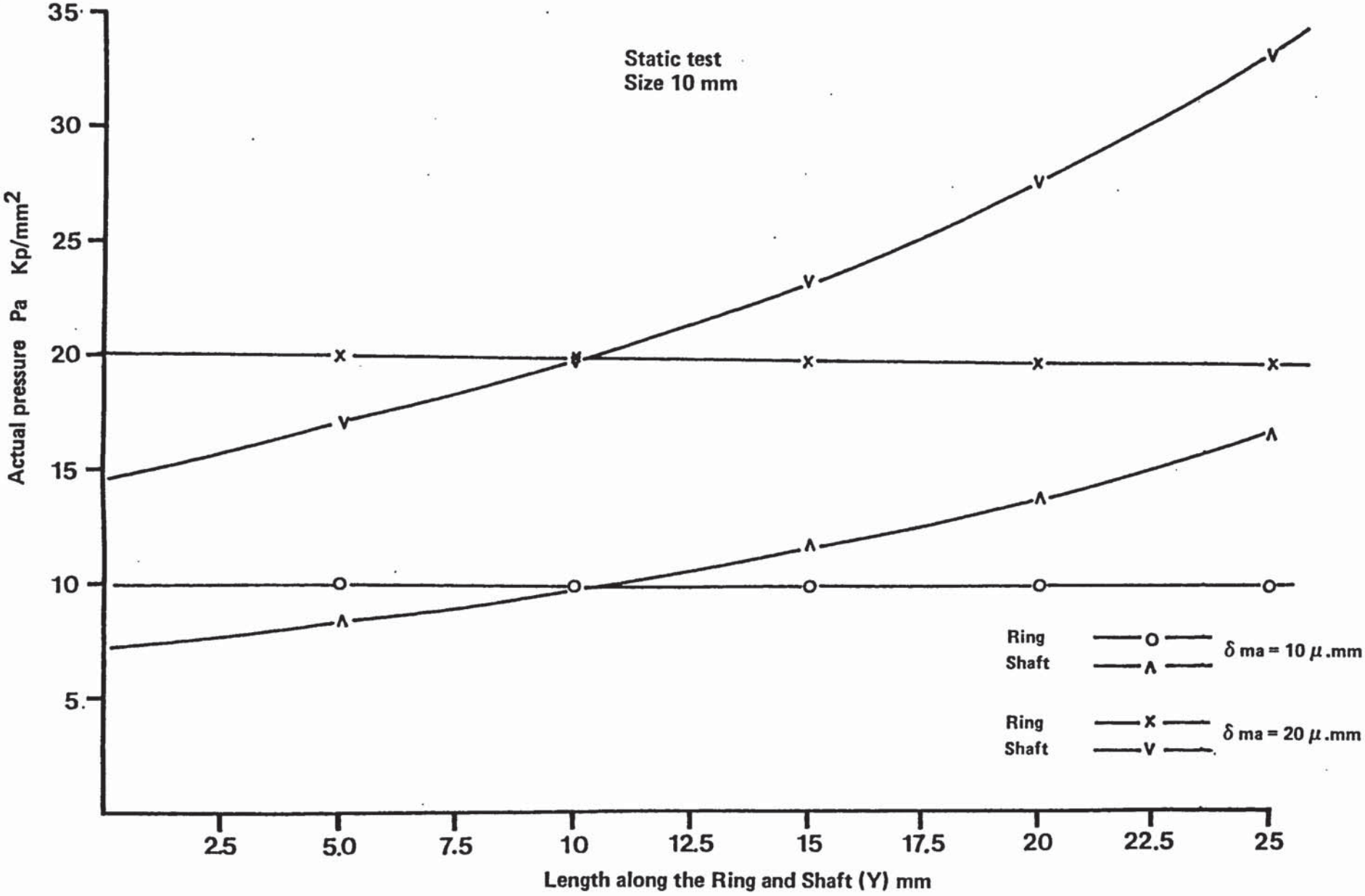

Fig 4 Pressure Distribution along the Ring and Shaft

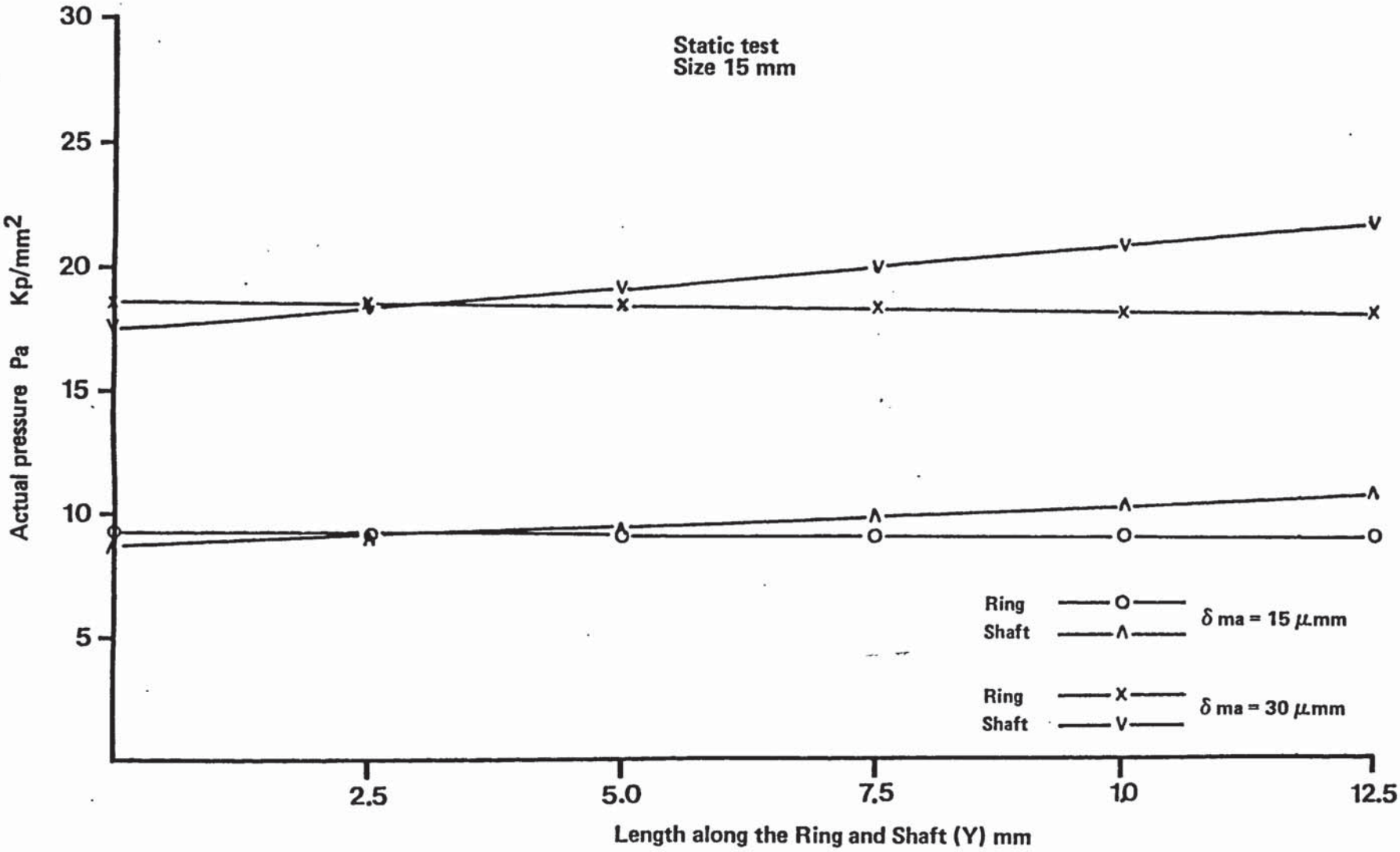

Fig 5 Pressure distribution along the Ring and Shaft

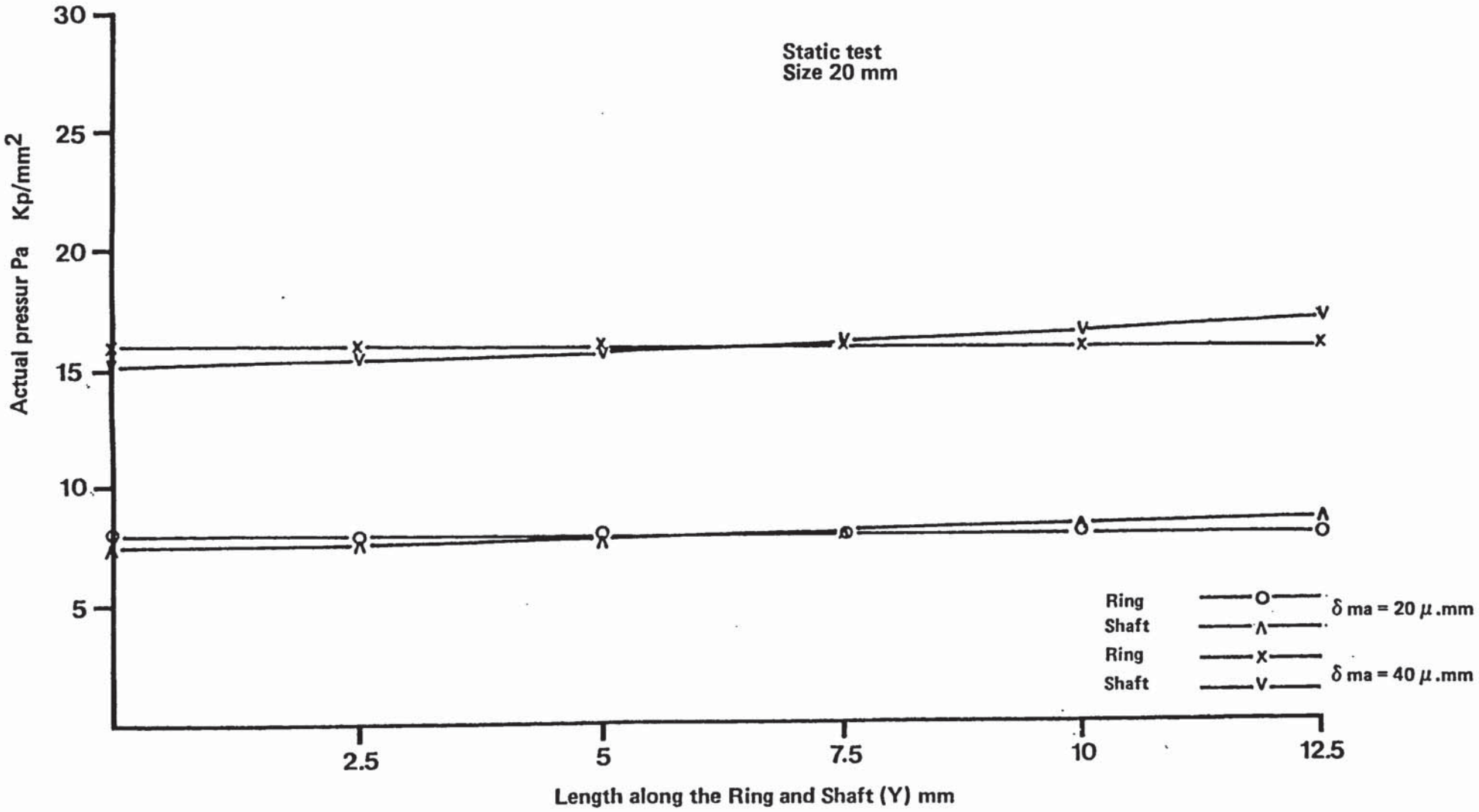

Fig 6 Pressure distribution along the Ring and Shaft

(a) (b)

Fig 7 Green's model showing the deformation of plasticine asperity

(a) initially,
(b) during deformation

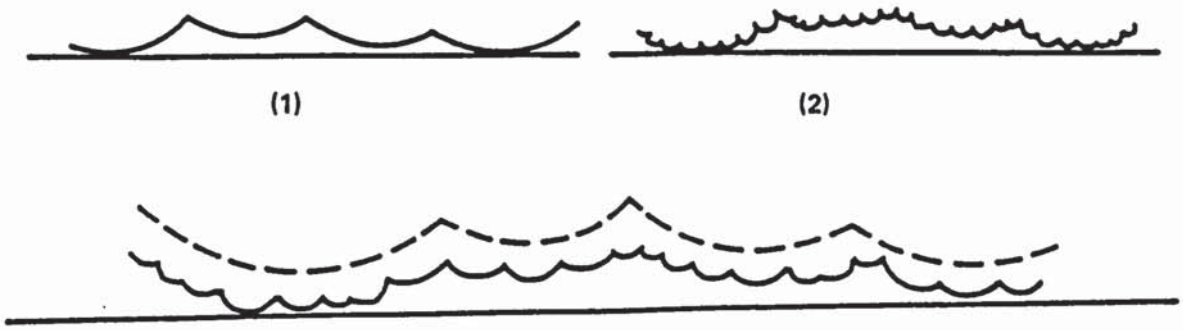

(1) (2)

(3)

1. Long wavelength only
2. Long plus short wavelengths
3. Long plus medium plus short wavelengths

Fig 8 Archard's representation of surface roughness

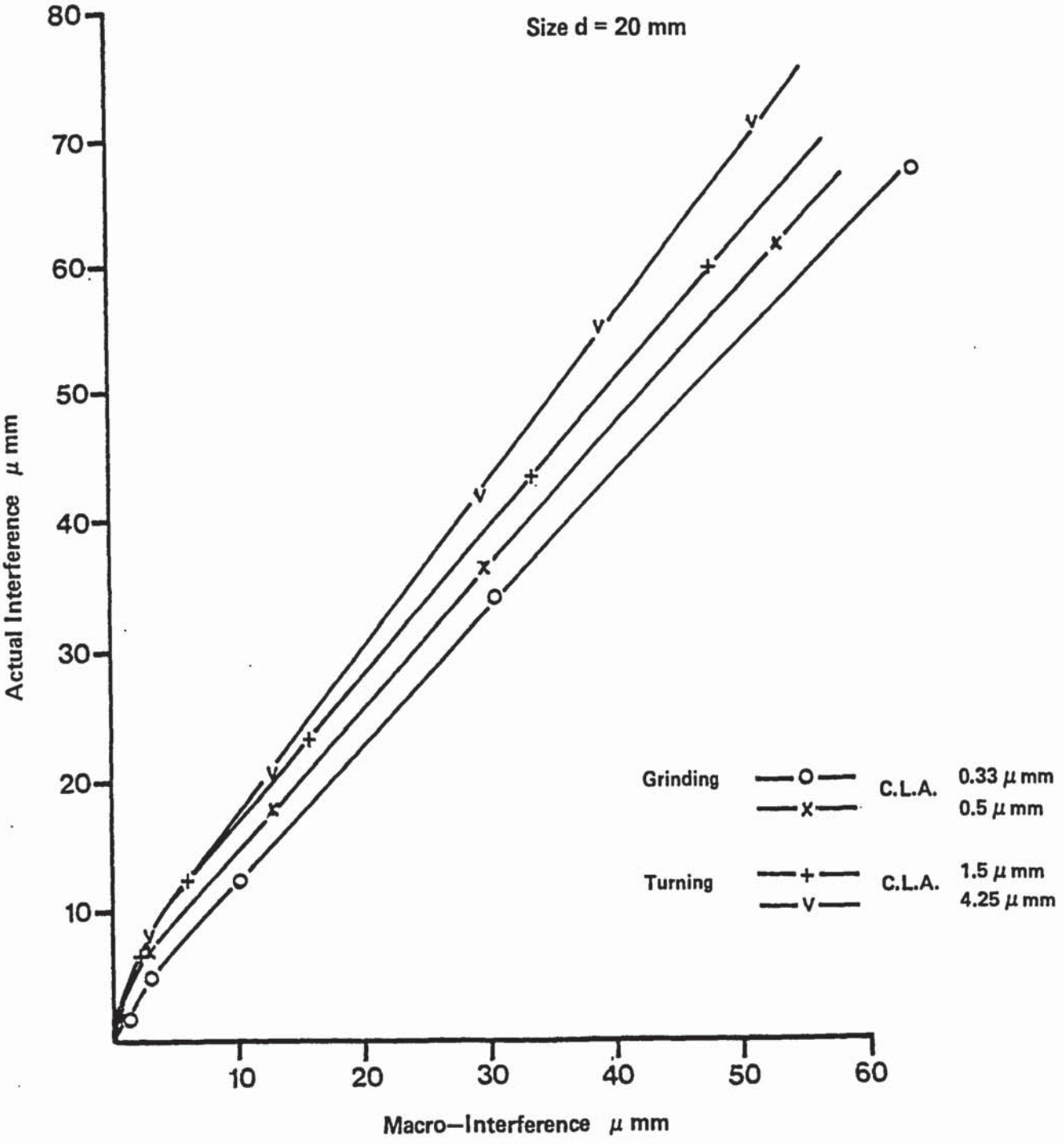

Fig 9 Relationship between Macro and actual Interference using the measured B.A.C.

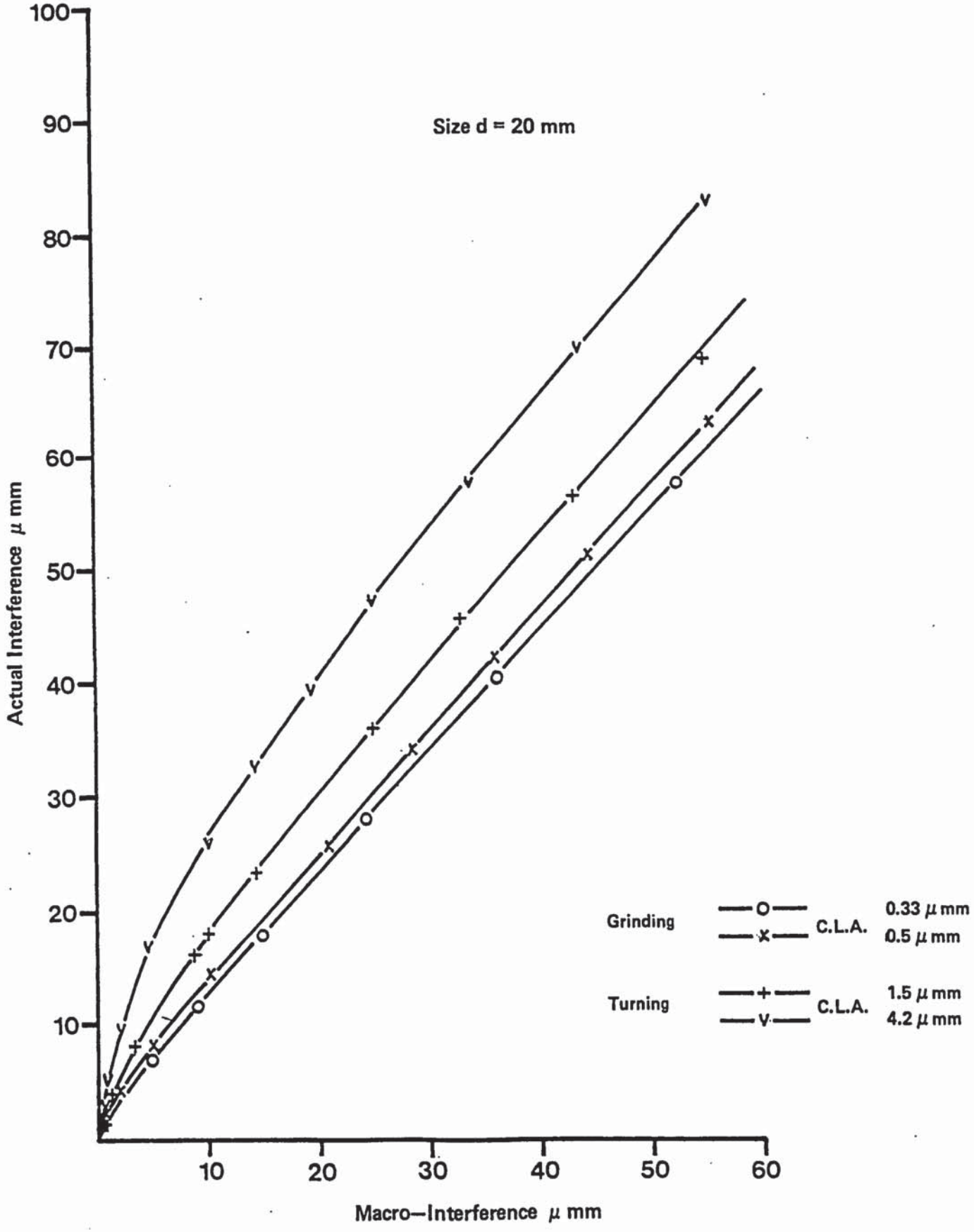

Fig 10 Relationship between Macro and actual Interference using the N.D.C.

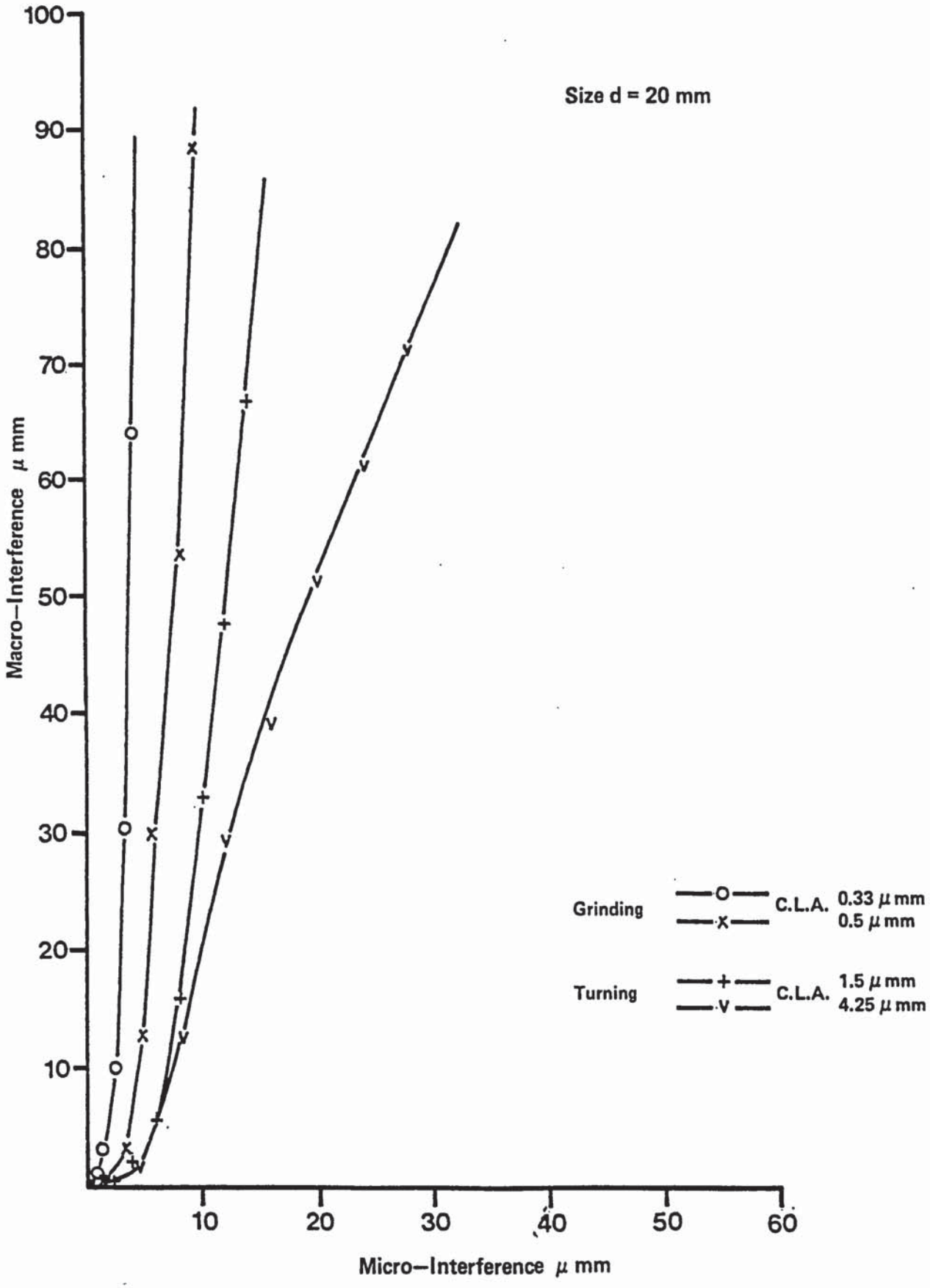

Fig 11 Relationship between Micro and Macro Interference using the measured B.A.C.

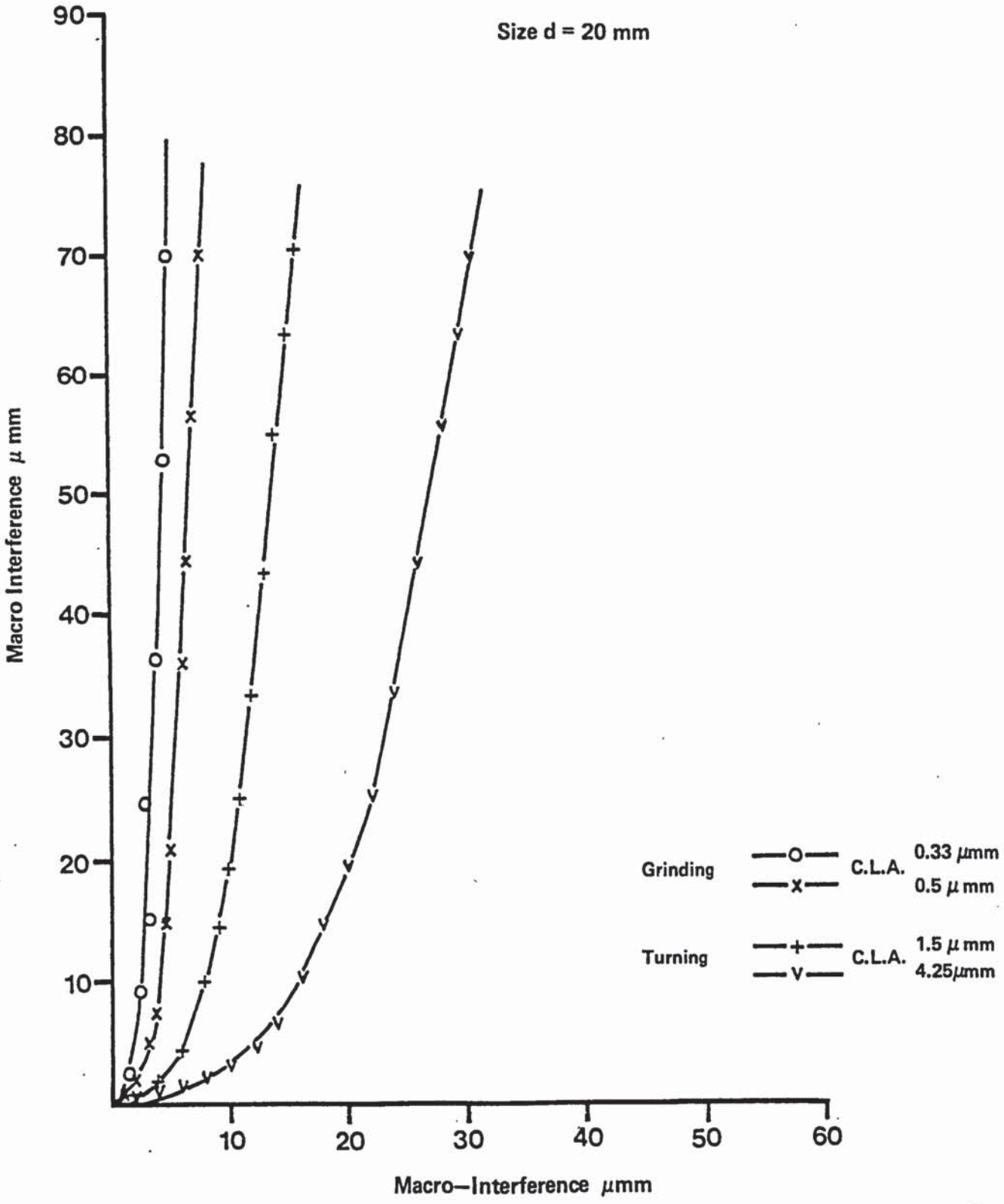

Fig 12 Relationship between Micro and Macro Interference using the N.D.C.

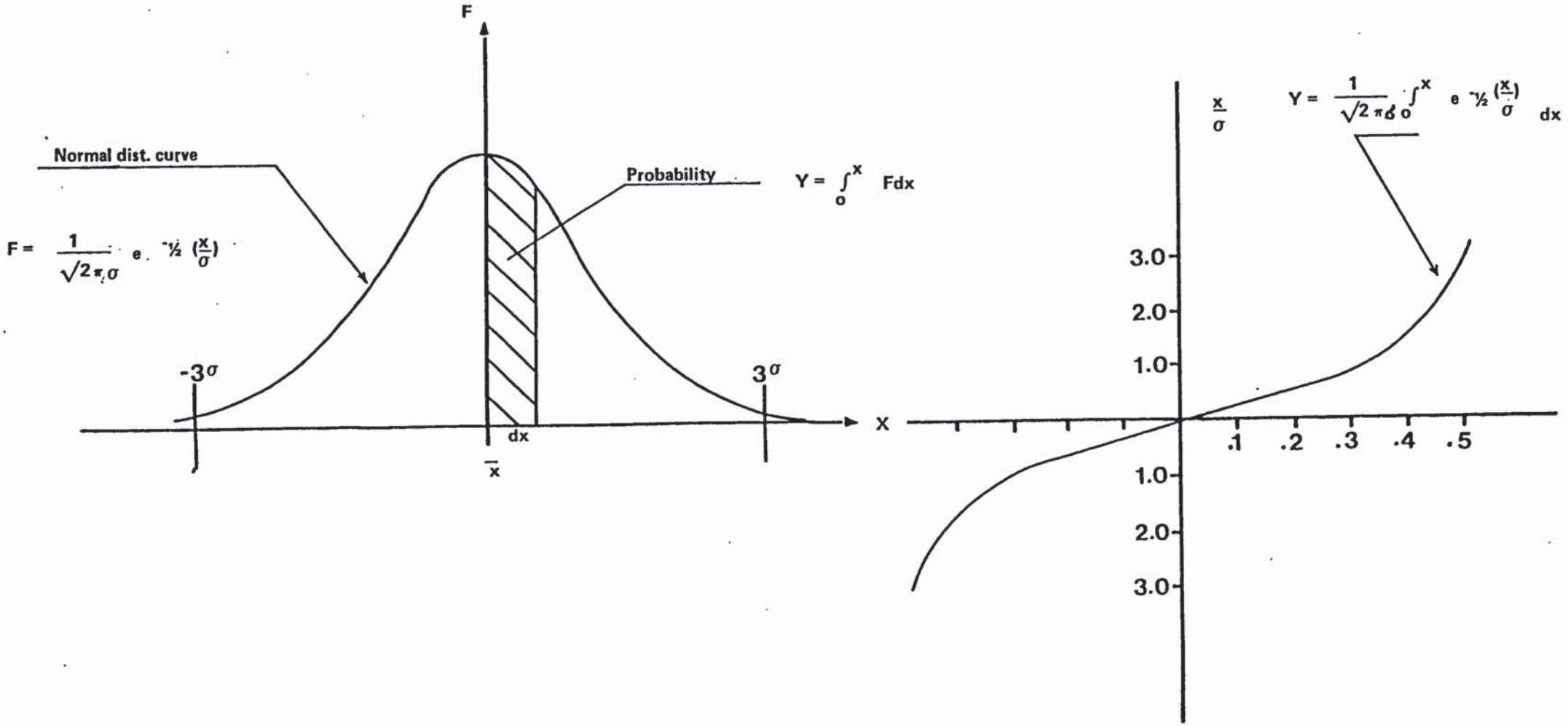

Fig 13 Normal distribution curve

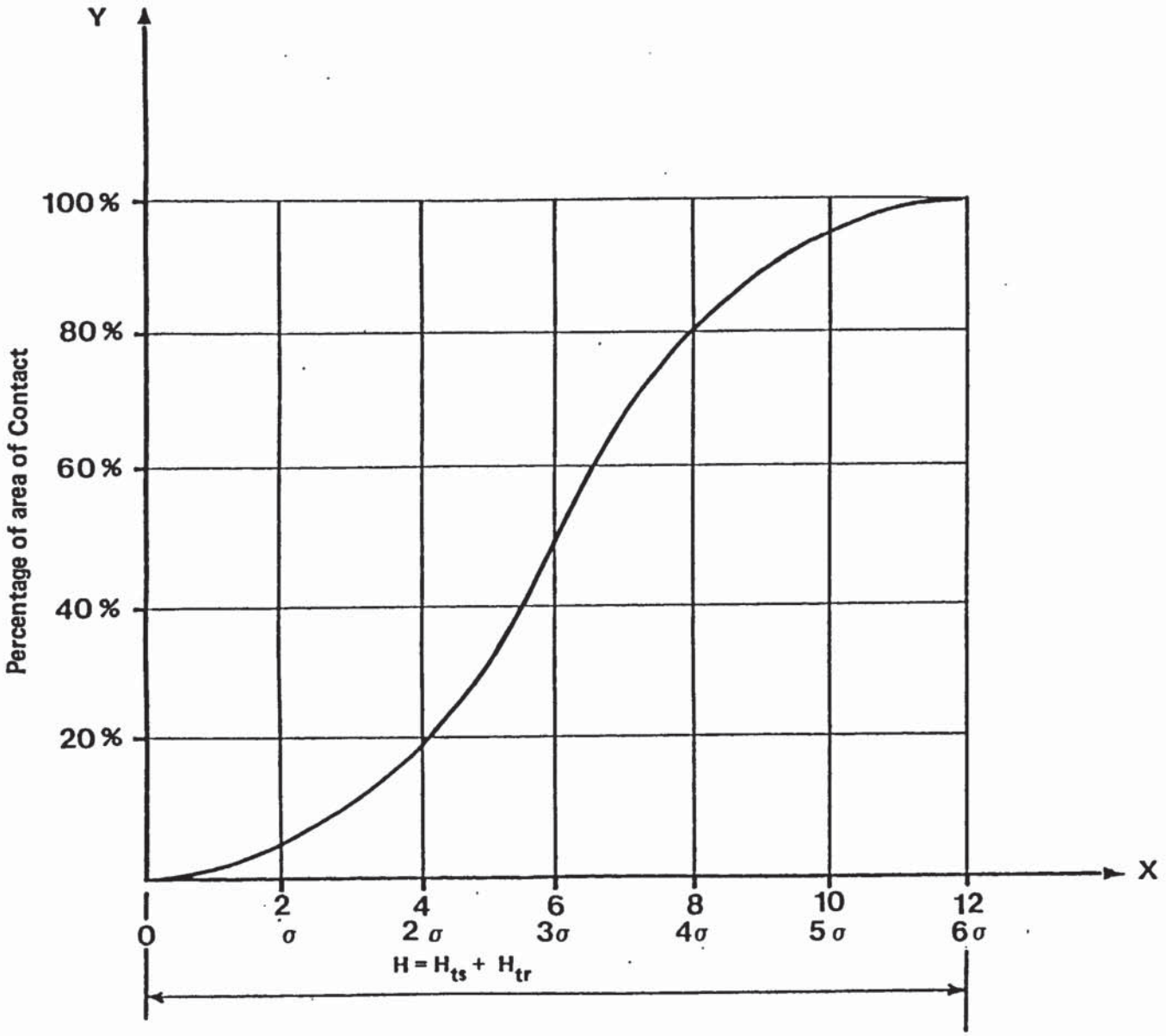

Fig 14 Theroretical relation between B.A.% and H_t

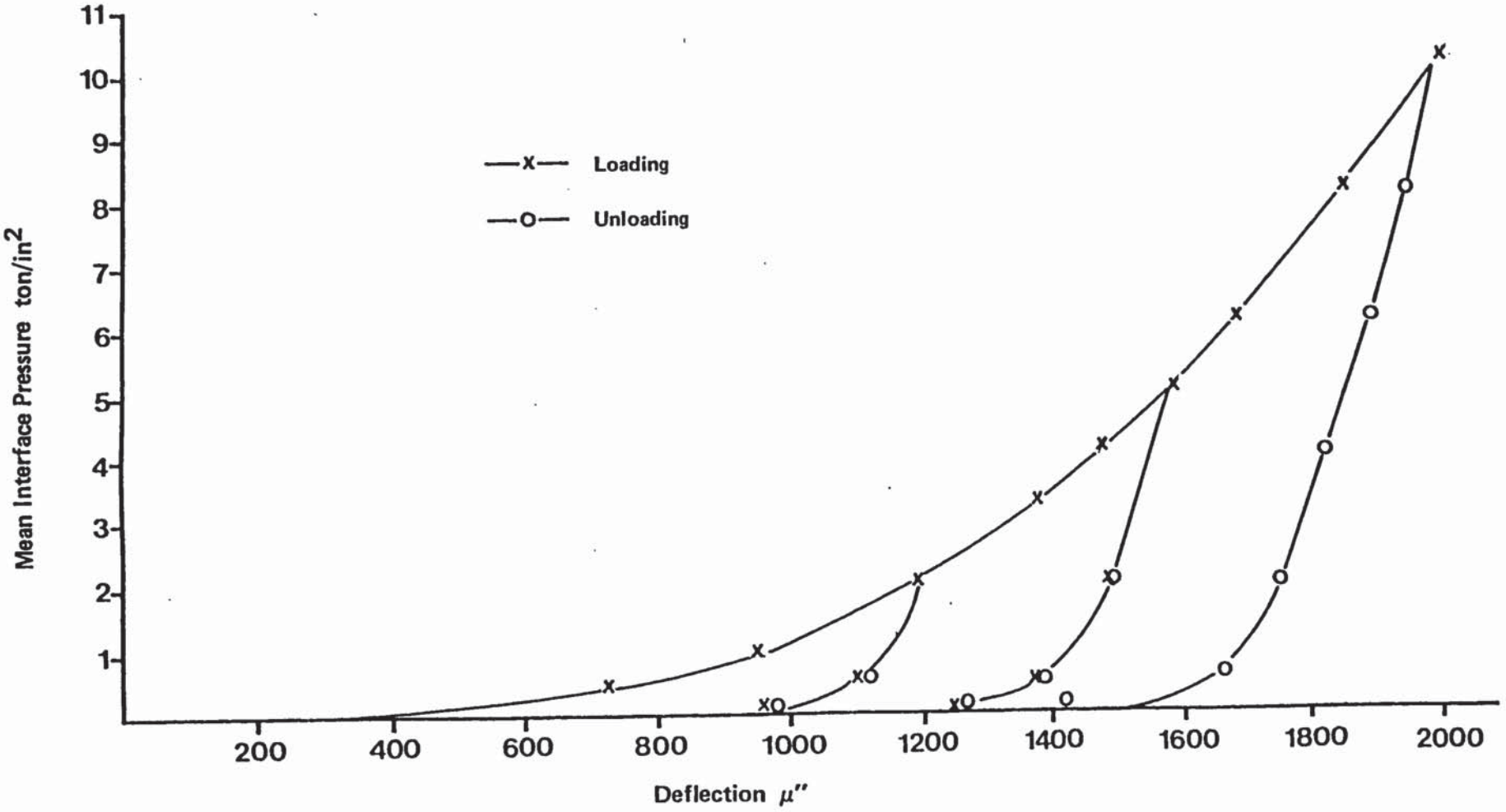

Fig 15 General Static Characteristics of Joints (after Connolly and Thornley)

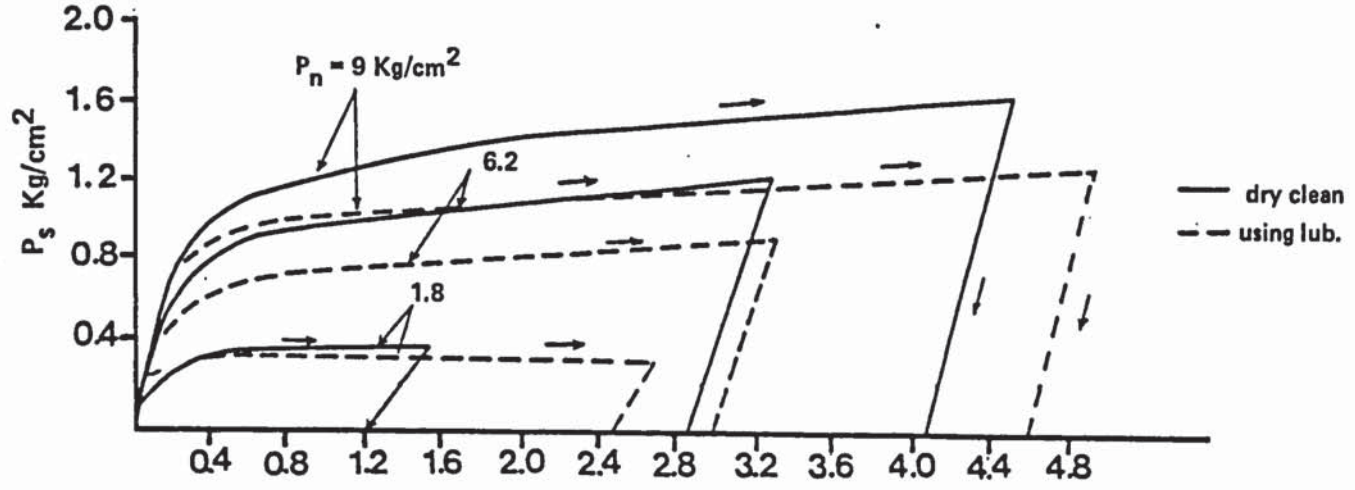

Fig 16 Shear deformations of cast iron surfaces

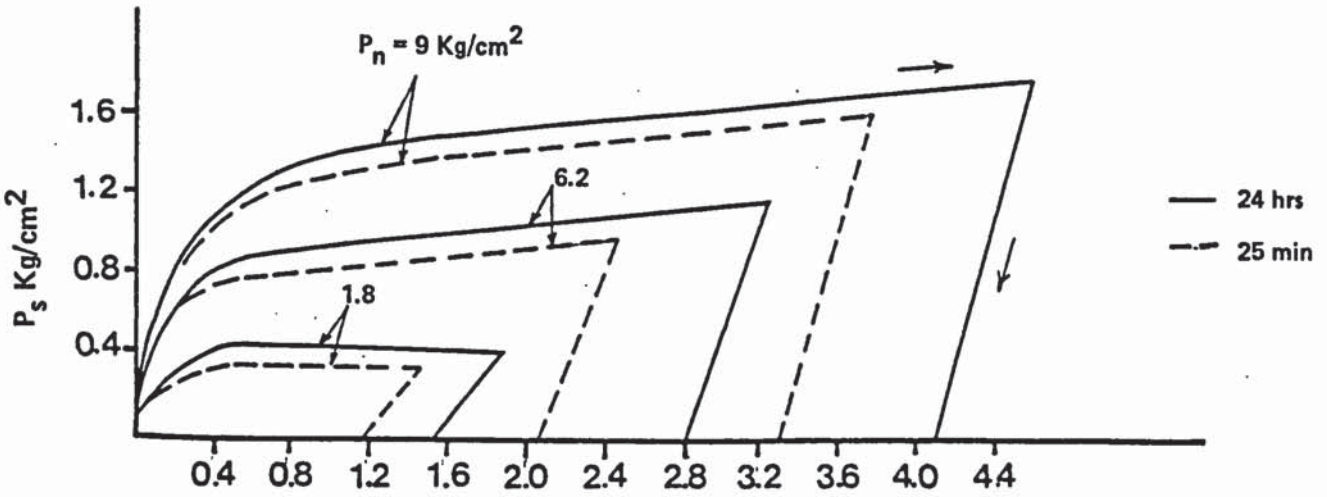

Fig 17 Shear deformations of cast iron surfaces

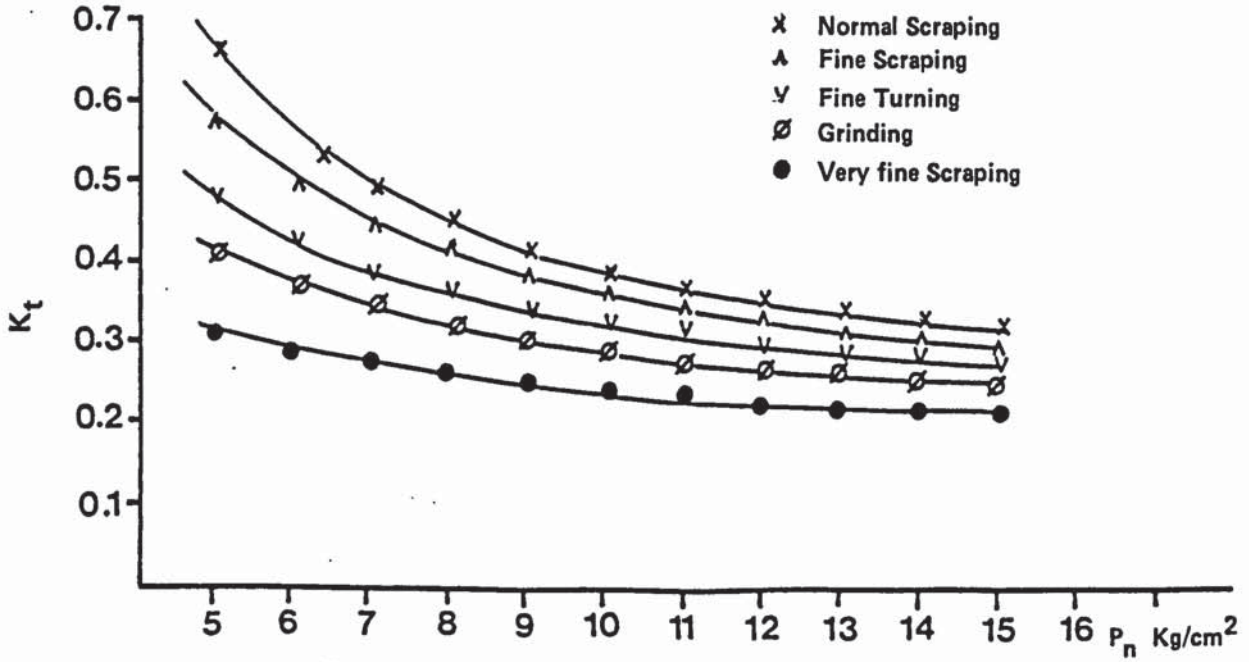

Fig 18 Kirsanova's experimental values of the shear compliance of cast iron

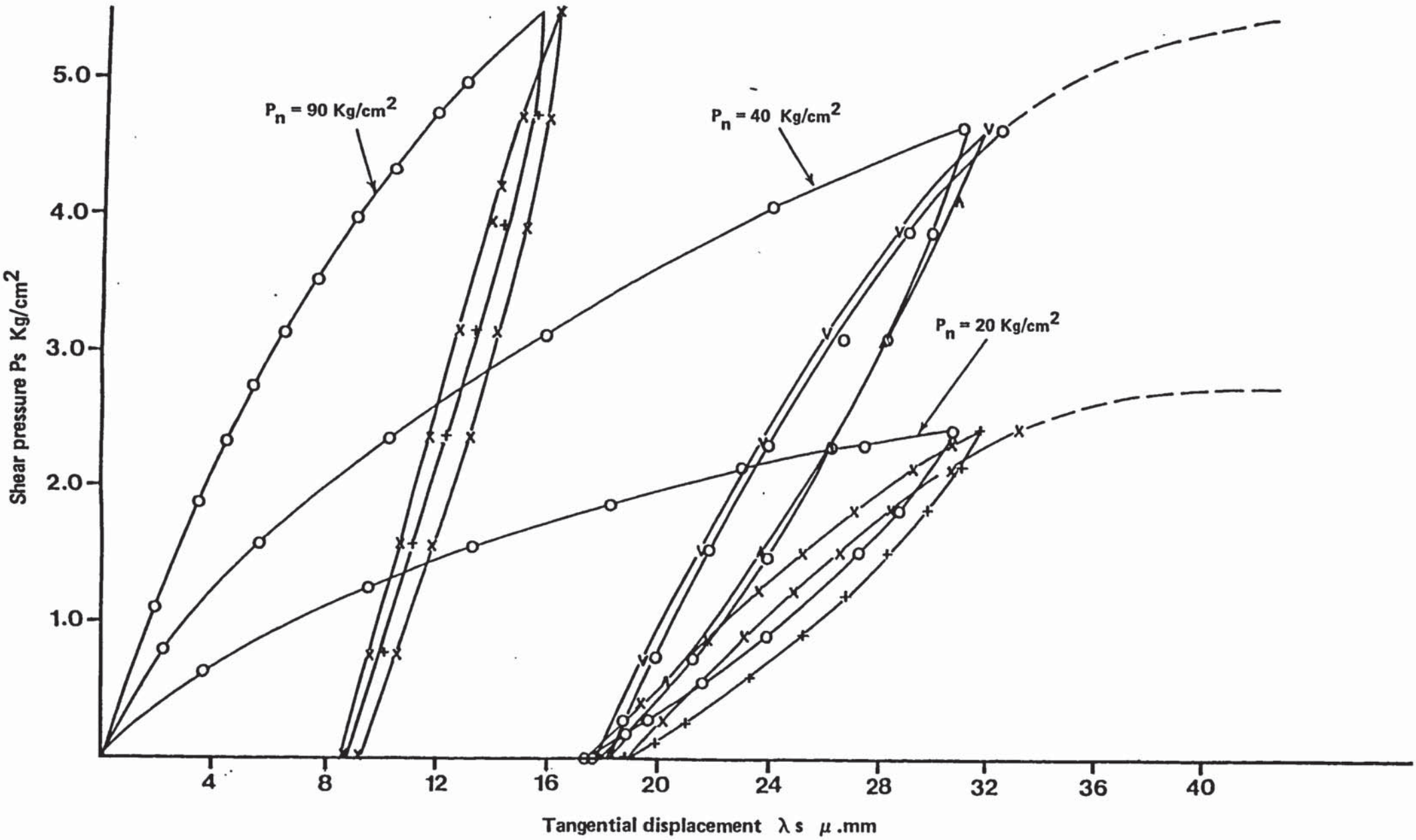

Fig 19 Back's Experimental values of the Shear Compliance of Cast Iron

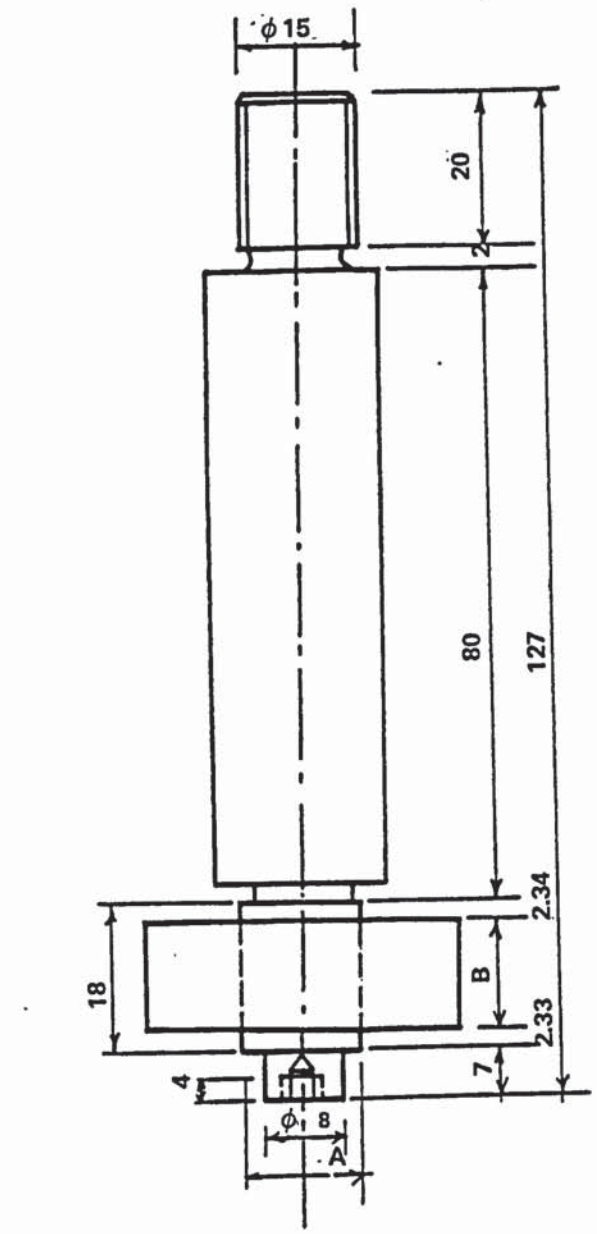

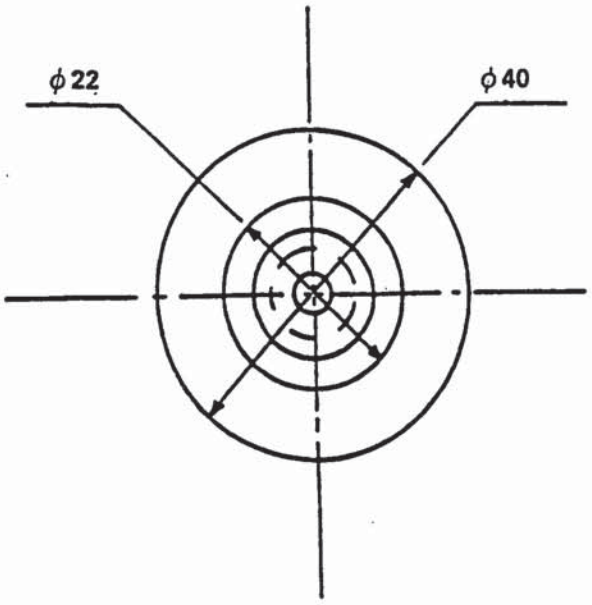

Fig	A ϕ mm	B mm
20 a	10	20
20 b	15	13.33
20 c	20	10

Material: Steel ENIA
Dims. in mm
Scale 1:1

Fig 20 Test specimen dimensions

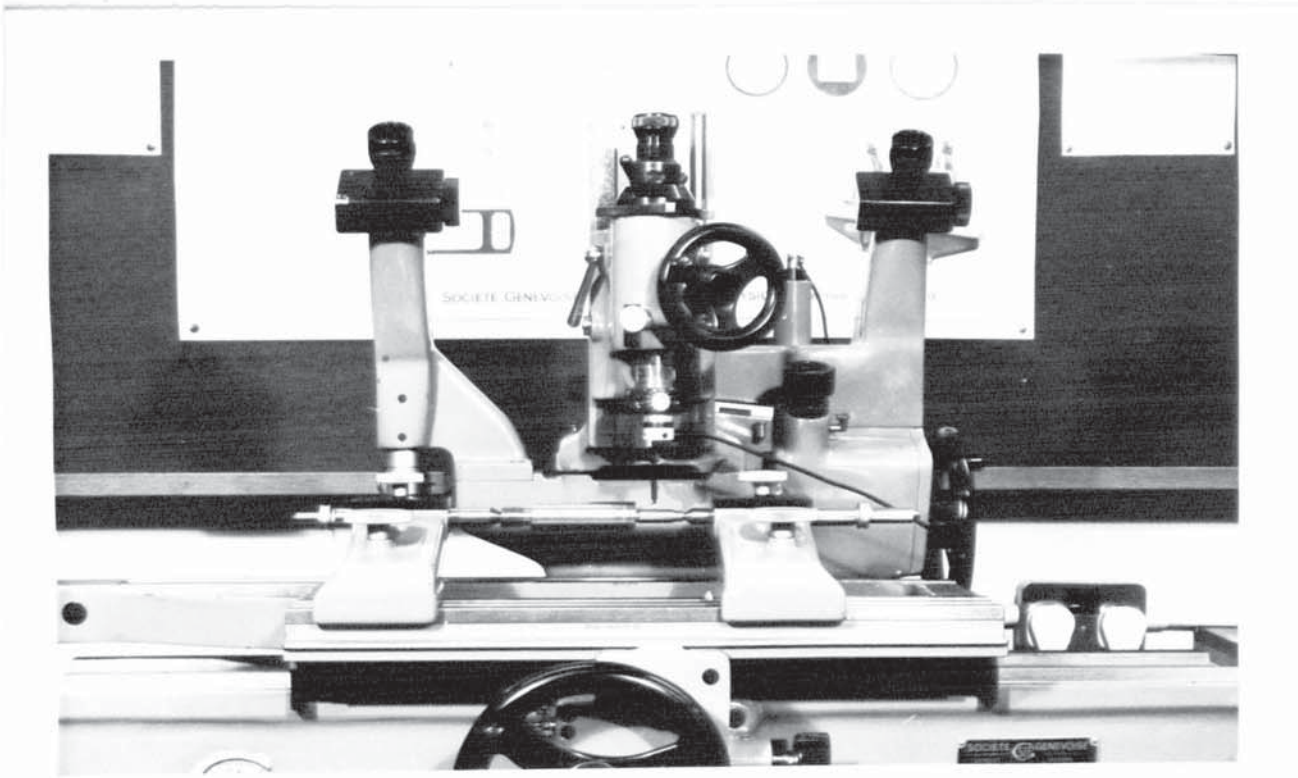

Fig 21 Dimensional measurements (U.M.M.)

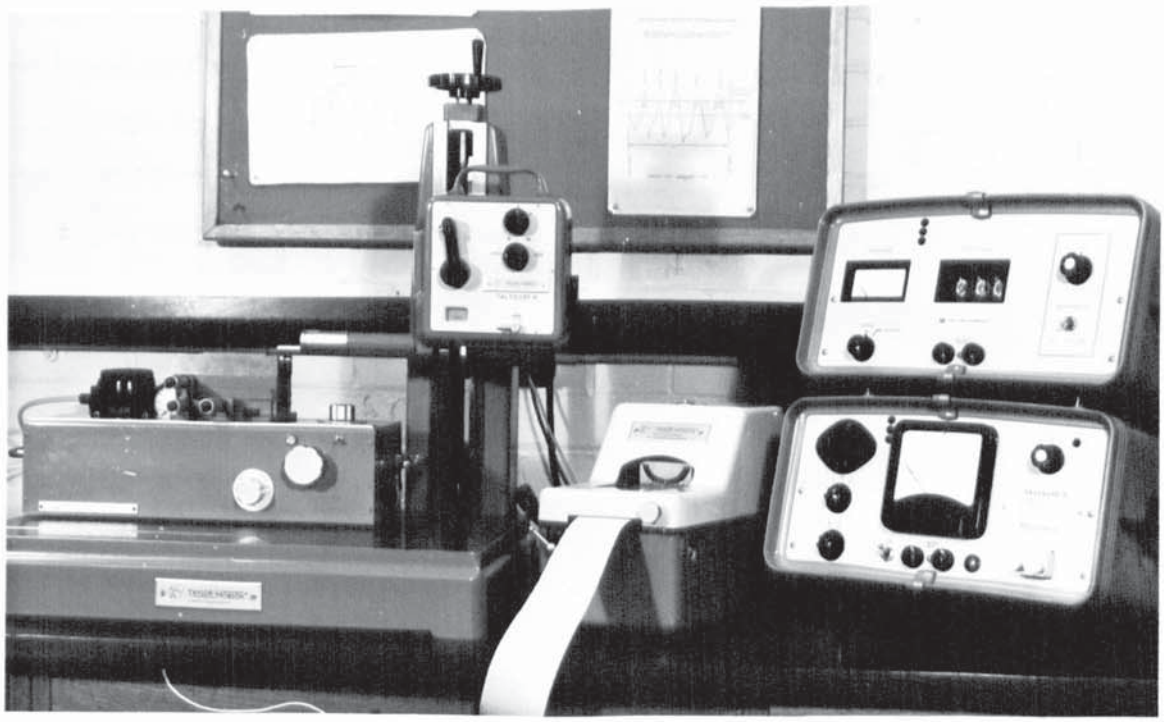

Fig 22 Surface roughness measurement (Talysurf)

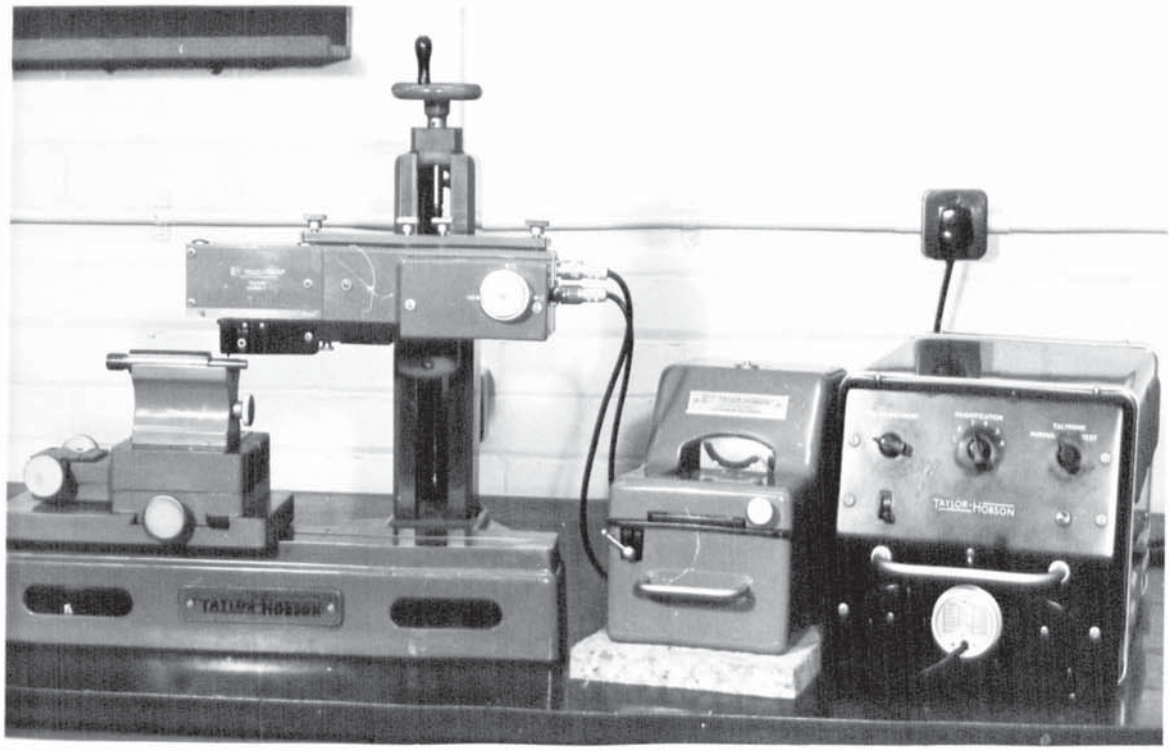

Fig 23 Straightness measurement (Talylin)

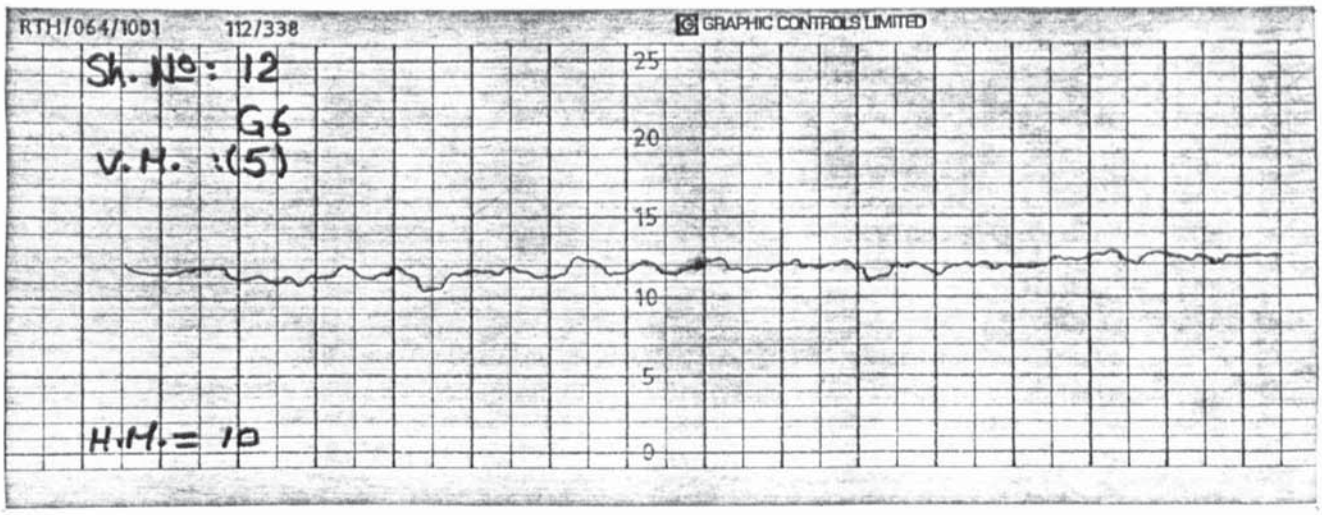

One div. = 0.5 μmm
Shaft straightness

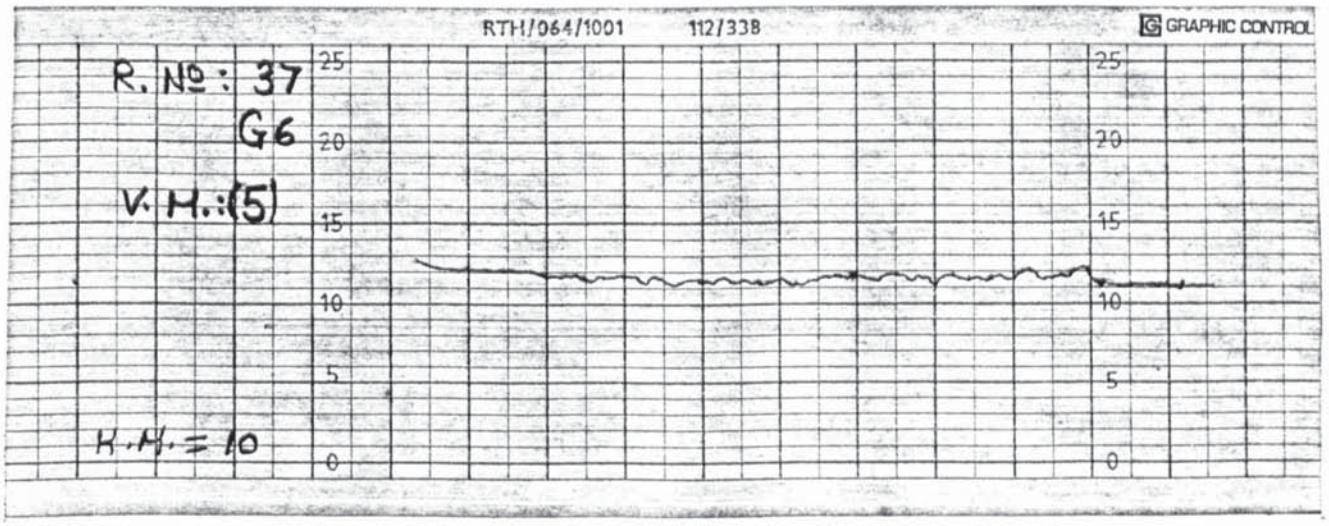

One div. = -.5 μmm
Ring straightness

Fig 24 Talylin trace for a shaft and ring (Grinding)

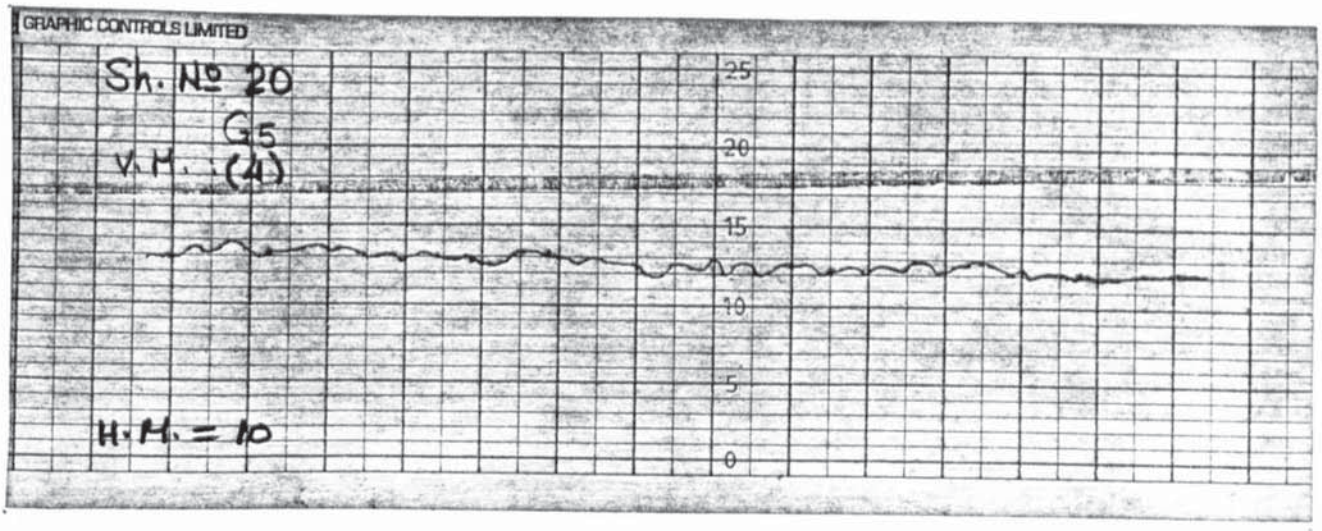

One div. = 1 μmm

Shaft straightness

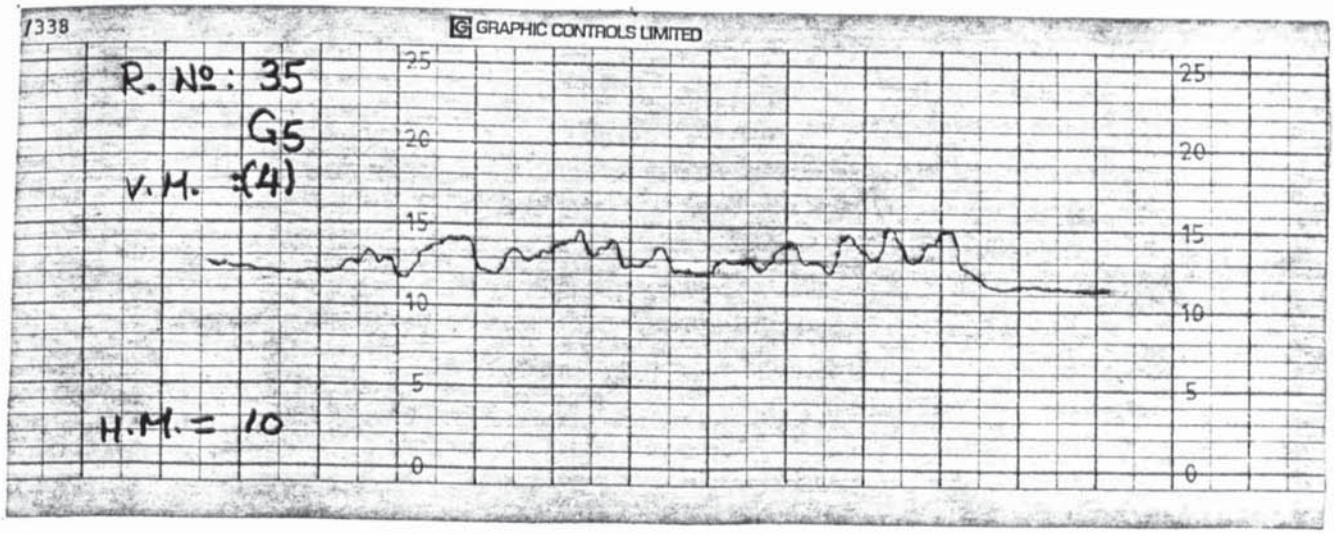

One div. = 1 μmm
Ring straightness

Fig 25 Talylin trace for a shaft and ring (Turning)

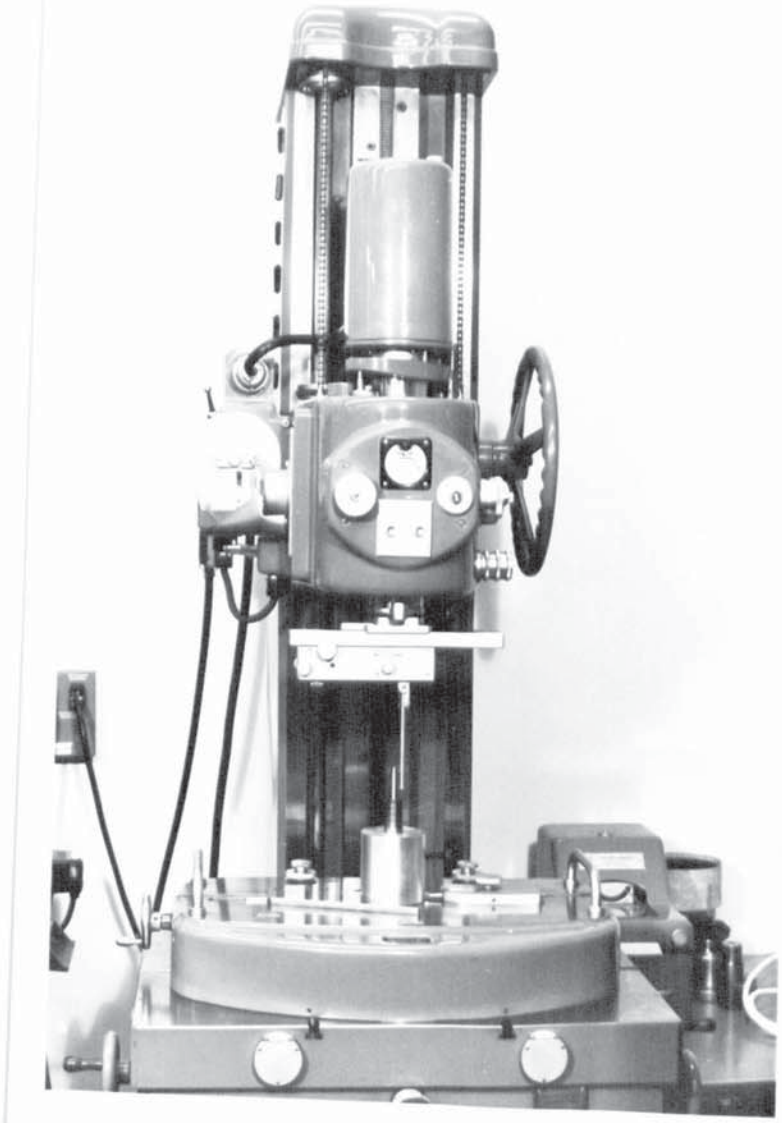

Fig 26 Roundness Measurement (Talyrond)

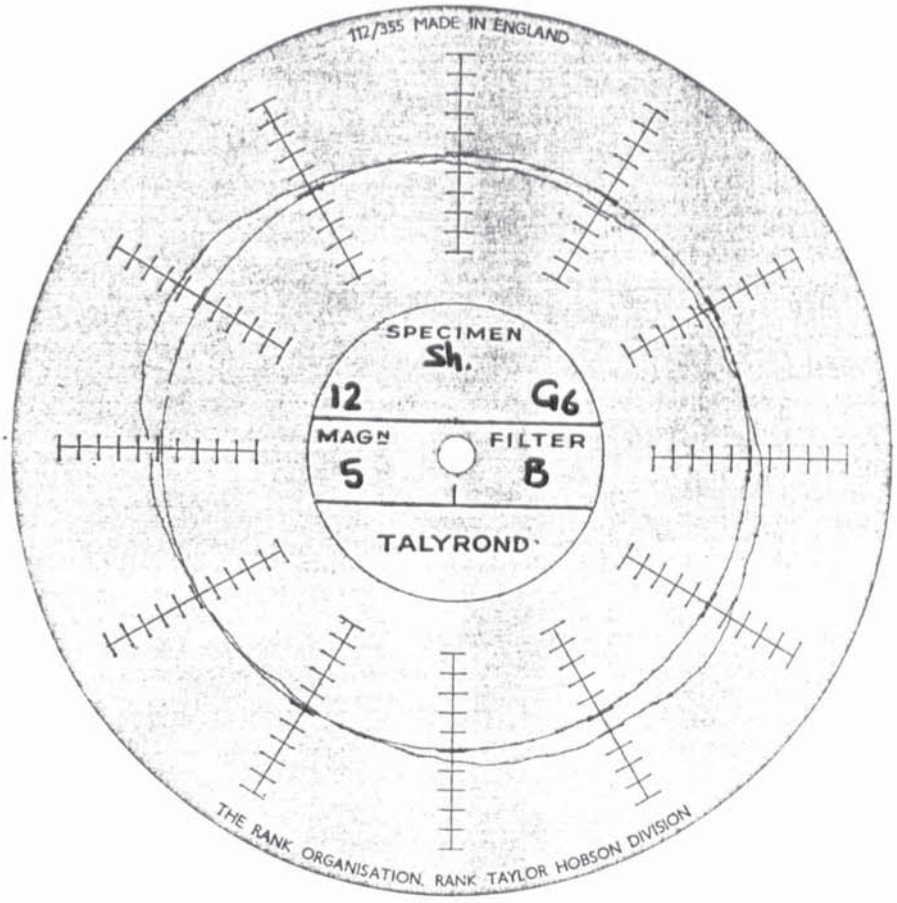

1 div. = .000025"

Shaft roundness

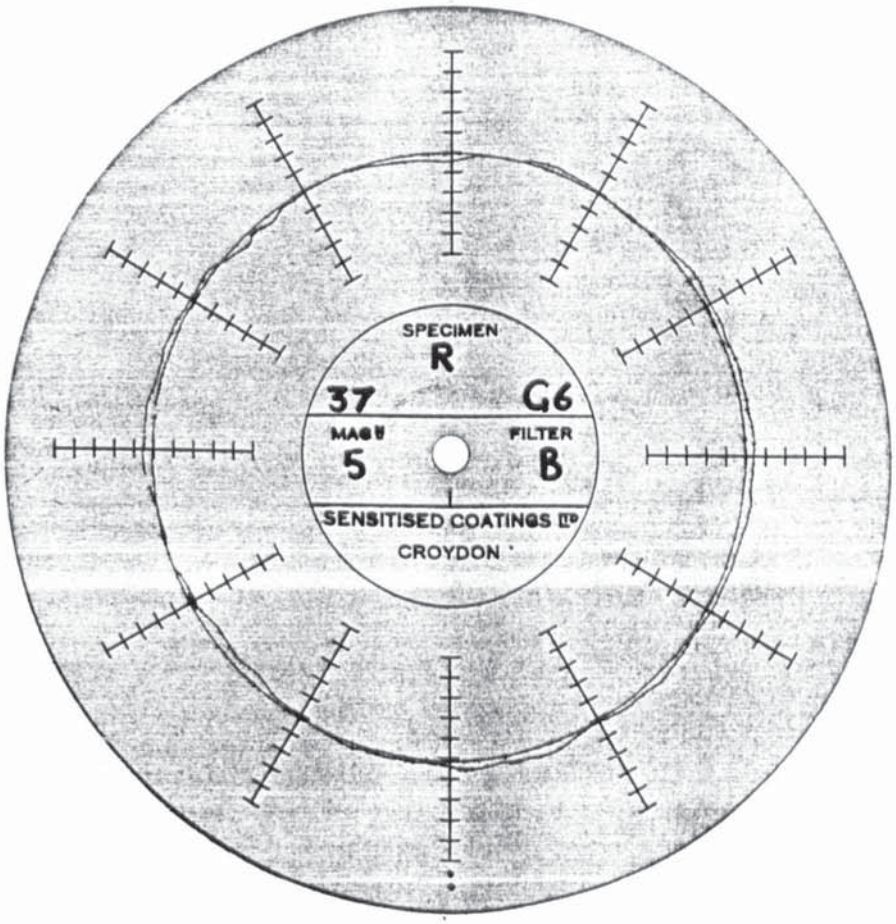

1 div. = .000025"

Ring roudness

Fig 27 Talyrond trace for a shaft and ring (Grinding)

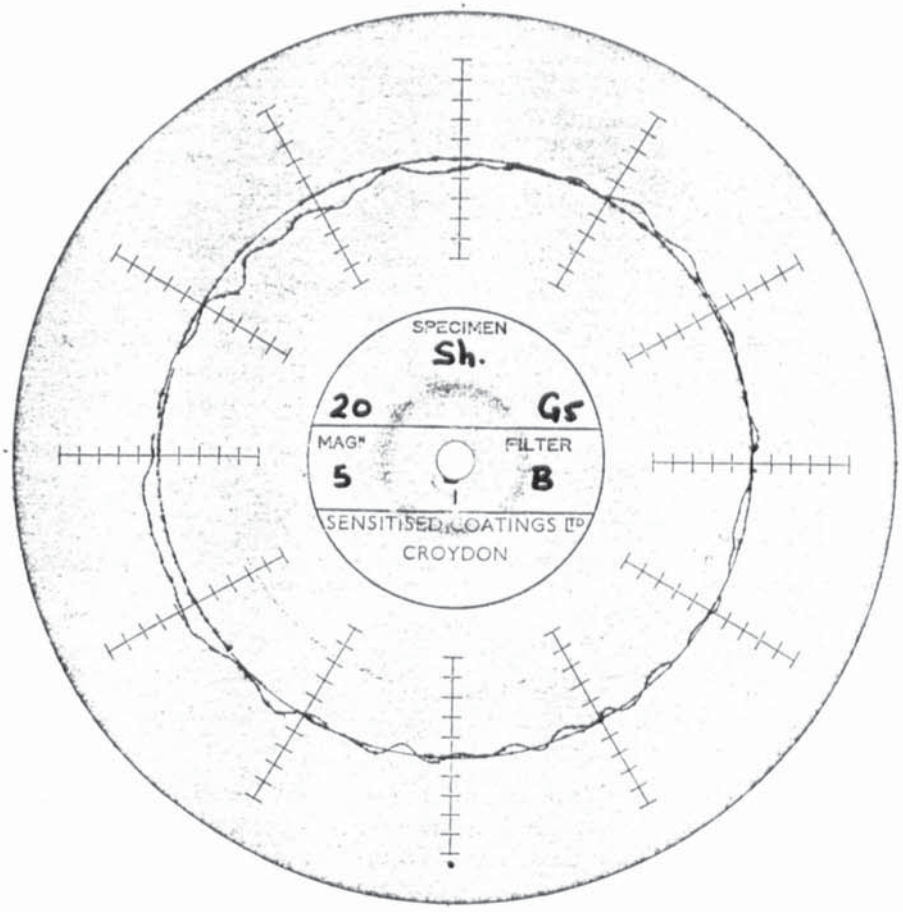

1 div. = .000025"

Shaft roundness

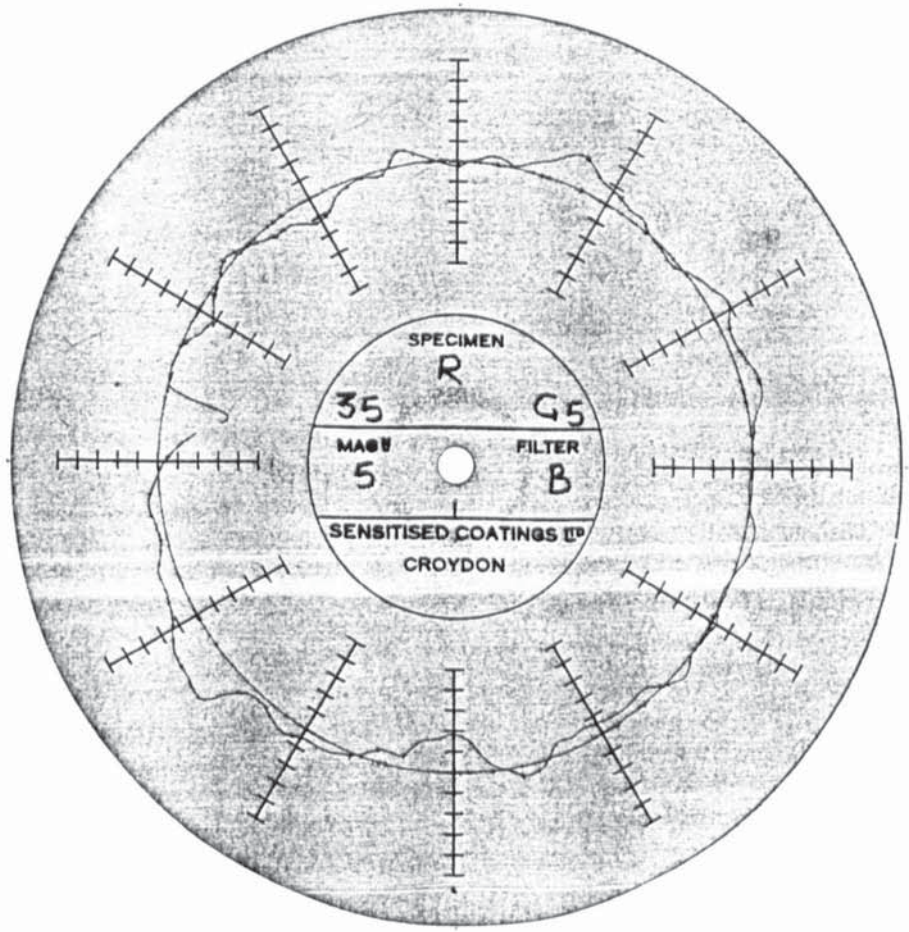

1 div. = .000025"

Ring roundess

Fig 28 Talyrond trace for a shaft and ring (Turning)

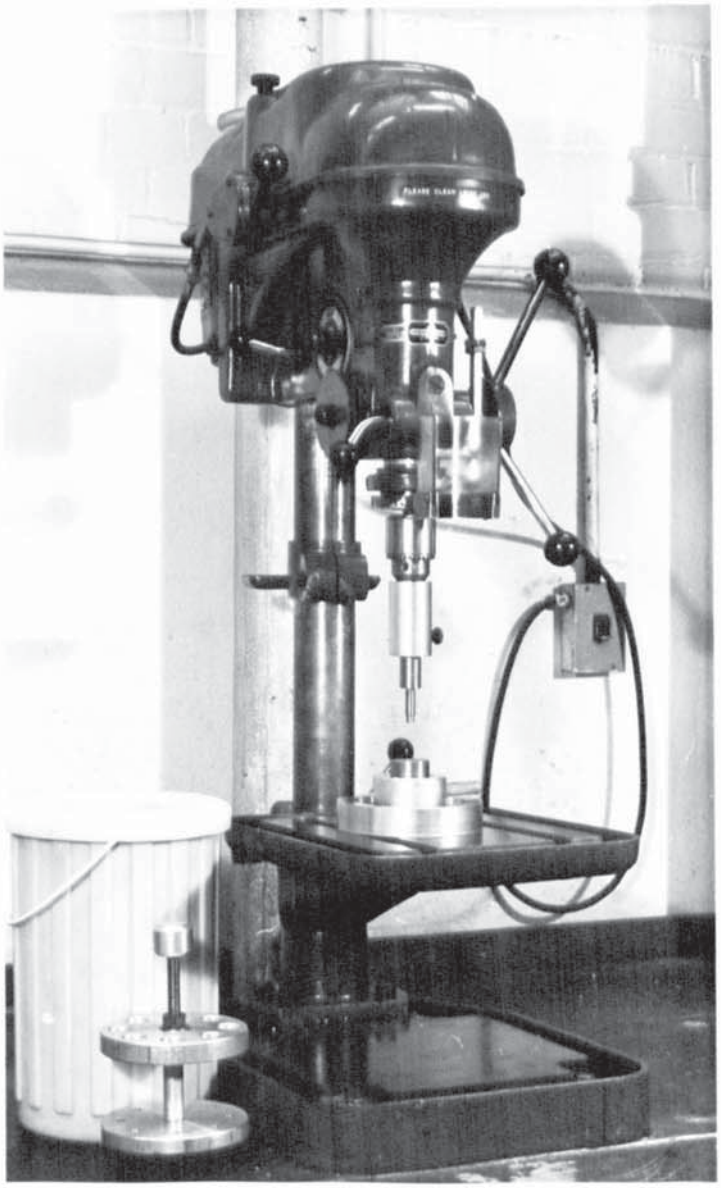

Fig 29 Fitting arrangement

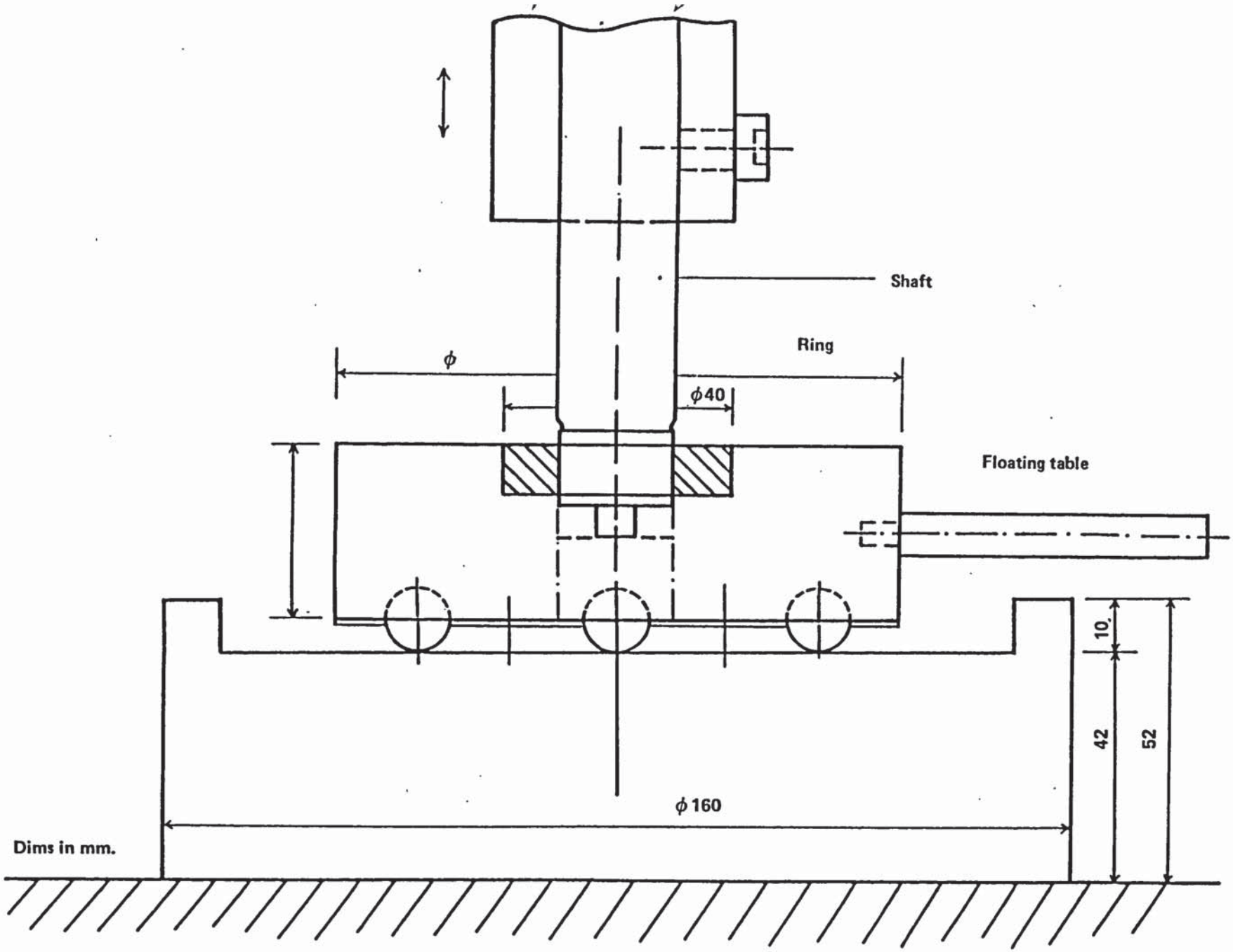

Fig 30 Shrink Fitting arrangement

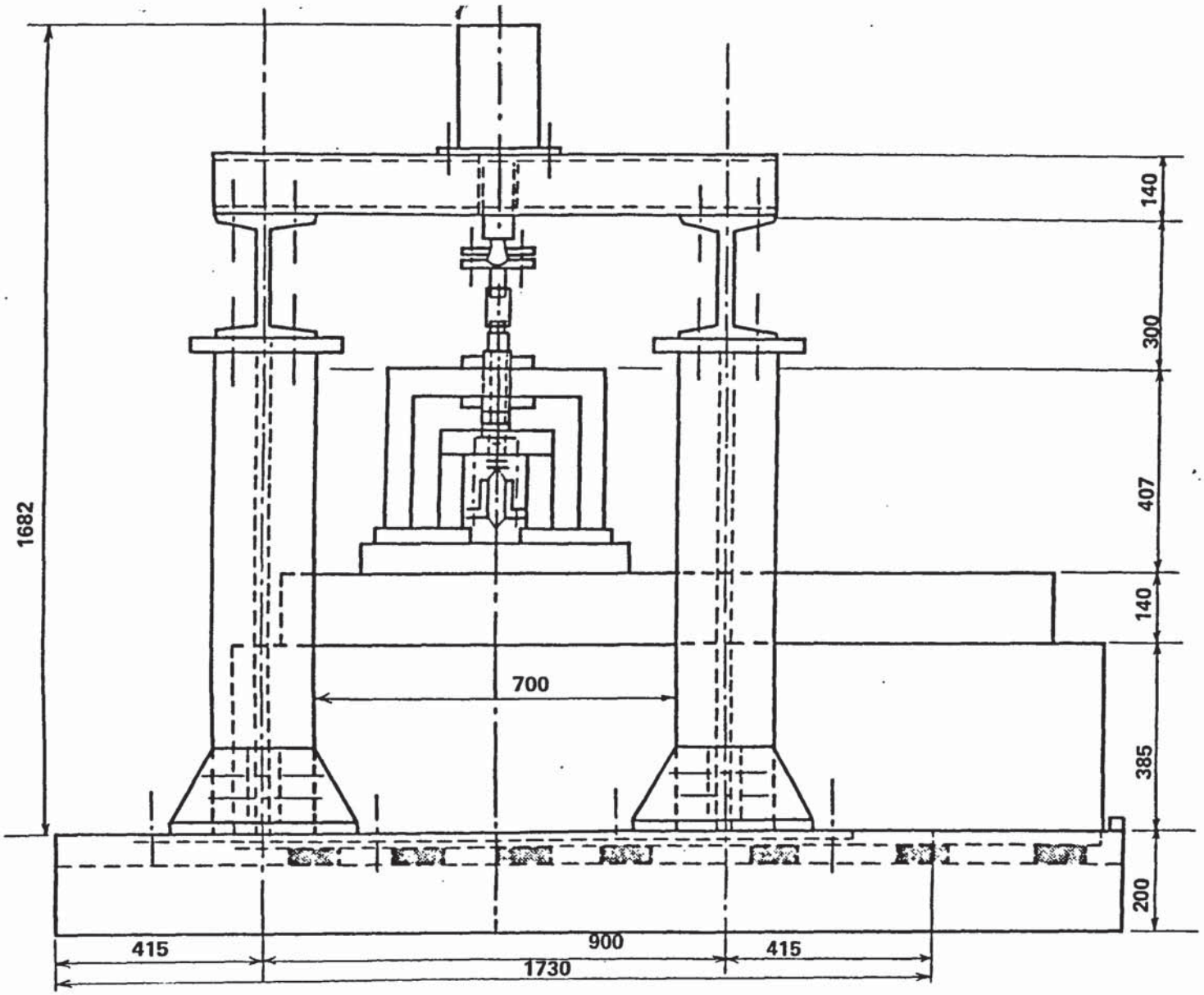

Dims. in mm.

Fig 31 Schematic diagram of the test rig

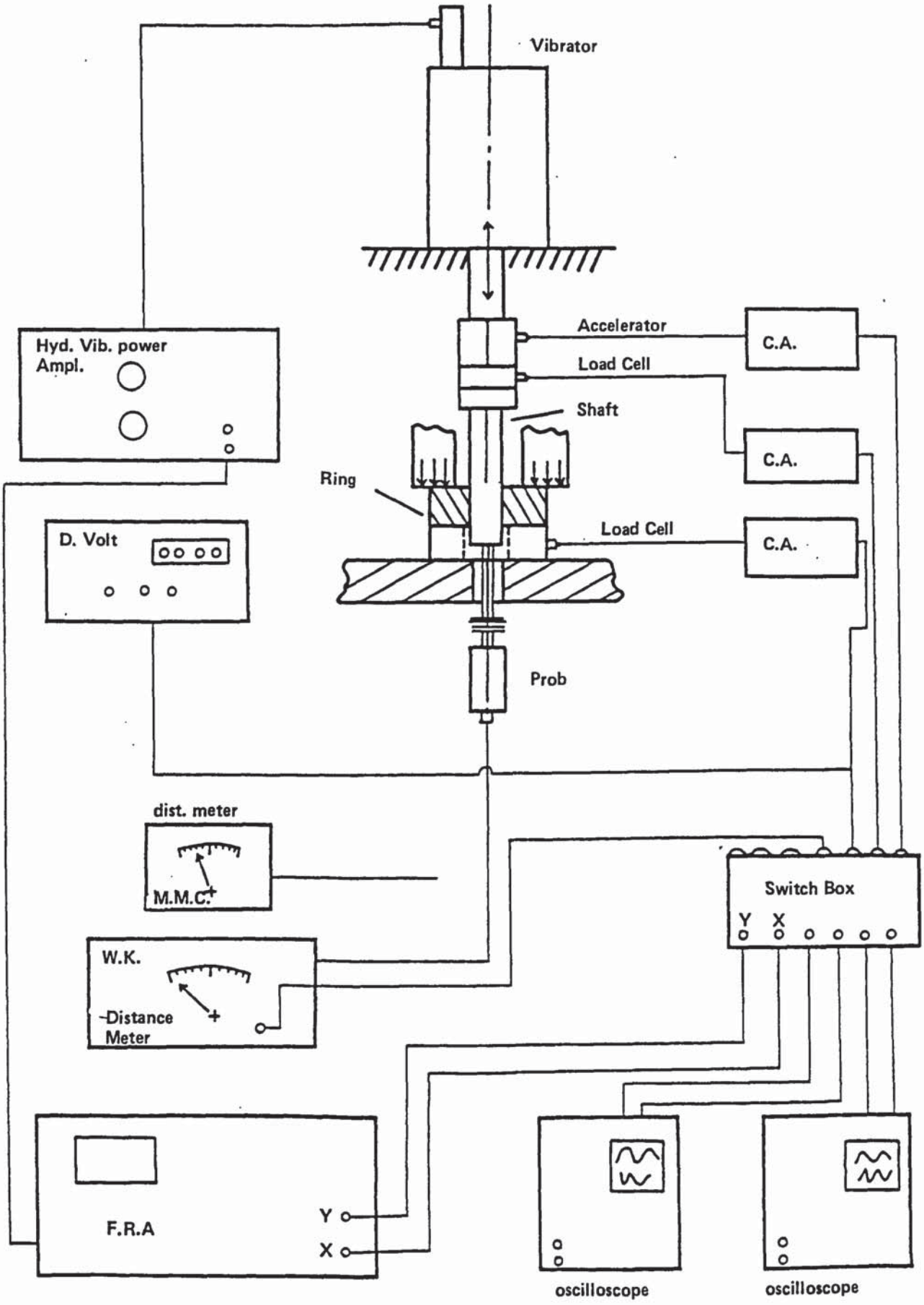

Fig 32 The testing system block diagram

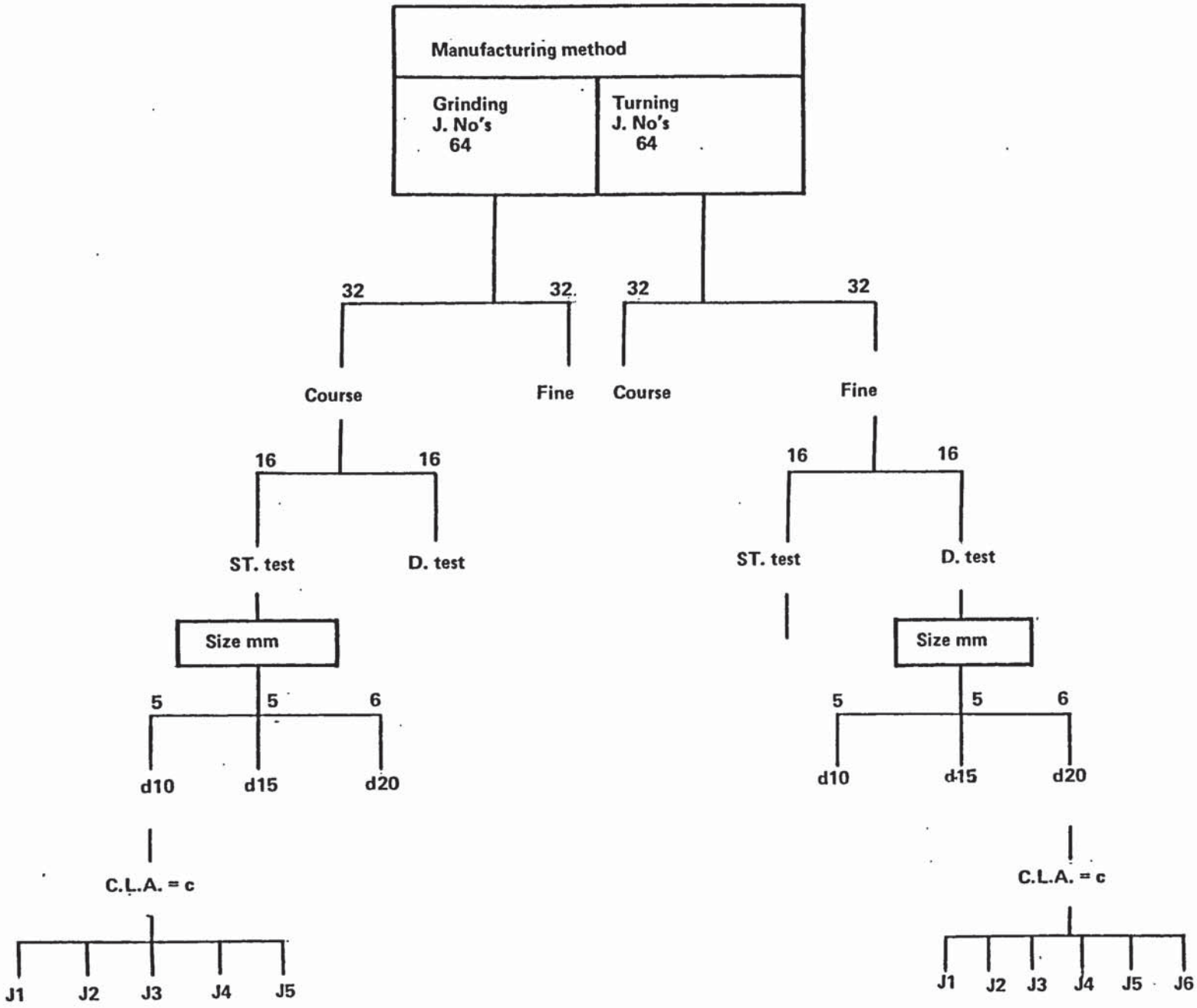

Fig 33 Block diagram of specimens Classification

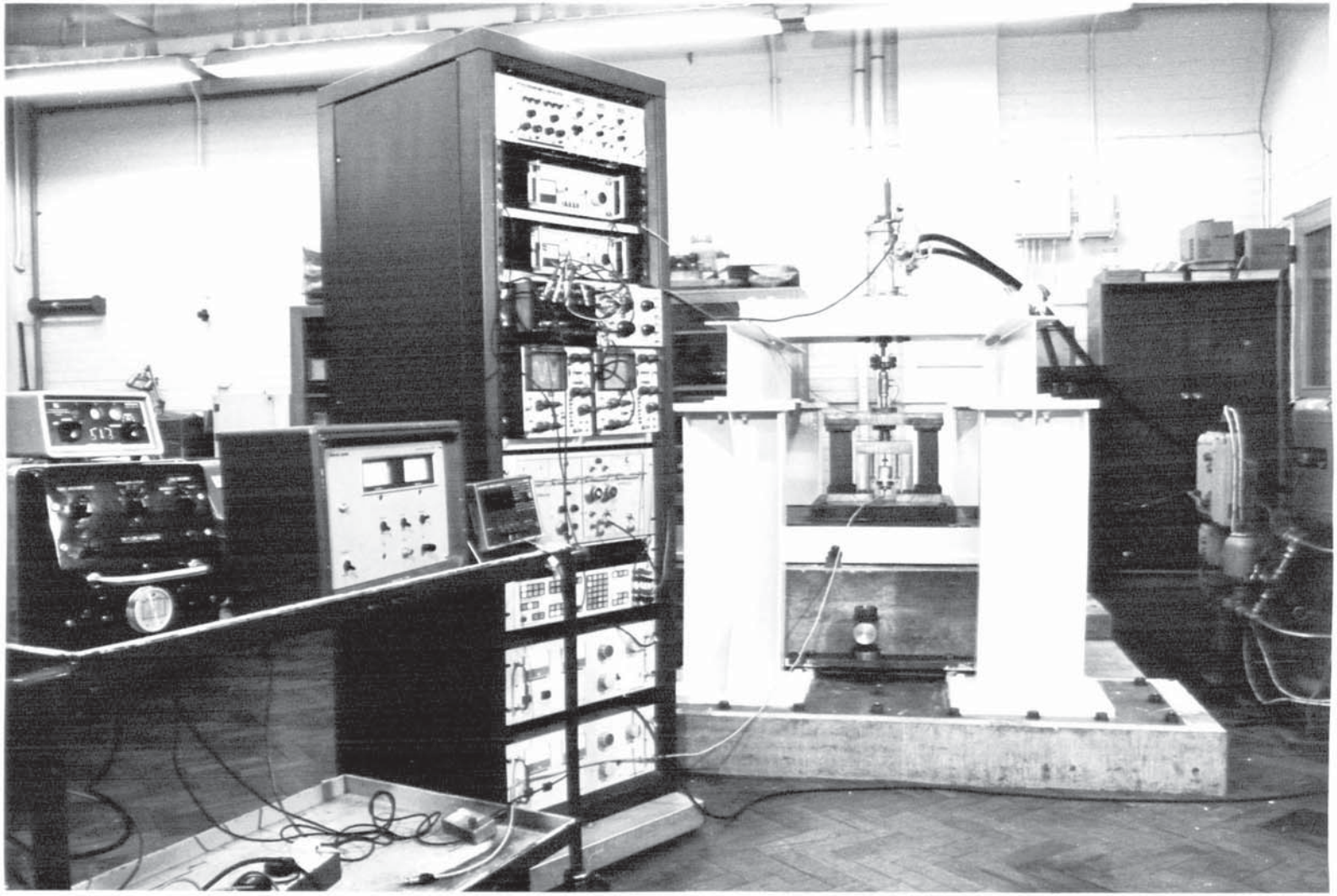

Fig 34 General view of the test rig

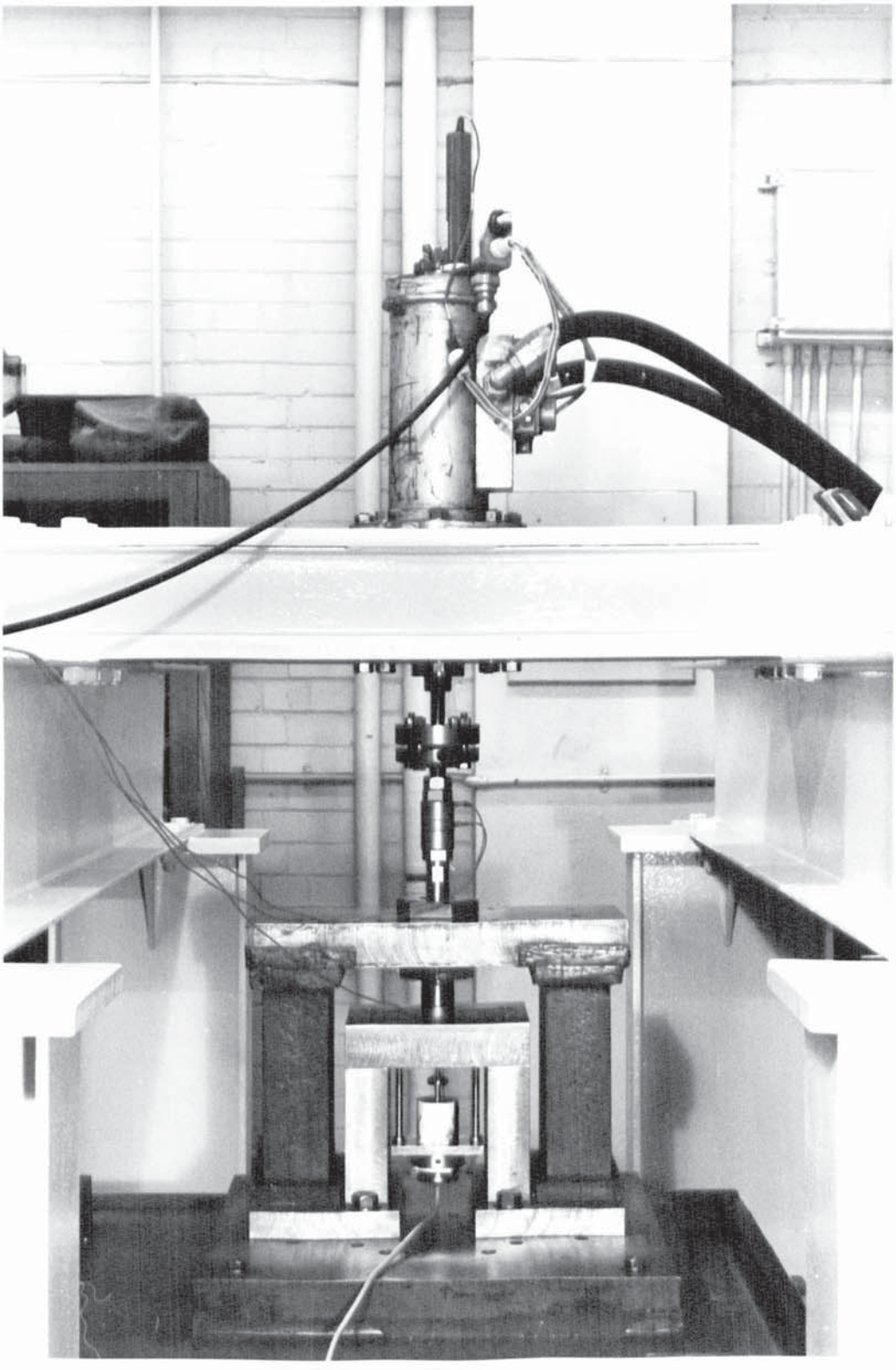

Fig 35 View of Specimen holding frame

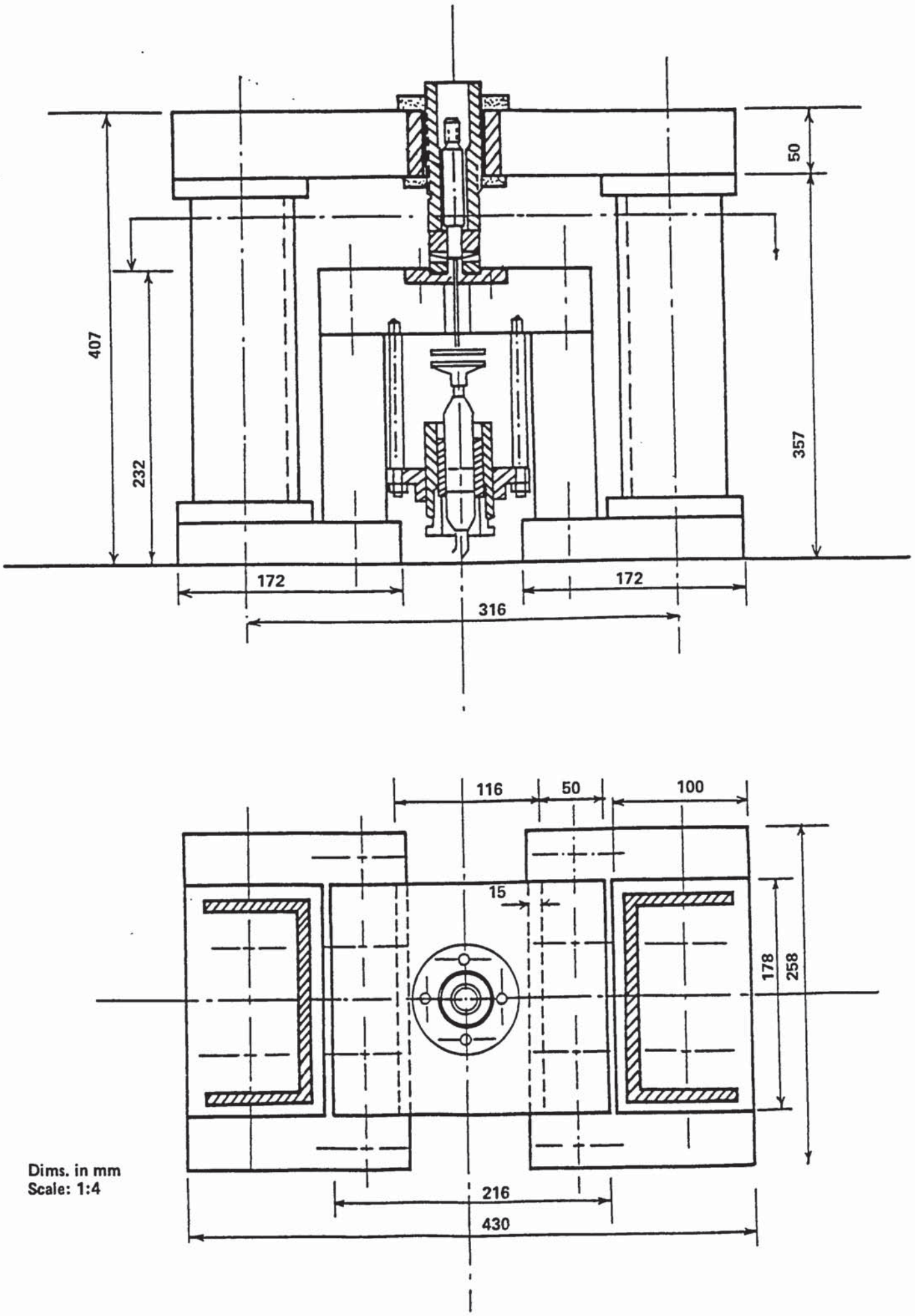

Fig 36 Schematic view of the specimen locating frame

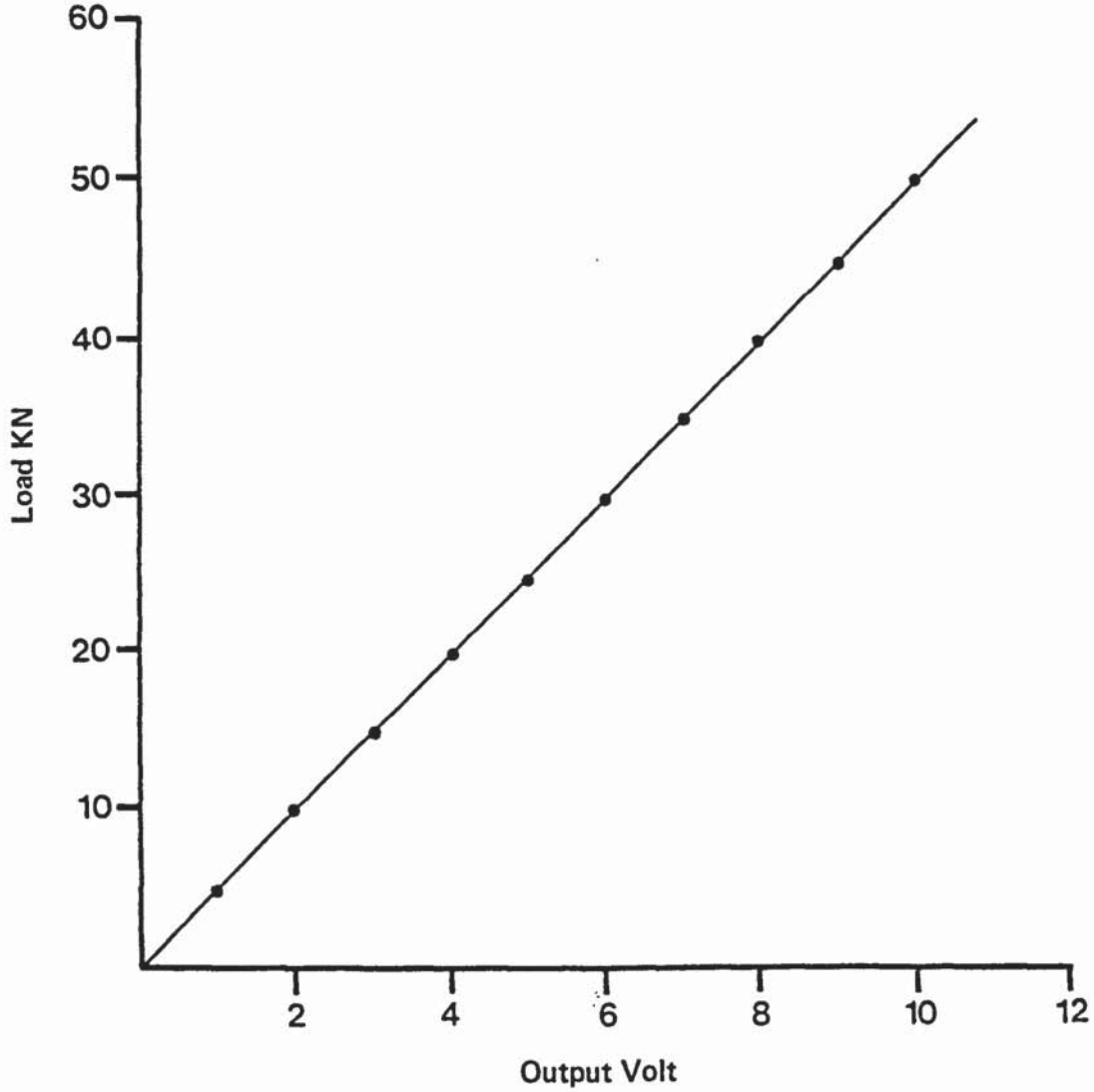

Fig 37 Static Calibration of Kistler Load Cell

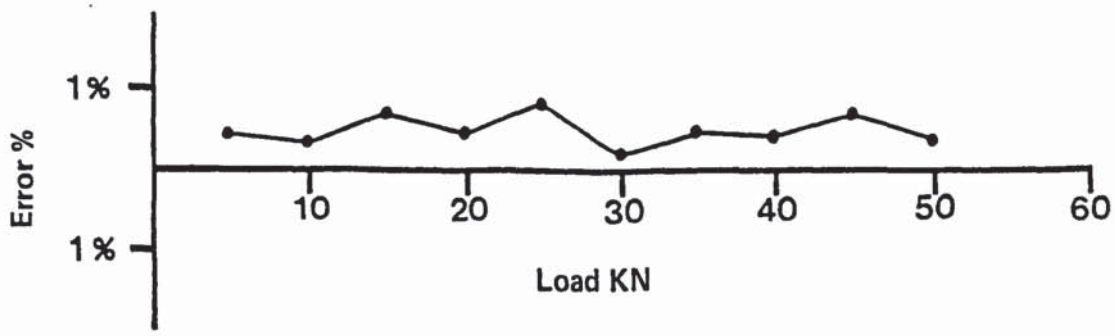

Fig 38 Gain error of Kistler Load Cell

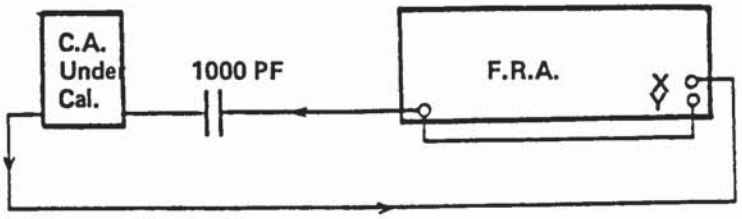

Fig 39 Set up for calibration of charge amplifier

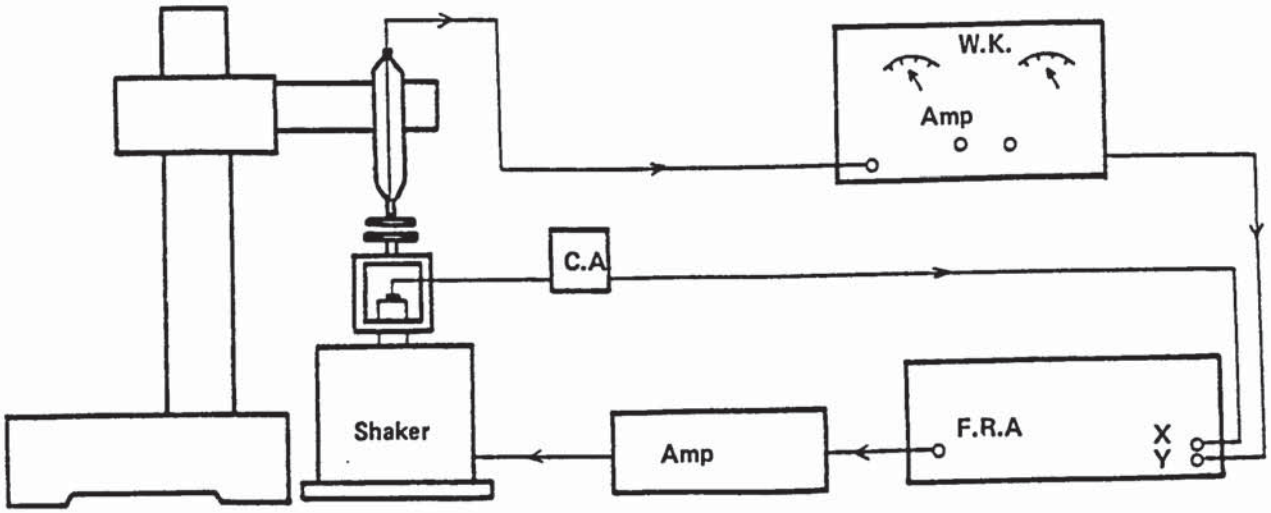

Fig 40 Set up for calibration of Wynne Kerr probe

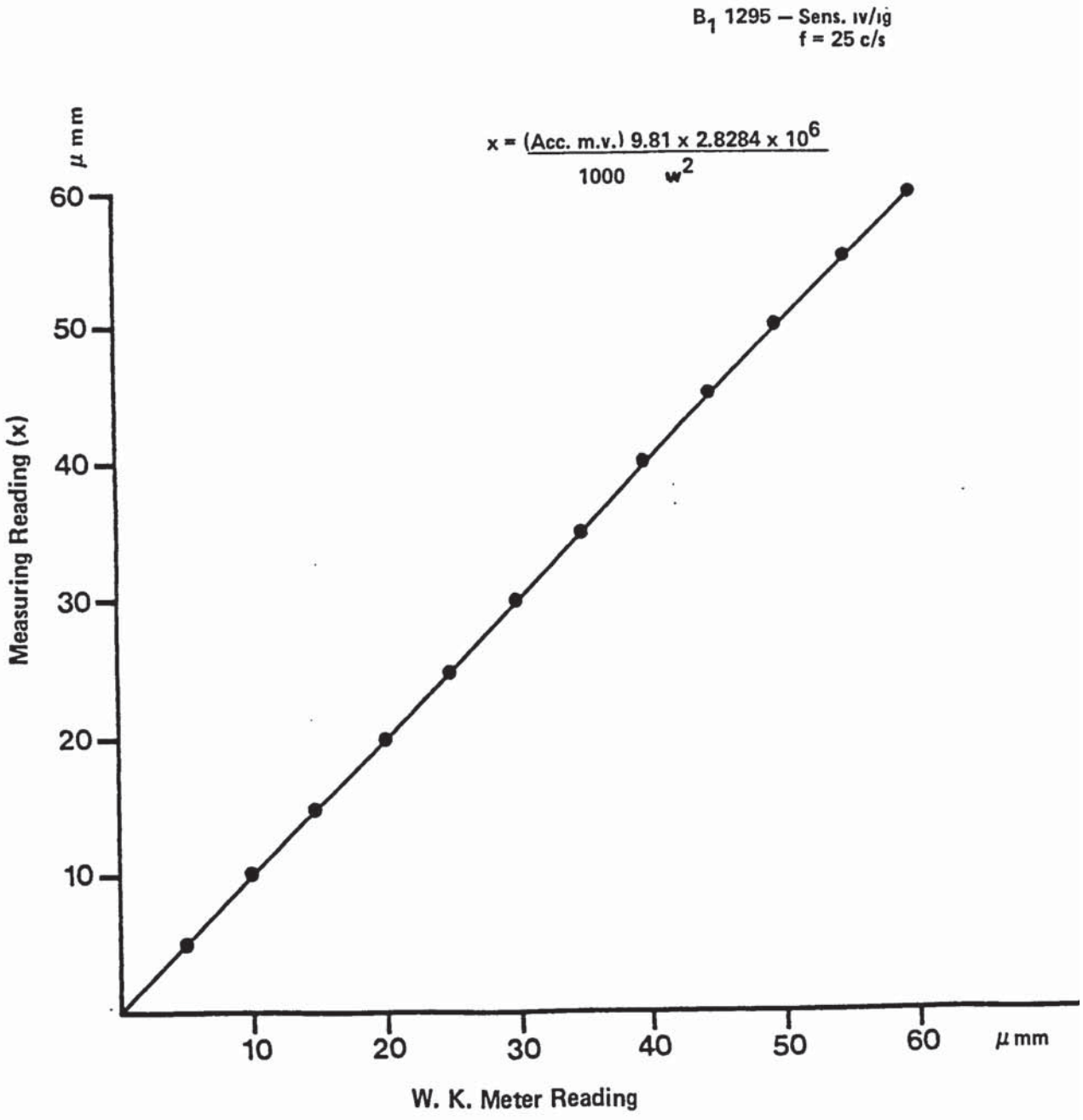

Fig 41 Dynamic Calibration of Wynne Kerr Probe

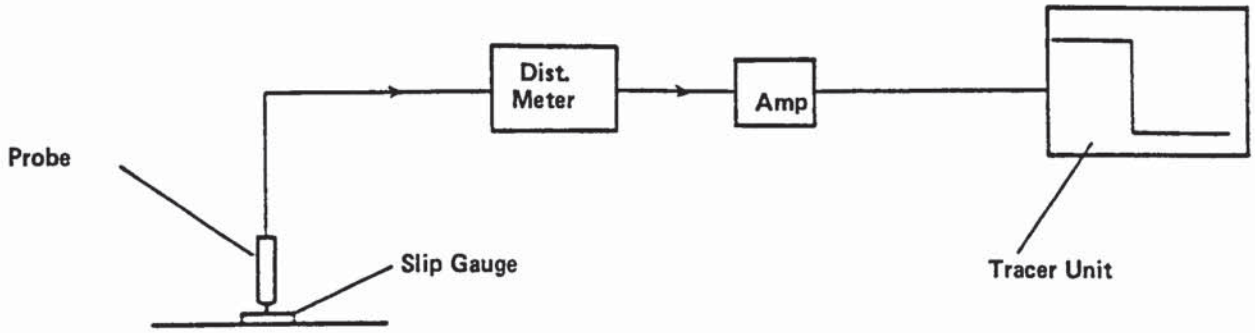

Fig 42 Calibration Circuit

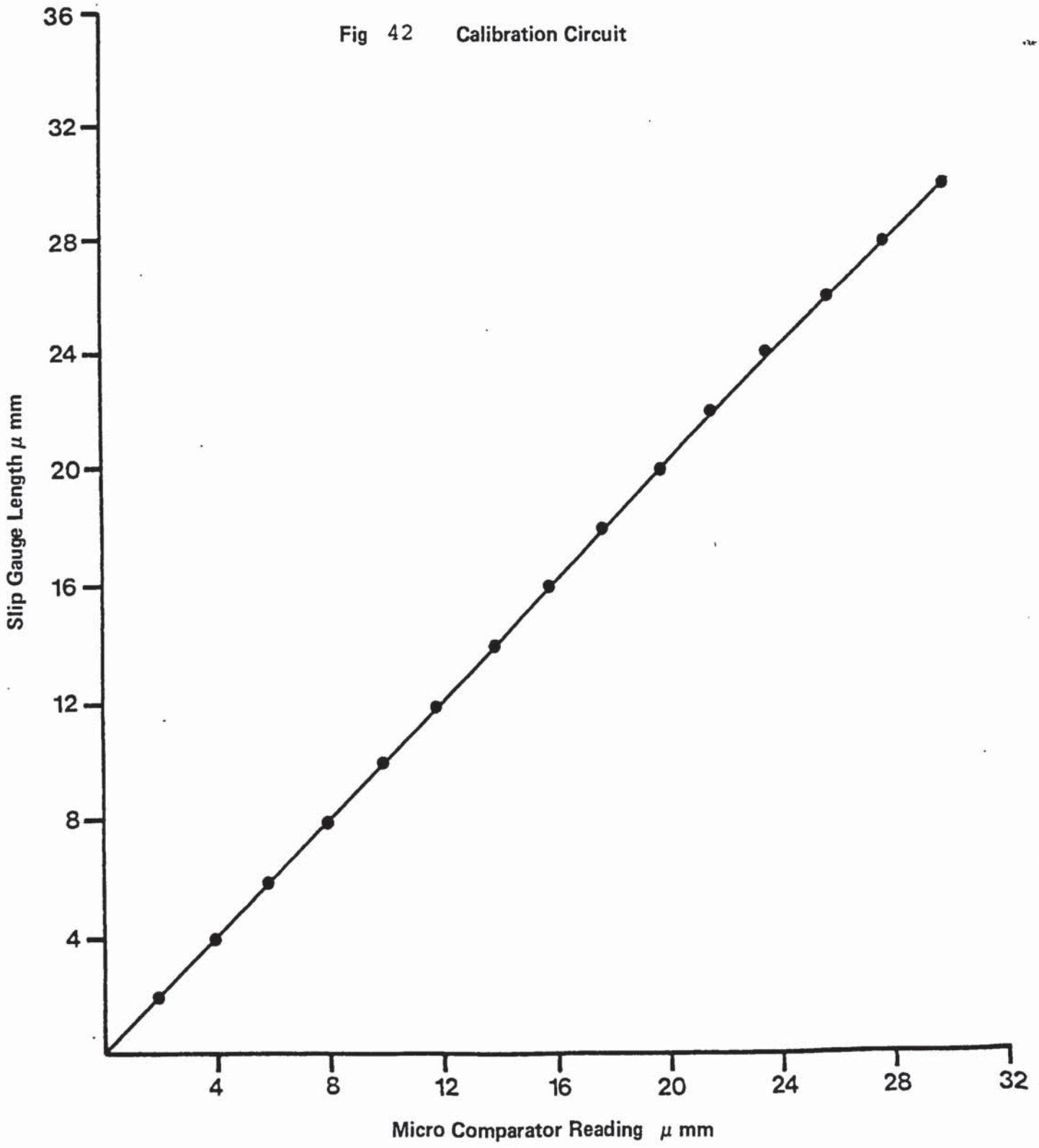

Fig 43 Calibration of Micro Comparator

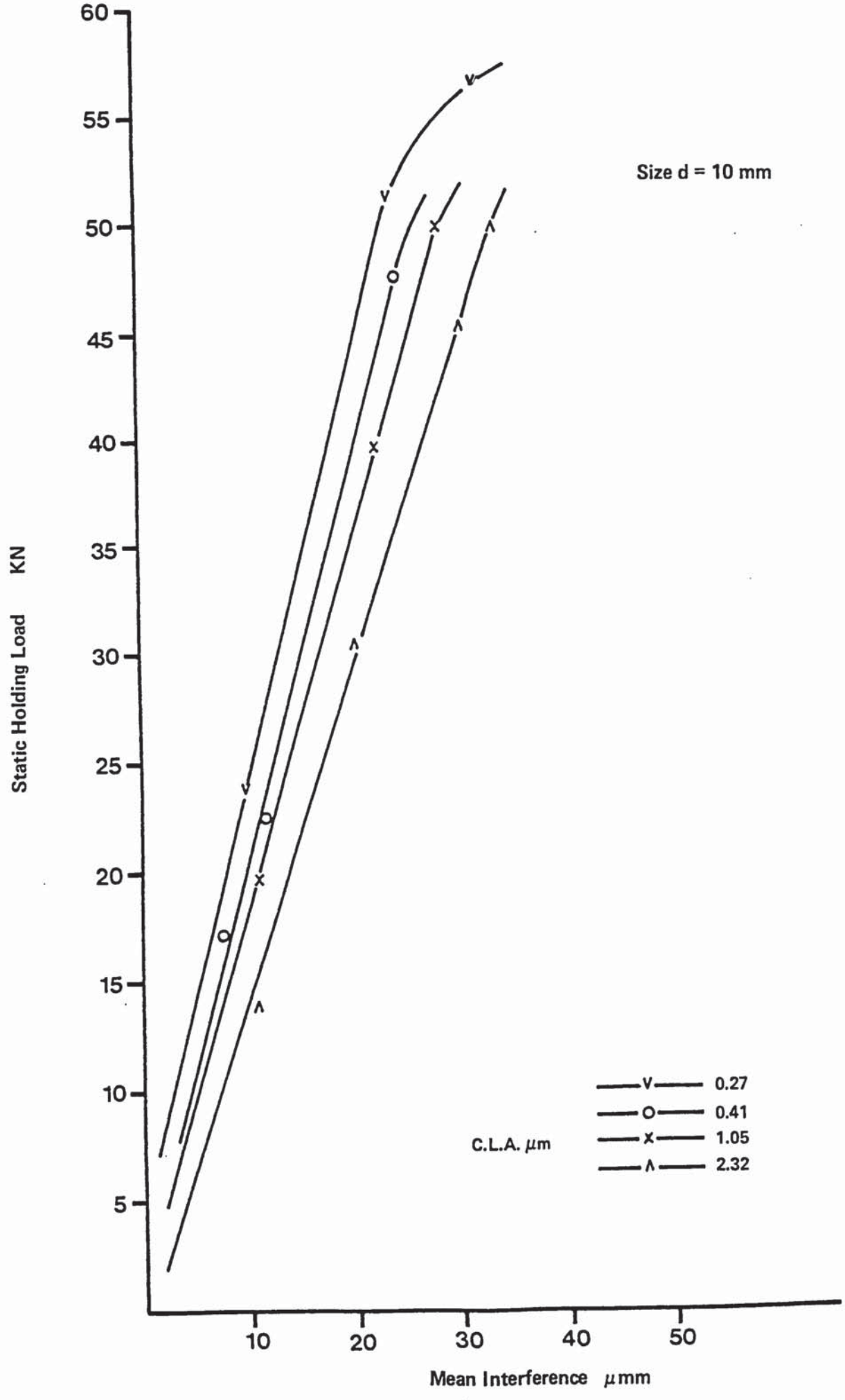

Fig 44 Effect of the interference value on the static Holding Load

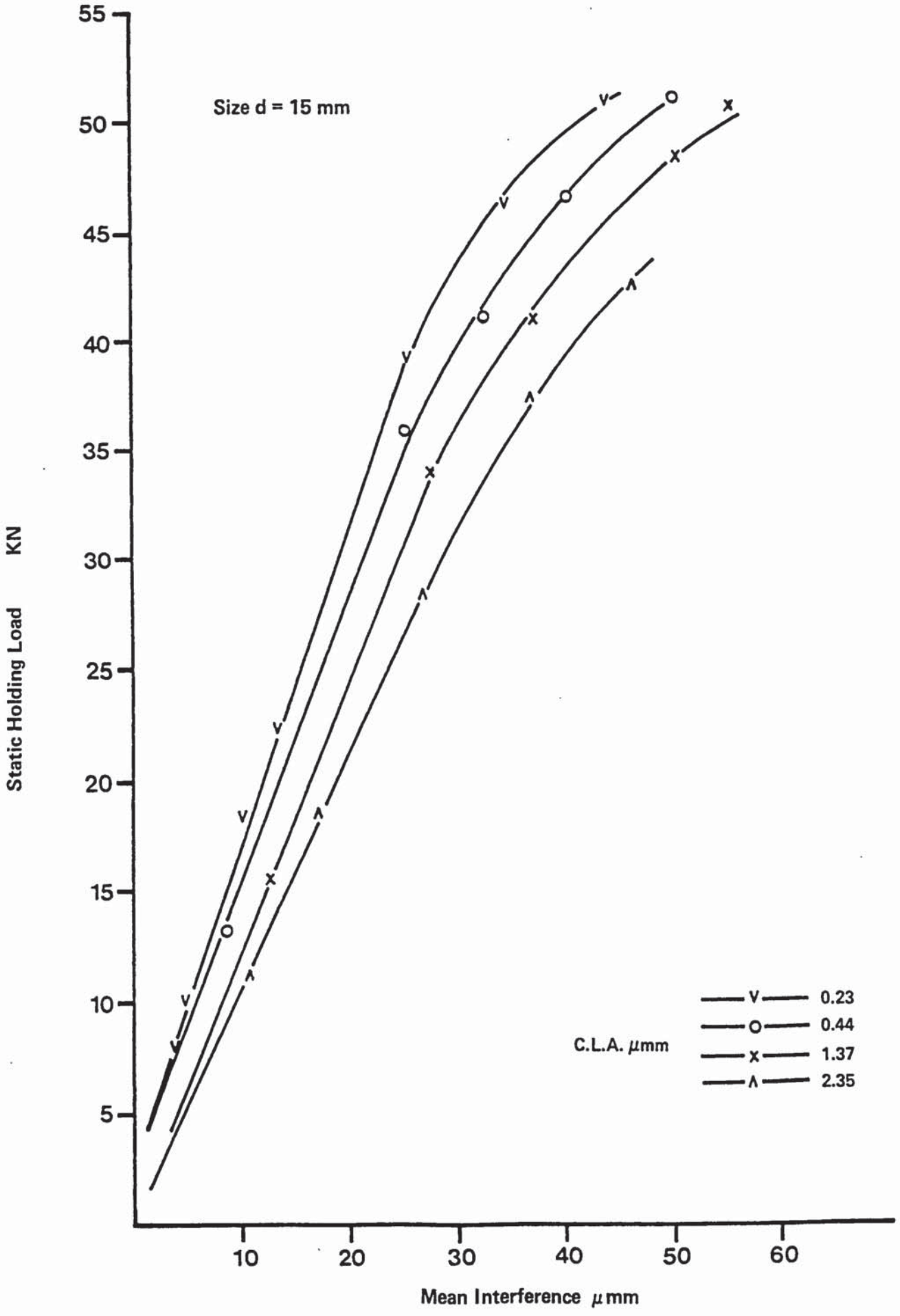

Fig 45 Effect of the interference value on the static Holding Load

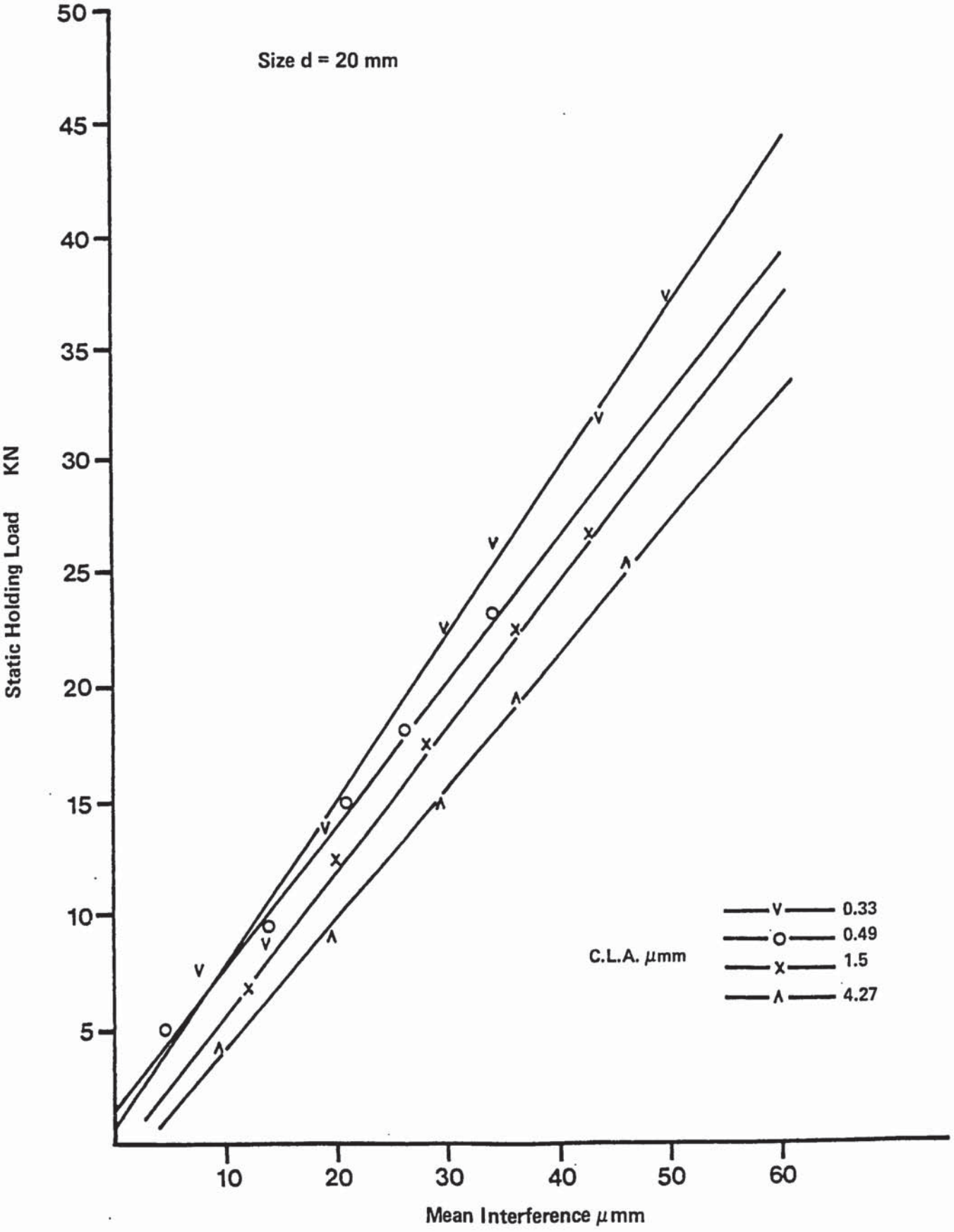

Fig 4·6 Effect of the interference value on the static Holding Load

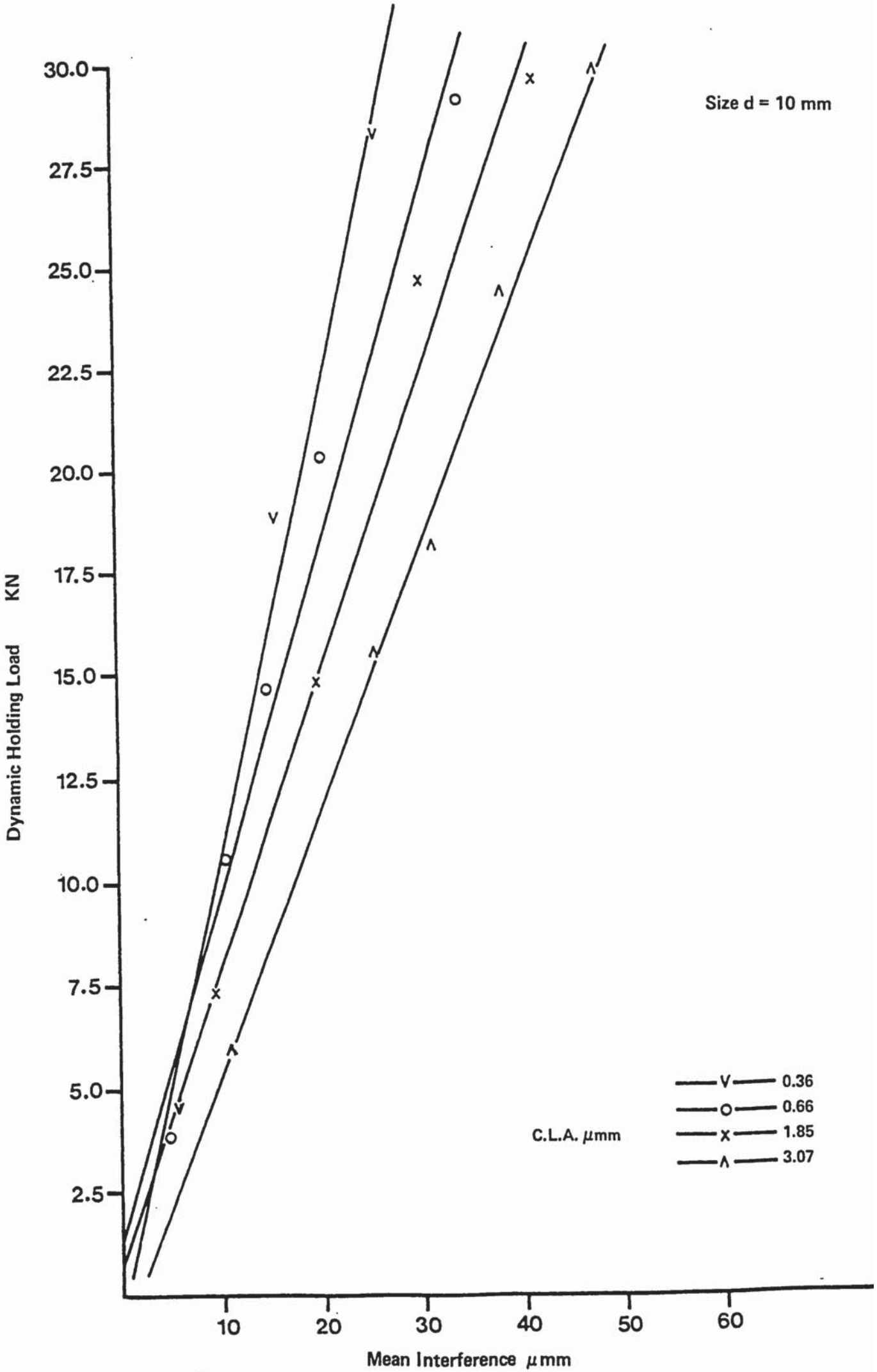

Fig 47 Effect of the interference value on the dynamic Holding Load

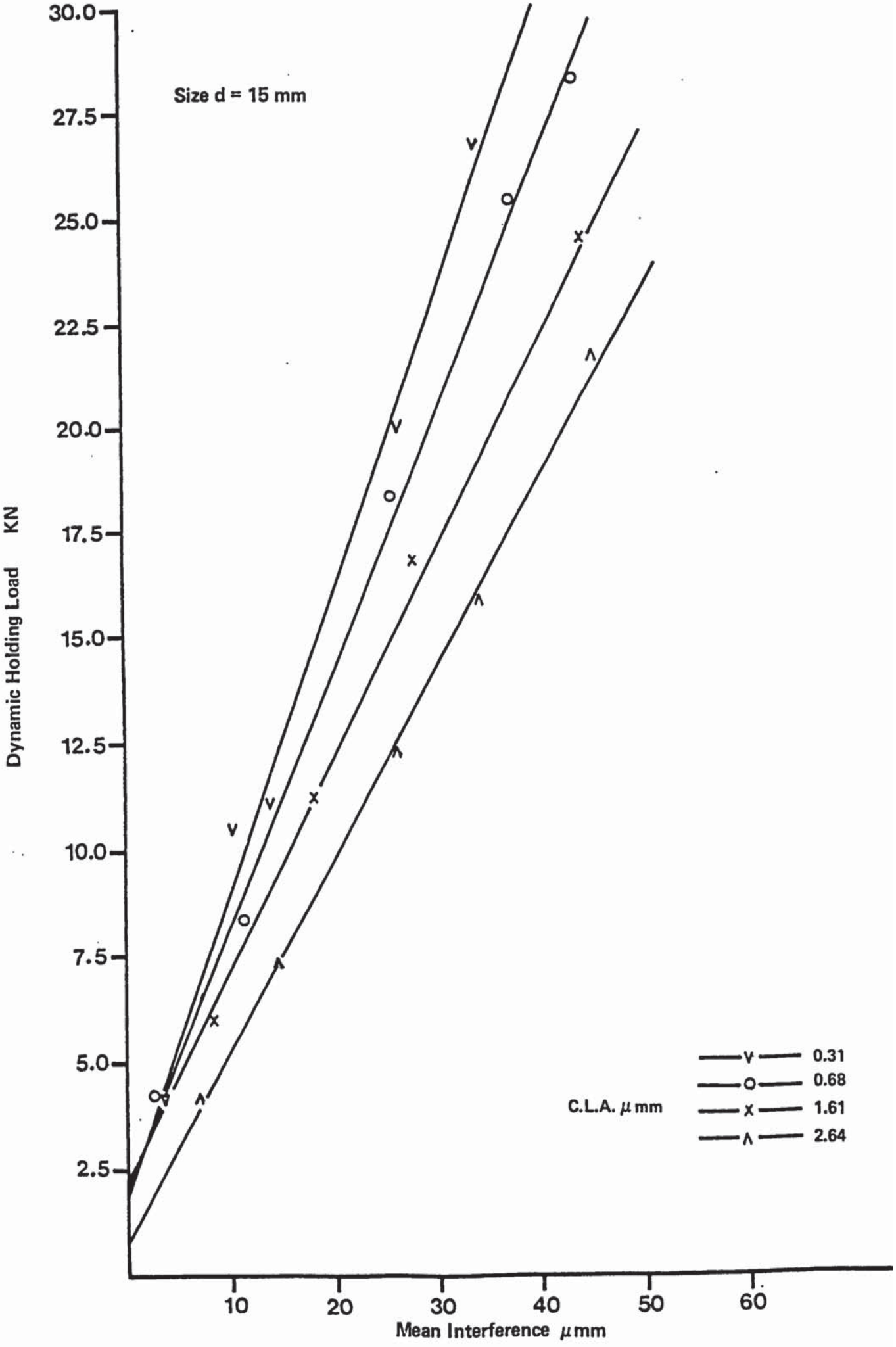

Fig 48 Effect of the interference value on the dynamic Holding Load

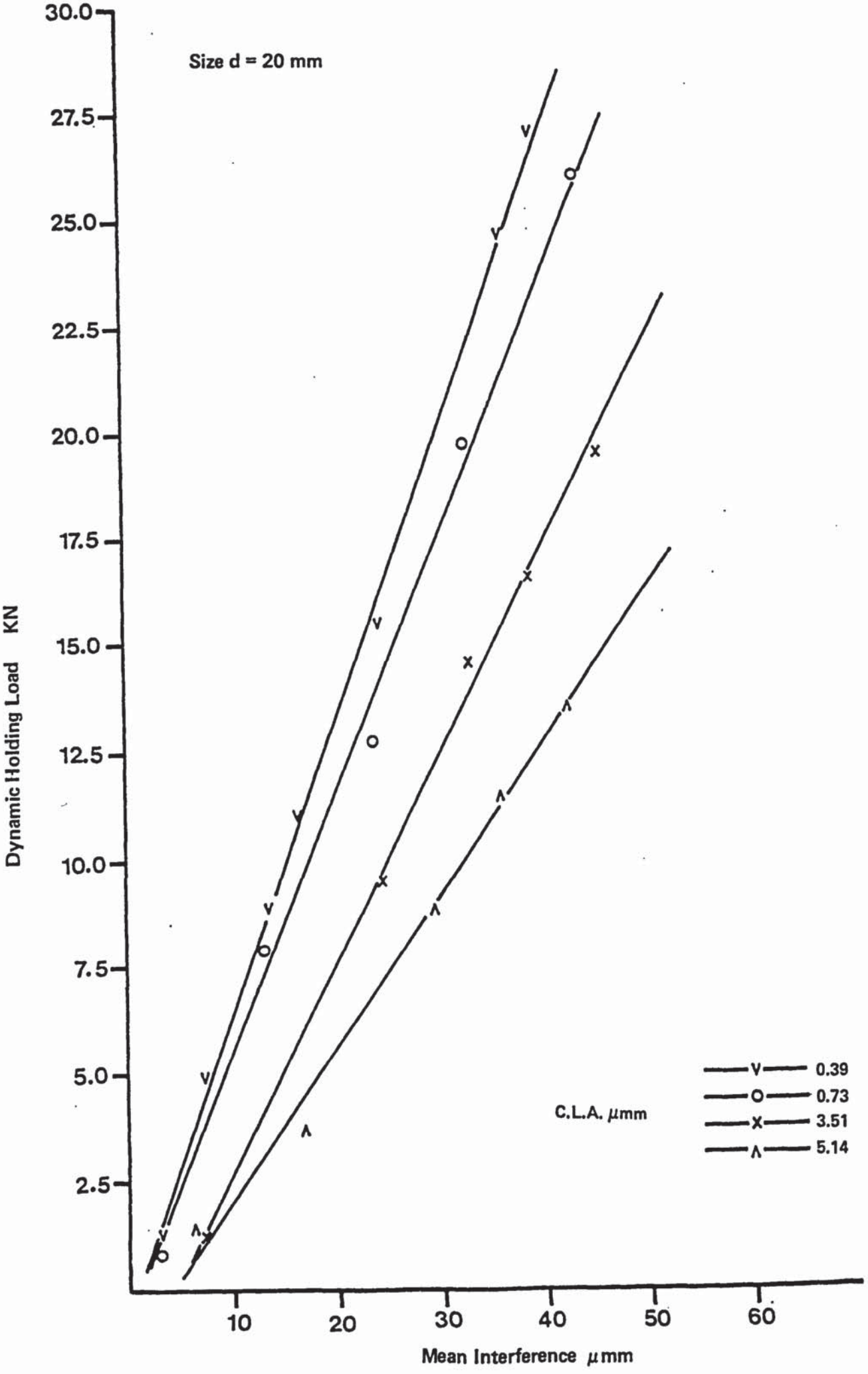

Fig. 49 Effect of the interference value on the dynamic Holding Load

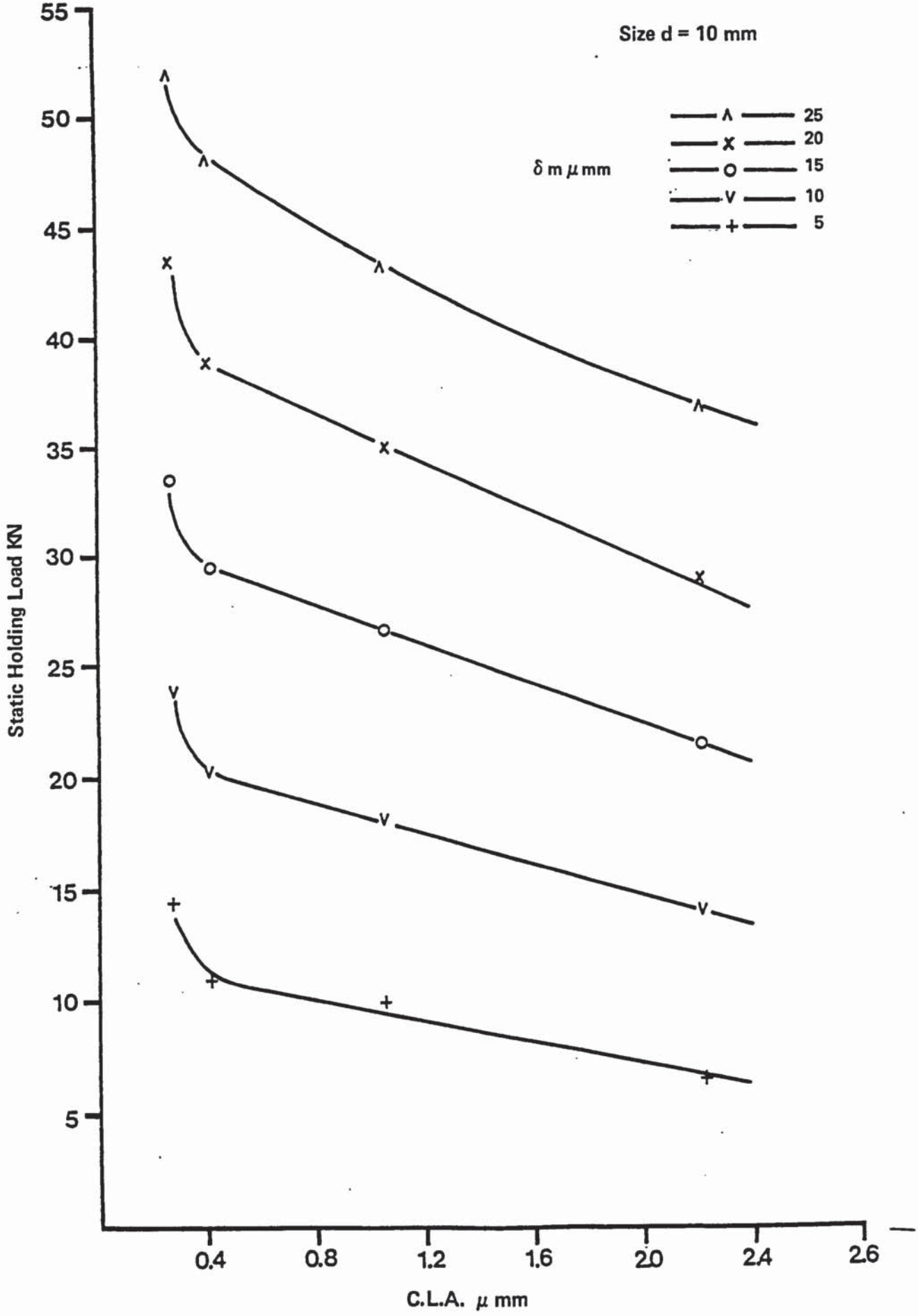

Fig 50 Effect of Surface roughness on the Static Holding Load

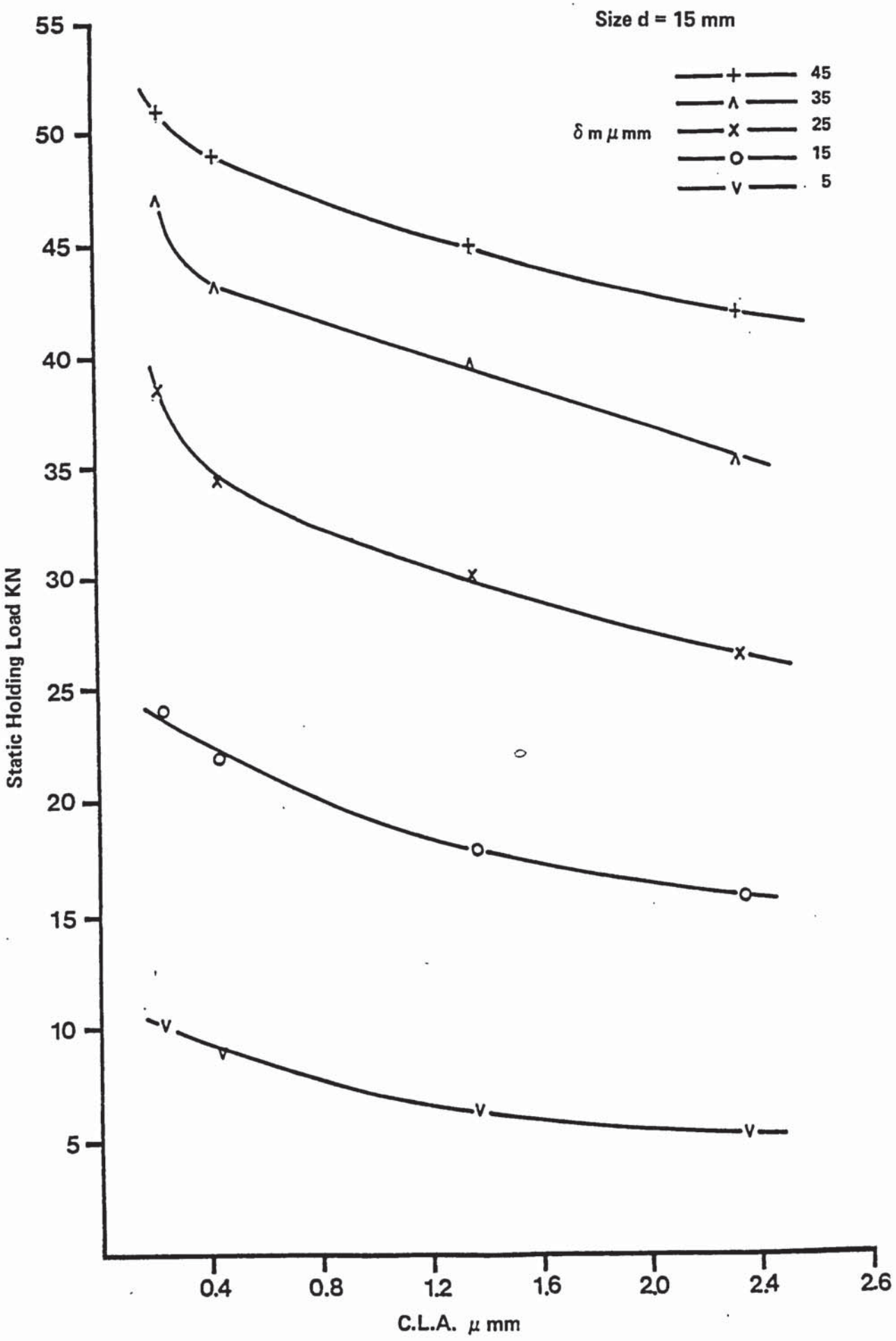

Fig 51 Effect of Surface roughness on the static Holding Load

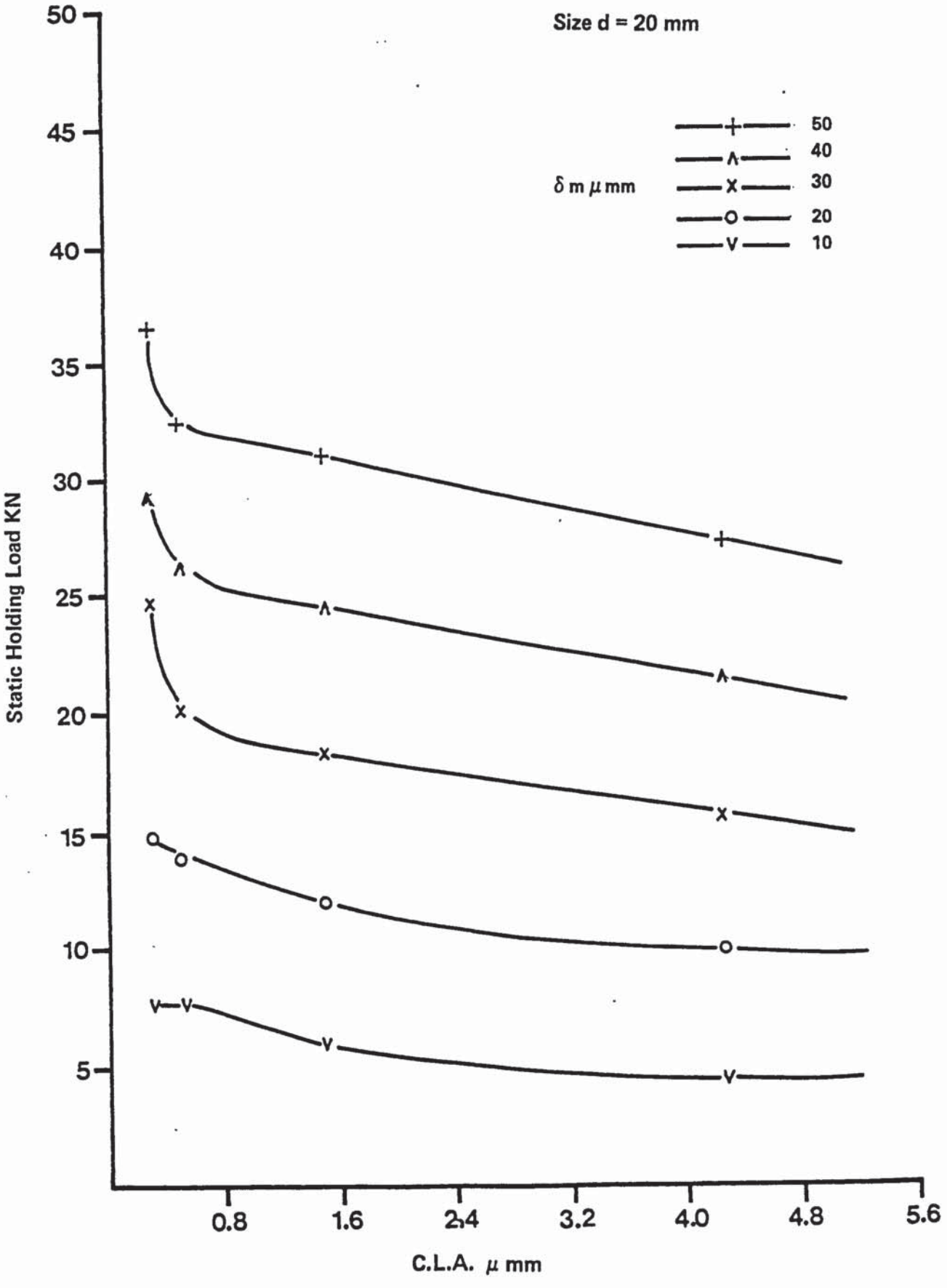

Fig 52 Effect of Surface roughness on the static holding load

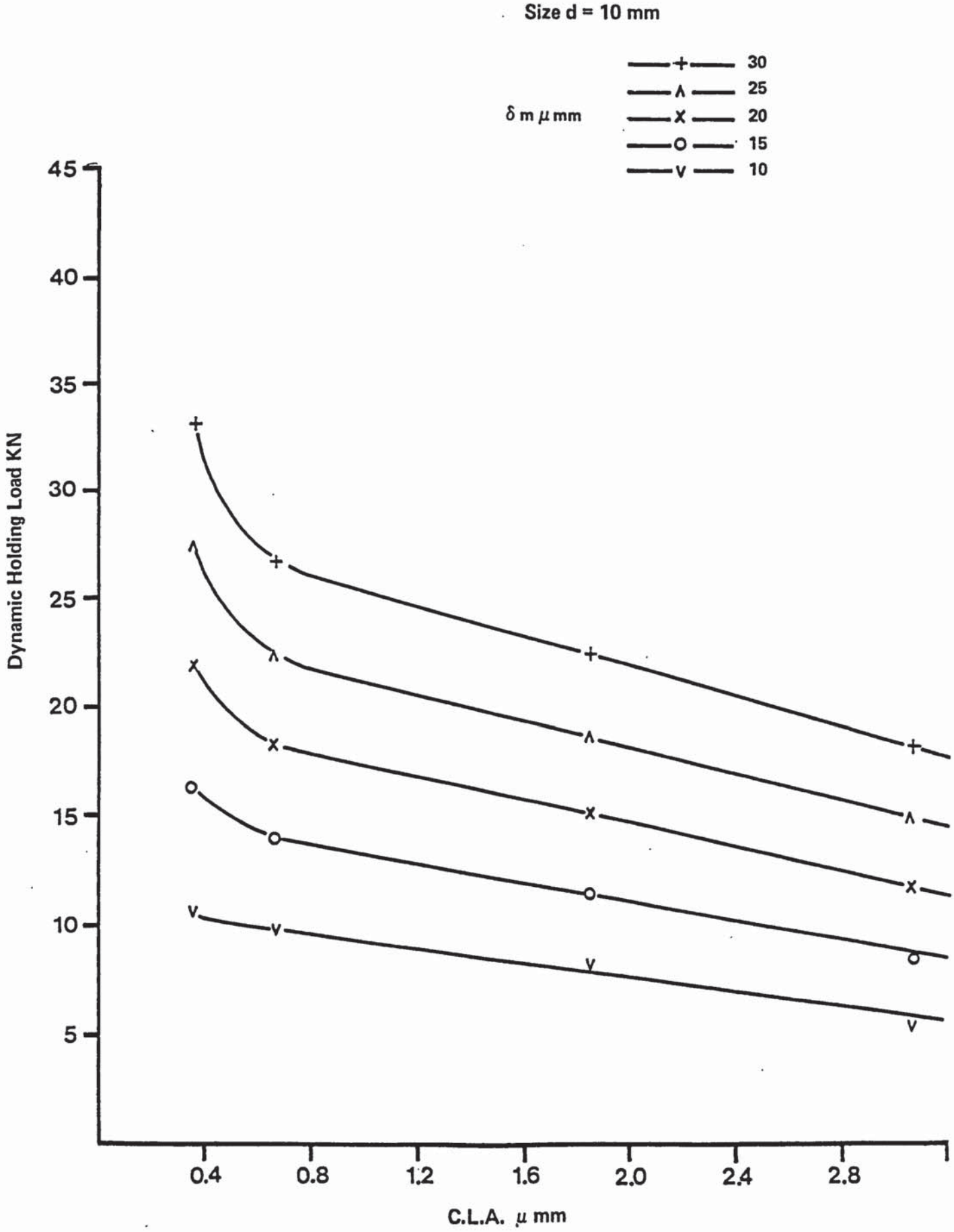

Fig 53 Effect of Surface roughness on the Dynamic Holding Load

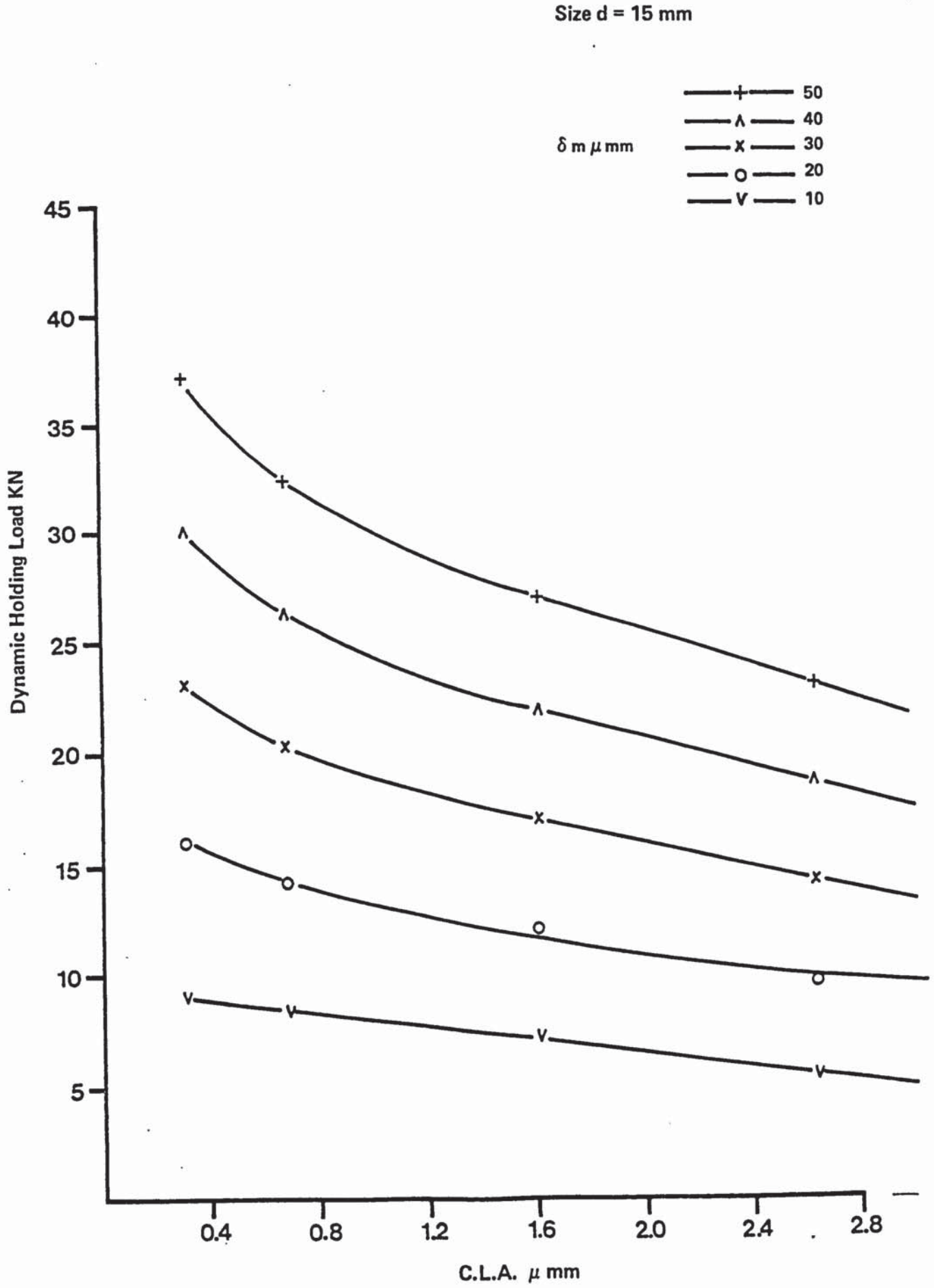

Fig 54 Effect of Surface roughness on the Dynamic Holding Load

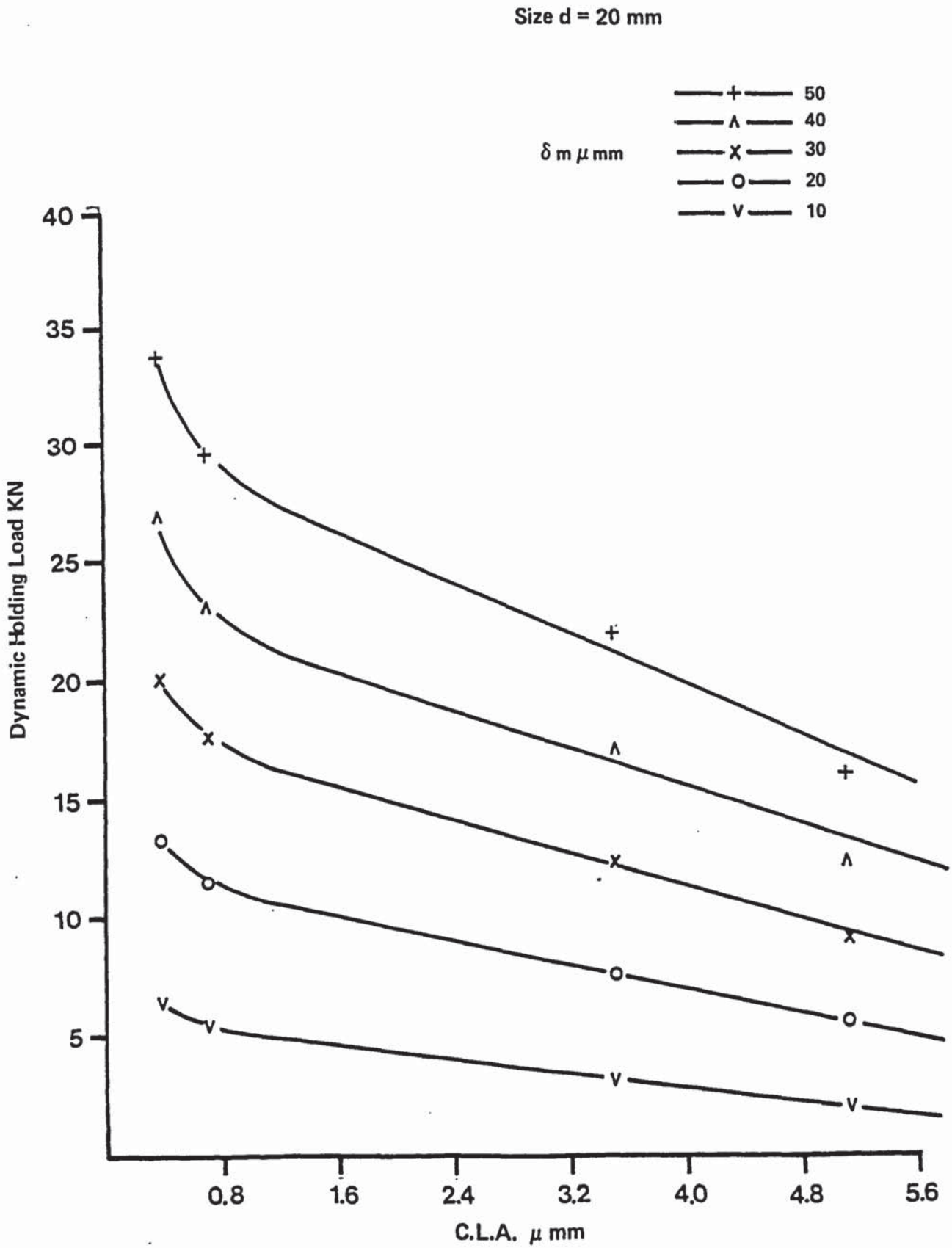

Fig 55 Effect of Surface roughness on the Dynamic Holding Load

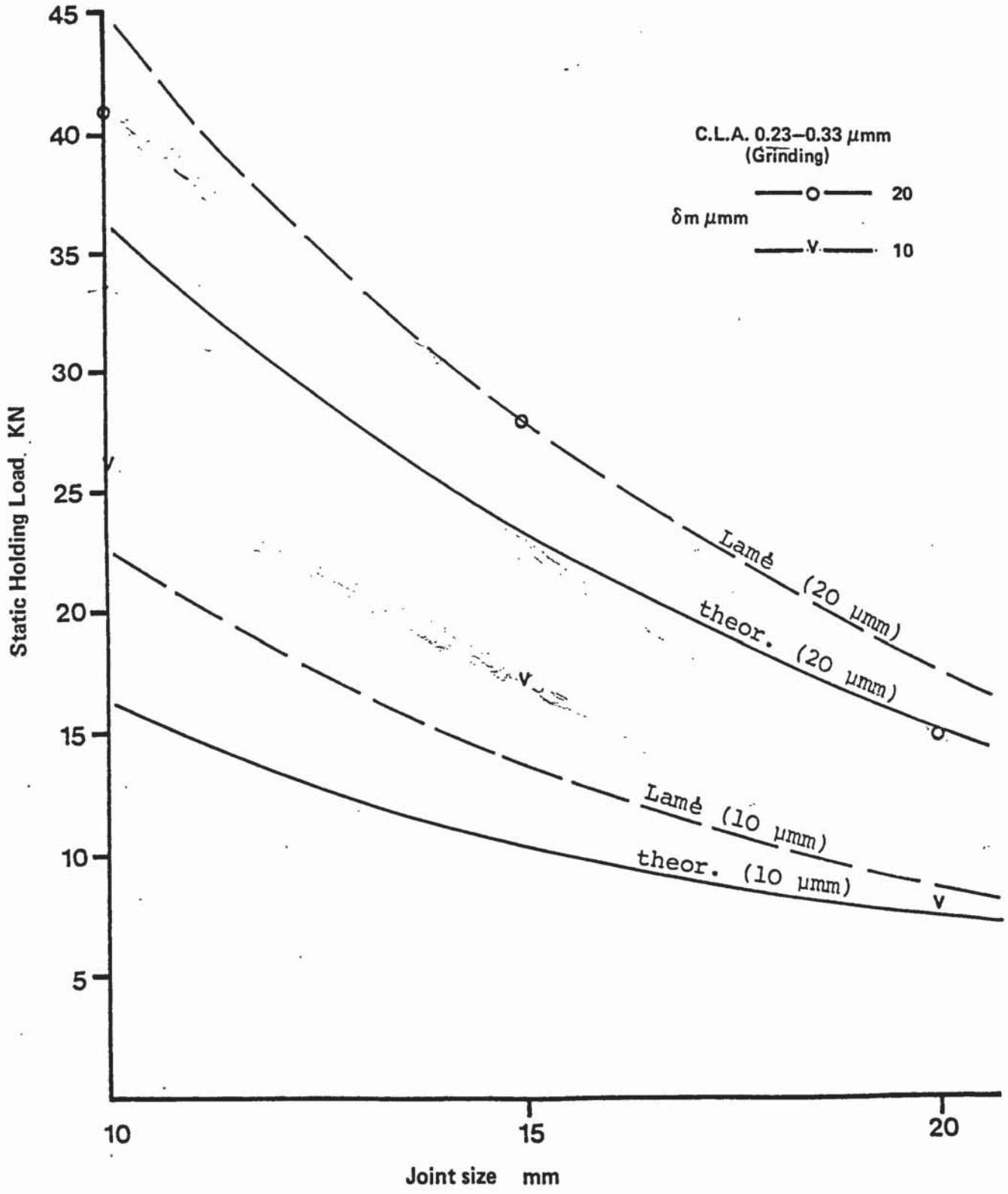

Fig 56 Effect of the joint size on the static holding load

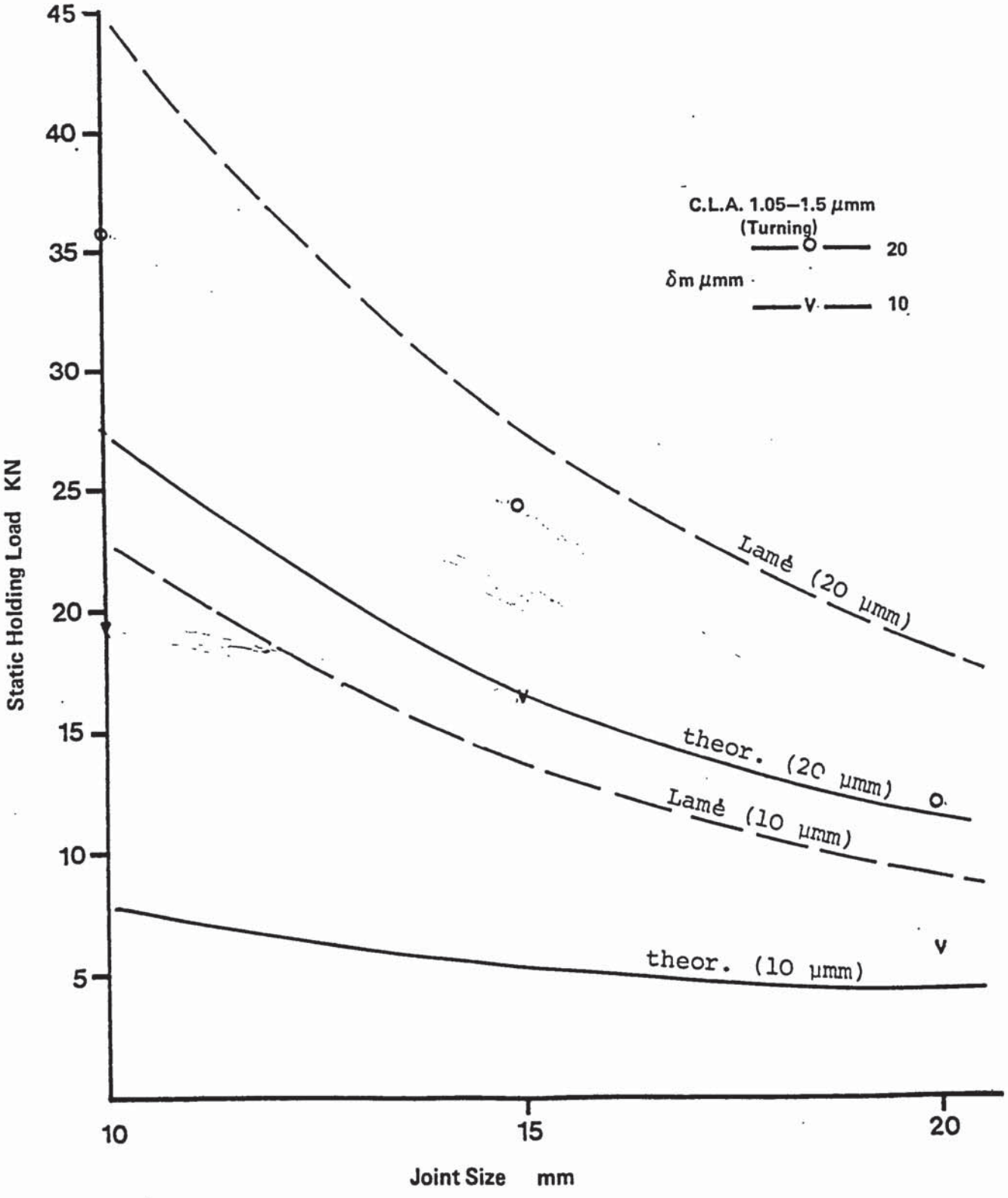

Fig 57 . Effect of the joint size on the static holding load

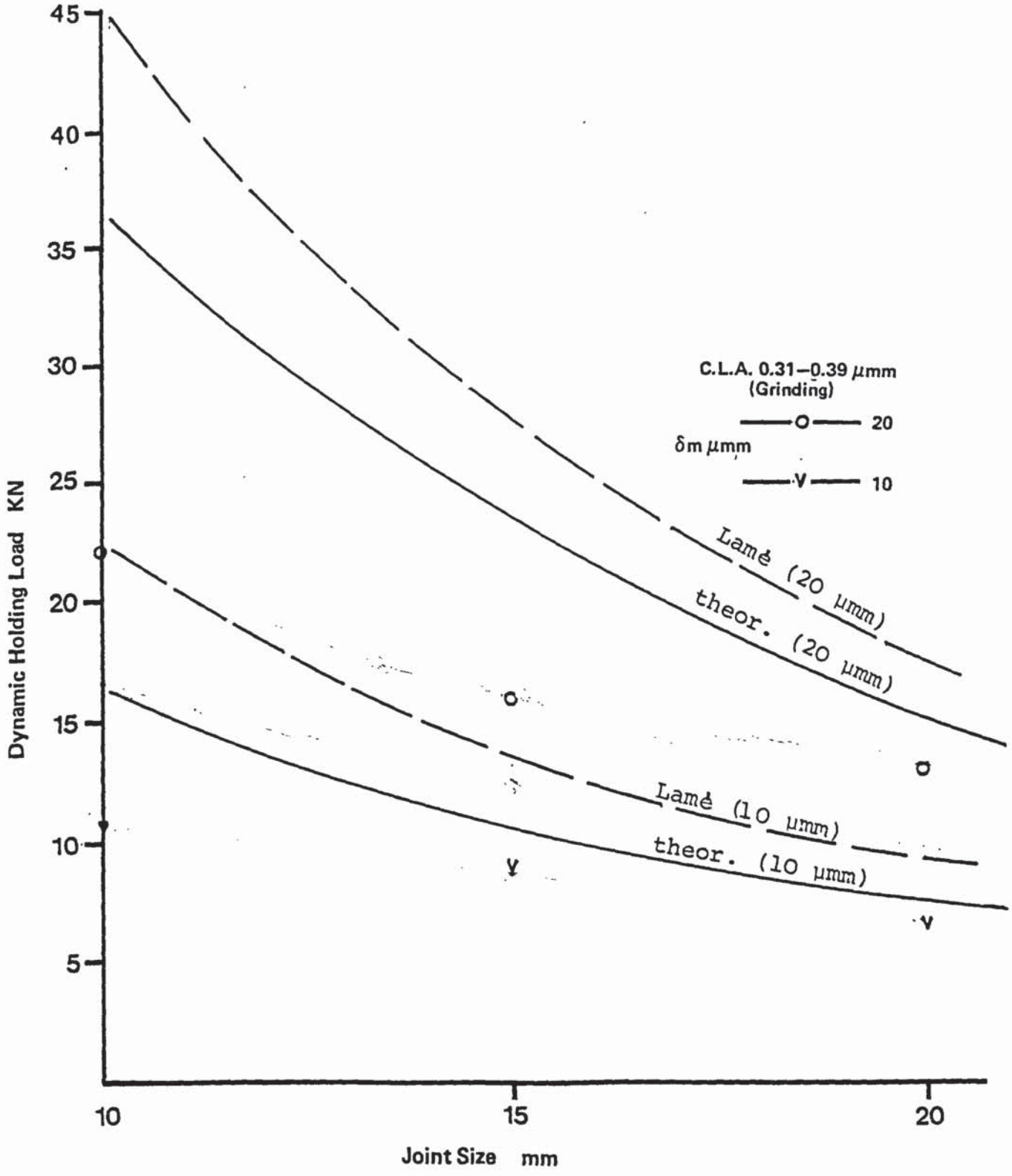

Fig 58 Effect of the joint size on the dynamic holding load

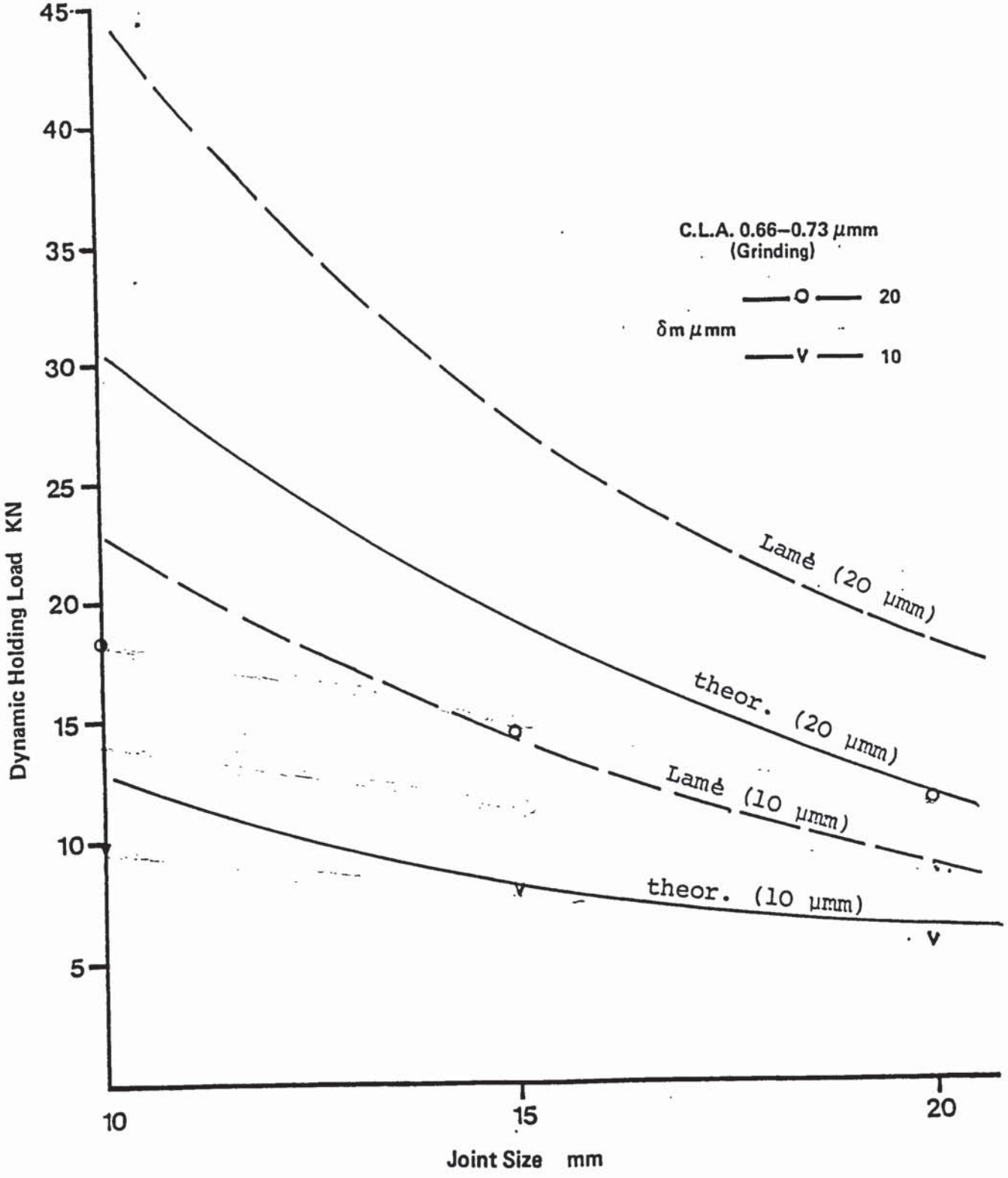

Fig 59 Effect of the joint size on the dynamic holding load

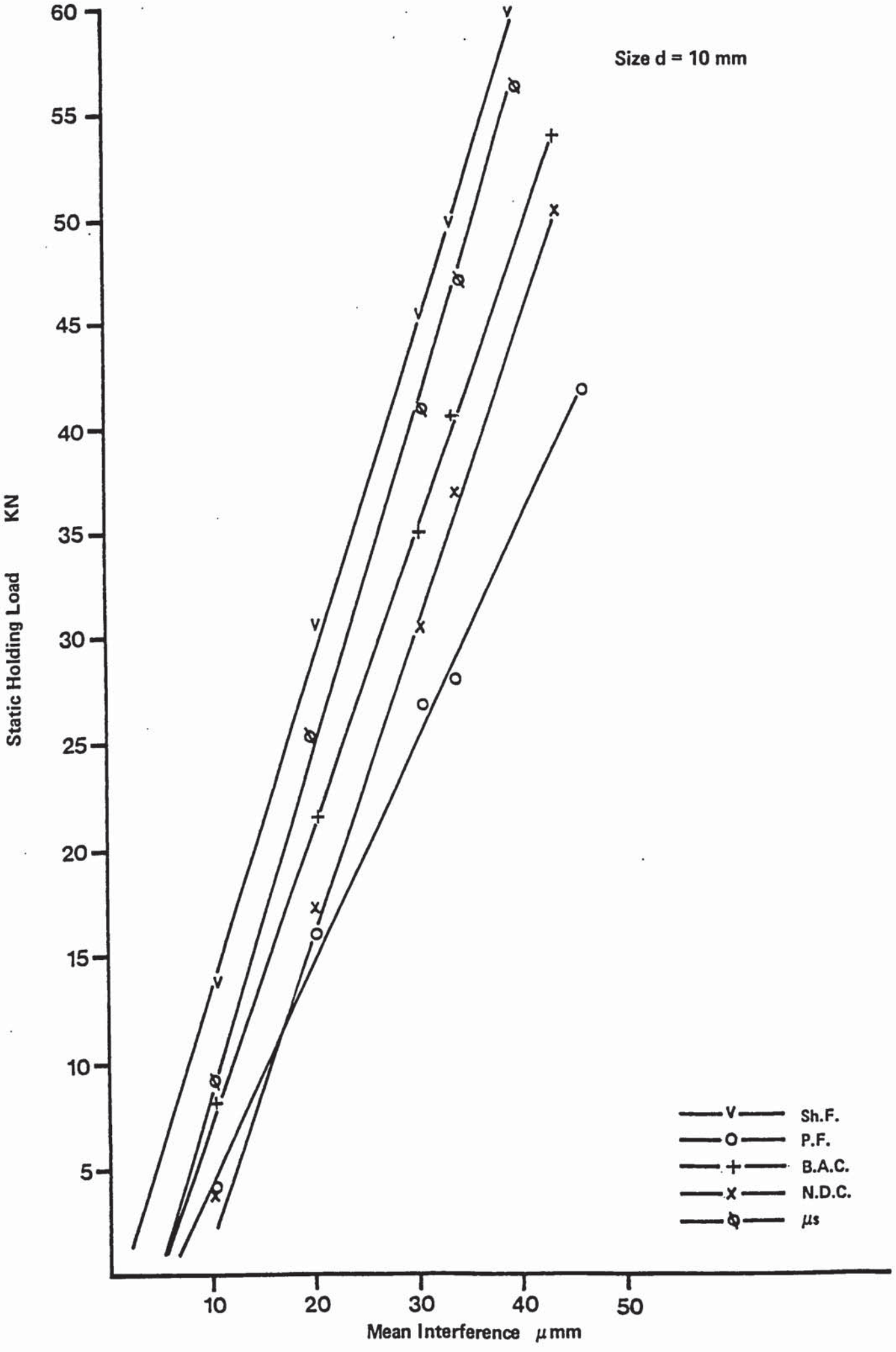

Fig 60 Experimental and theoretical Holding Load of ST11 joints

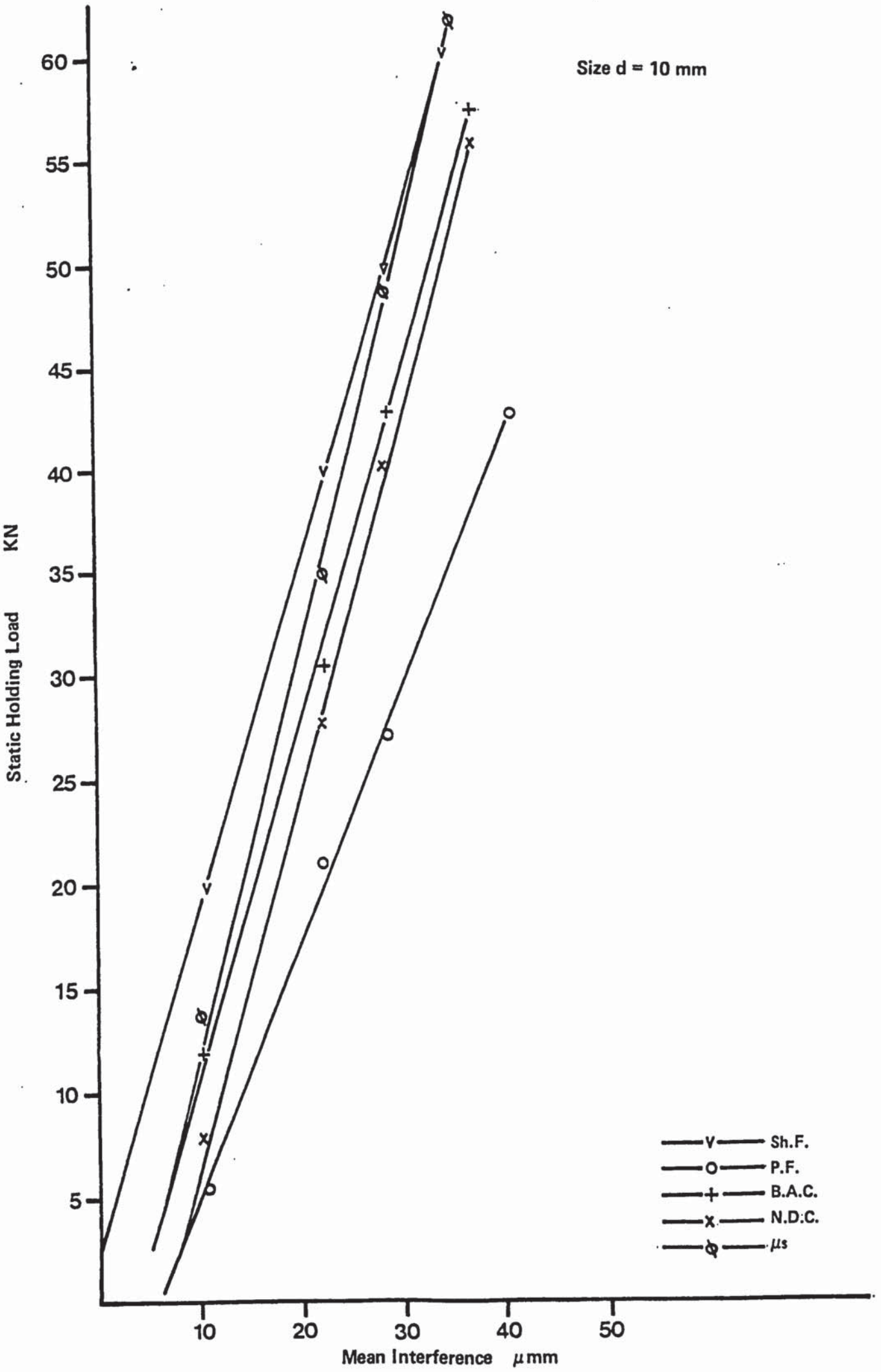

Fig 61 Experimental and theoretical Holding Load of ST12 joints

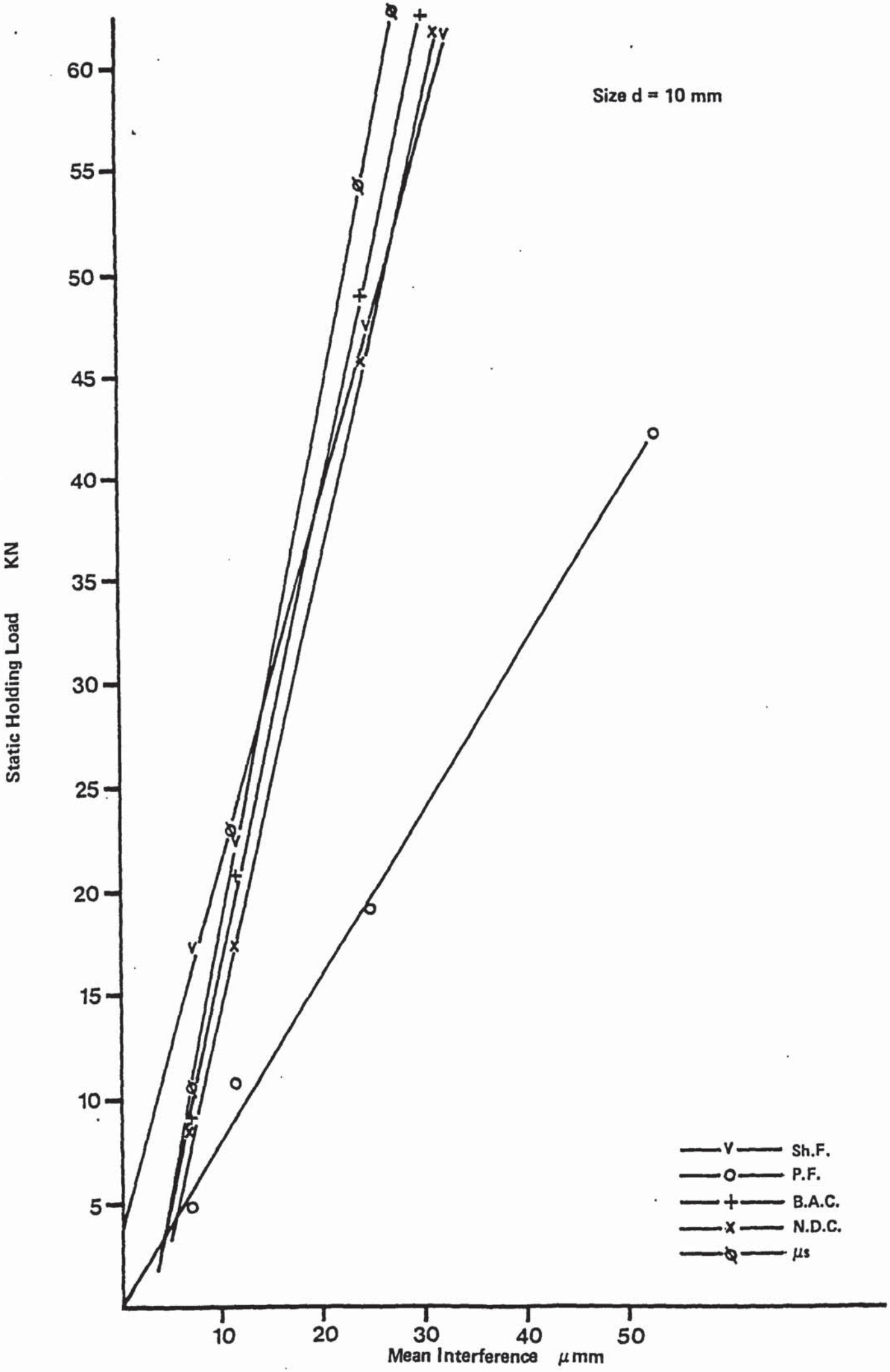

Fig 62 Experimental and theoretical Holding Load of ST21 joints

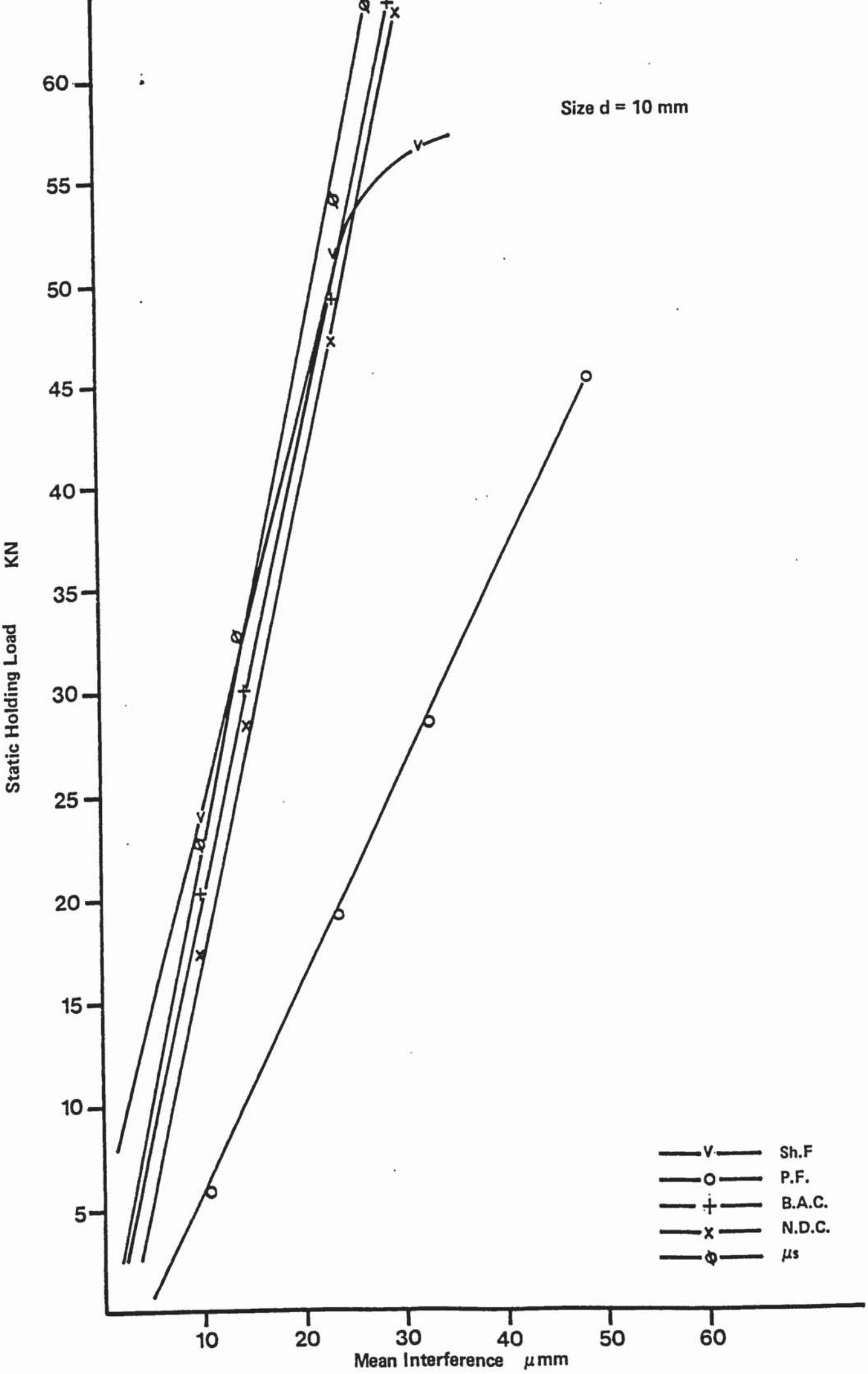

Fig 63 Experimental and theoretical Holding Load of ST22 joints

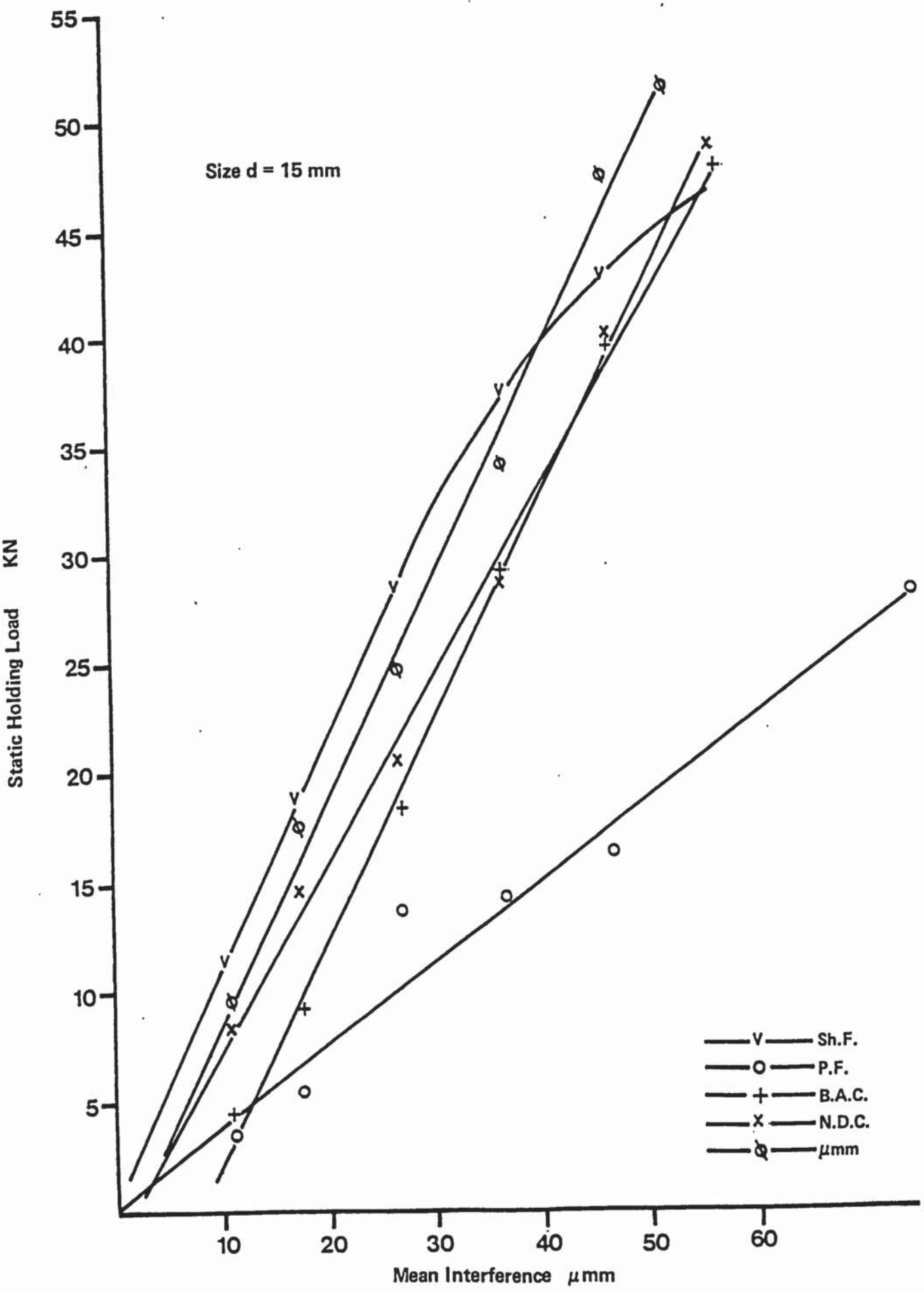

Fig 64 Experimental and theoretical Holding Load of ST31 joints

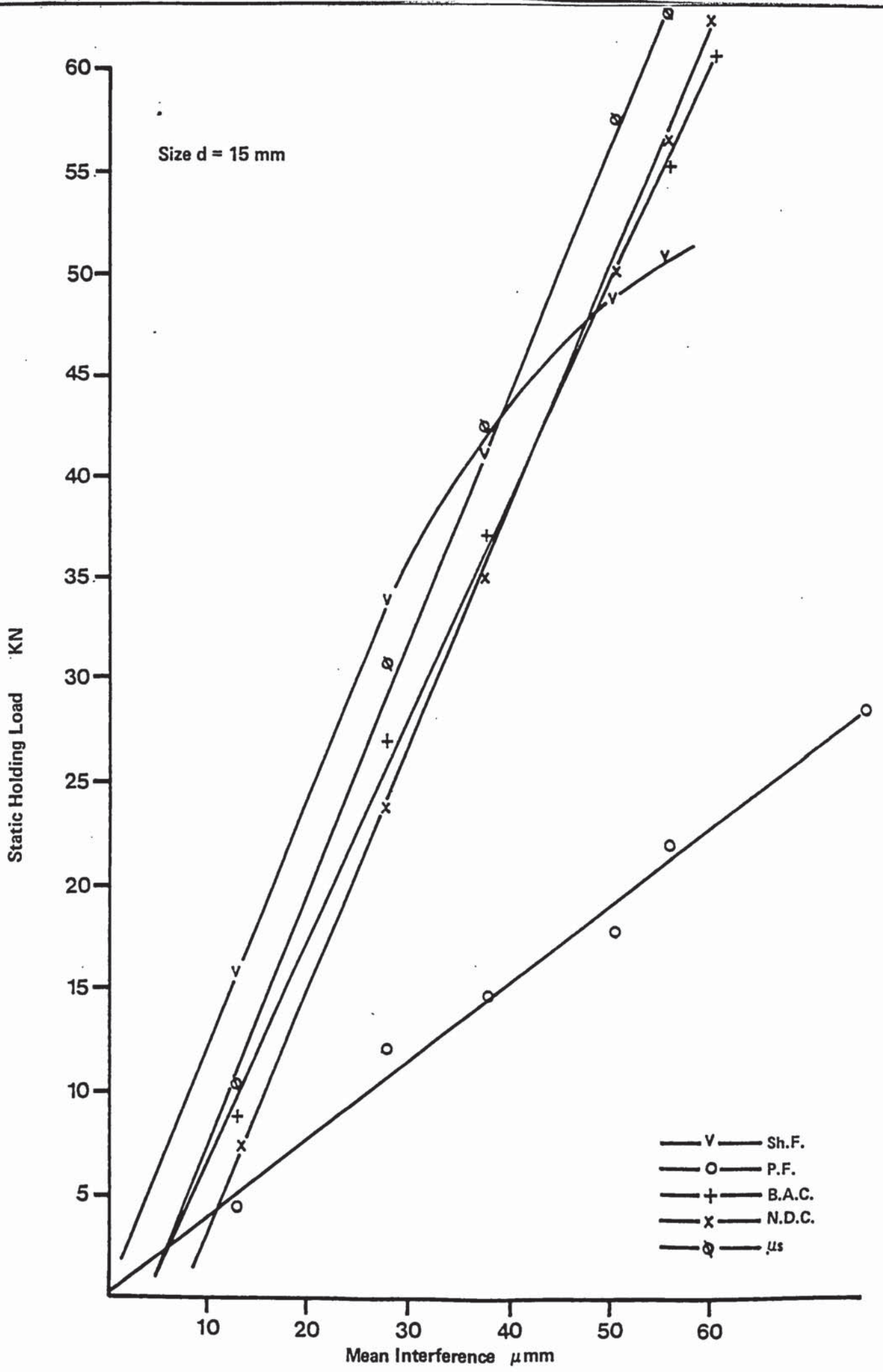

Fig 65 Experimental and theoretical Holding Load of ST32 joints

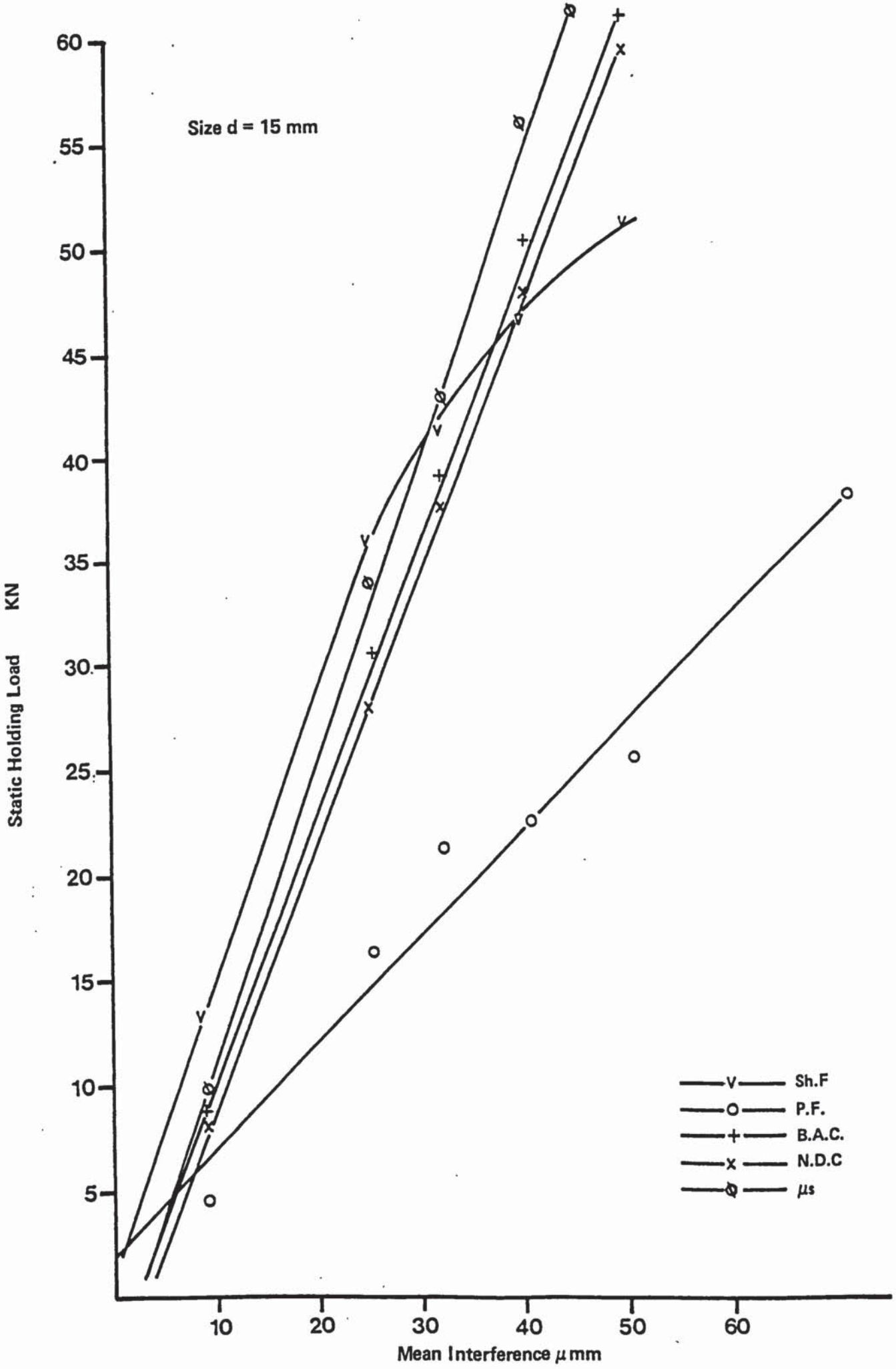

Fig 66 Experimental and theoretical Holding Load of ST41 joints

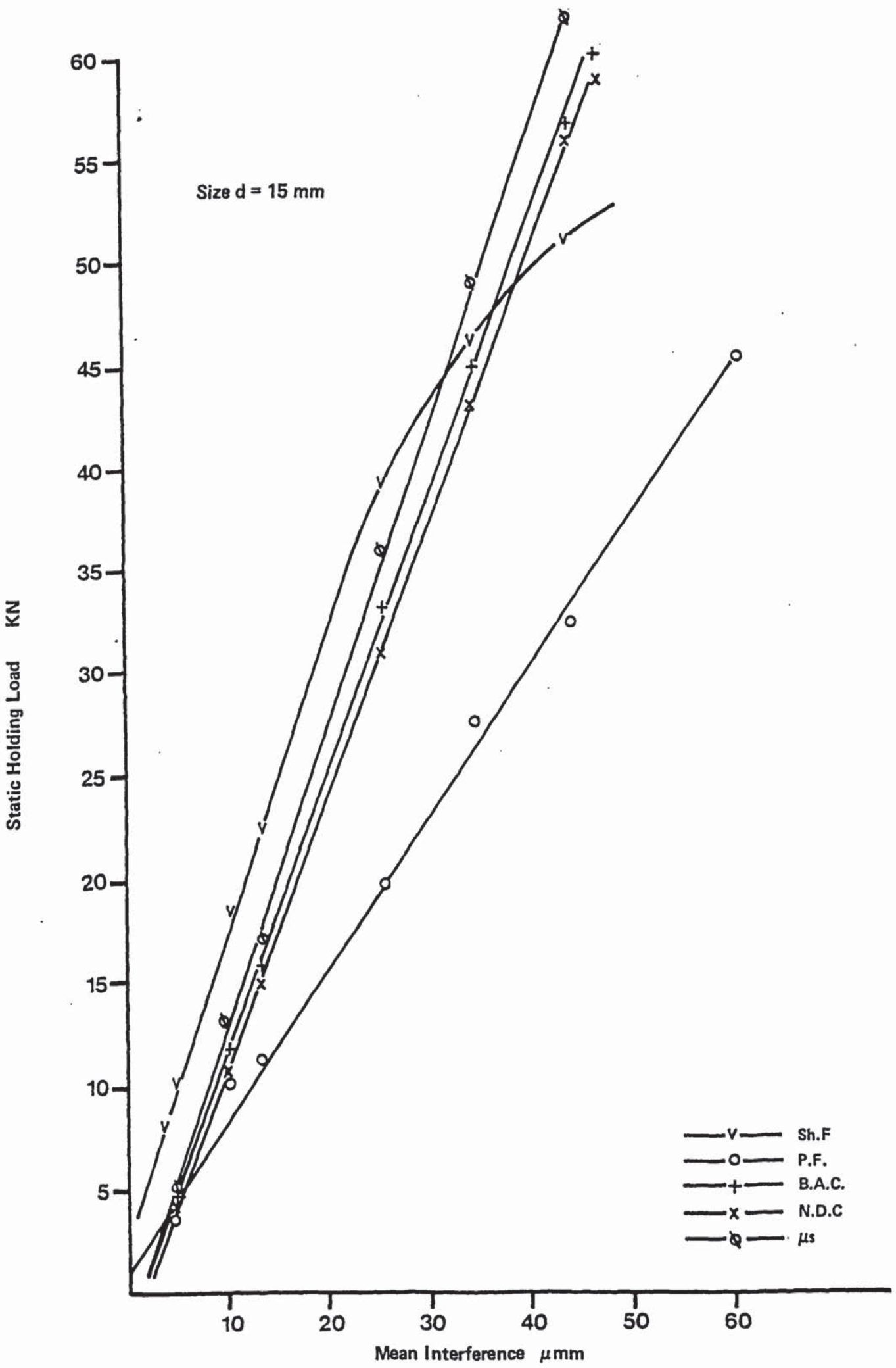

Fig 67 Experimental and theoretical Holding Load of ST42 joints

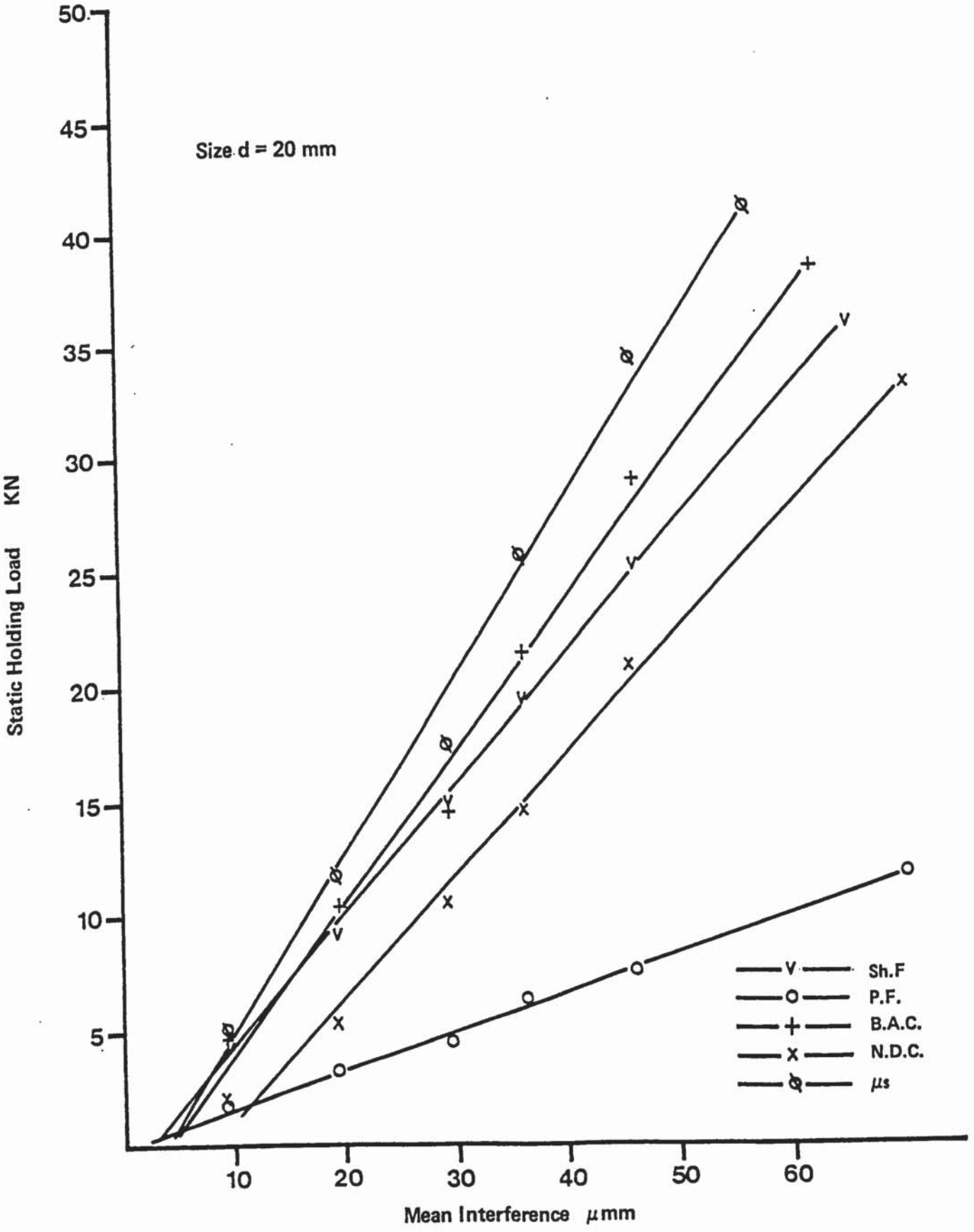

Fig 68 Experimental and theoretical Holding Load of ST51 joints

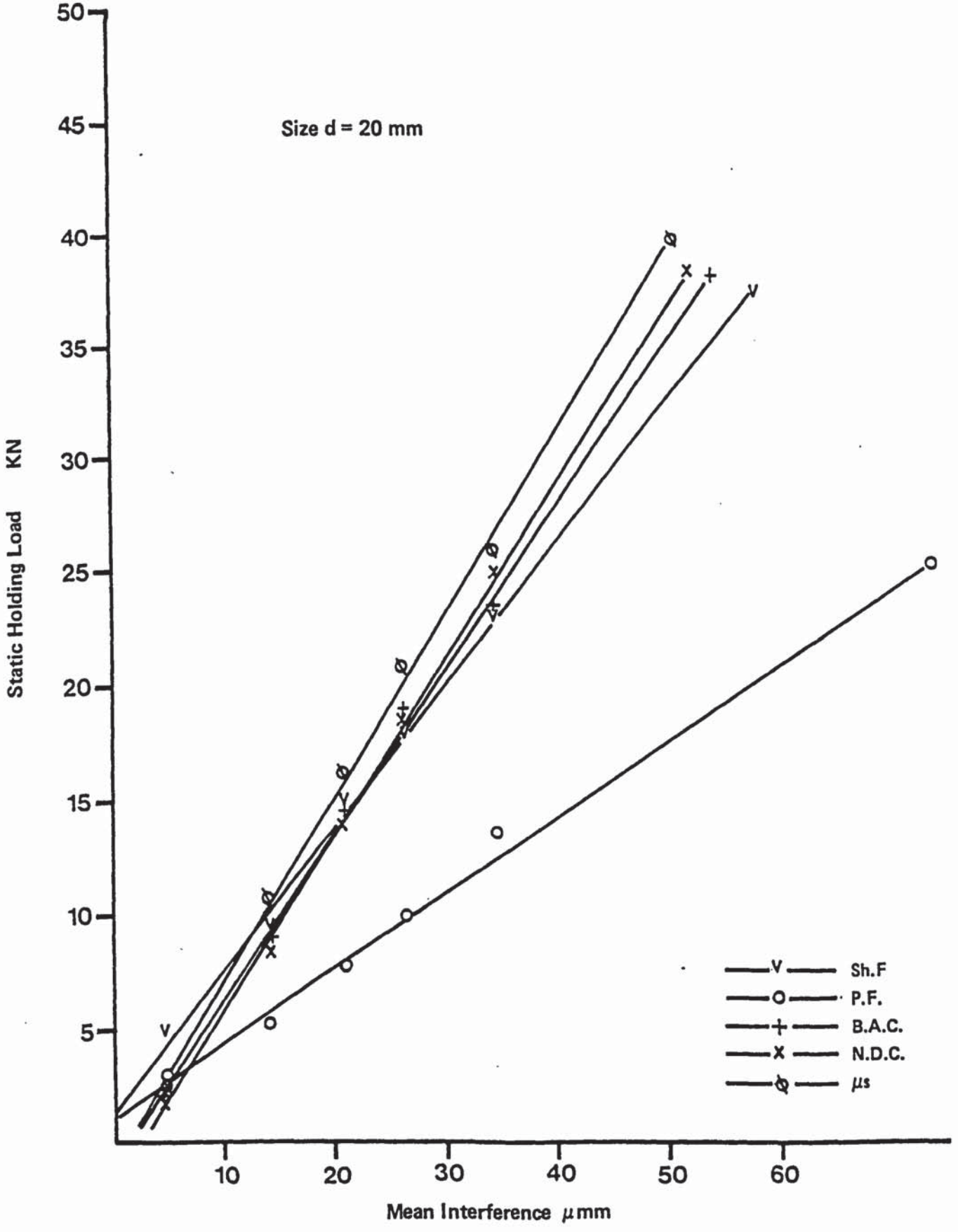

Fig 69 Experimental and theoretical Holding Load of ST52 joints

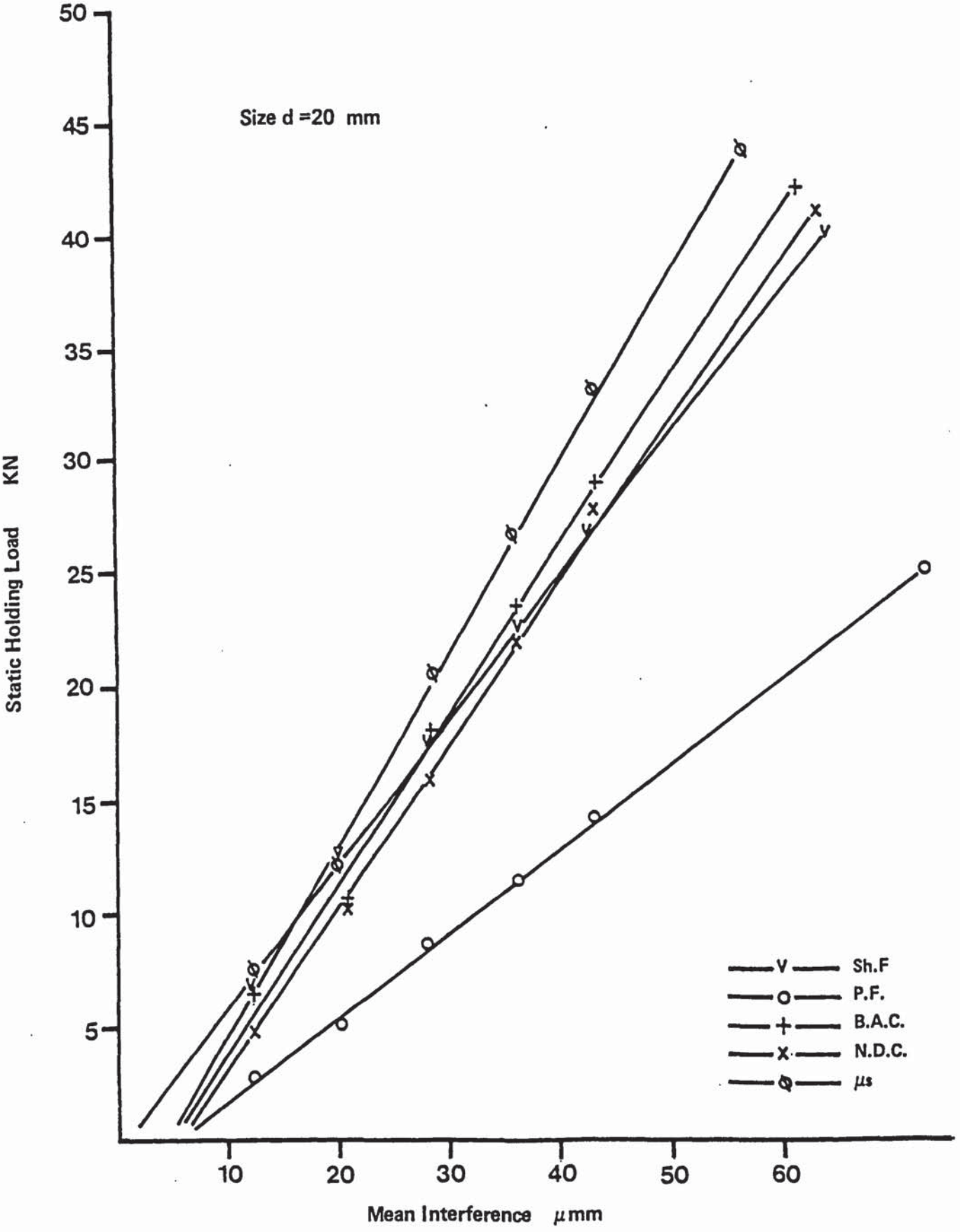

Fig 70 Experimental and theoretical Holding Load of ST61 joints

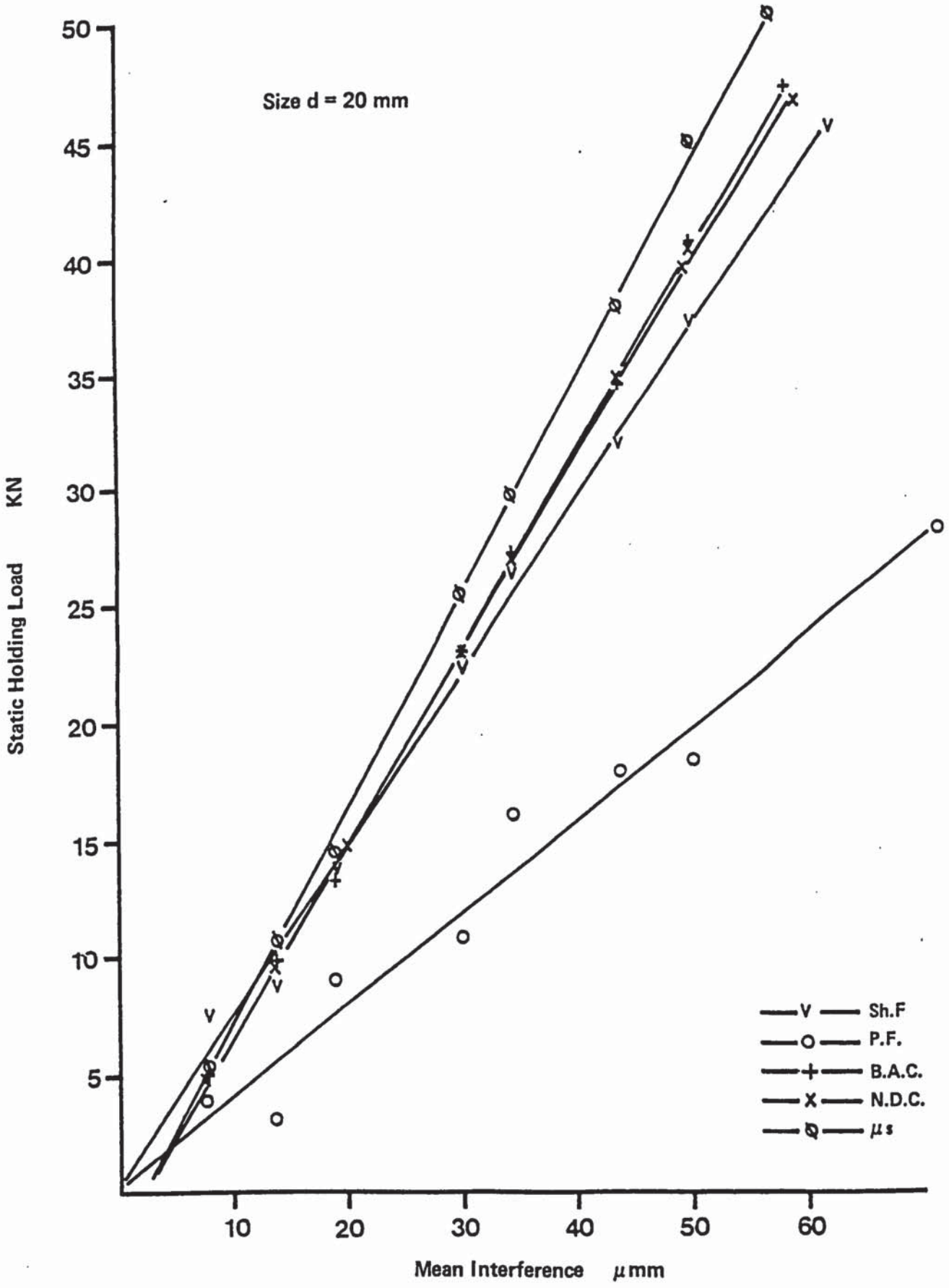

Fig 71 Experimental and theoretical Holding Load of ST62 joints

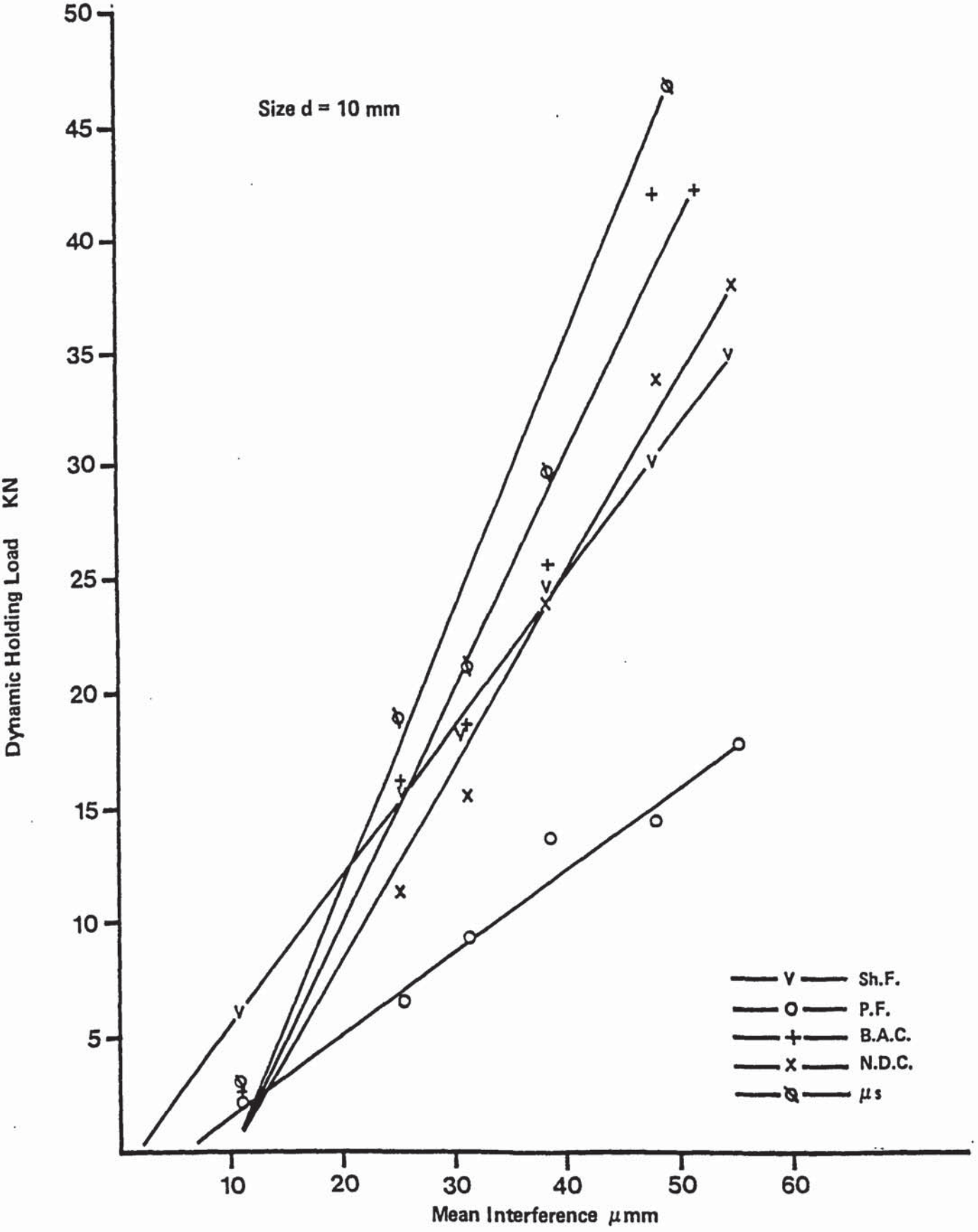

Fig 72 Experimental and theoretical Holding Load of D11 joints

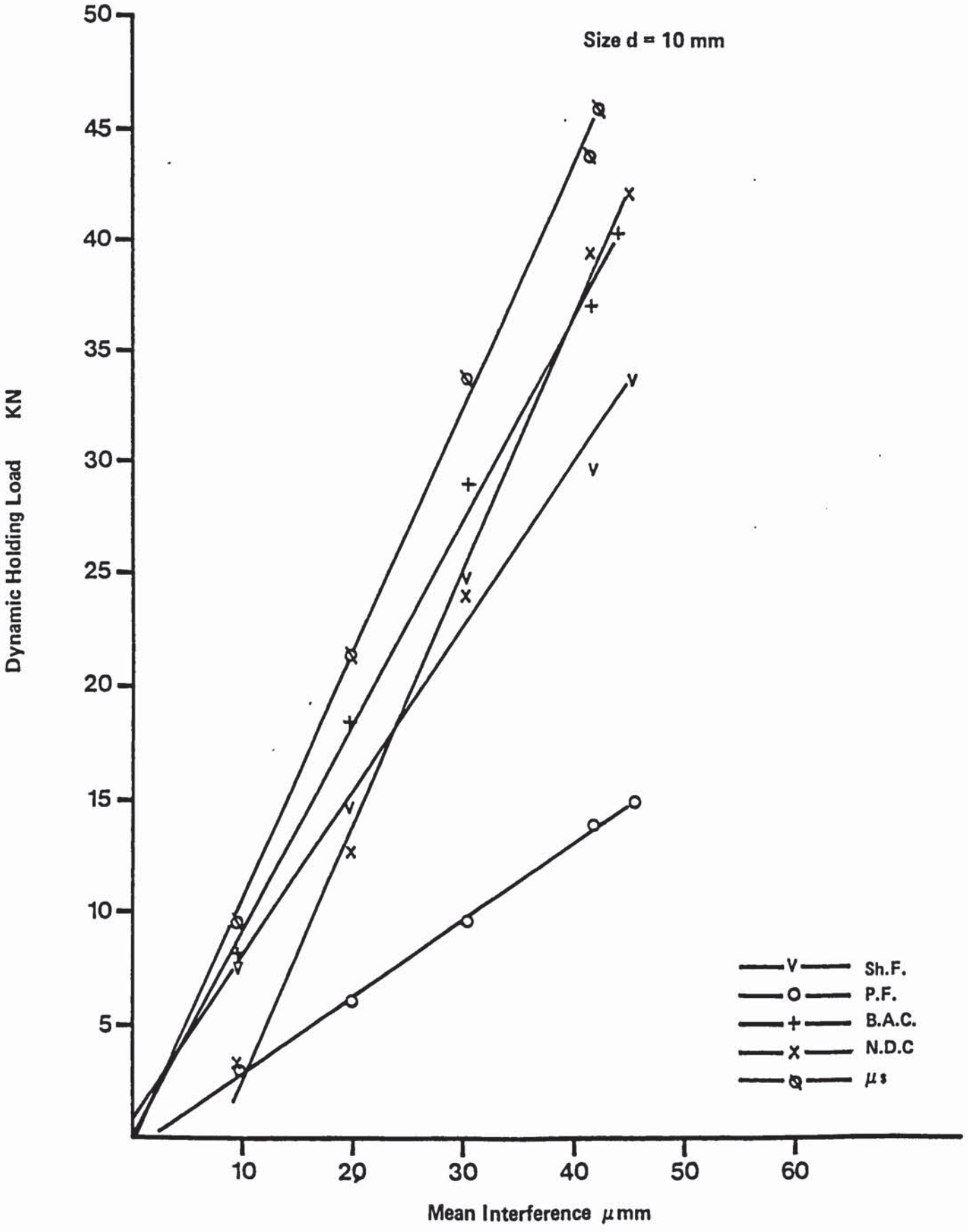

Fig 73 Experimental and theoretical Holding Load of D12 joints

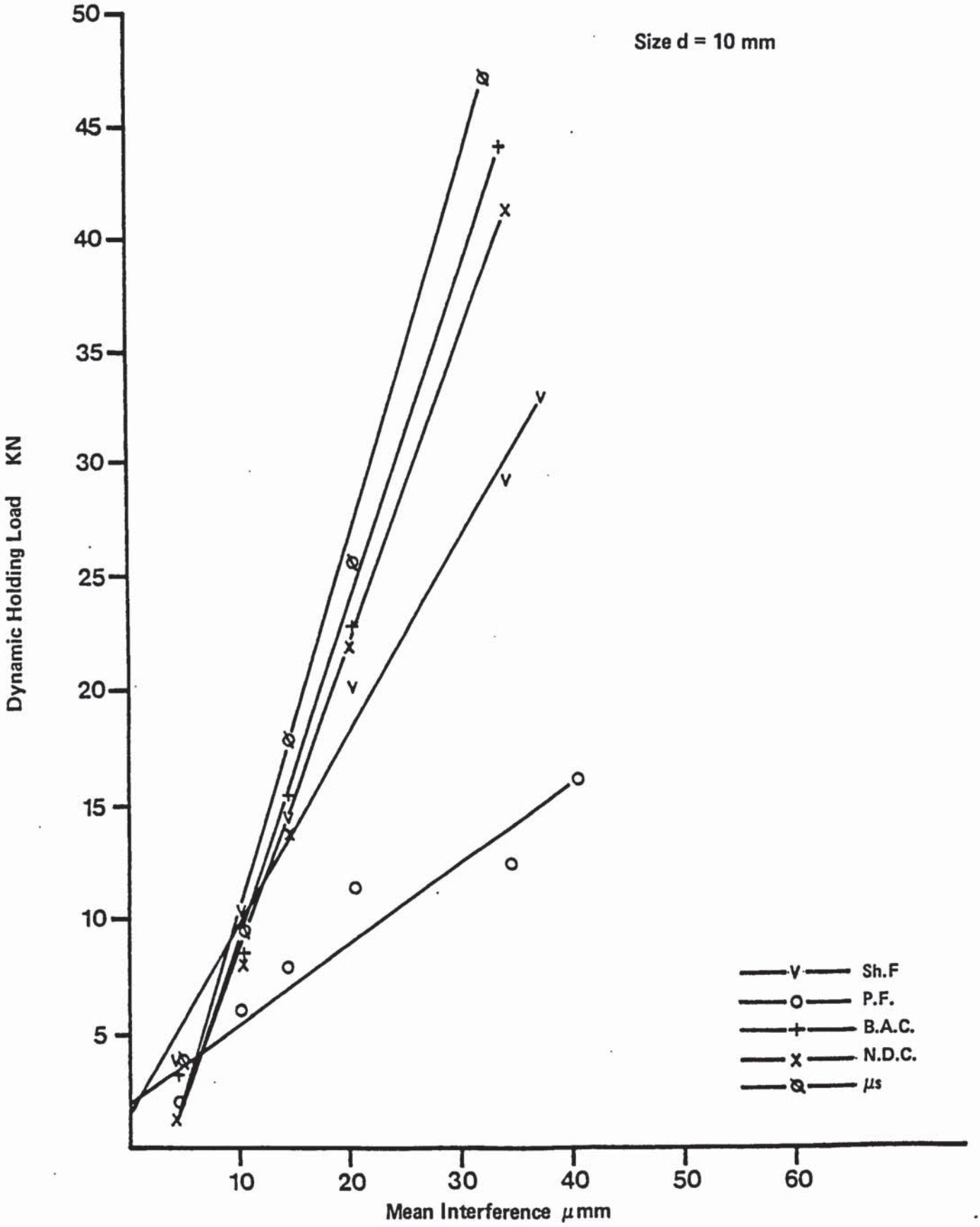

Fig 74 Experimental and theoretical Holding Load of D21 joints

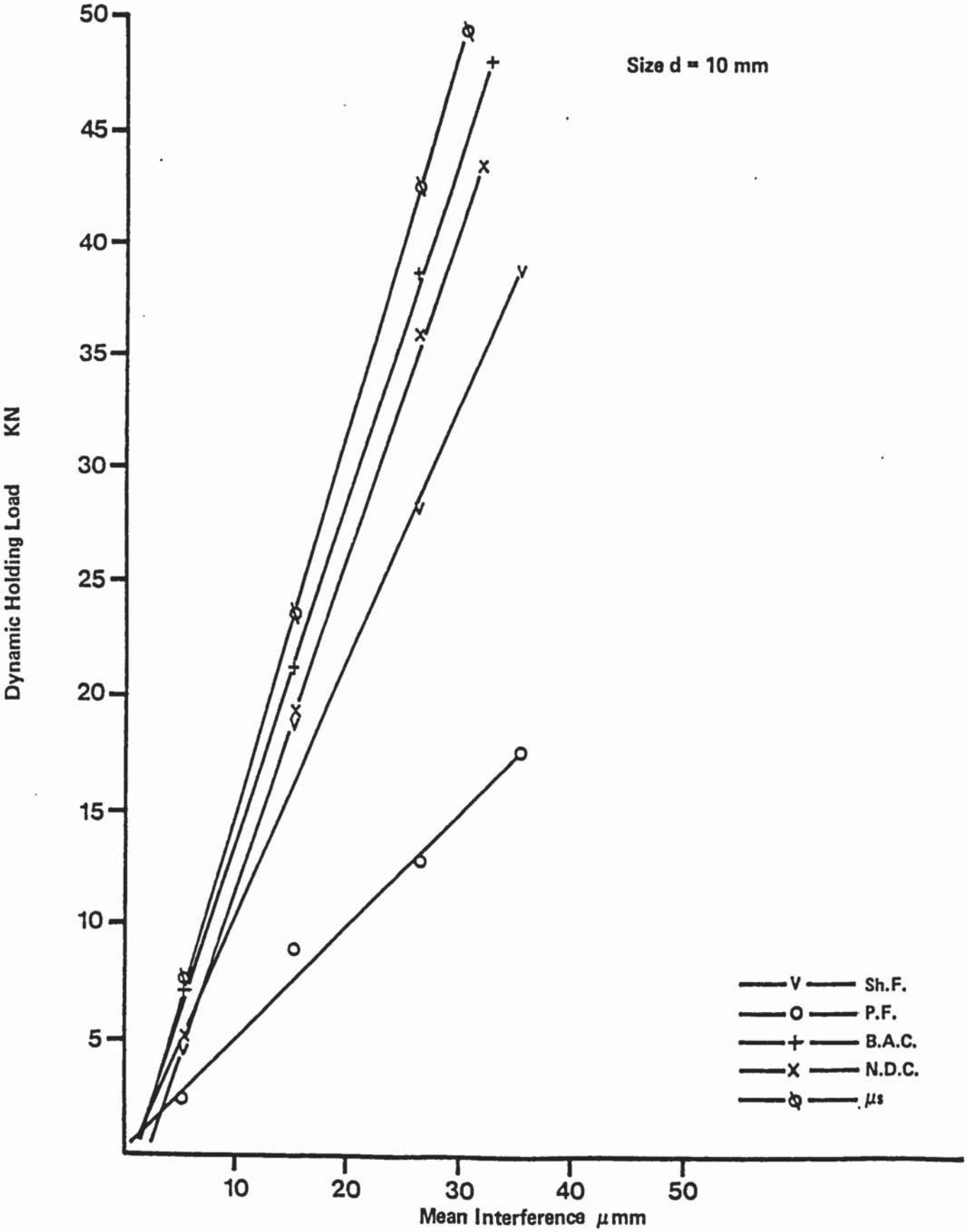

Fig 75 Experimental and theoretical Holding Load of D22 joints

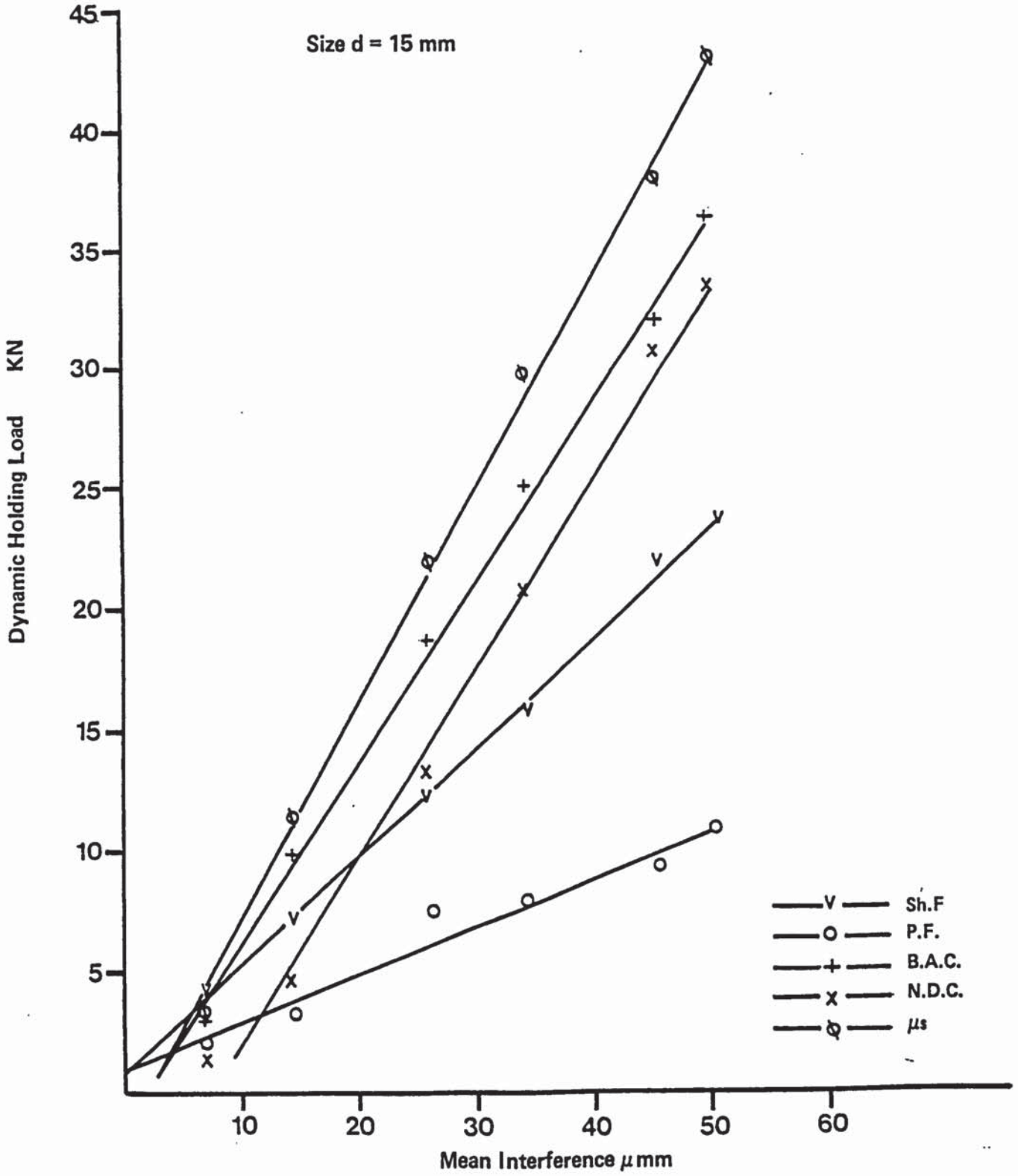

Fig 76 Experimental and theoretical Holding Load of D31 joints

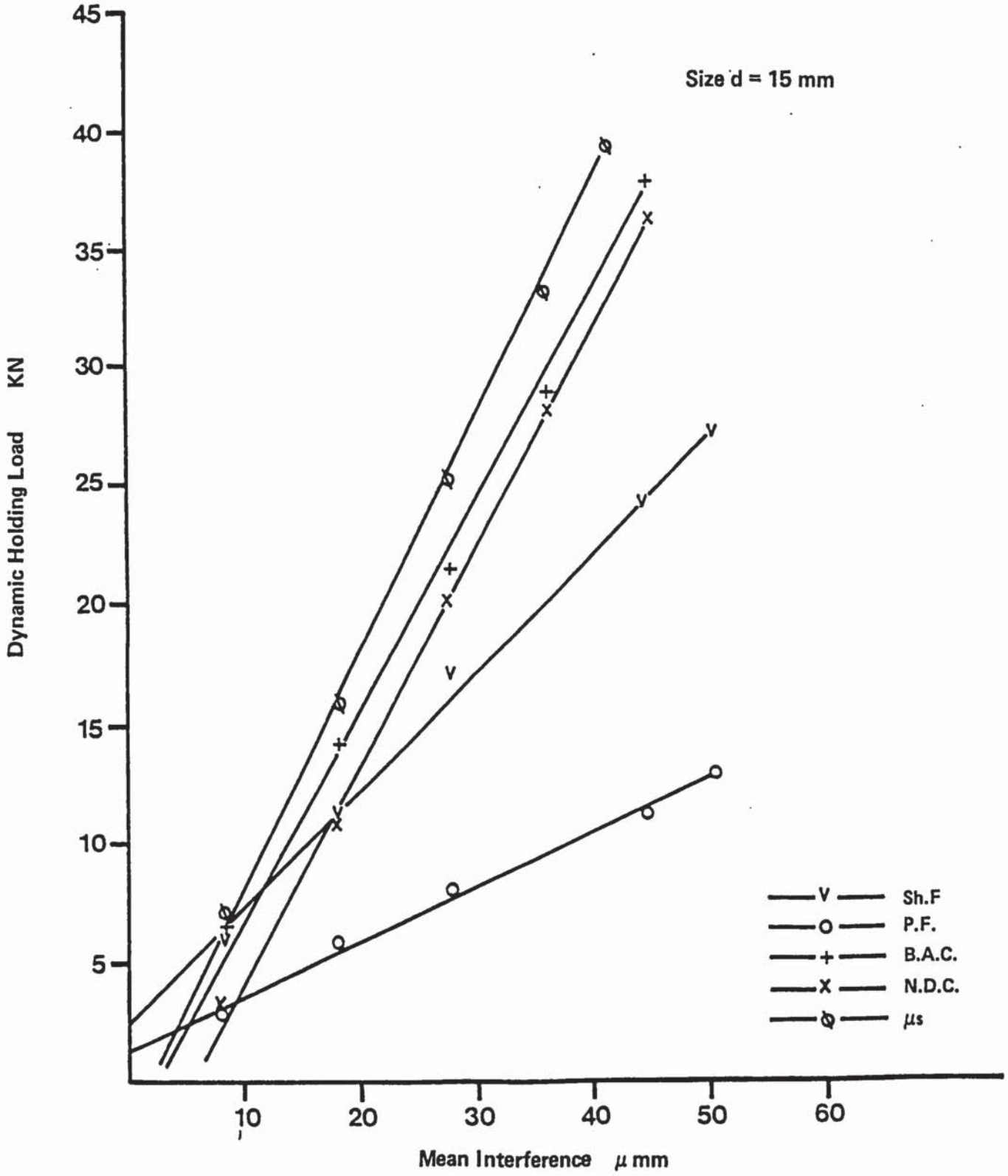

Fig 77 Experimental and theoretical Holding Load of D32 joints

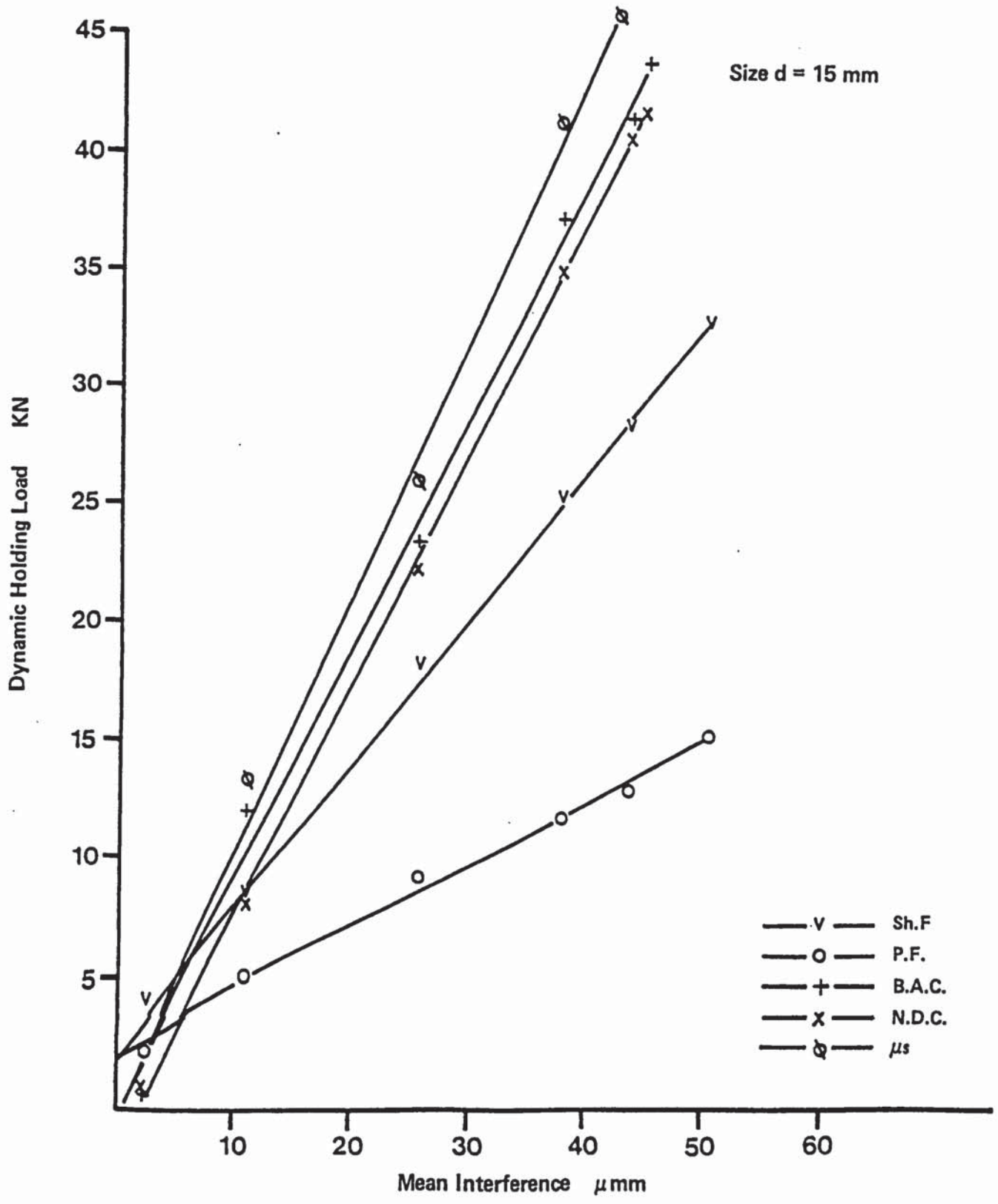

Fig 78 Experimental and theoretical Holding Load of D41 joints

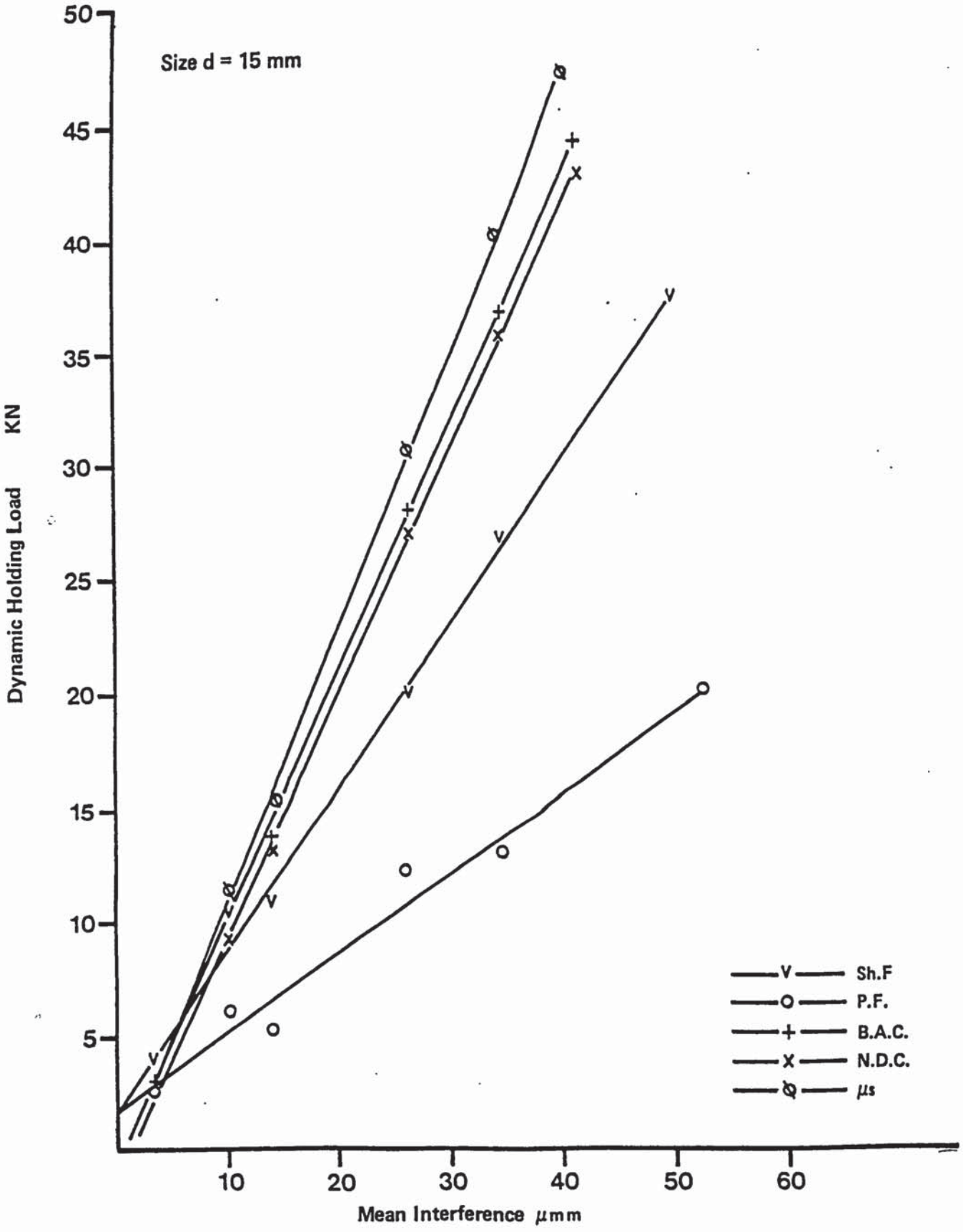

Fig 79 Experimental and theoretical Holding Load of D42 joints

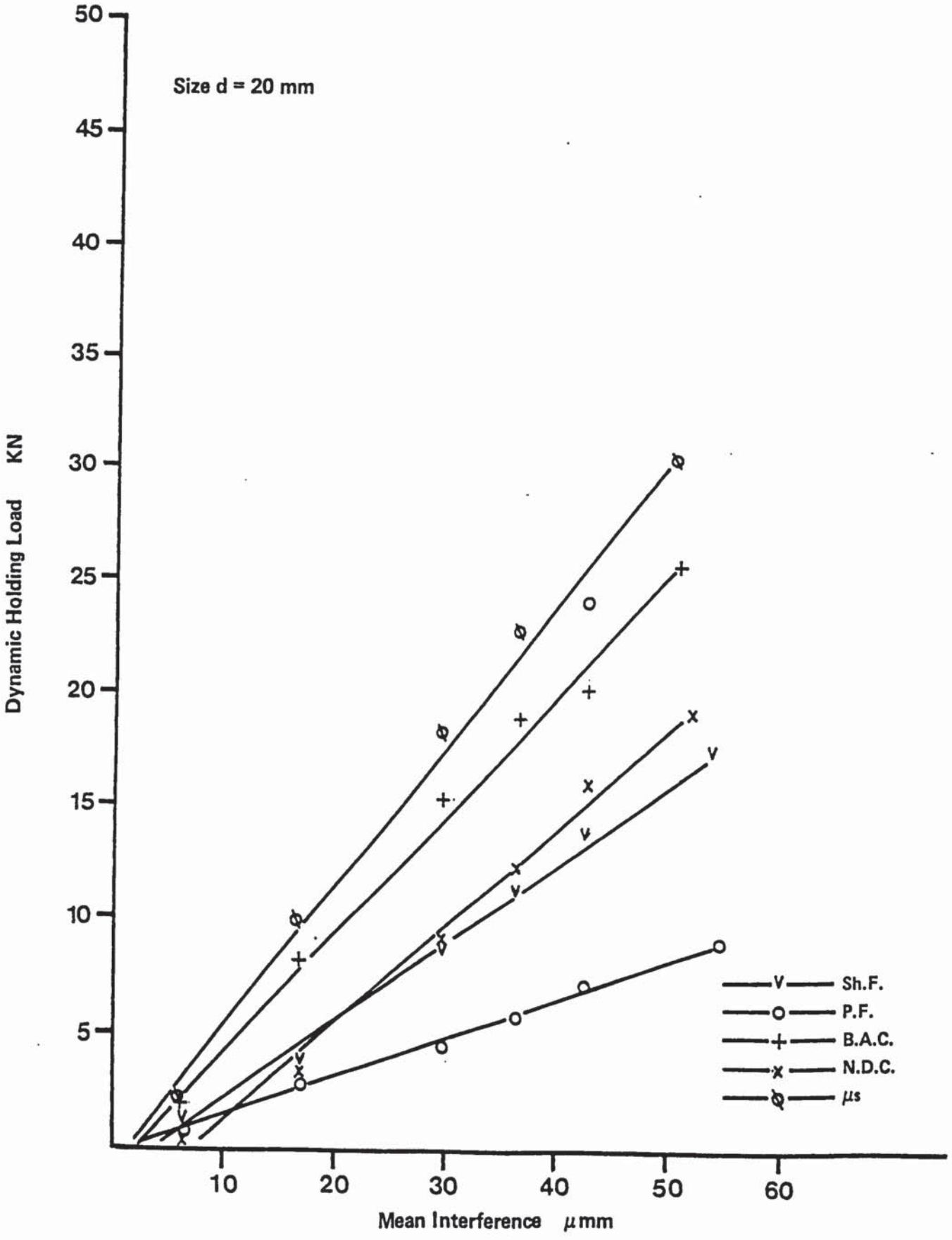

Fig 80 Experimental and theoretical Holding Load of D51 joints

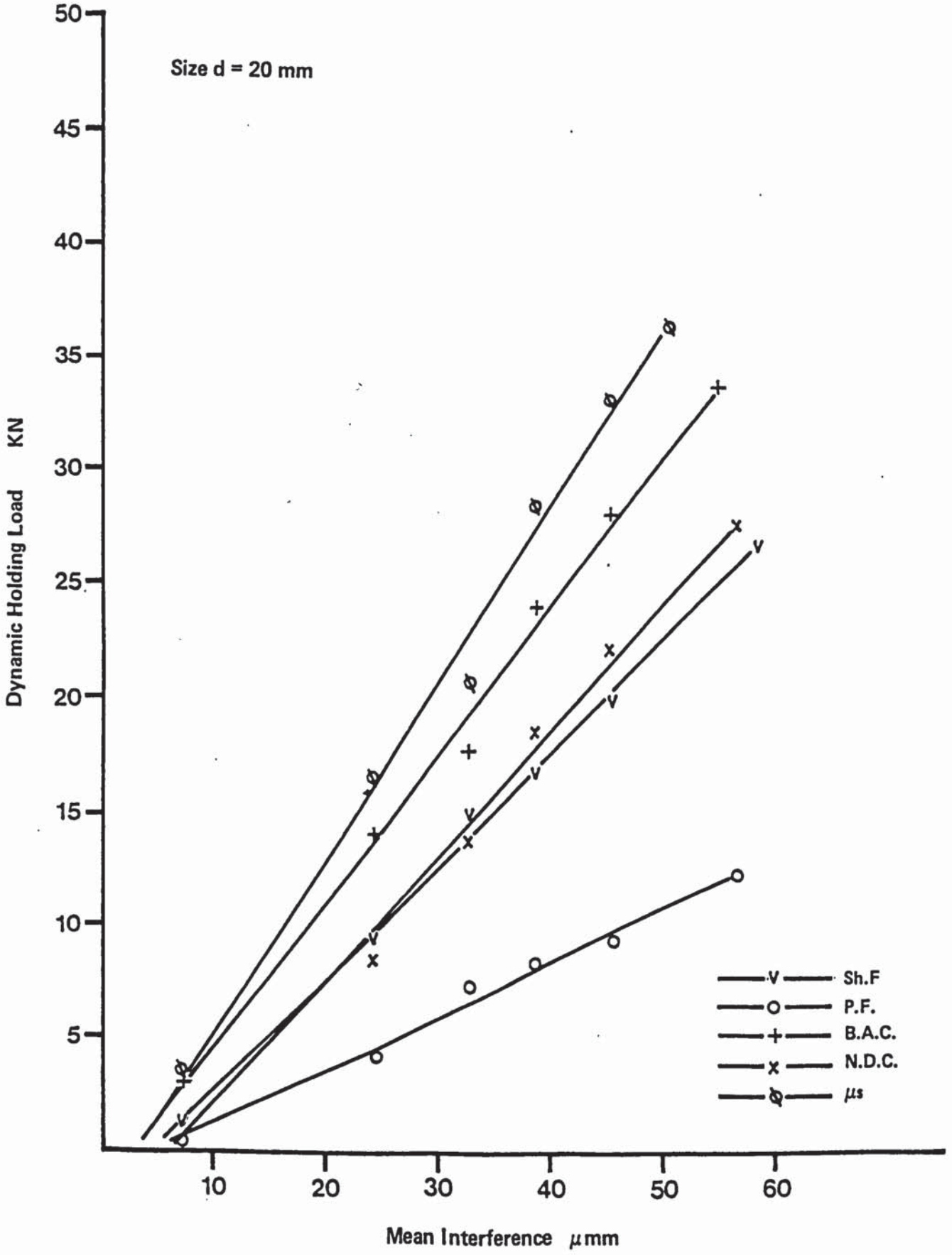

Fig 81 Experimental and theoretical Holding Load of D52 joints

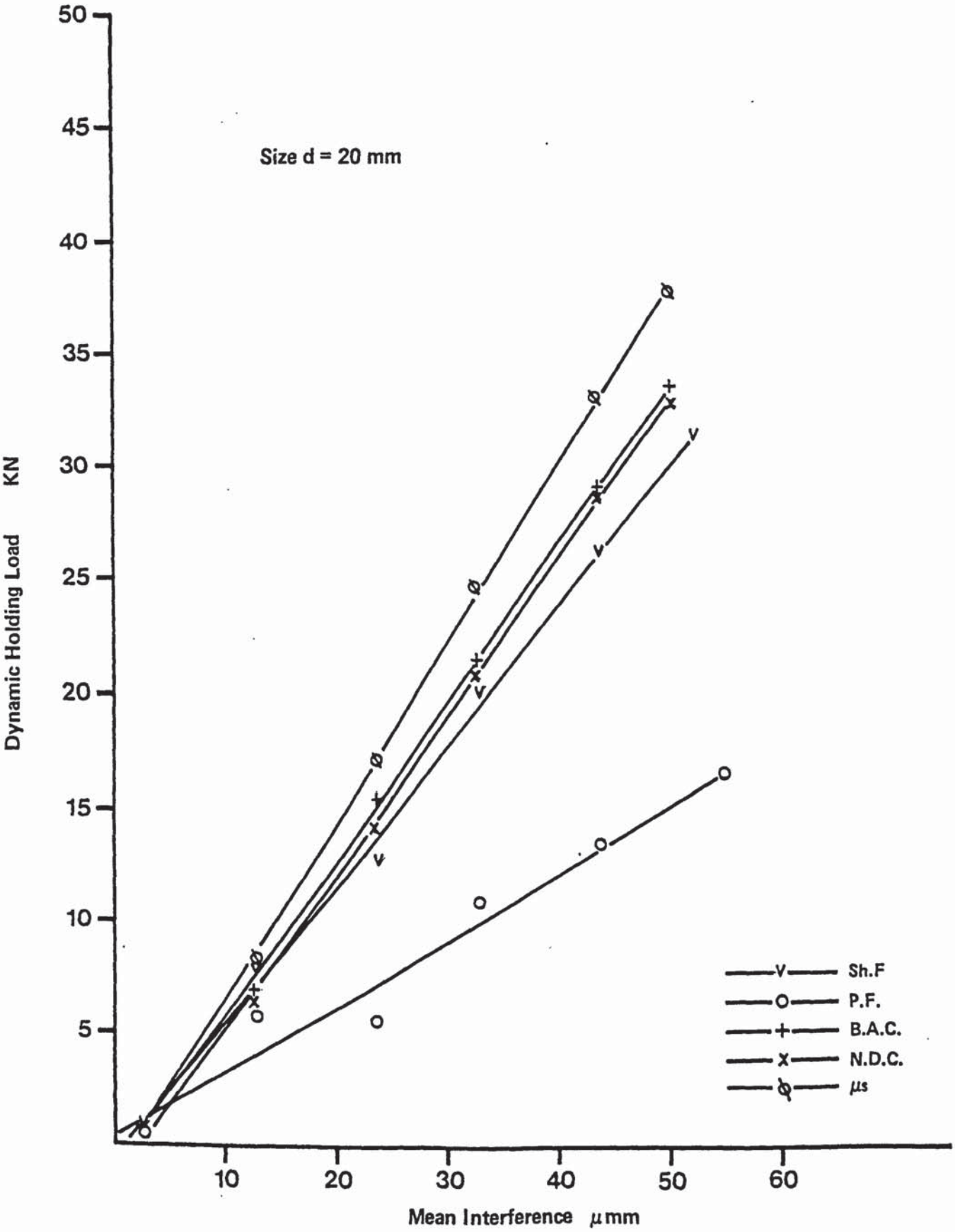

Fig 82 Experimental and theoretical Holding Load of D61 joints

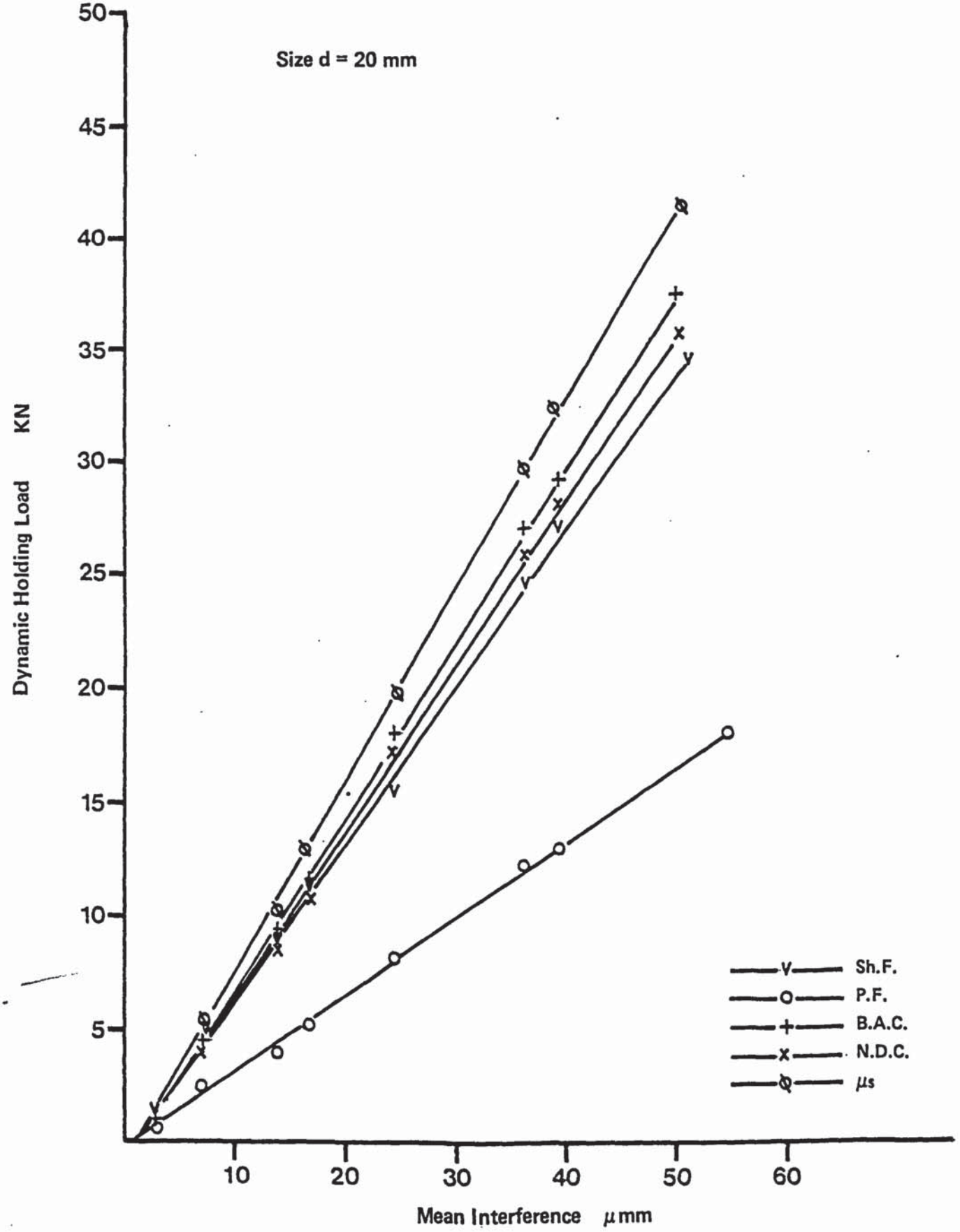

Fig 83 Experimental and theoretical Holding Load of D62 joints

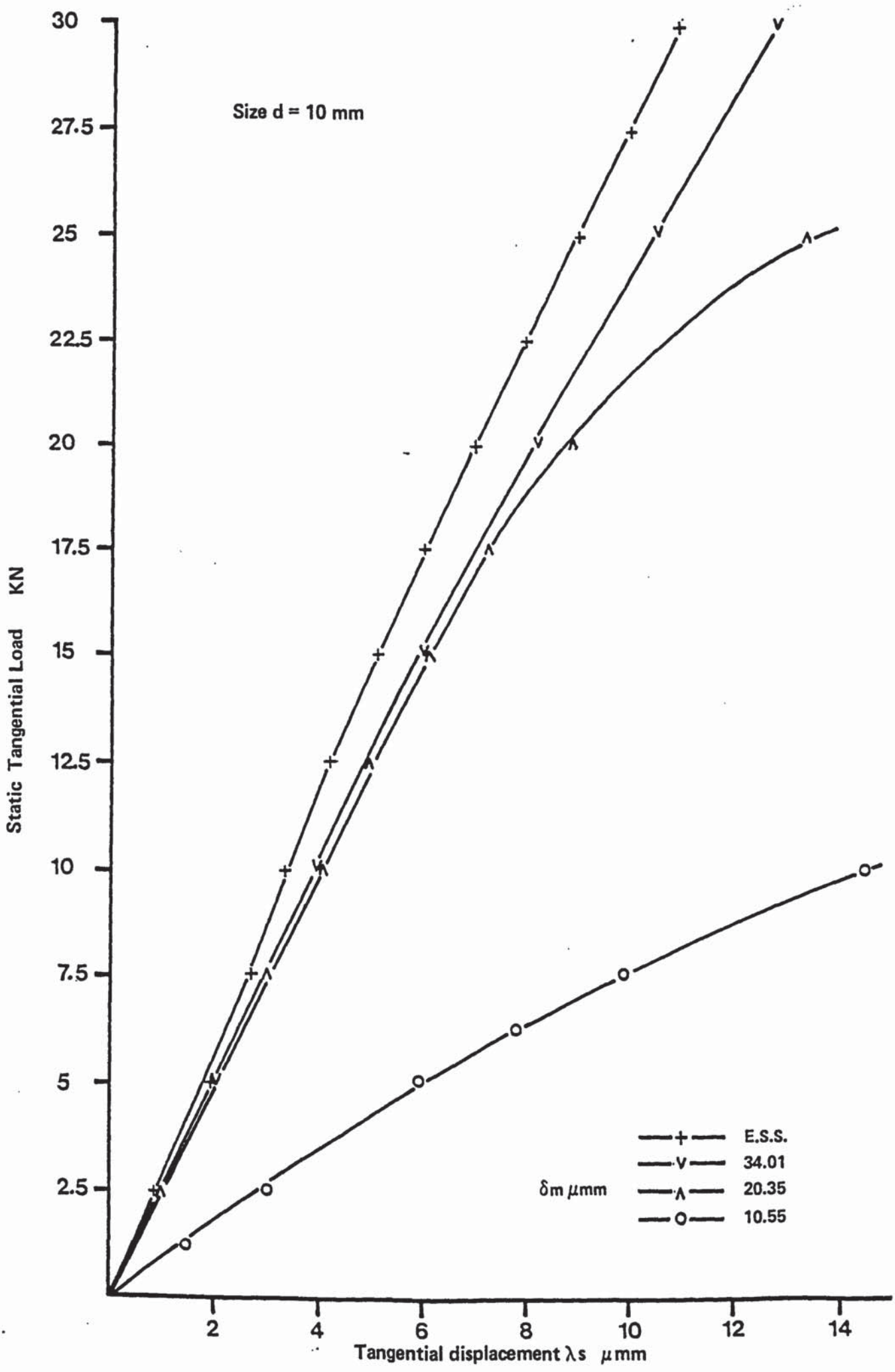

Fig 84 Effect of the interference value on λs of ST11 joints

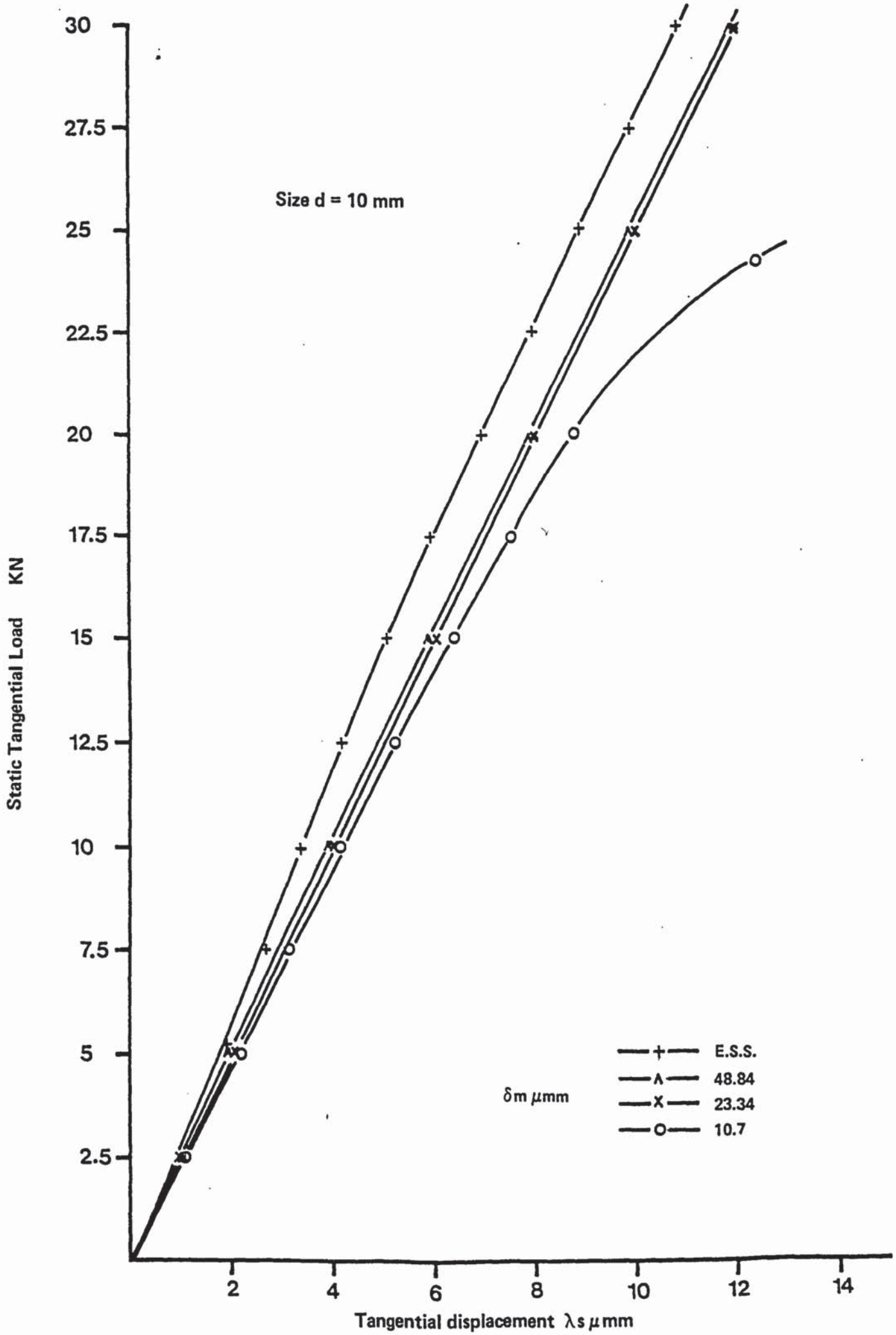

Fig 85 Effect of the interference value on λs of ST22 joints

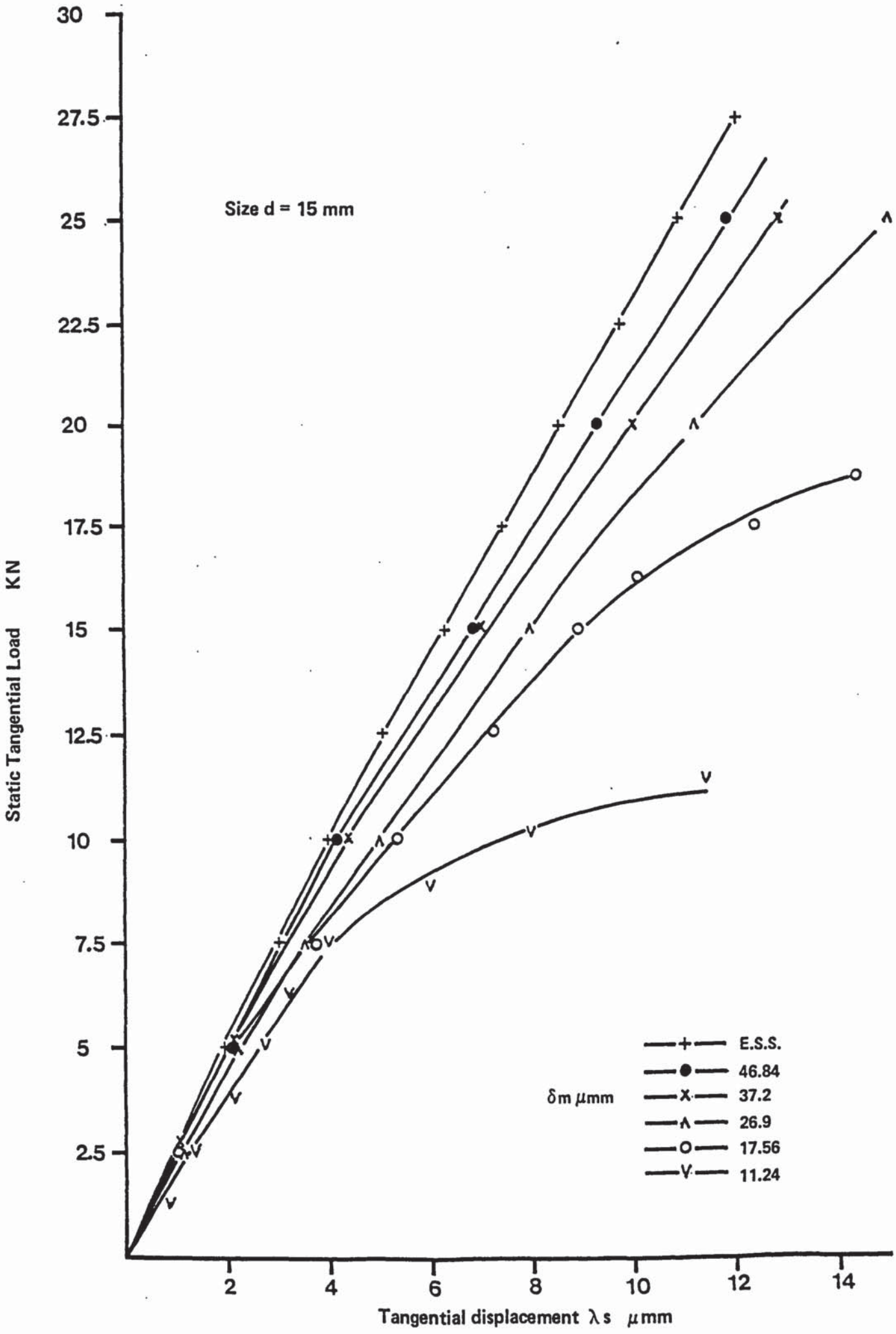

Fig 86 Effect of the interference value on λs of ST31 joints

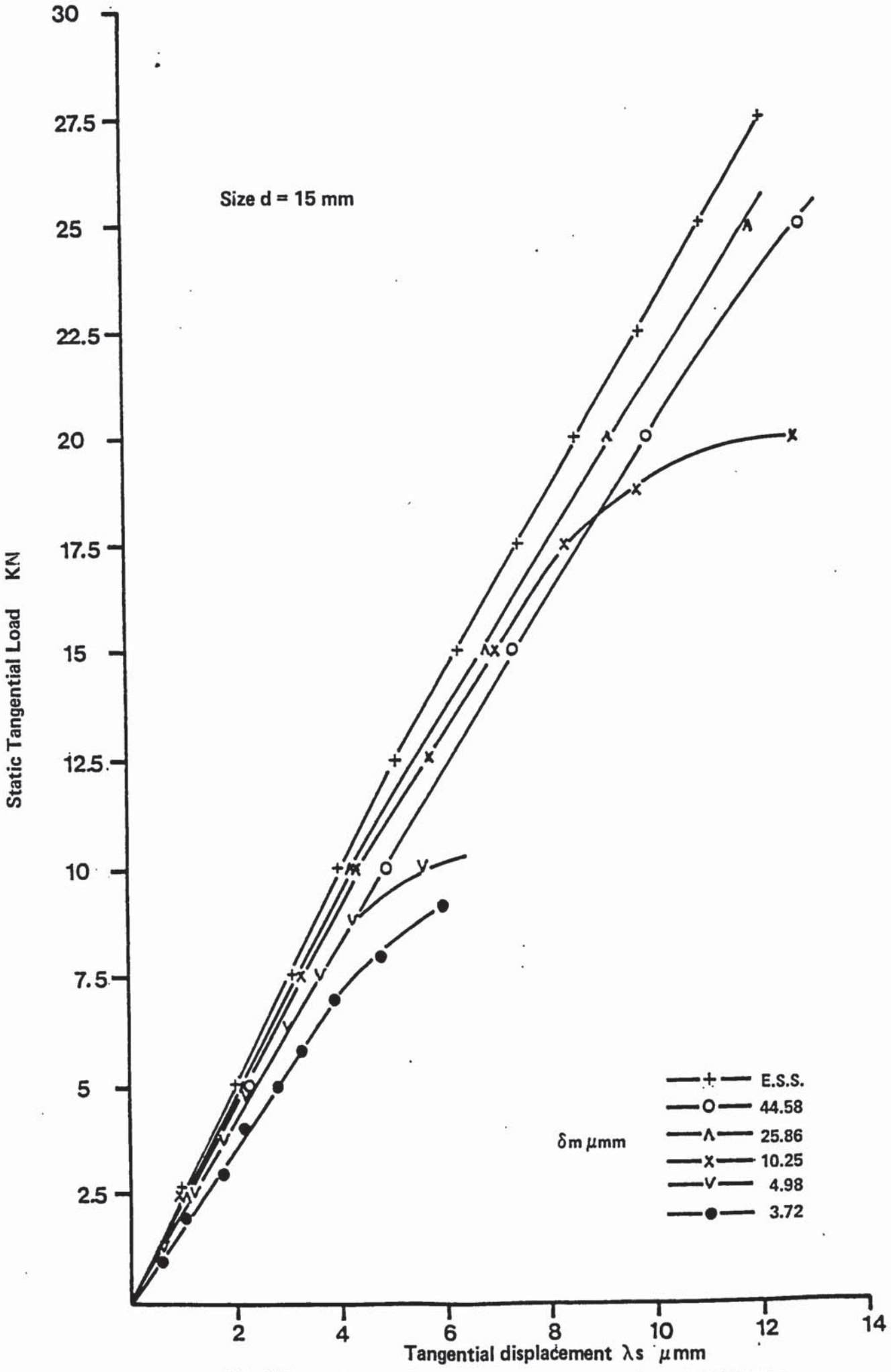

Fig 87 Effect of the interference value on λs of ST42 joints

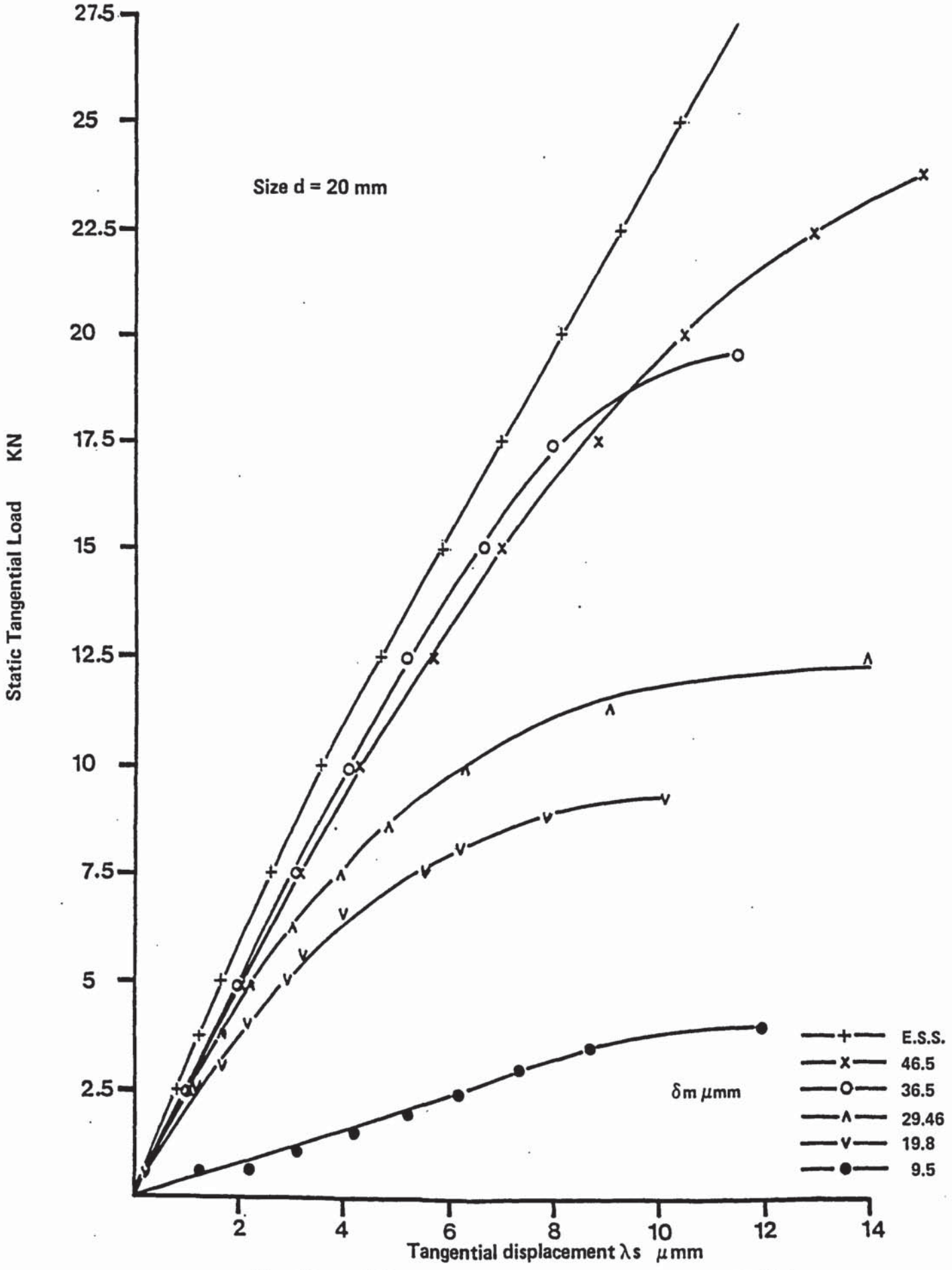

Fig 88 Effect of the interference value on λs of ST51 joints

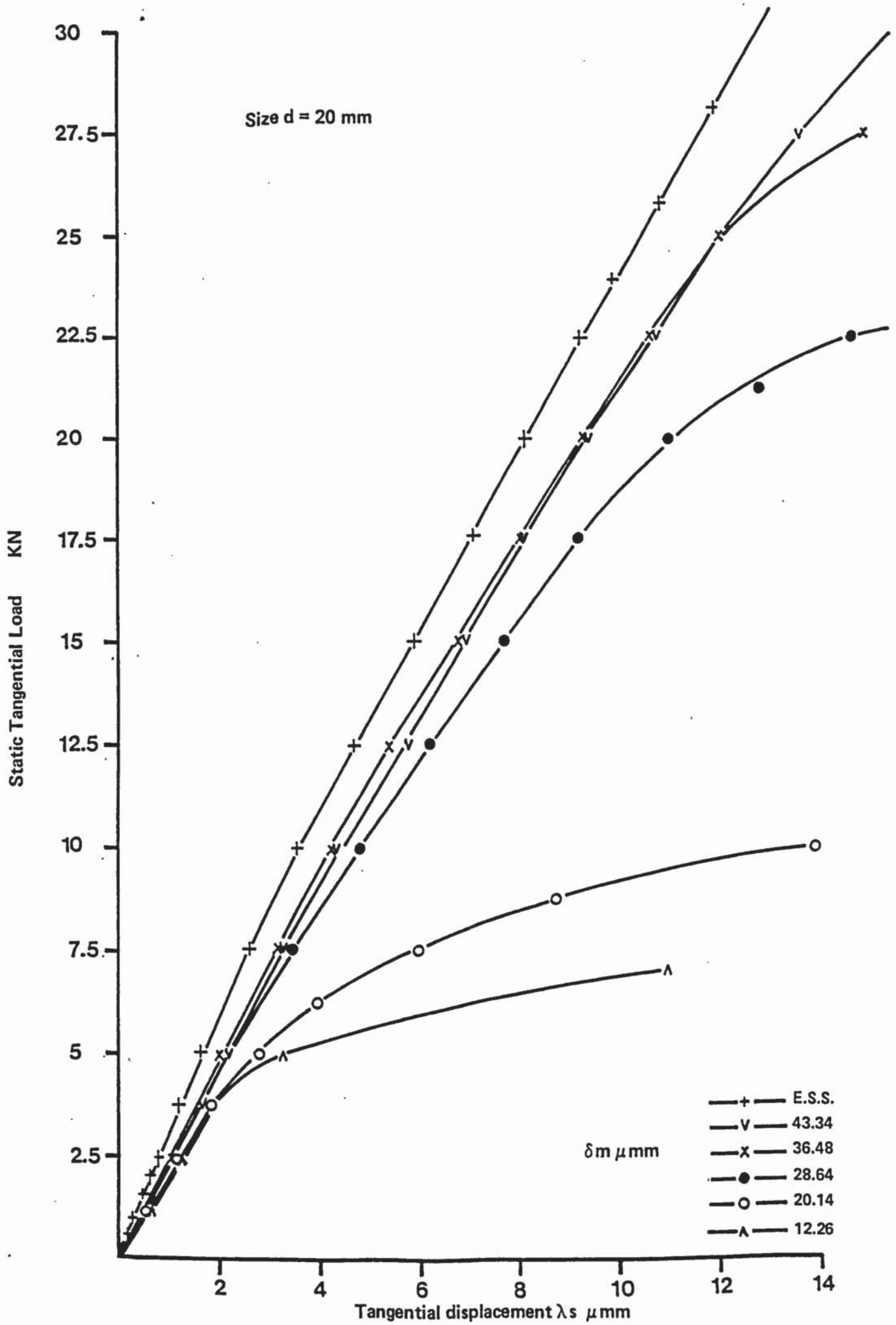

Fig 89 Effect of the interference value on λs of ST52 joints

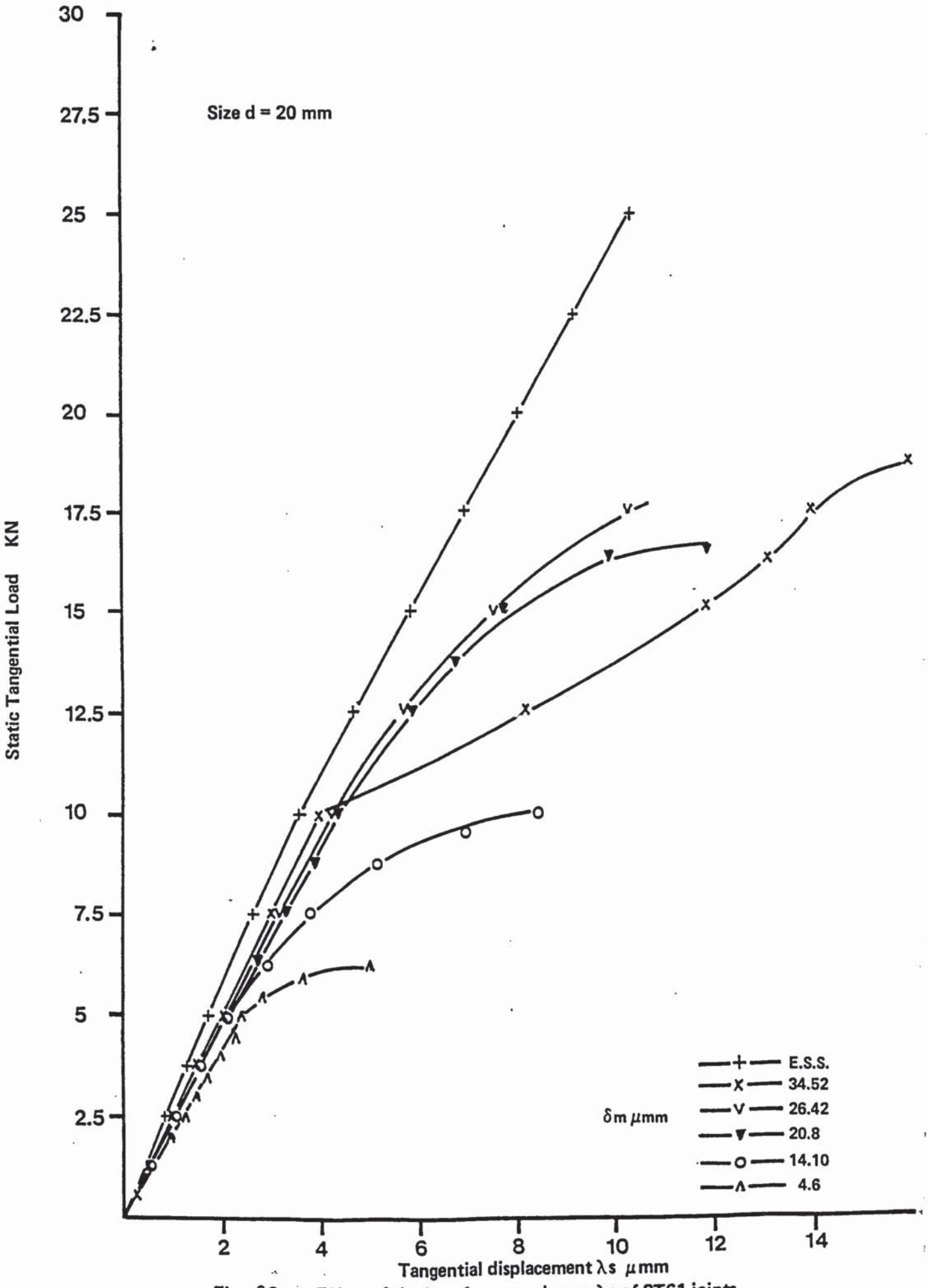

Fig 90 Effect of the interference value on λs of ST61 joints

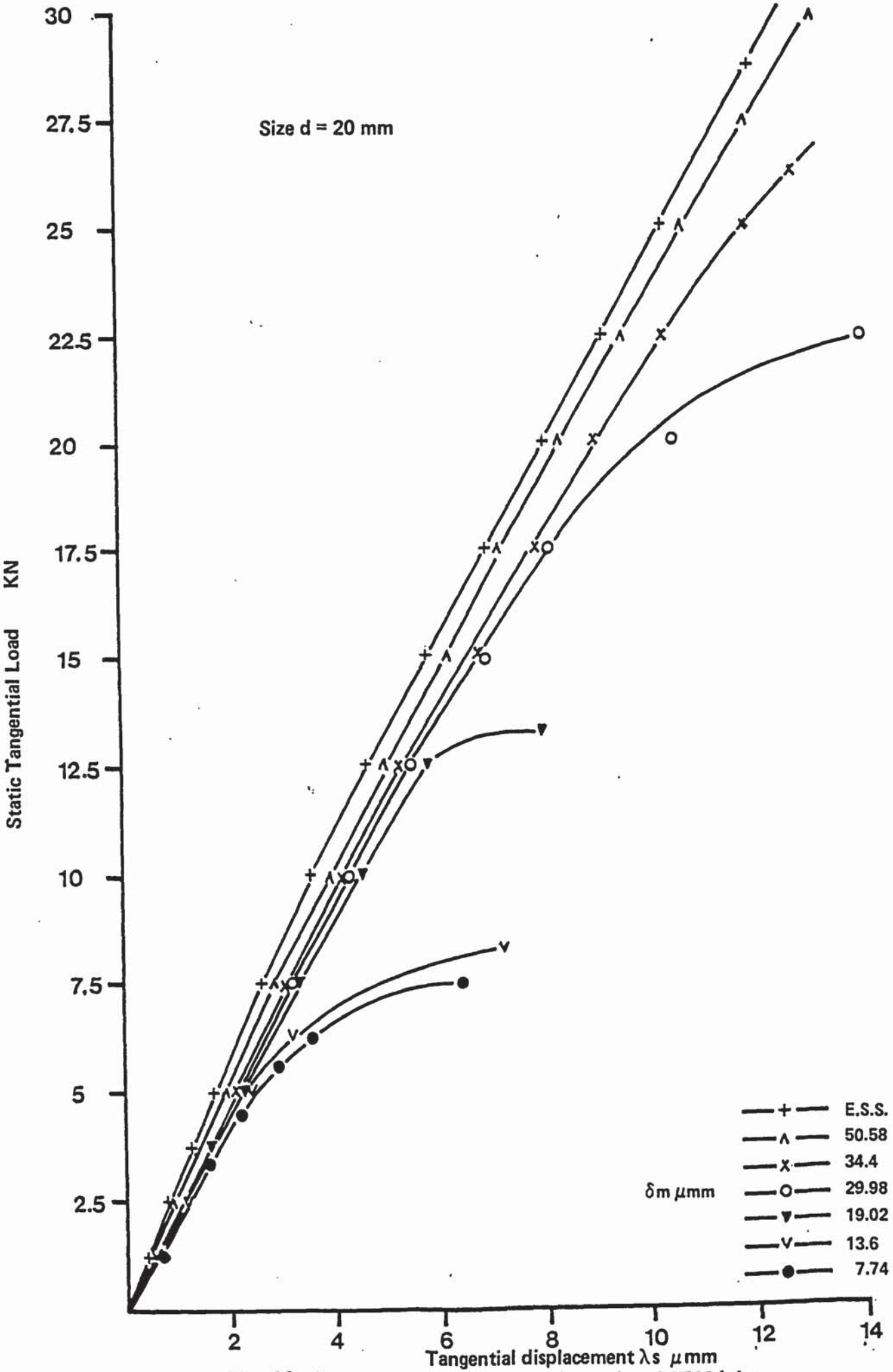

Fig 91 Effect of the interference value on λs of ST62 joints

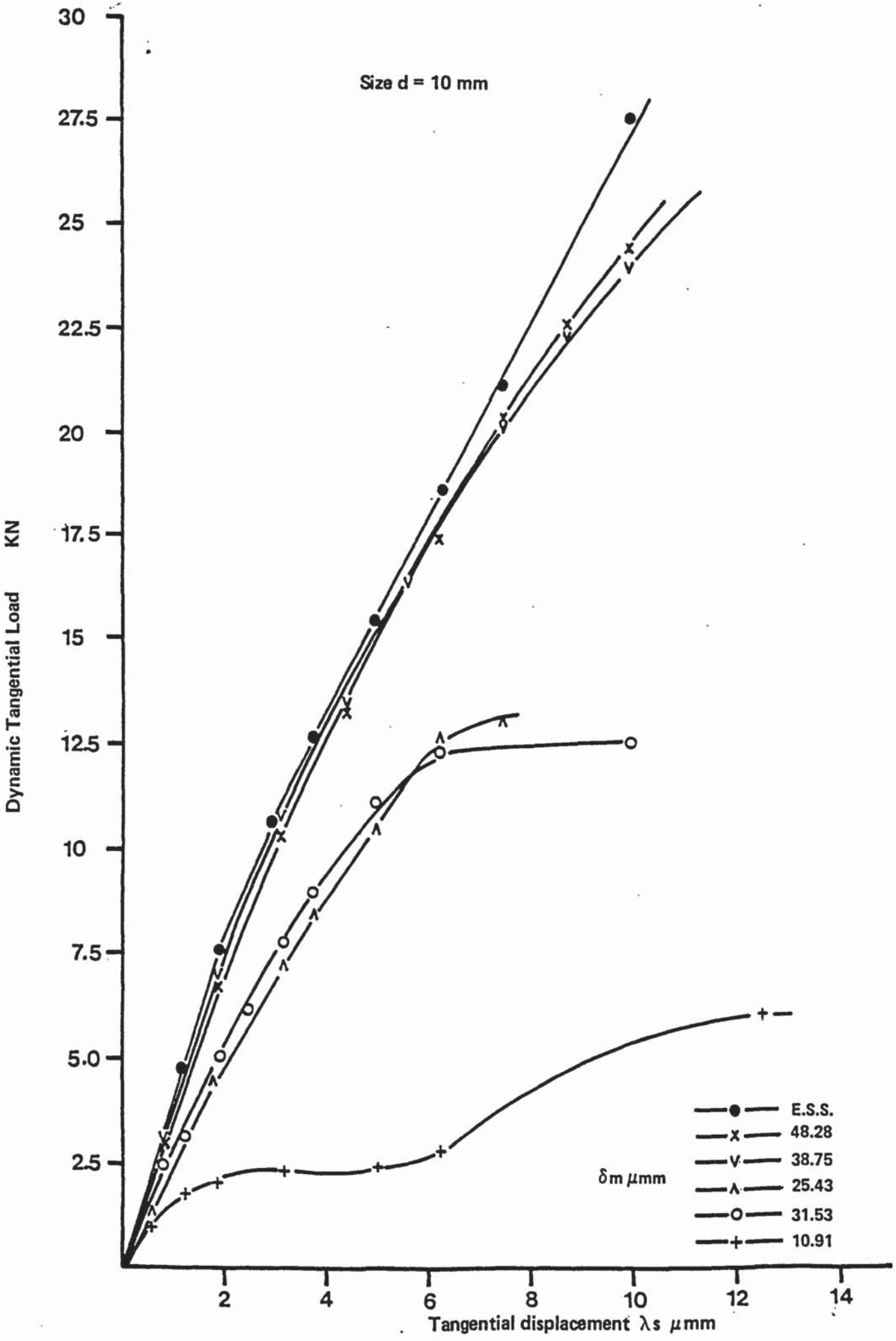

Fig 92 Effect of the interference value on λs of D11 joints

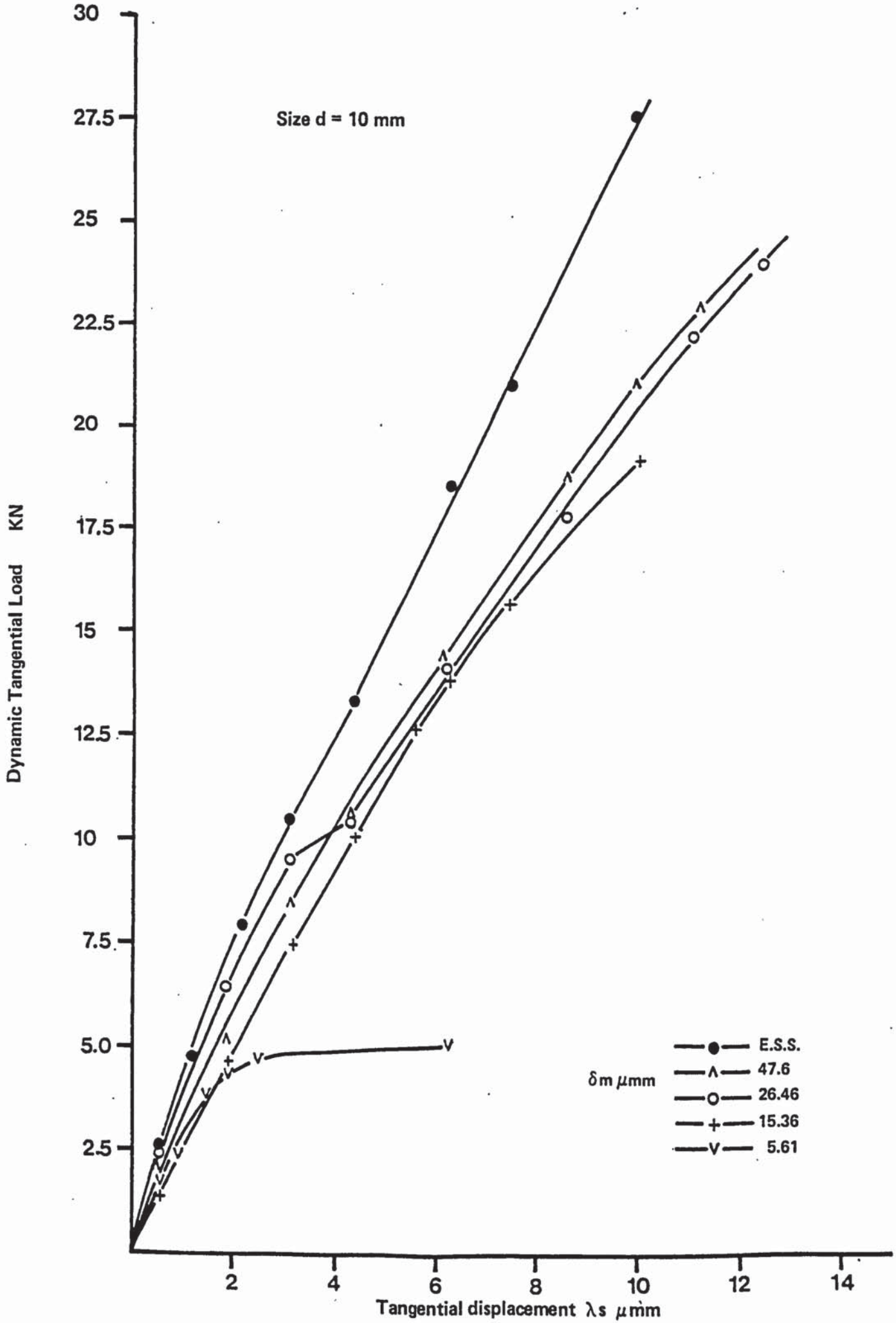

Fig 93 Effect of the interference value on λs of D22 joints

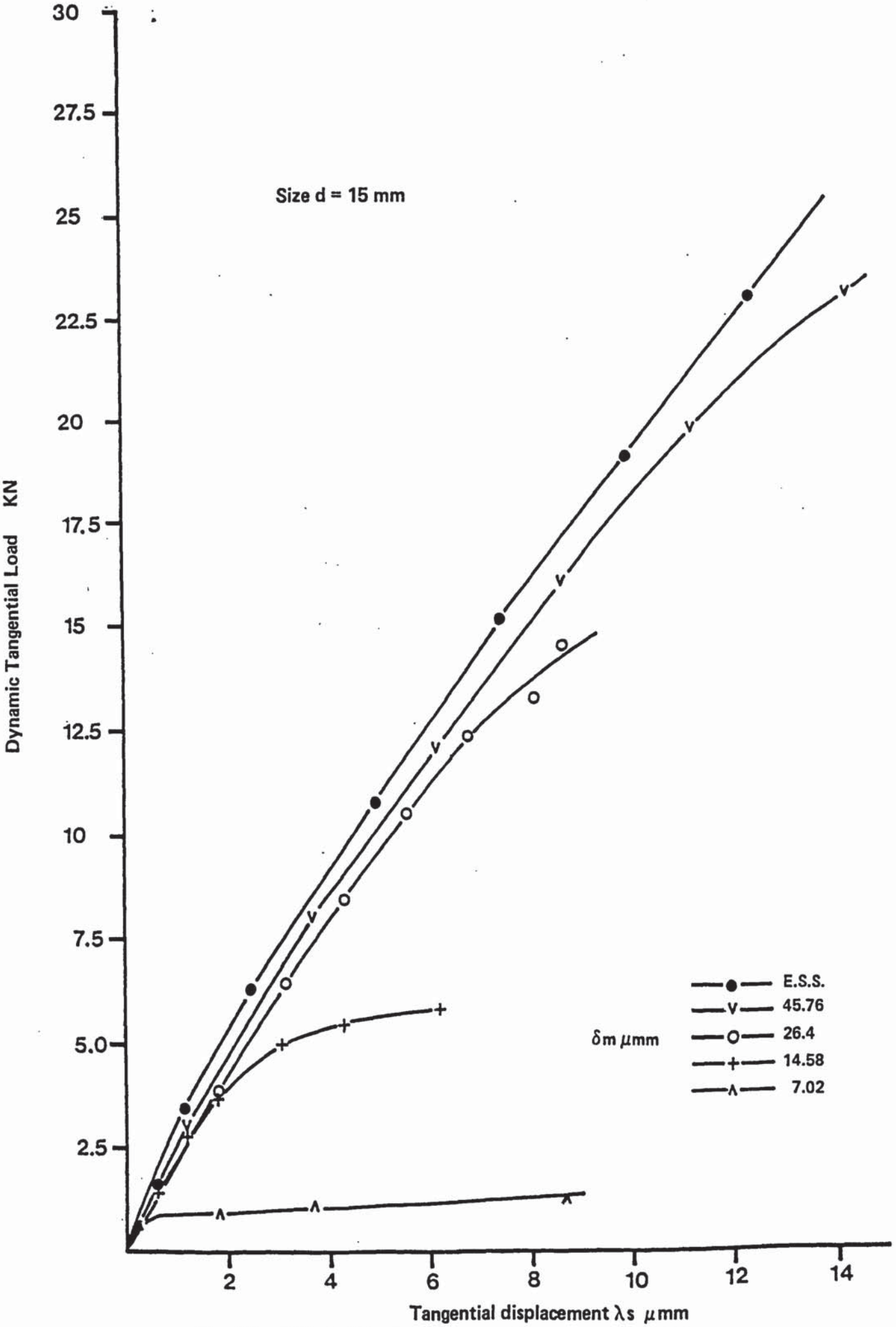

Fig 94 Effect of the interference value on λs of D31 joints

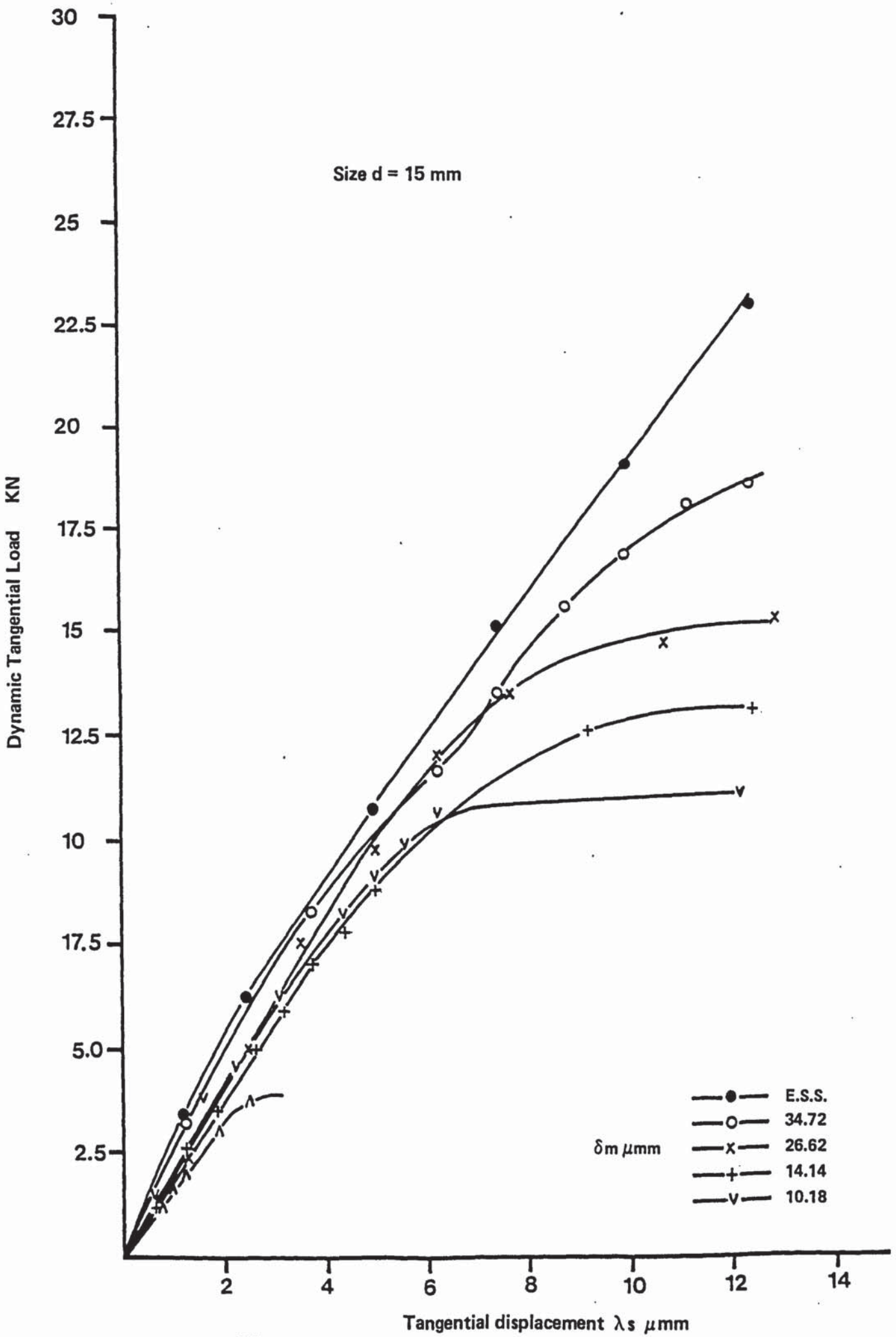

Fig 95 Effect of the interference value on λs of D42 joints

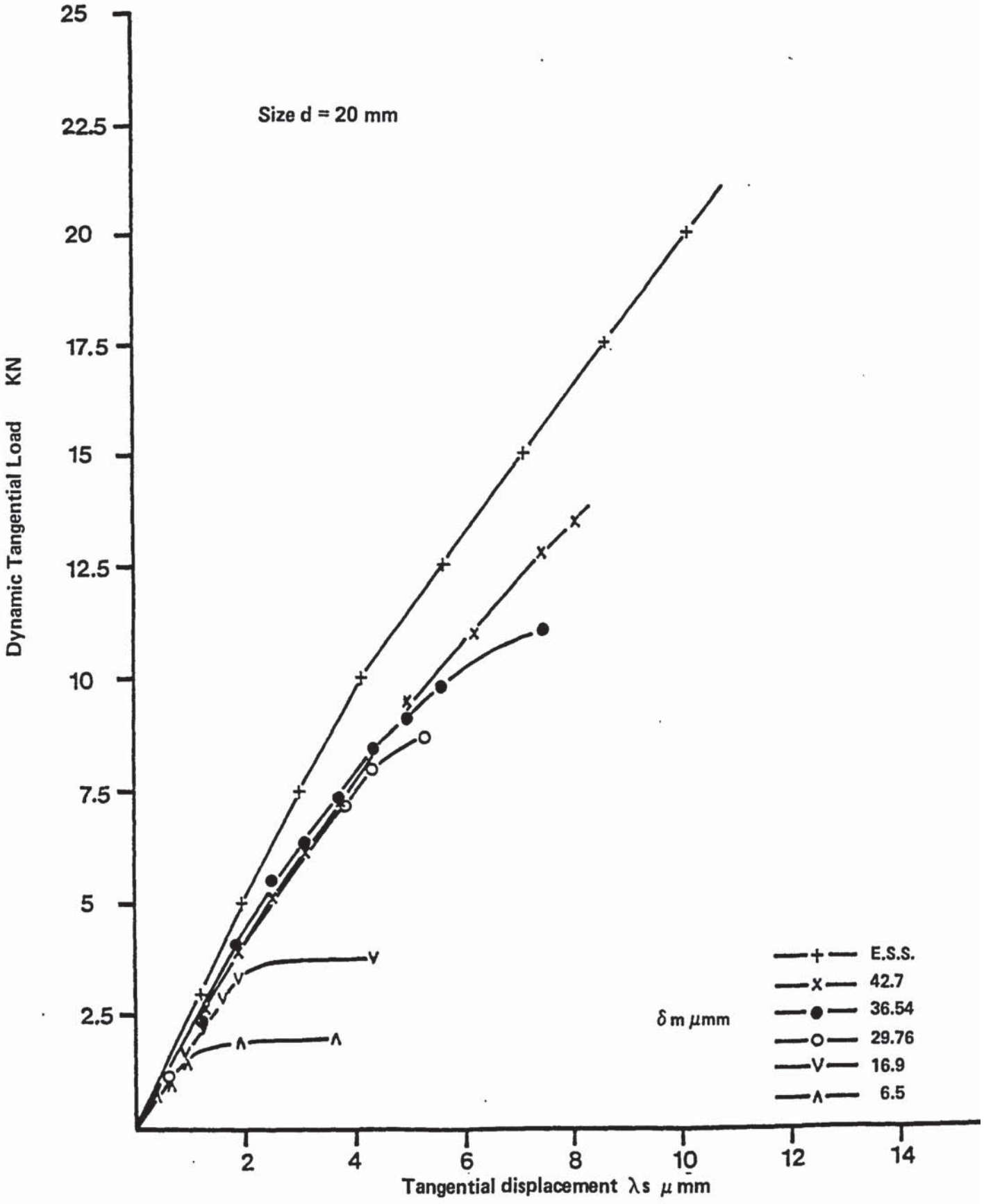

Fig 96 Effect of the interference value on λs of D51 joints

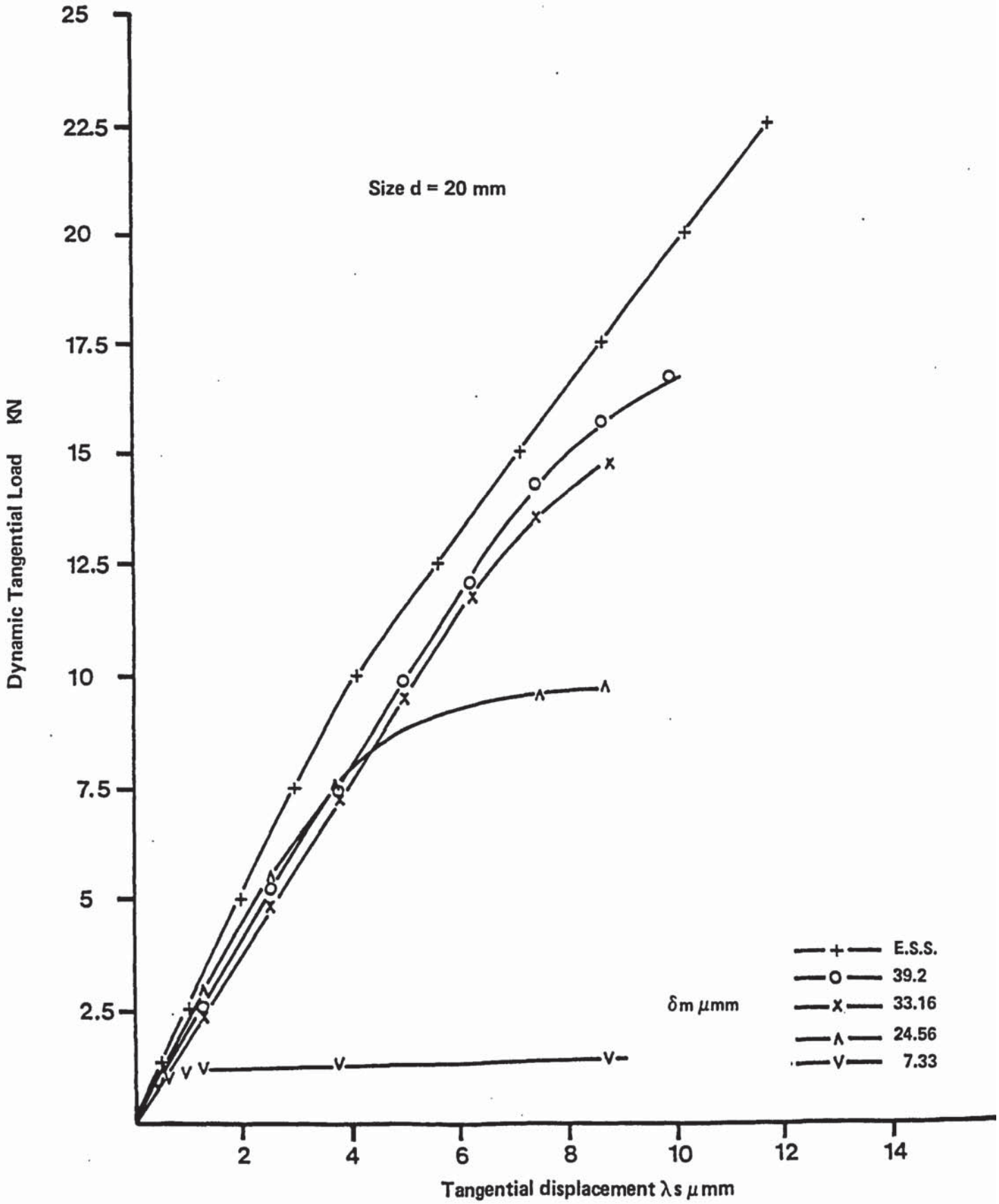

Fig 97 Effect of the interference value on λs of D52 joints

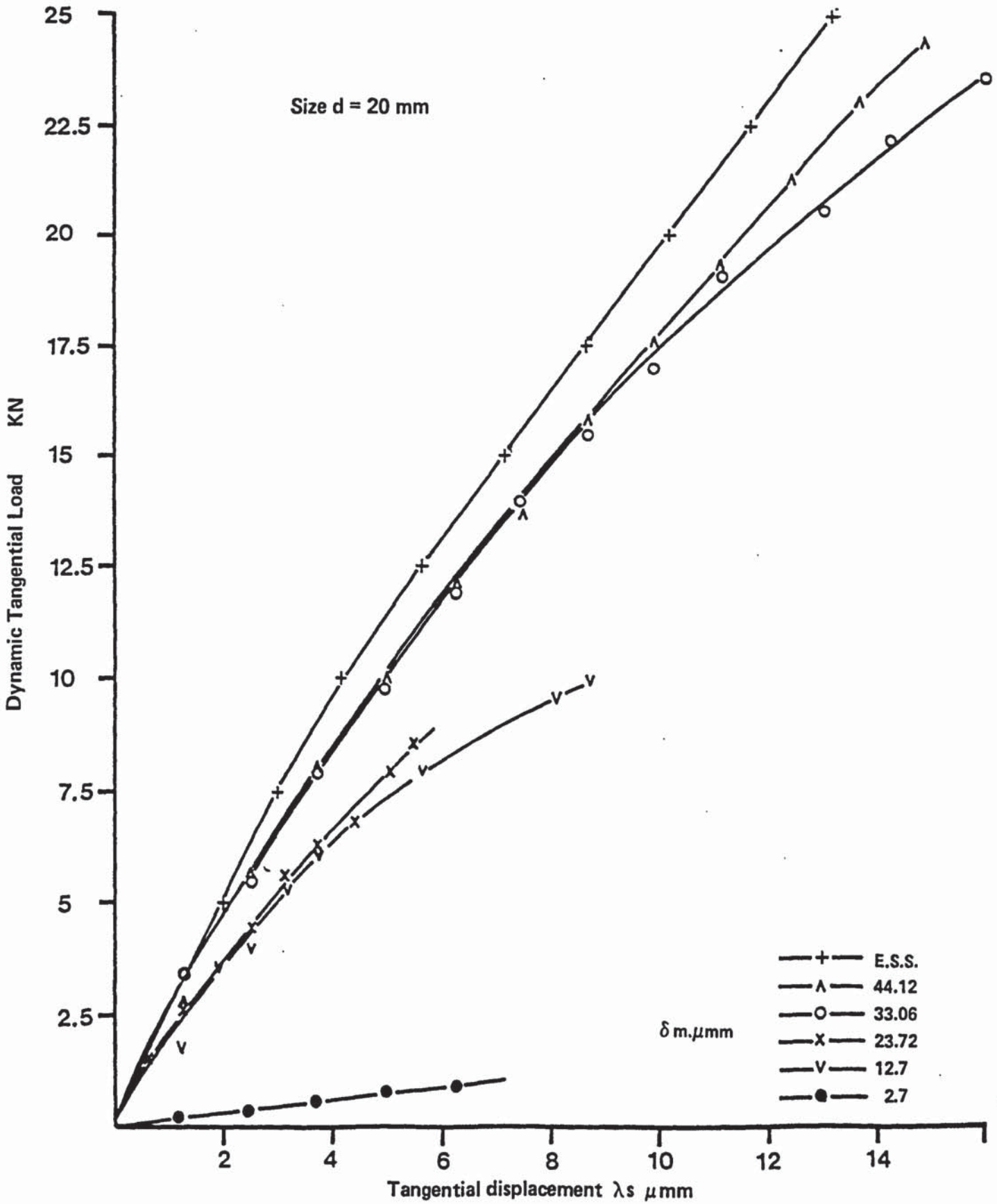

Fig 98 Effect of the interference value on λs of D61 joints

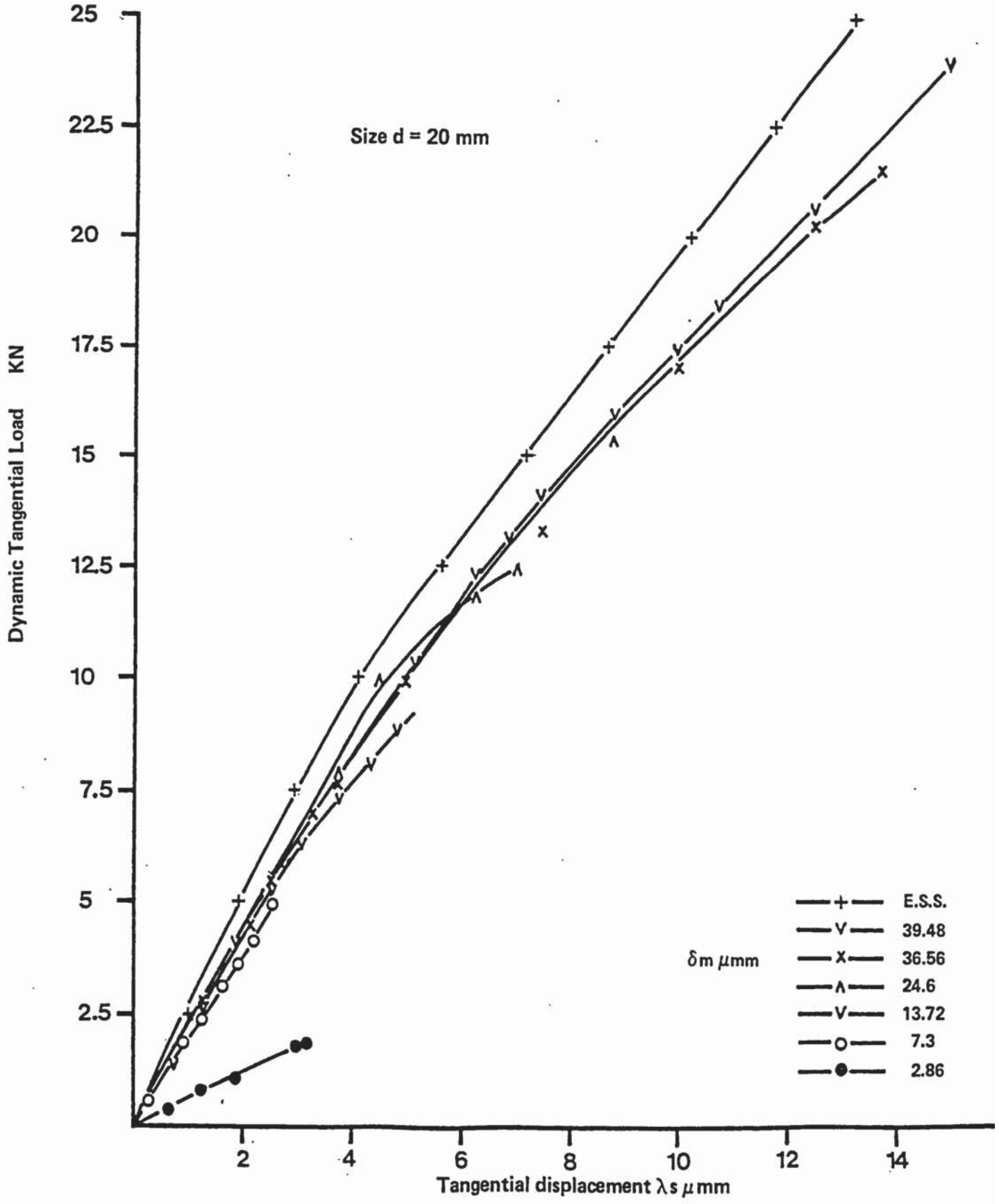

Fig 99 Effect of the interference value on λs of D62 joints

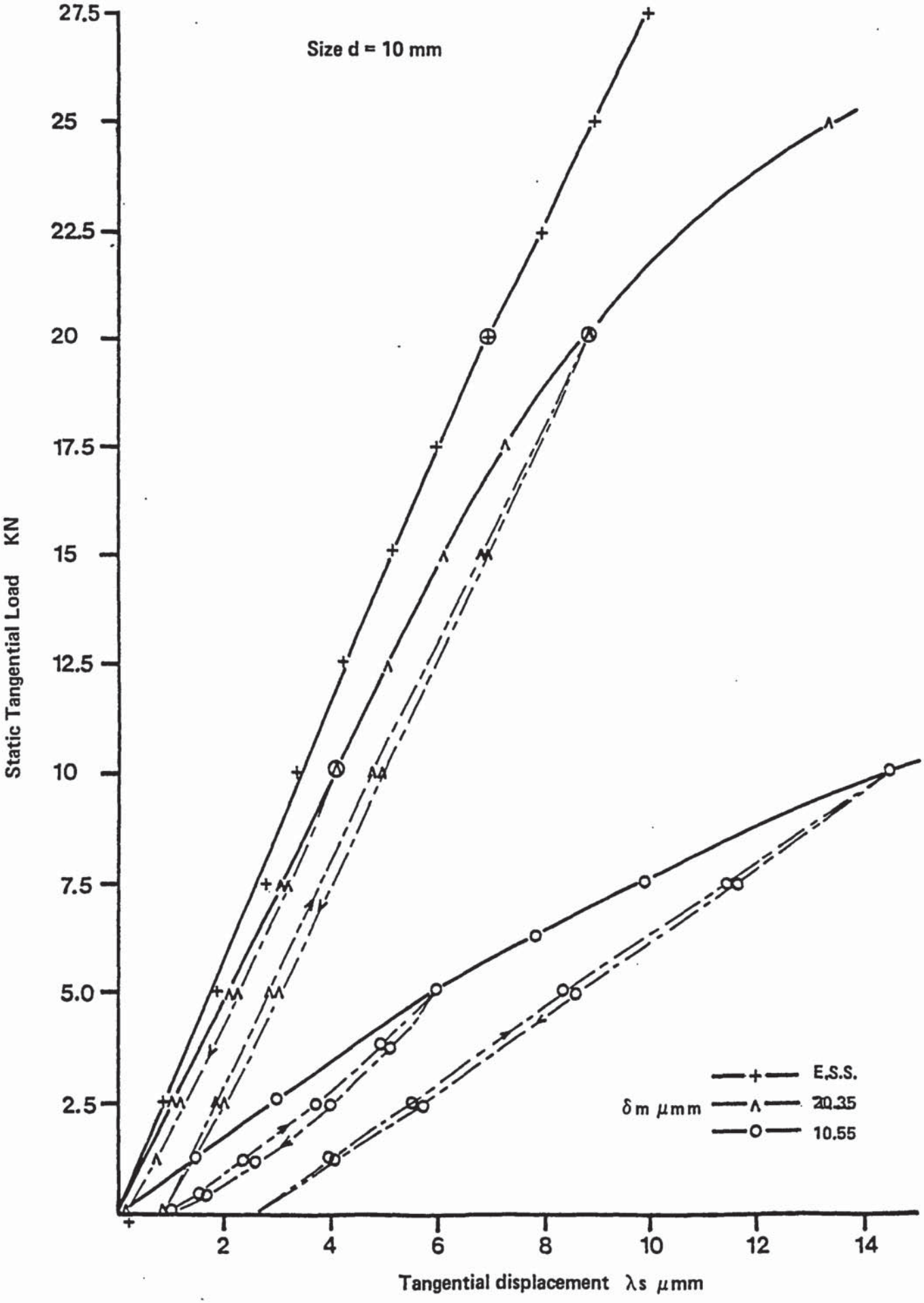

Fig 100 Effect of the interference value on the micro-slip of ST11 joints

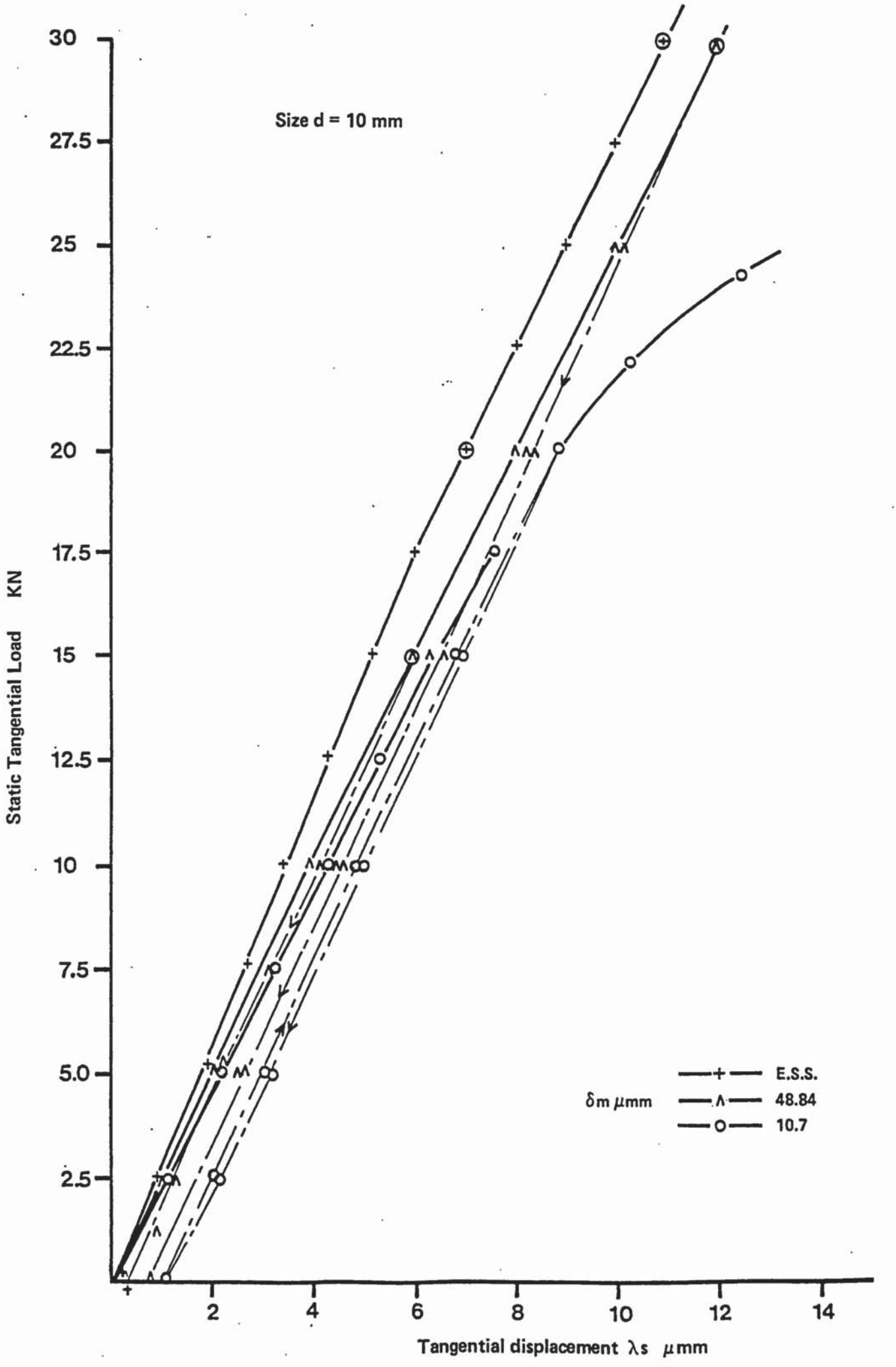

Fig 101 Effect of the interference value on the micro-slip of ST22 Joints

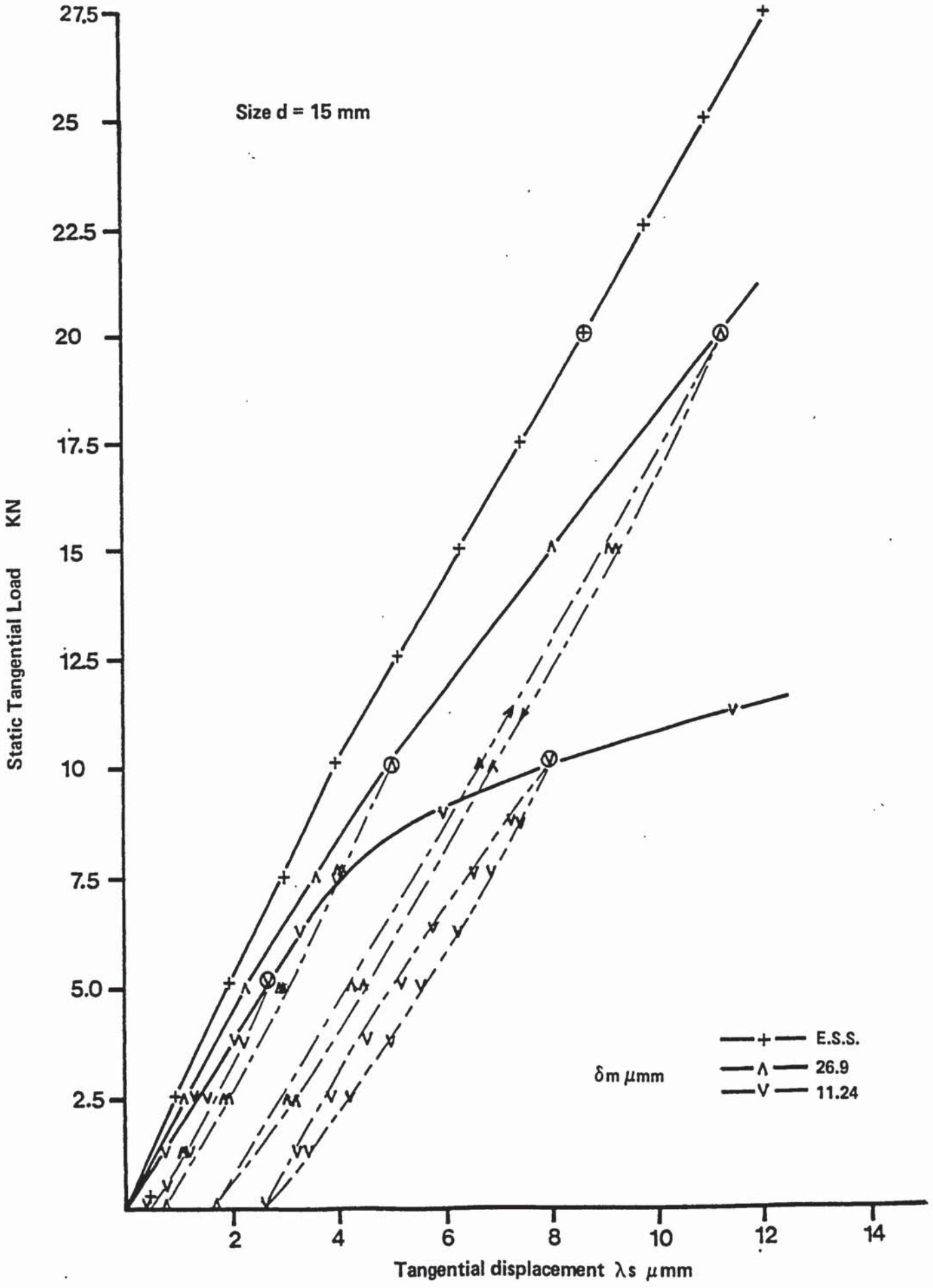

Fig 102 Effect of the interference on the micro-slip of ST31 joints

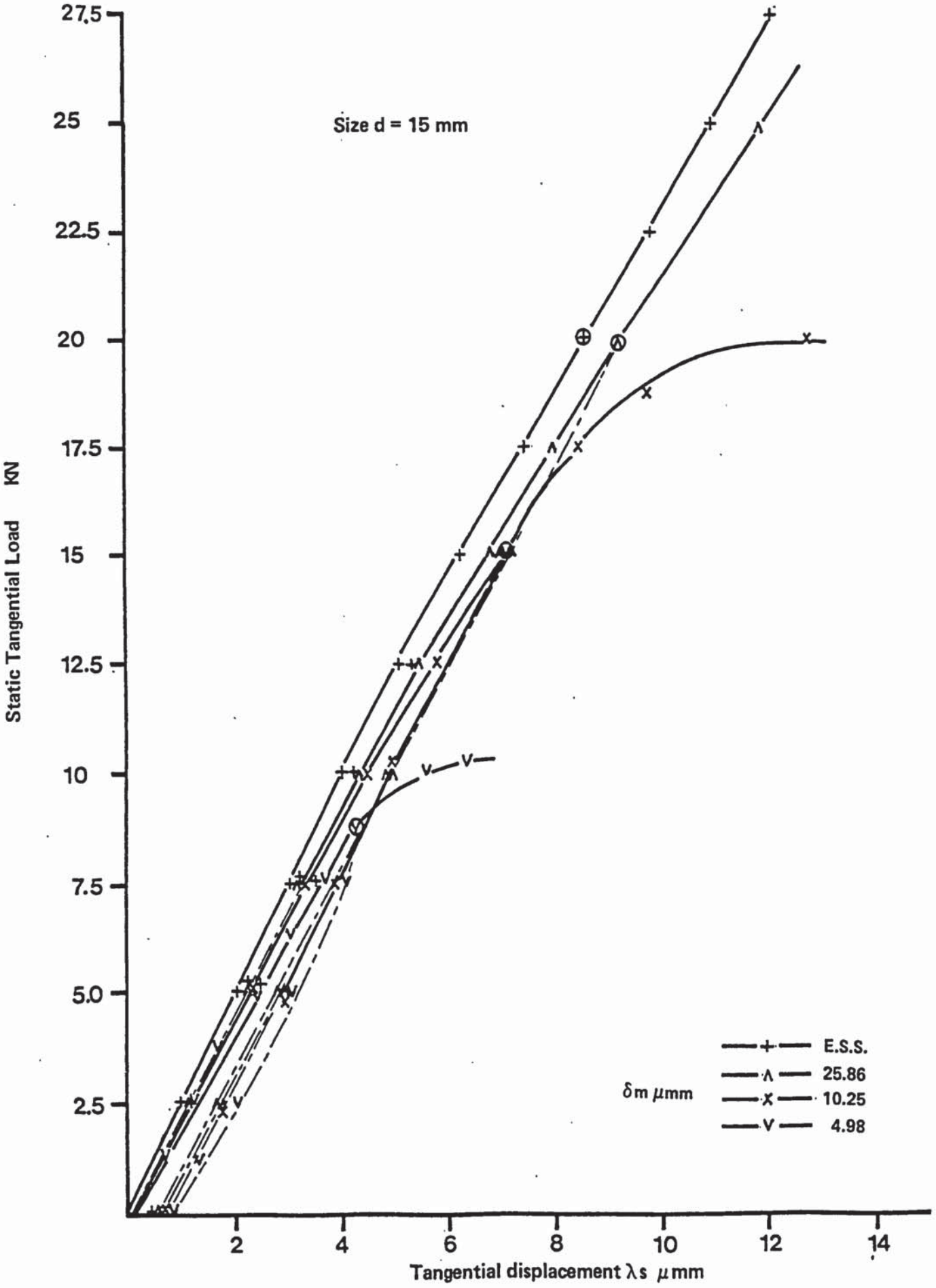

Fig 103 Effect of the interference value on the micro-slip of ST42 joints

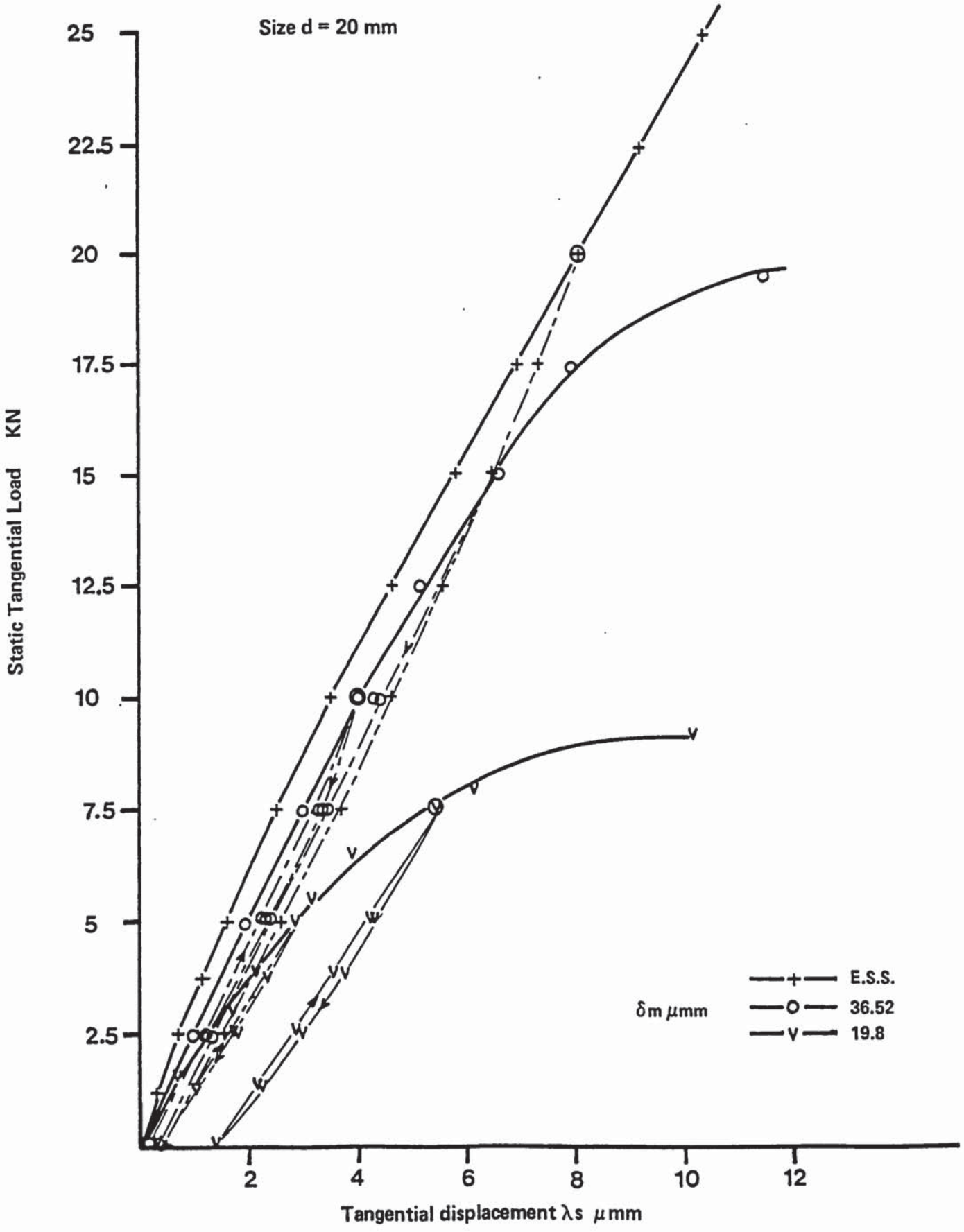

Fig 104 Effect of the interference value on the micro-slip of ST51 joints

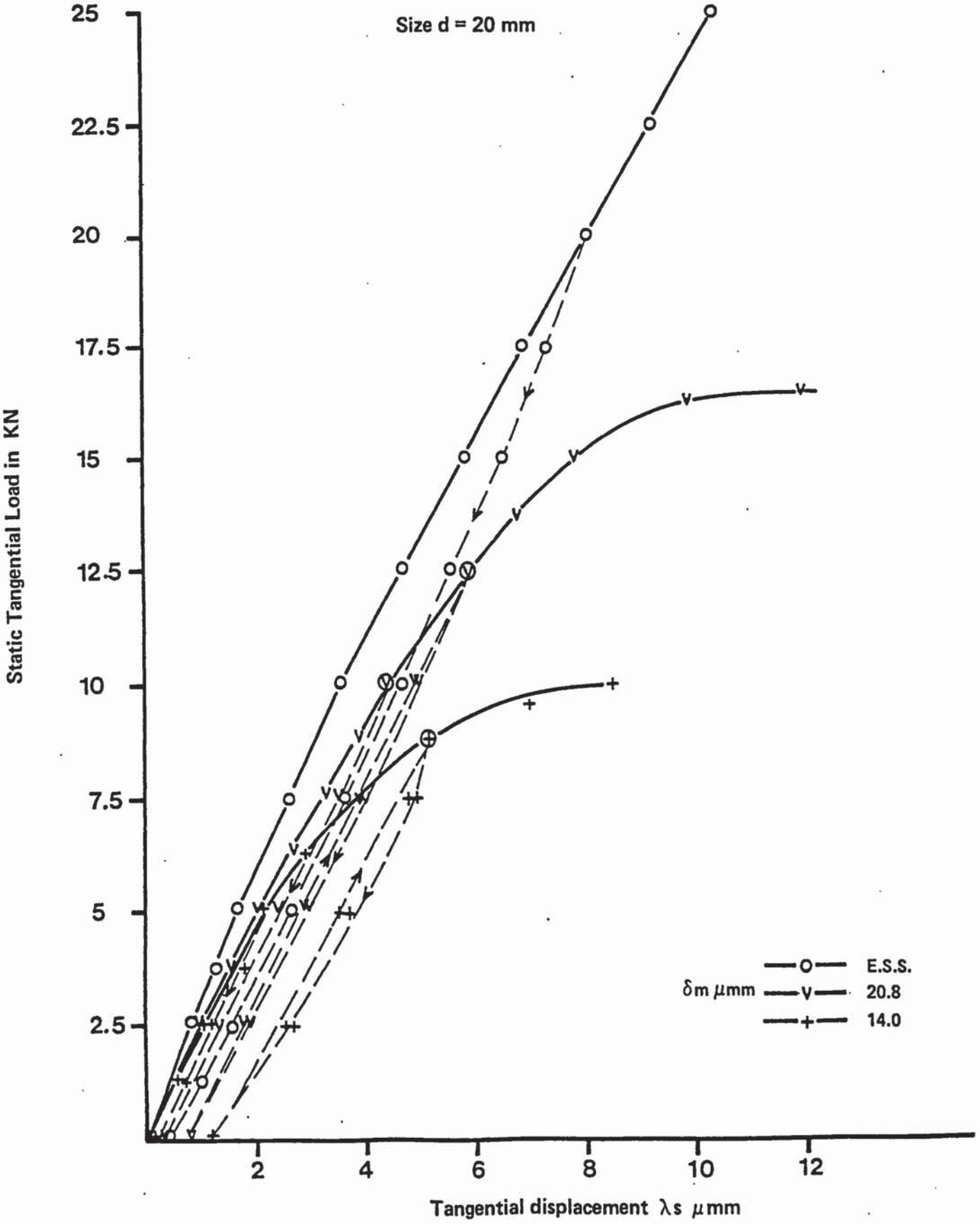

Fig 105 Effect of the interference value on the micro-slip of ST61 joints

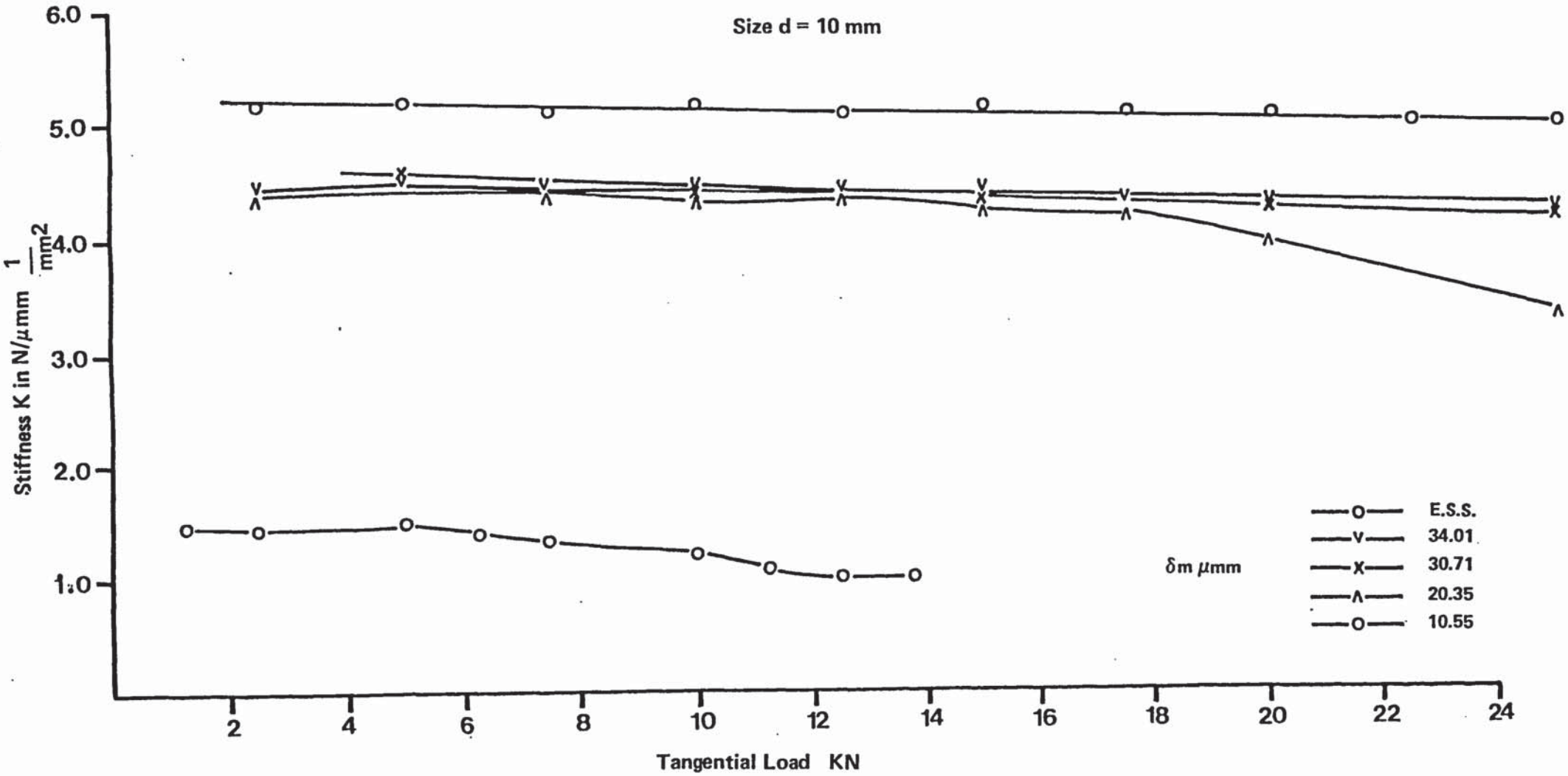

Fig 106 Static stiffness of ST11 joints

TEXT CUT OFF IN ORIGINAL

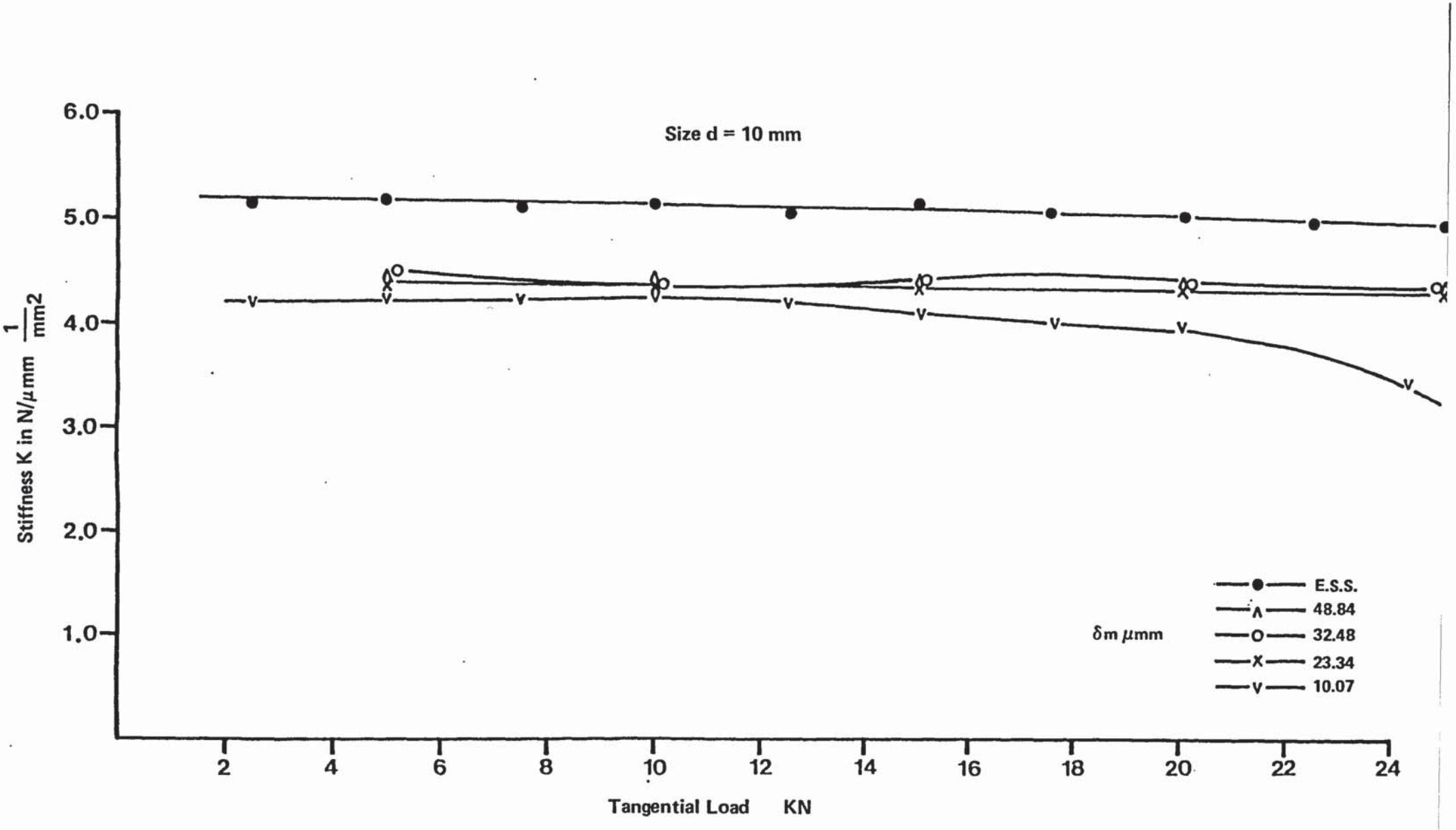

Fig 107 Static stiffness of ST22 joints

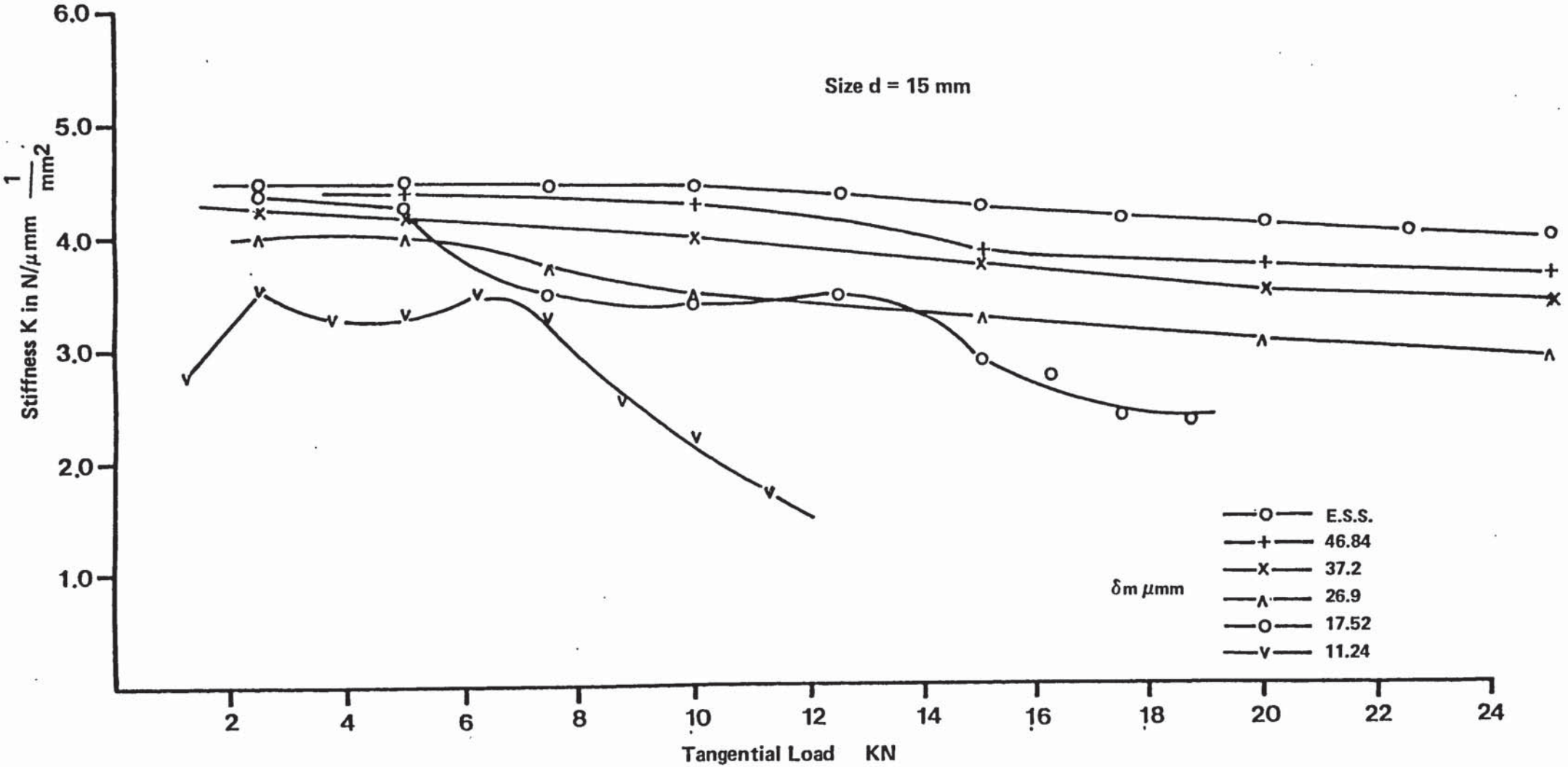

Fig 108 Static stiffness of ST31 joints

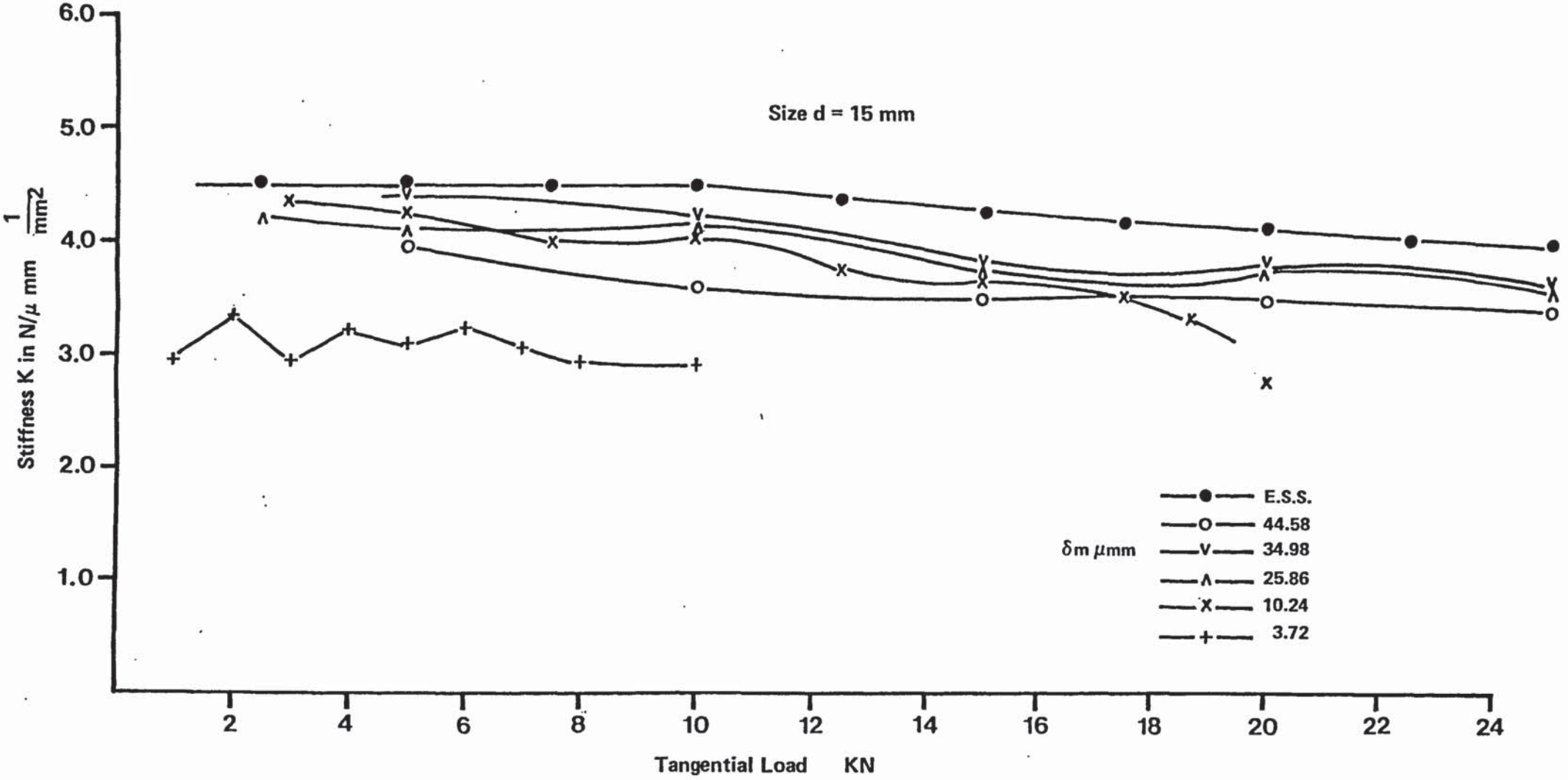

Fig 109 Static stiffness of ST42 joints

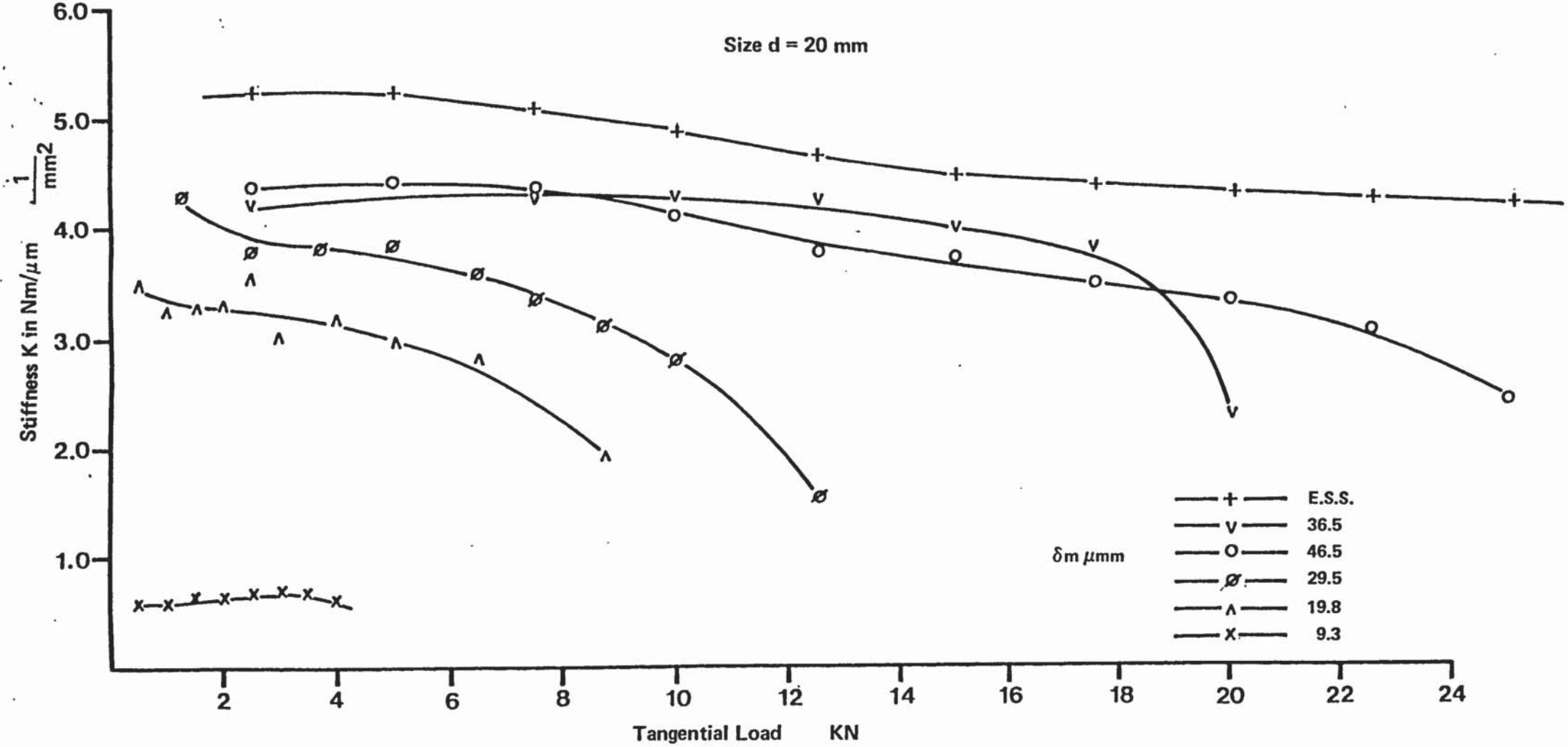

Fig 110 Static stiffness of ST51 joints

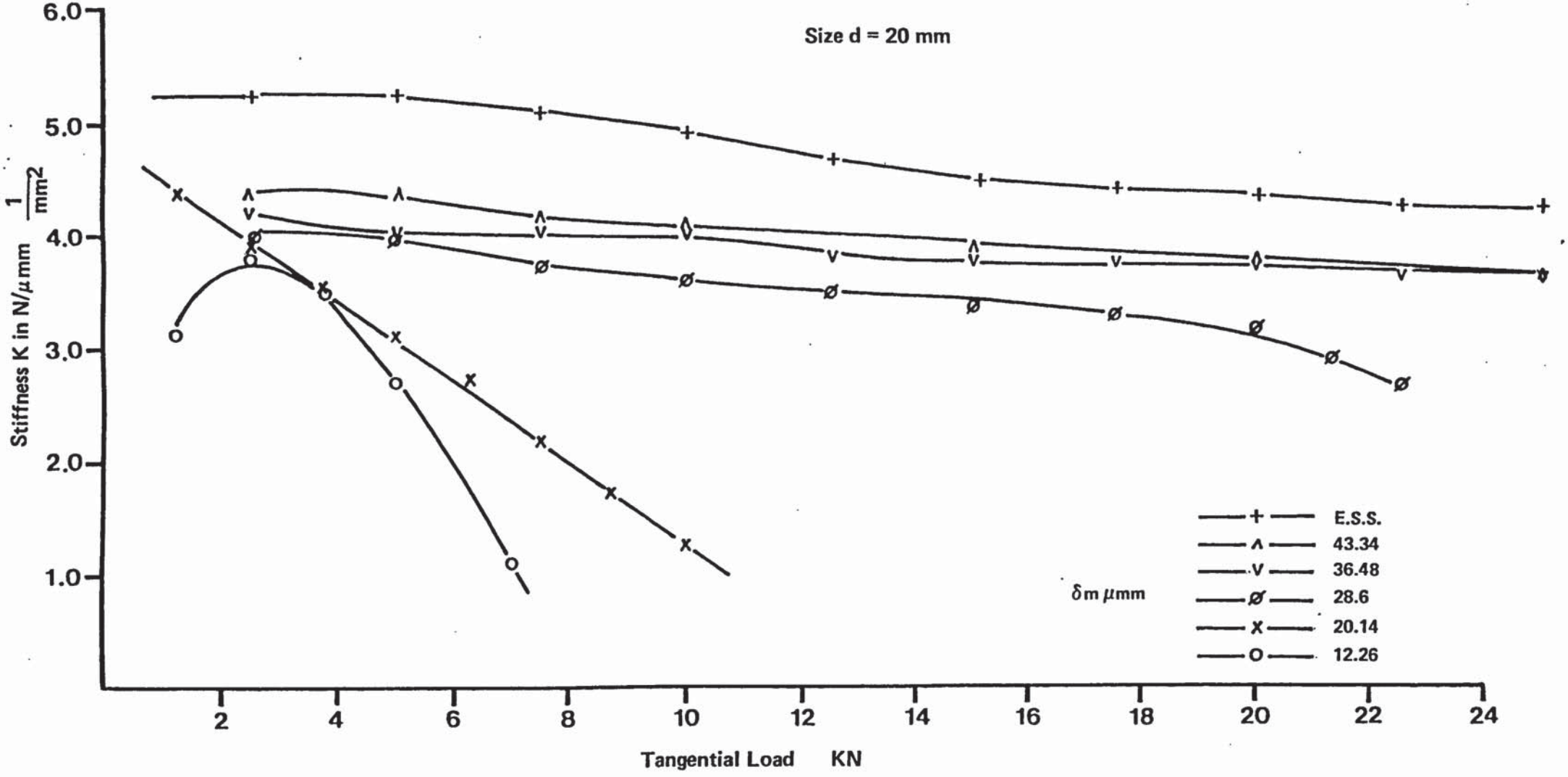

Fig 111 Static stiffness of ST52 joints

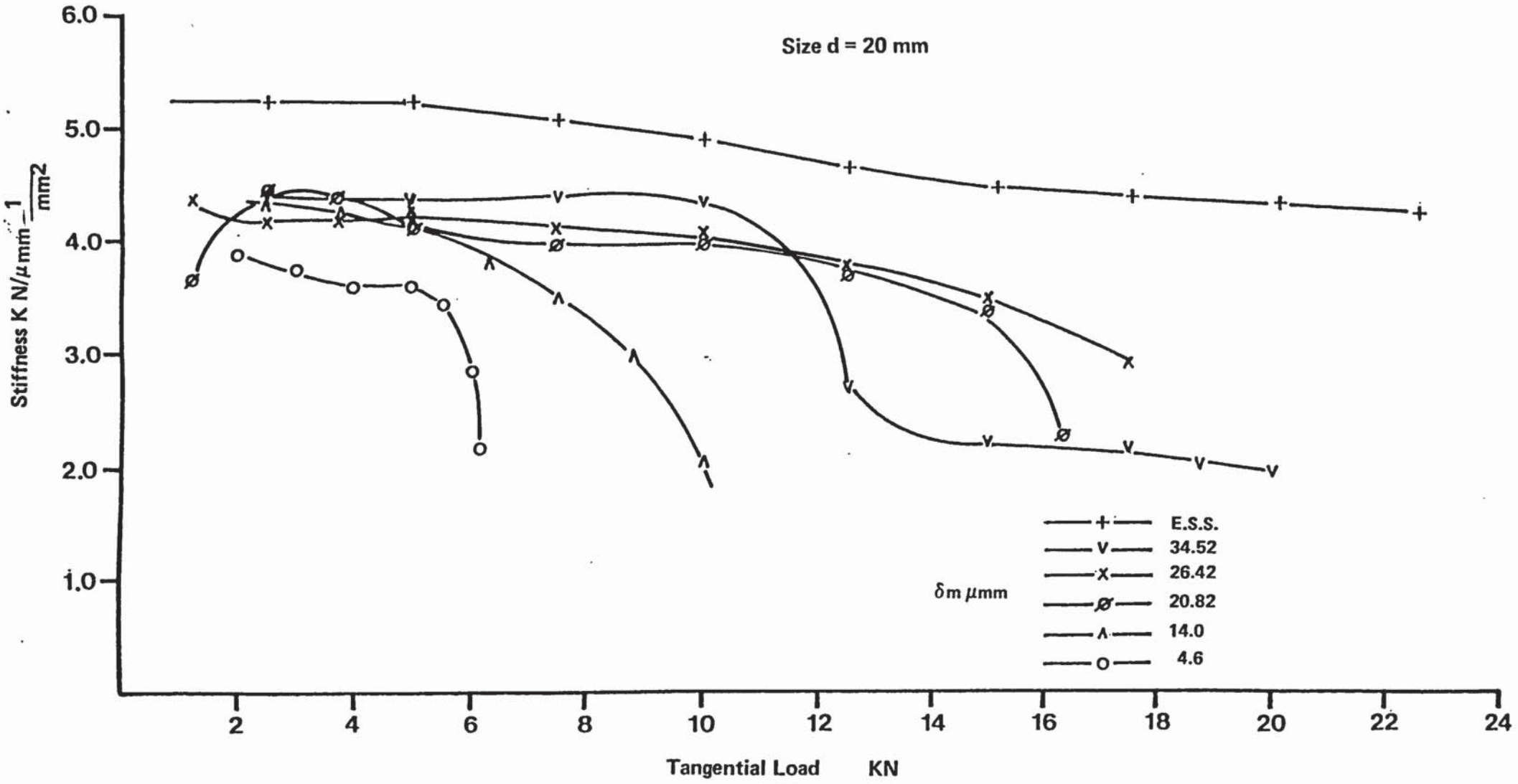

Fig 112 Static stiffness of ST61 joints

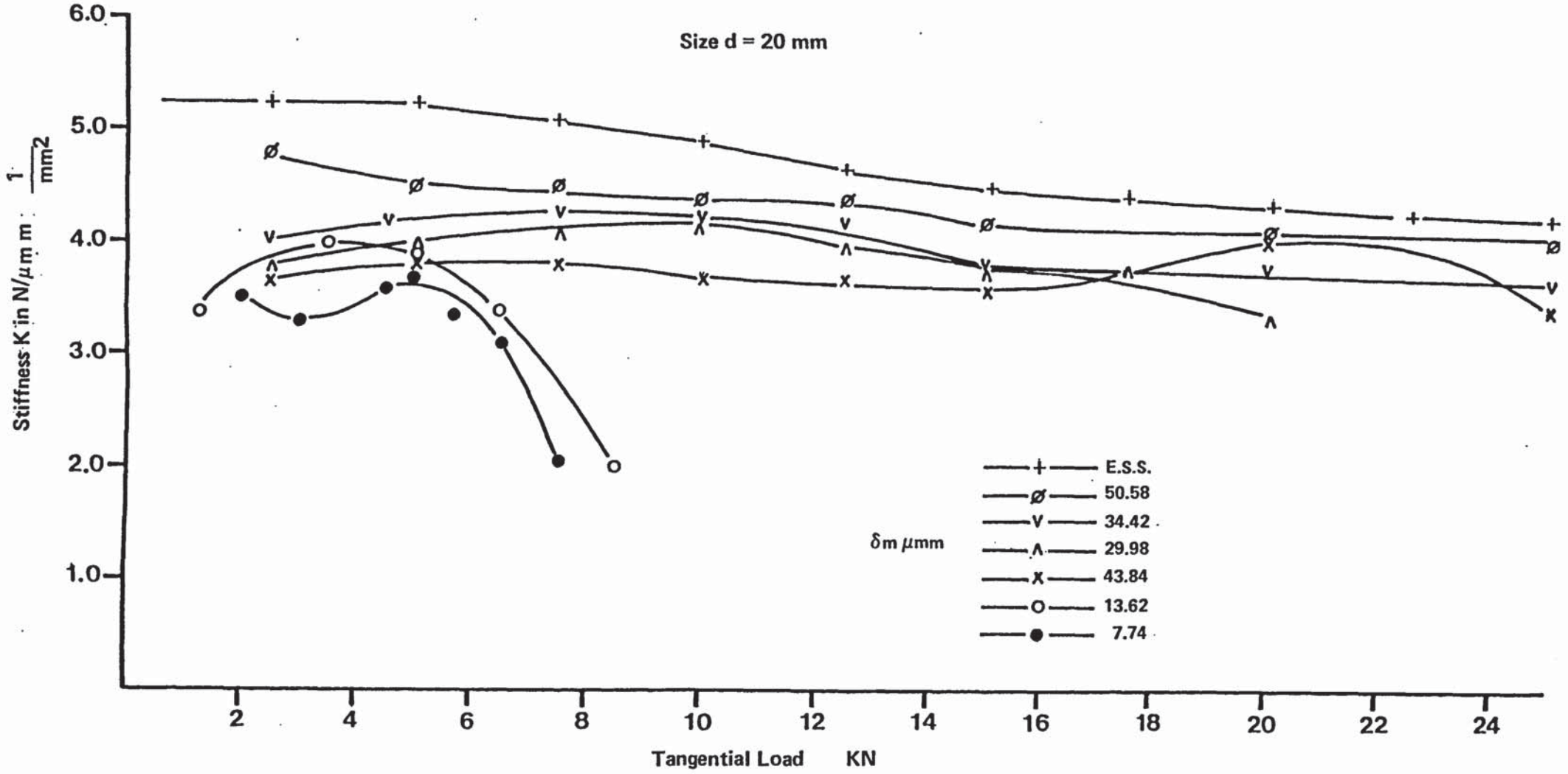

Fig 113 Static stiffness of ST62 joints

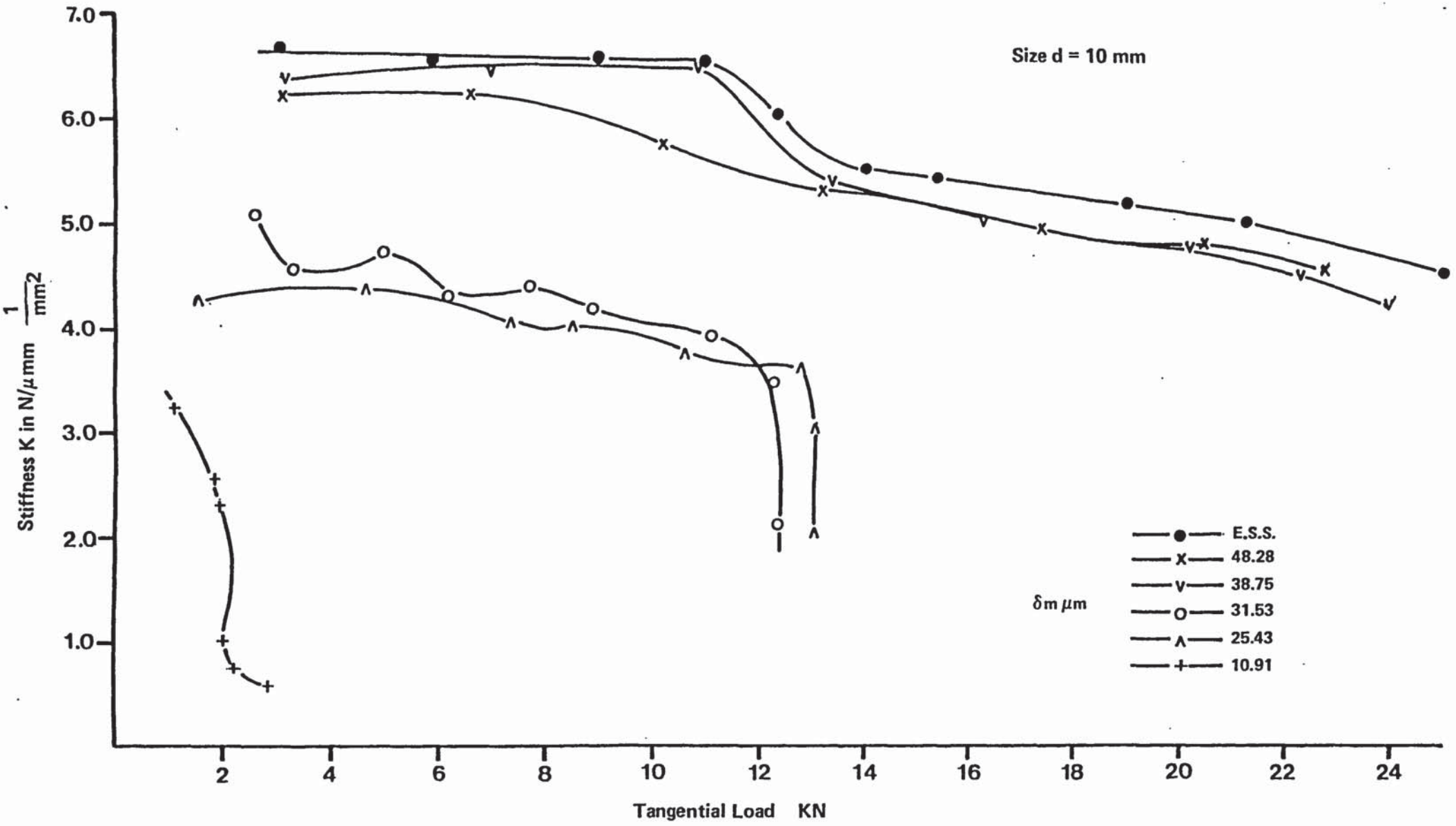

Fig 114 Dynamic Stiffness of D11 joints

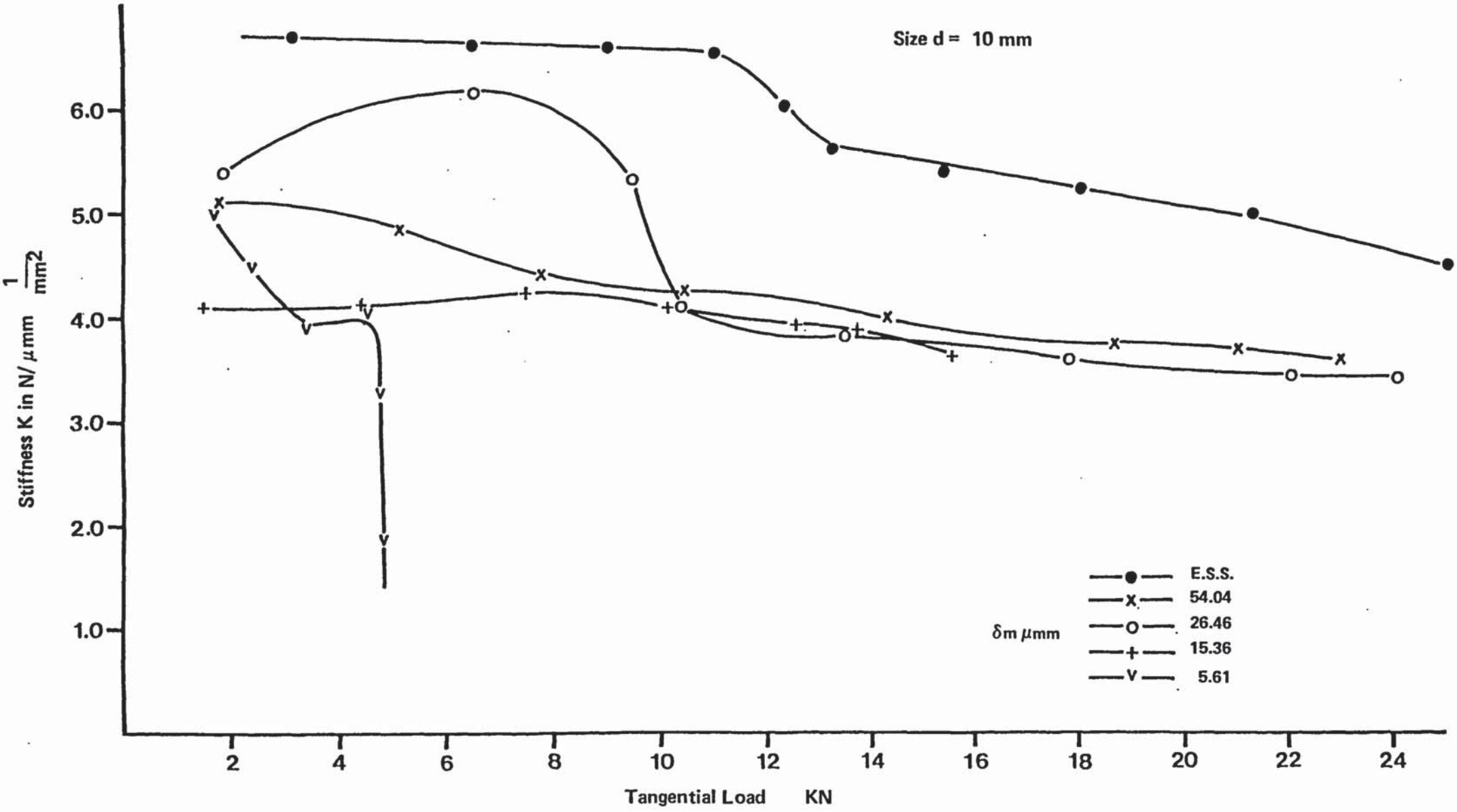

Fig 115 Dynamic stiffness of D22 joints

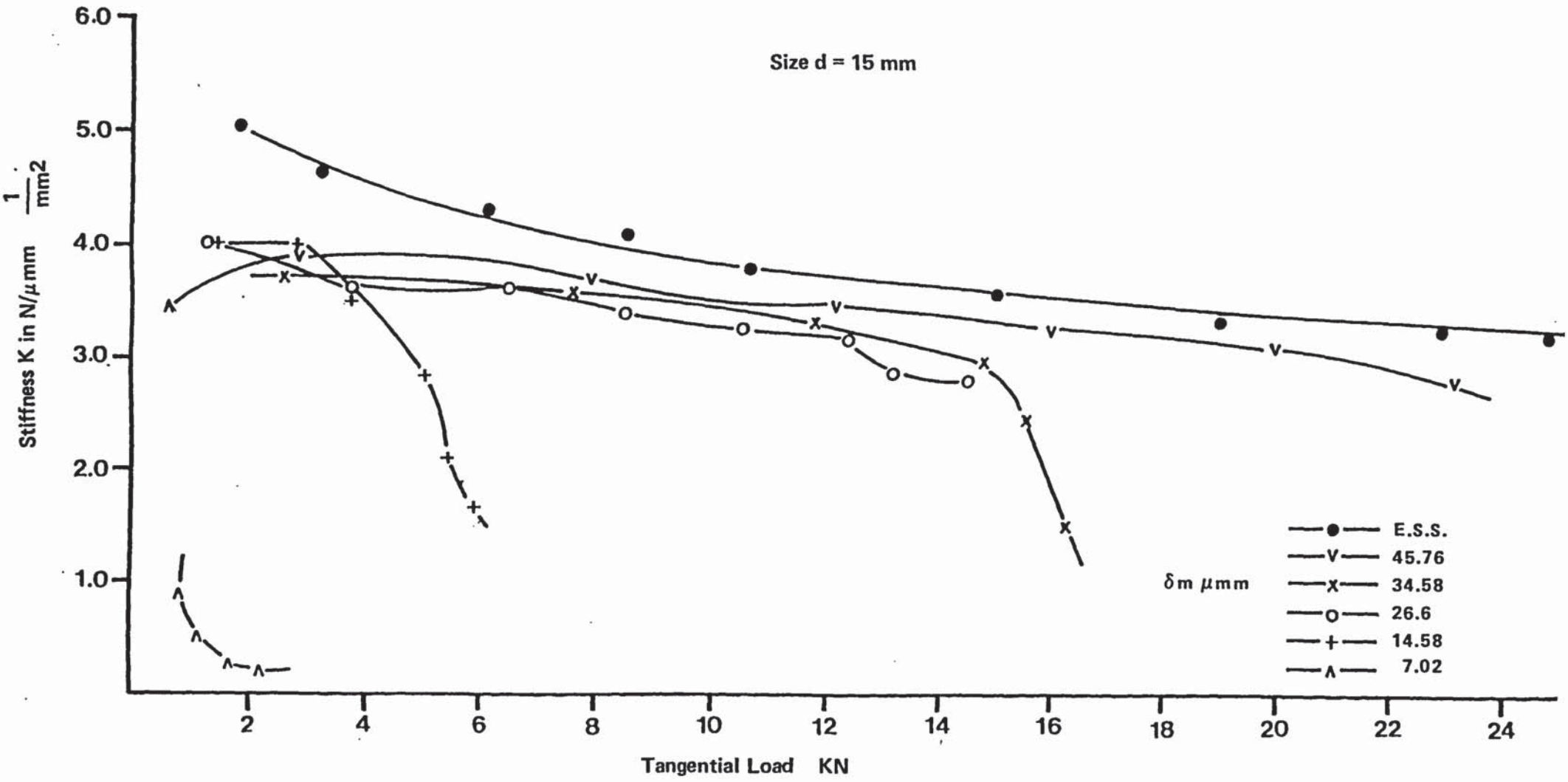

Fig 116 Dynamic stiffness of D31 joints

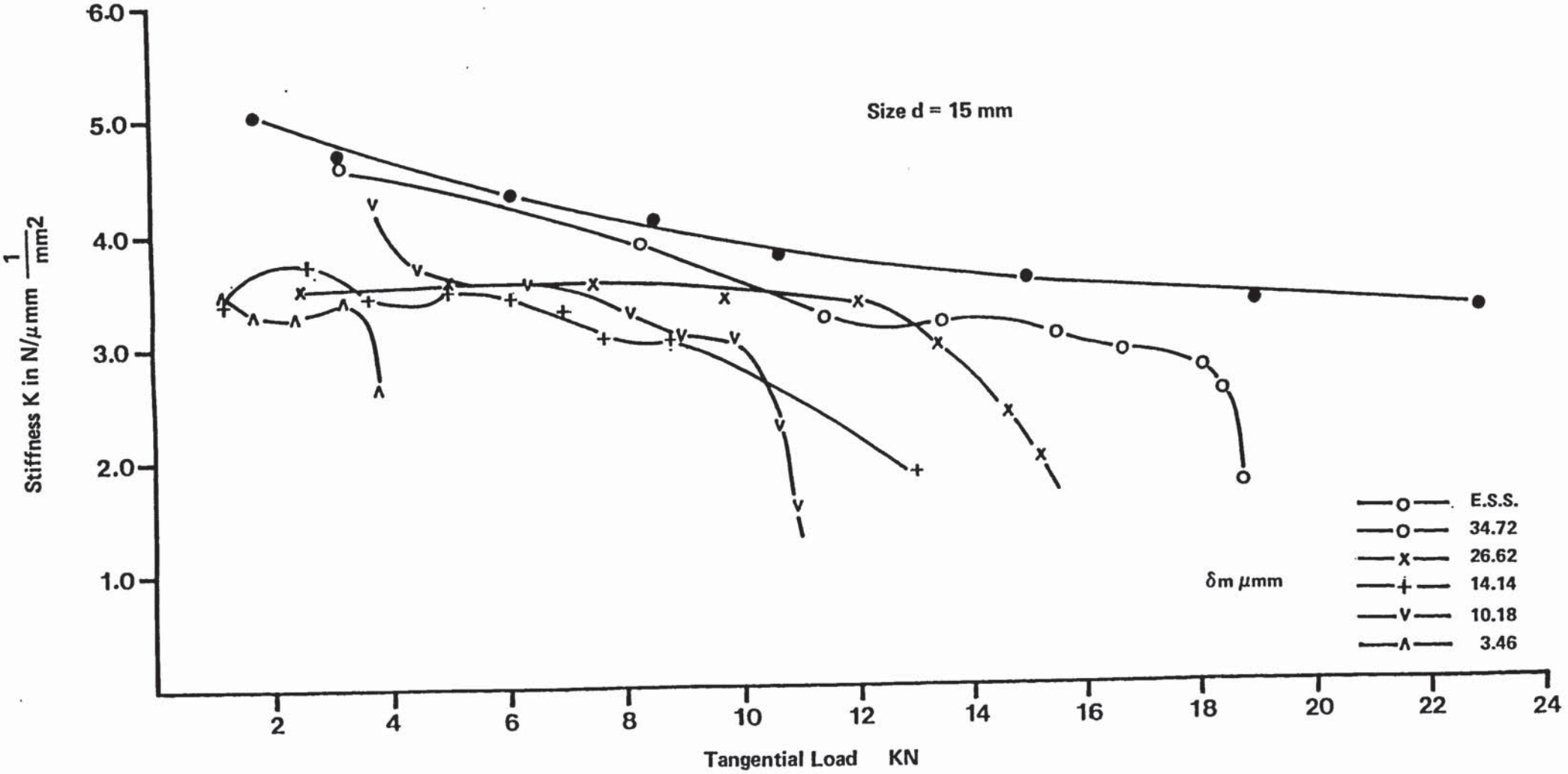

Fig 117 Dynamic stiffness of D42 joints

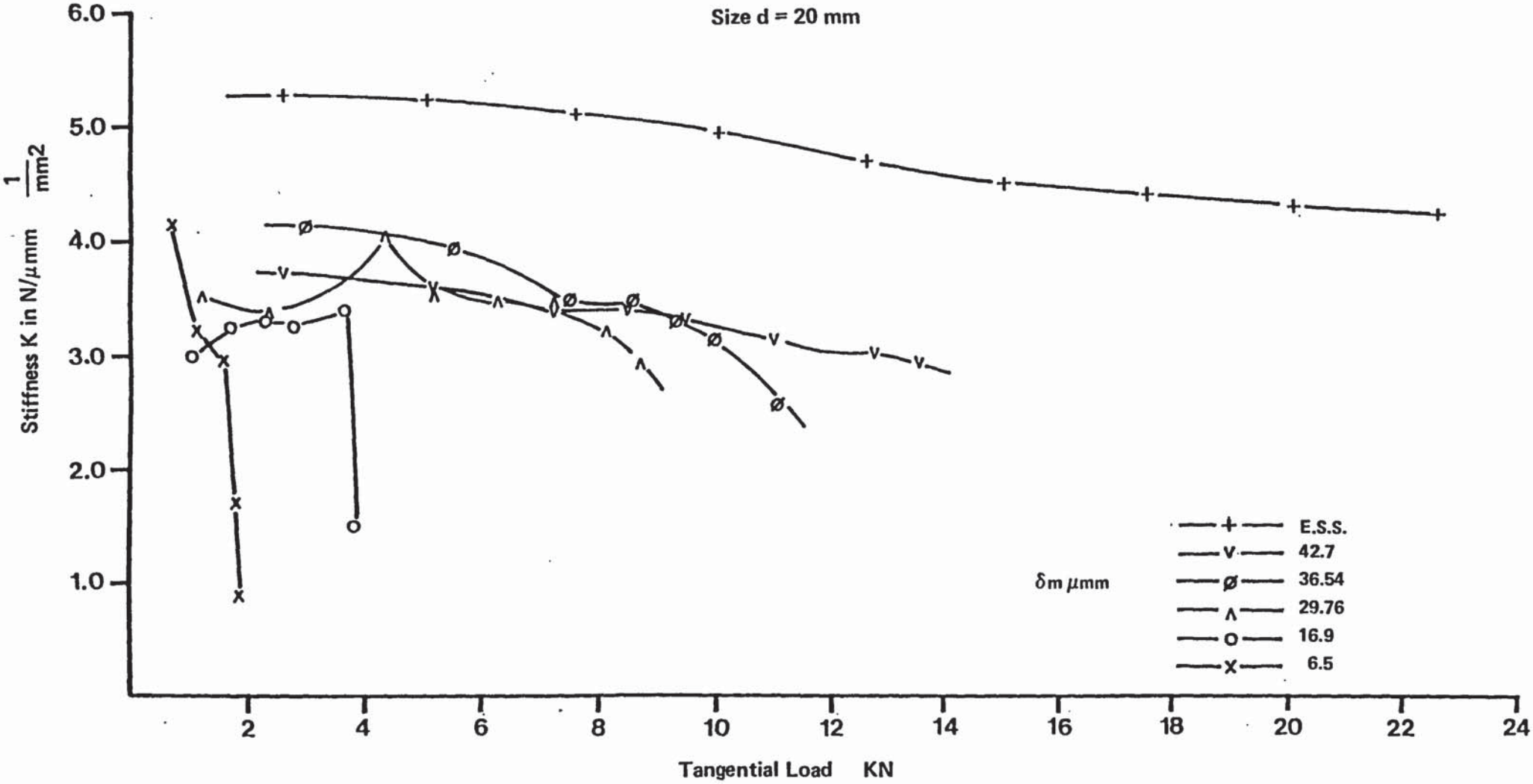

Fig 118 Dynamic stiffness of D51 joints

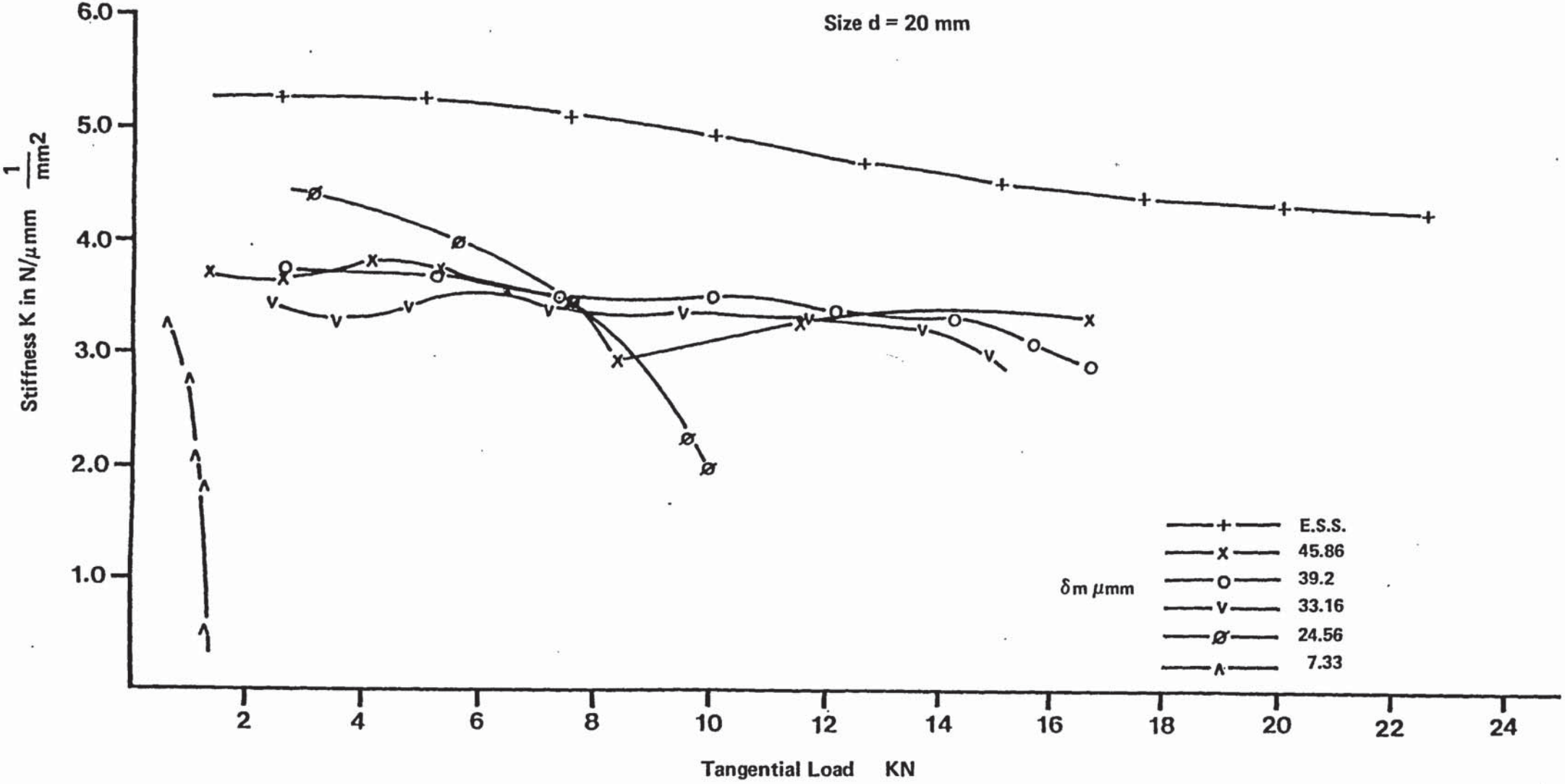

Fig 119 Dynamic Stiffness of D52 joints

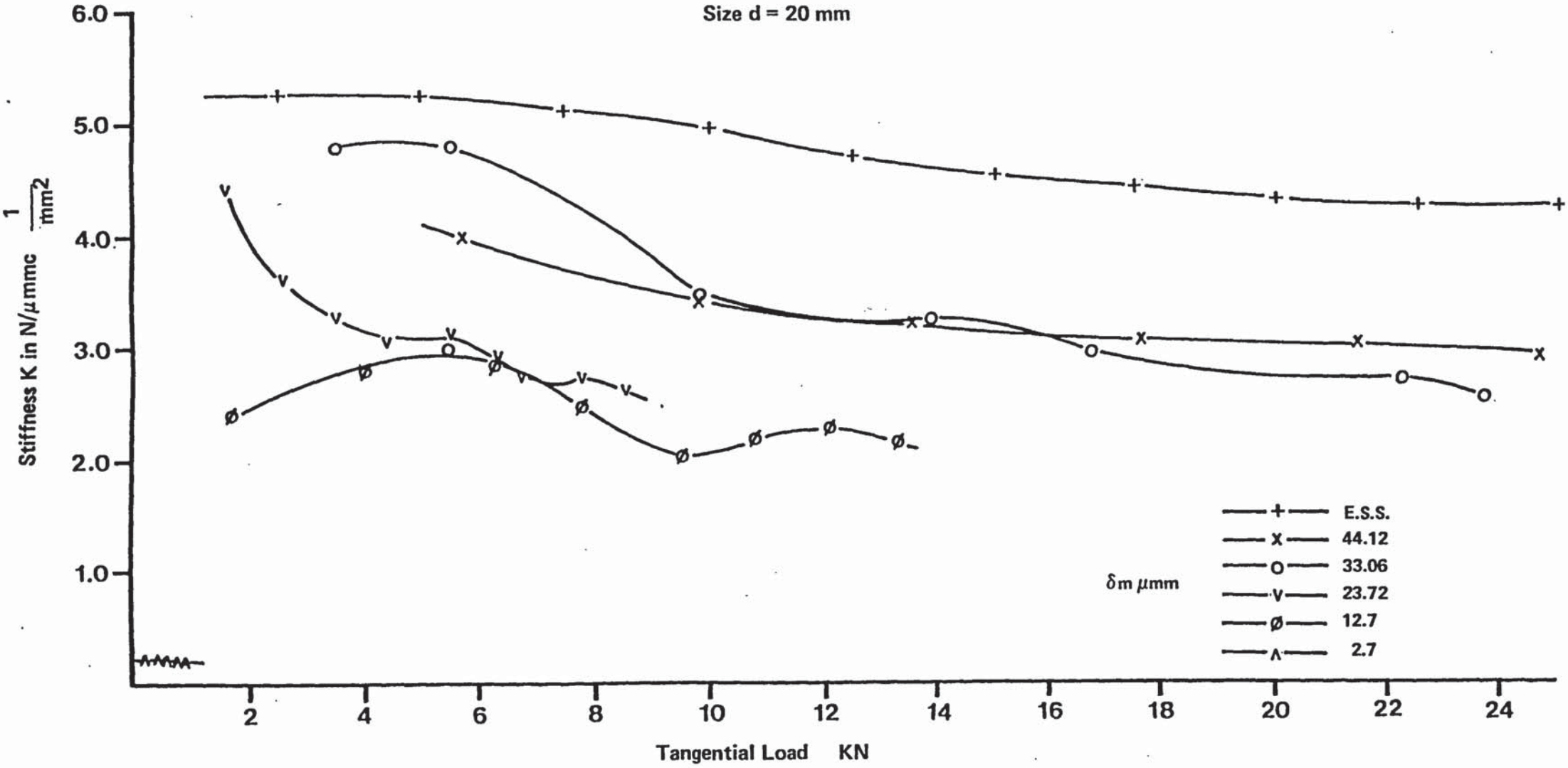

Fig 120 Dynamic stiffness of D61 joints

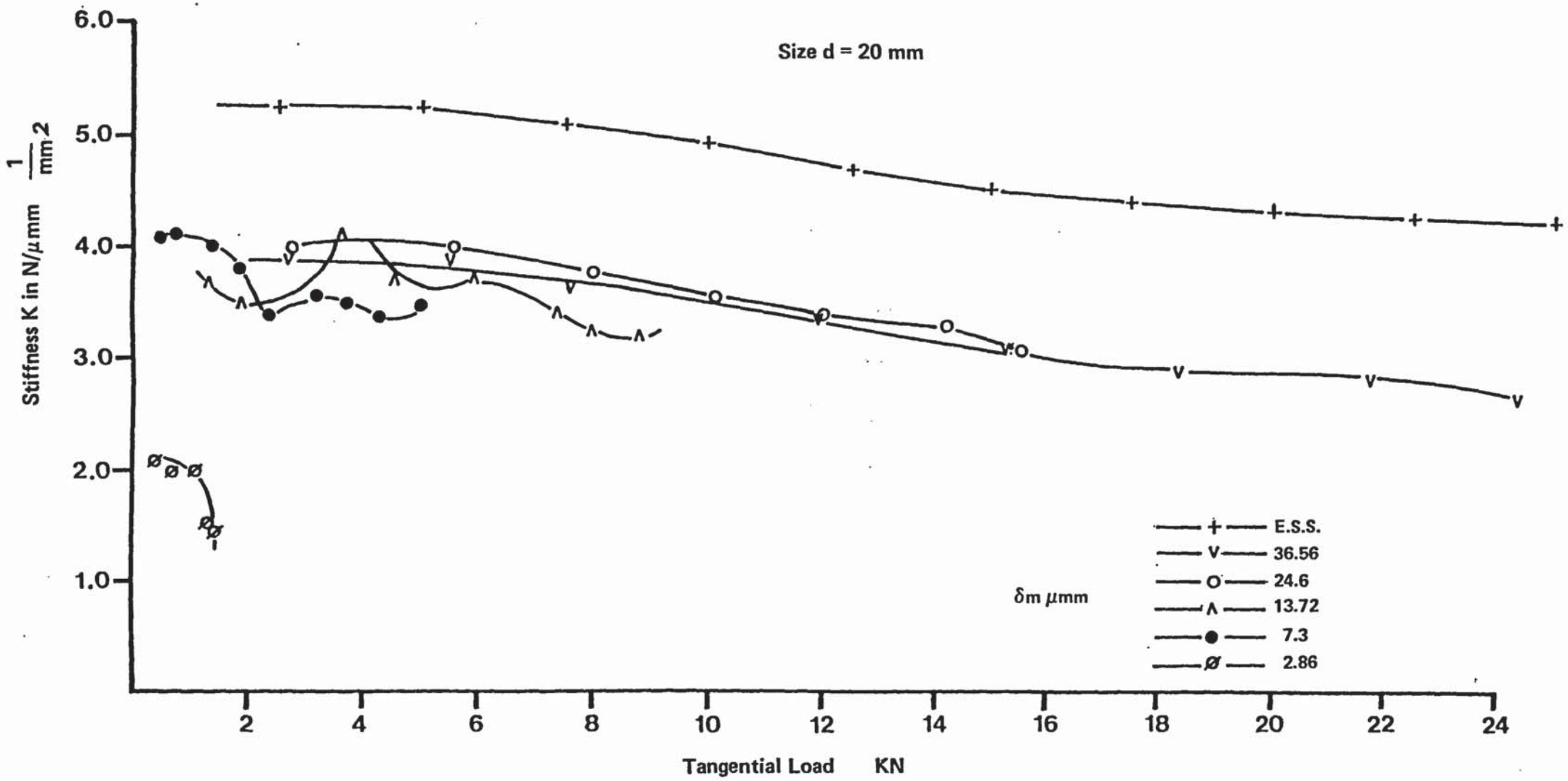

Fig 121 Dynamic stiffness of D62 joints

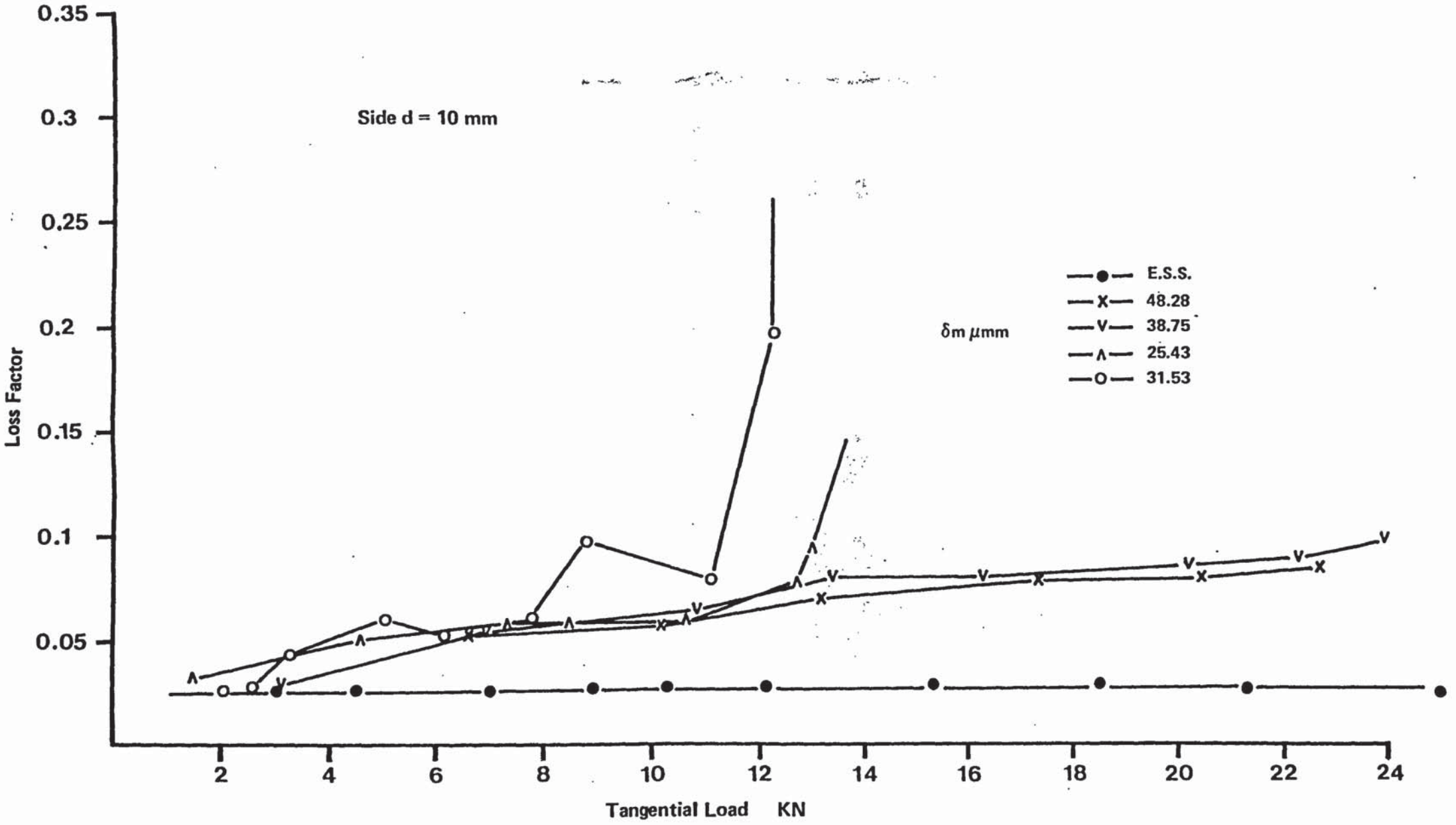

Fig 122 Loss Factor of D11 joints

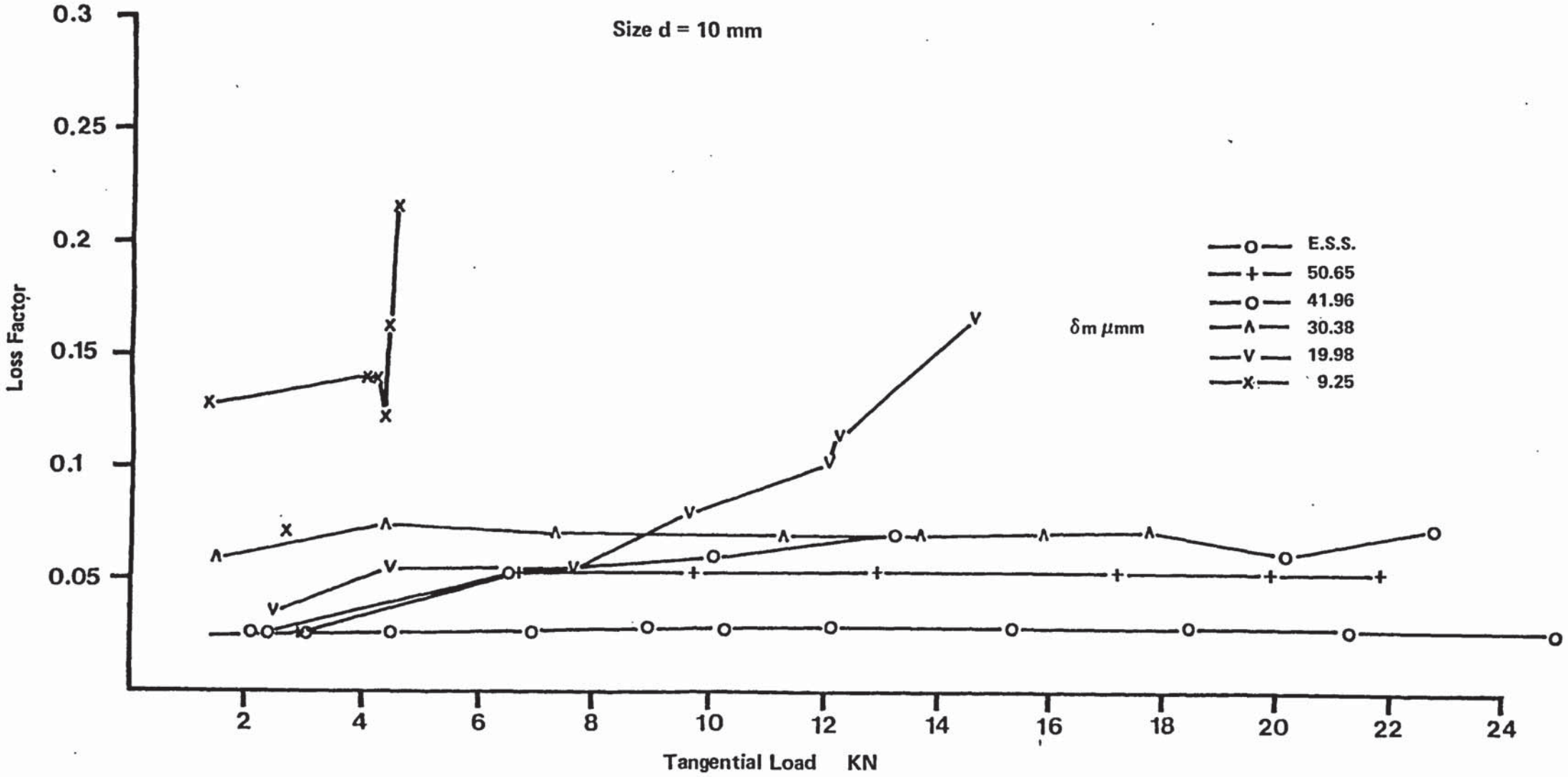

Fig 123 Loss Factor of D12 joints

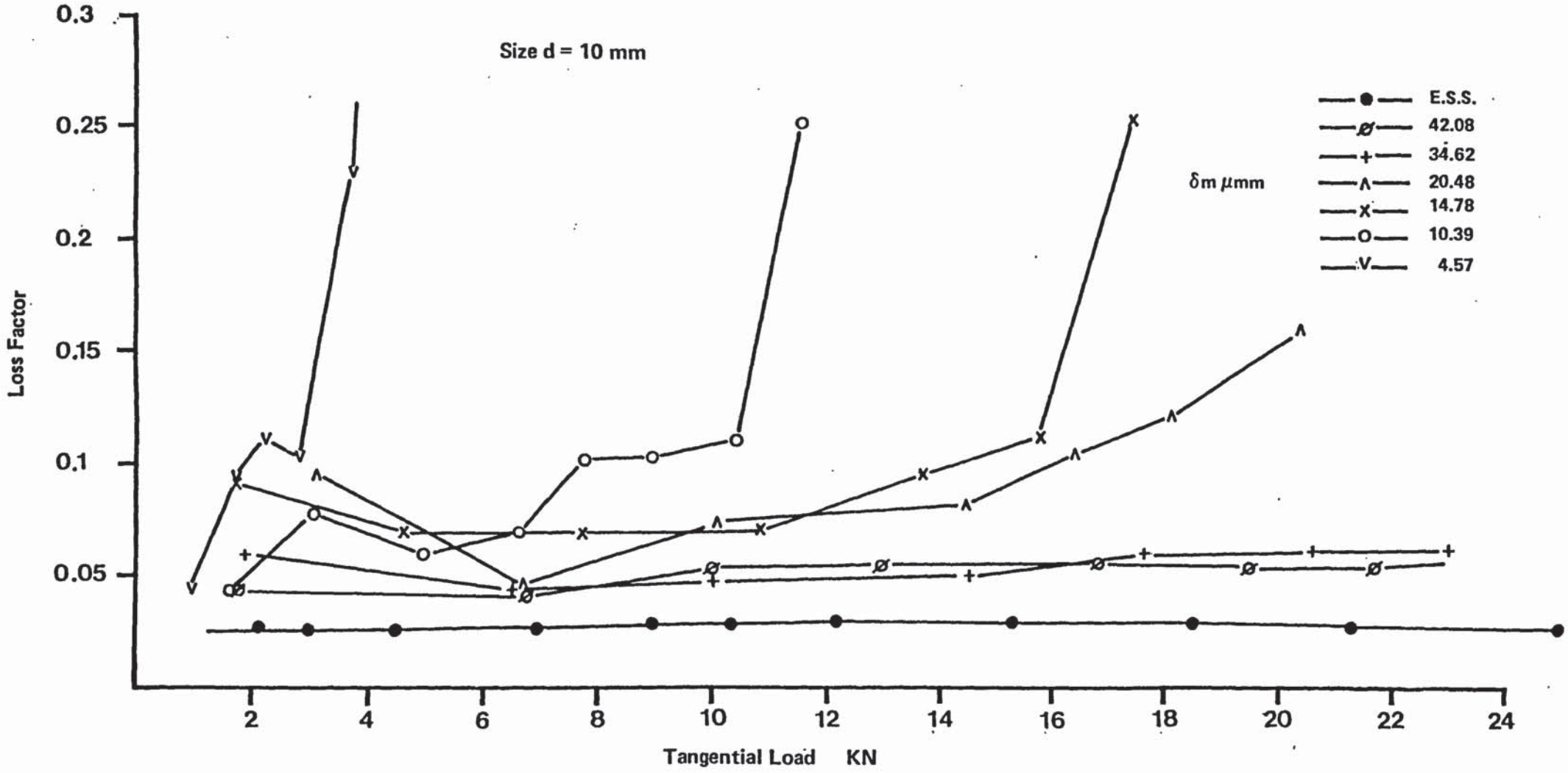

Fig 124 Loss Factor of D21 joints

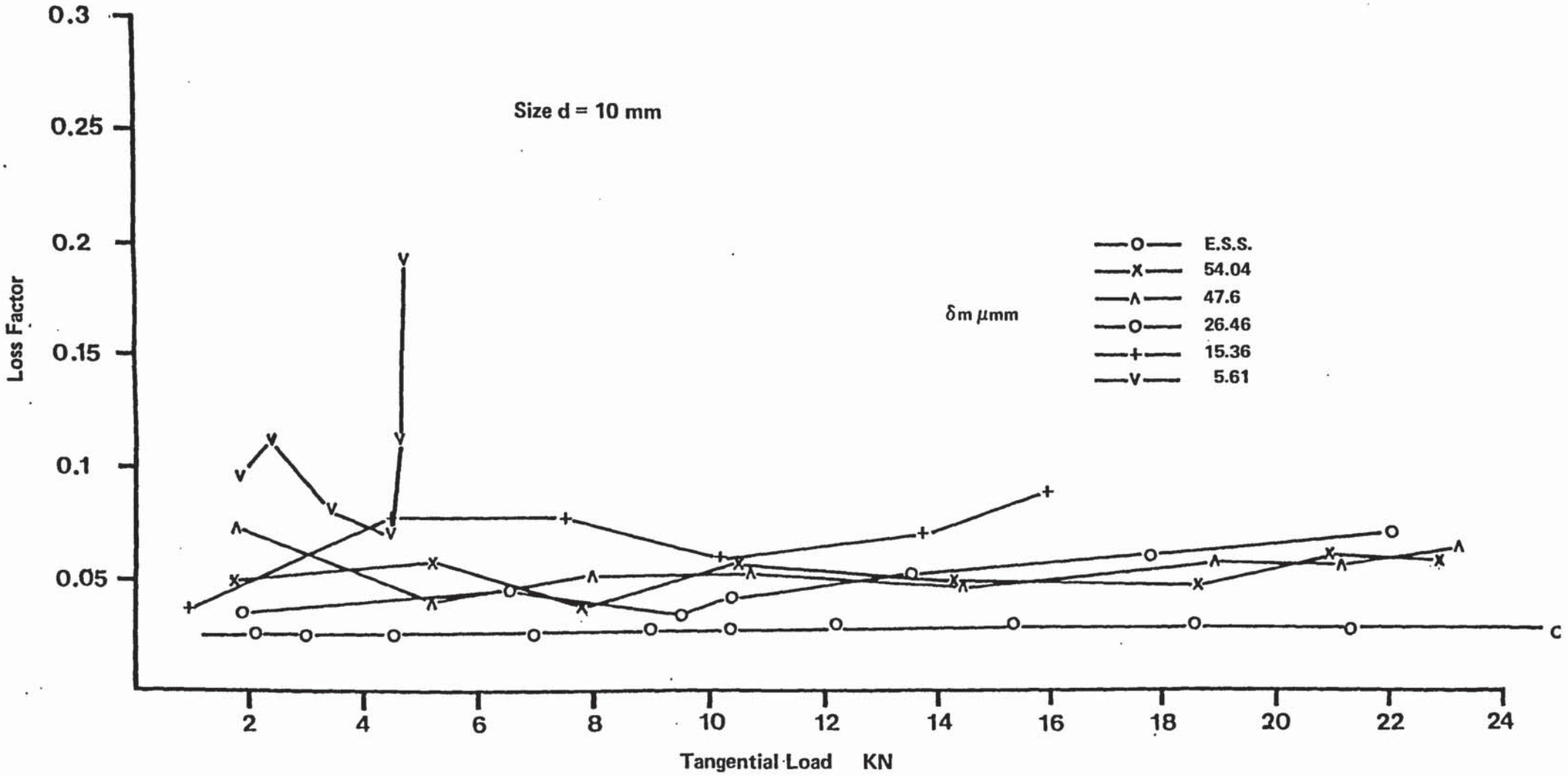

Fig 125 Loss Factor of D22 joints

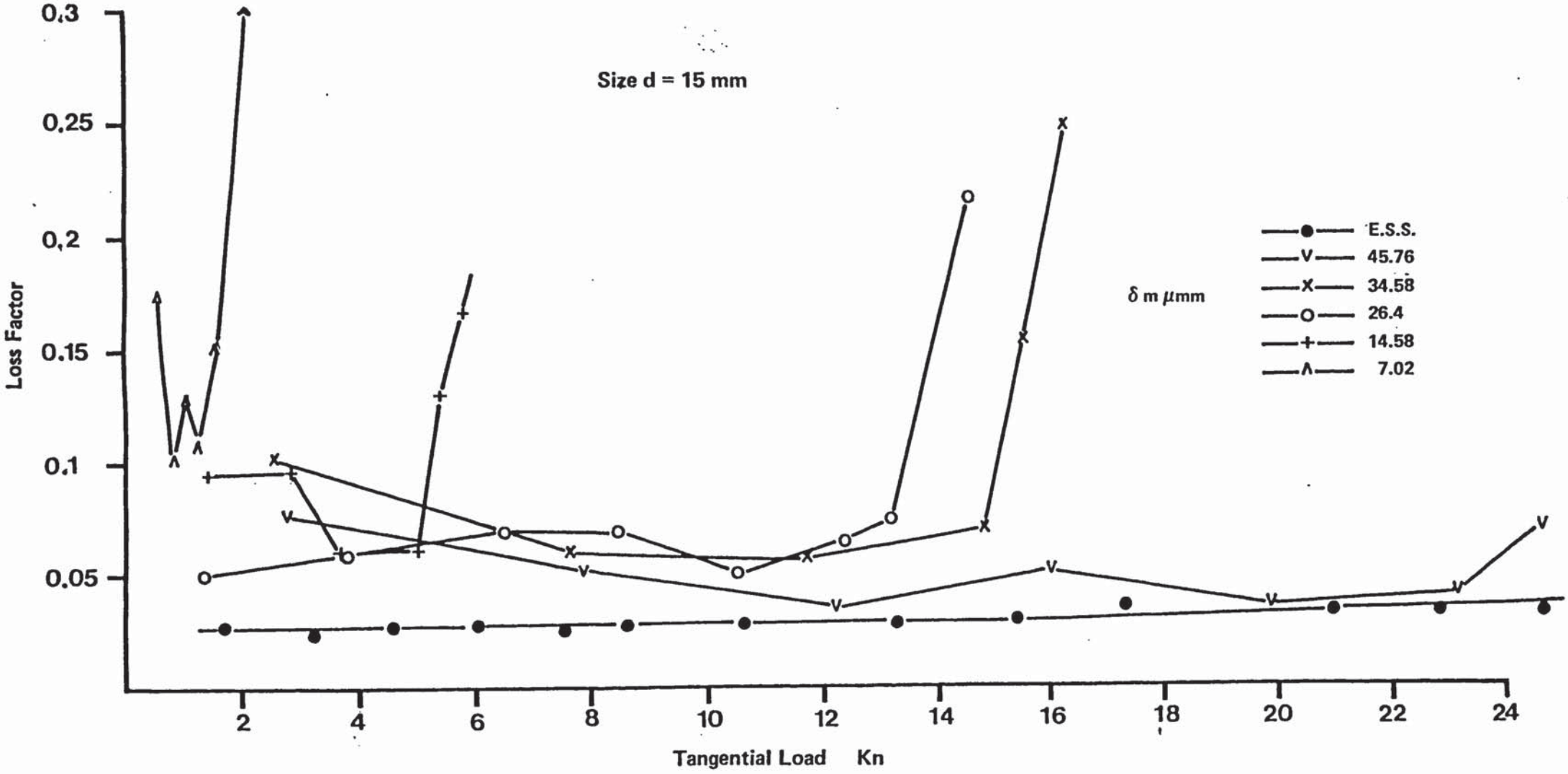

Fig 126 Loss Factor of D31 joints

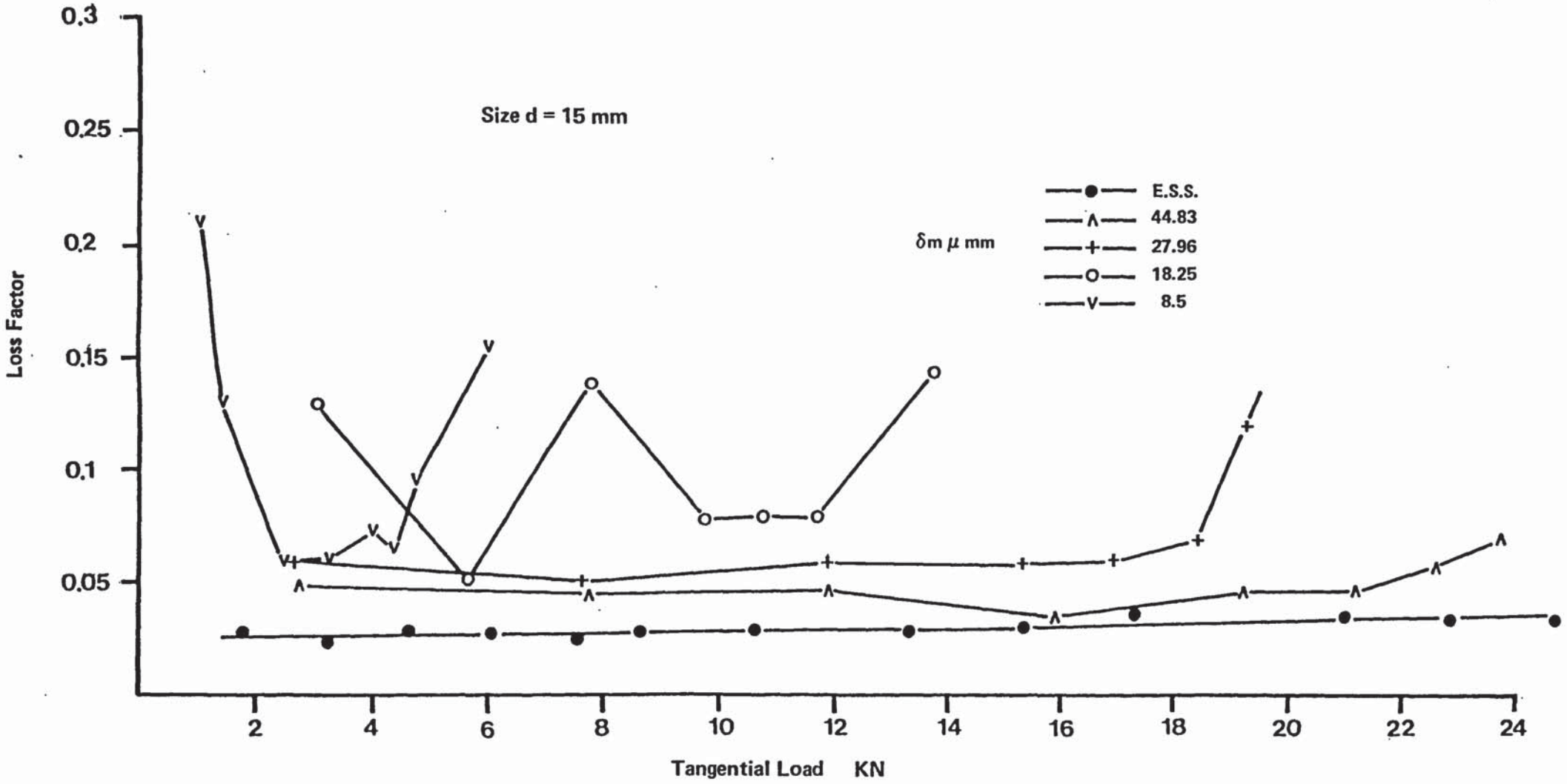

Fig 127 Loss Factor of D32 joints

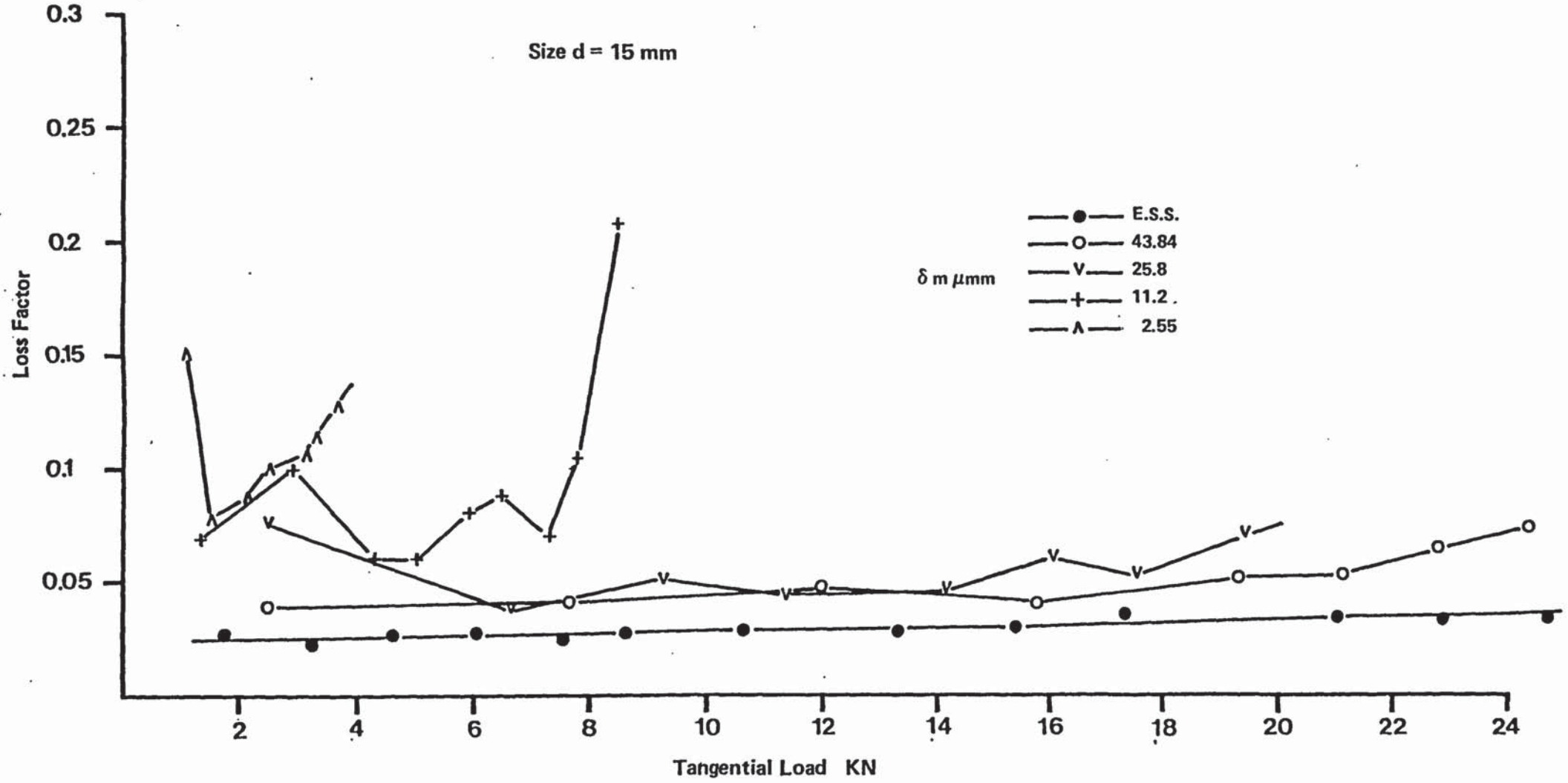

Fig 128 Loss Factor of D41 joints

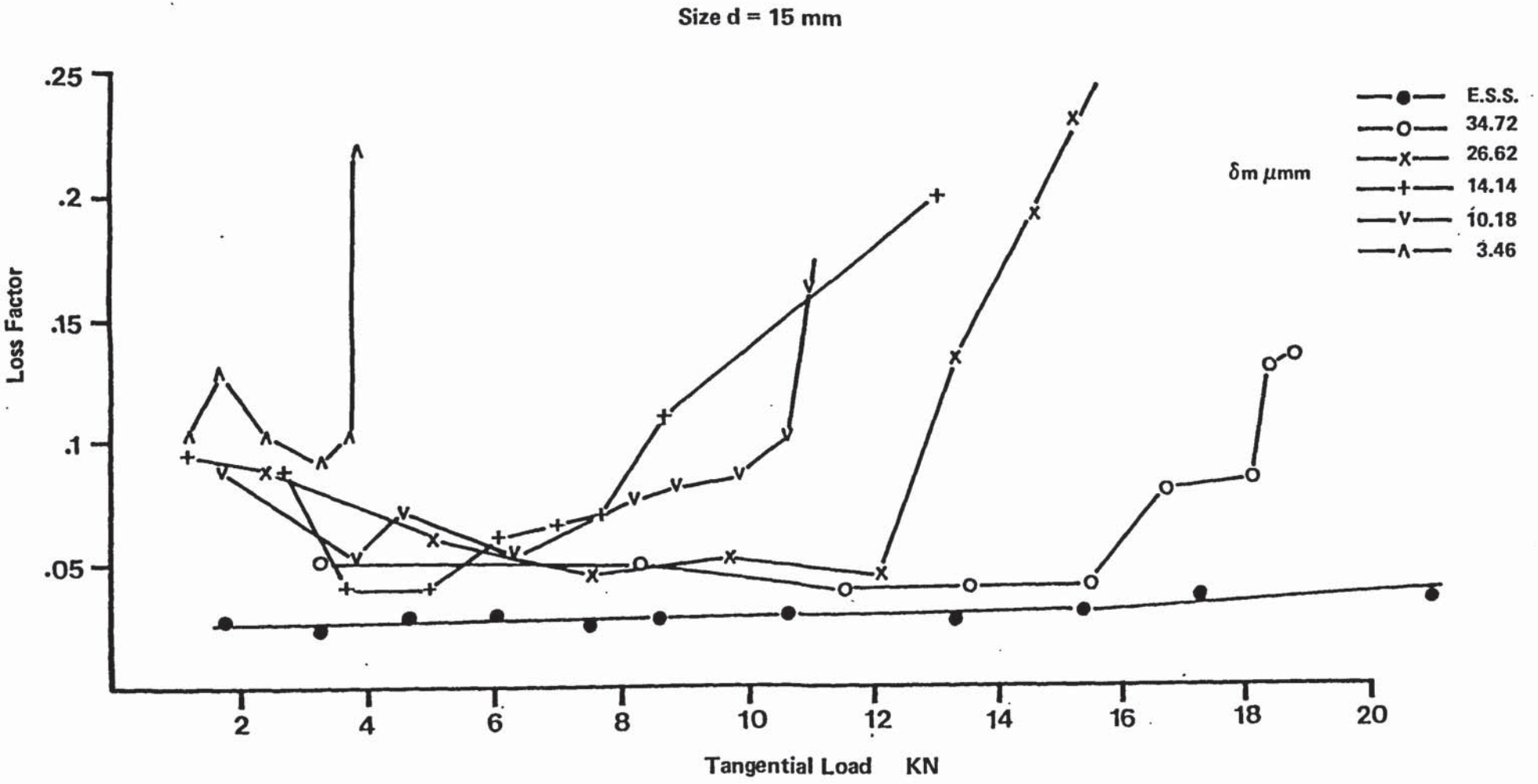

Fig 129 Loss Factor of D42 joints

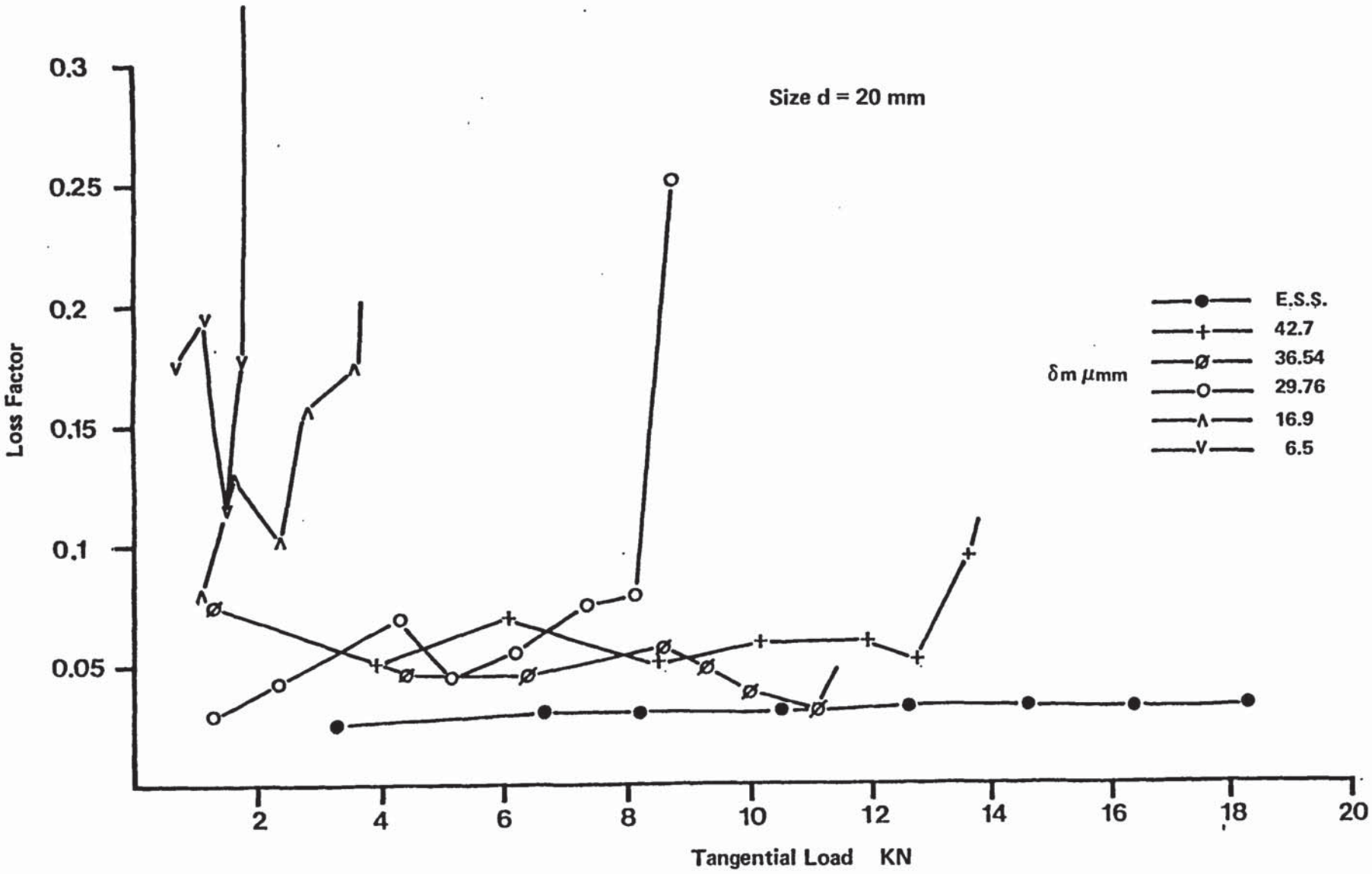

Fig 130 Loss Factor of D51 joints

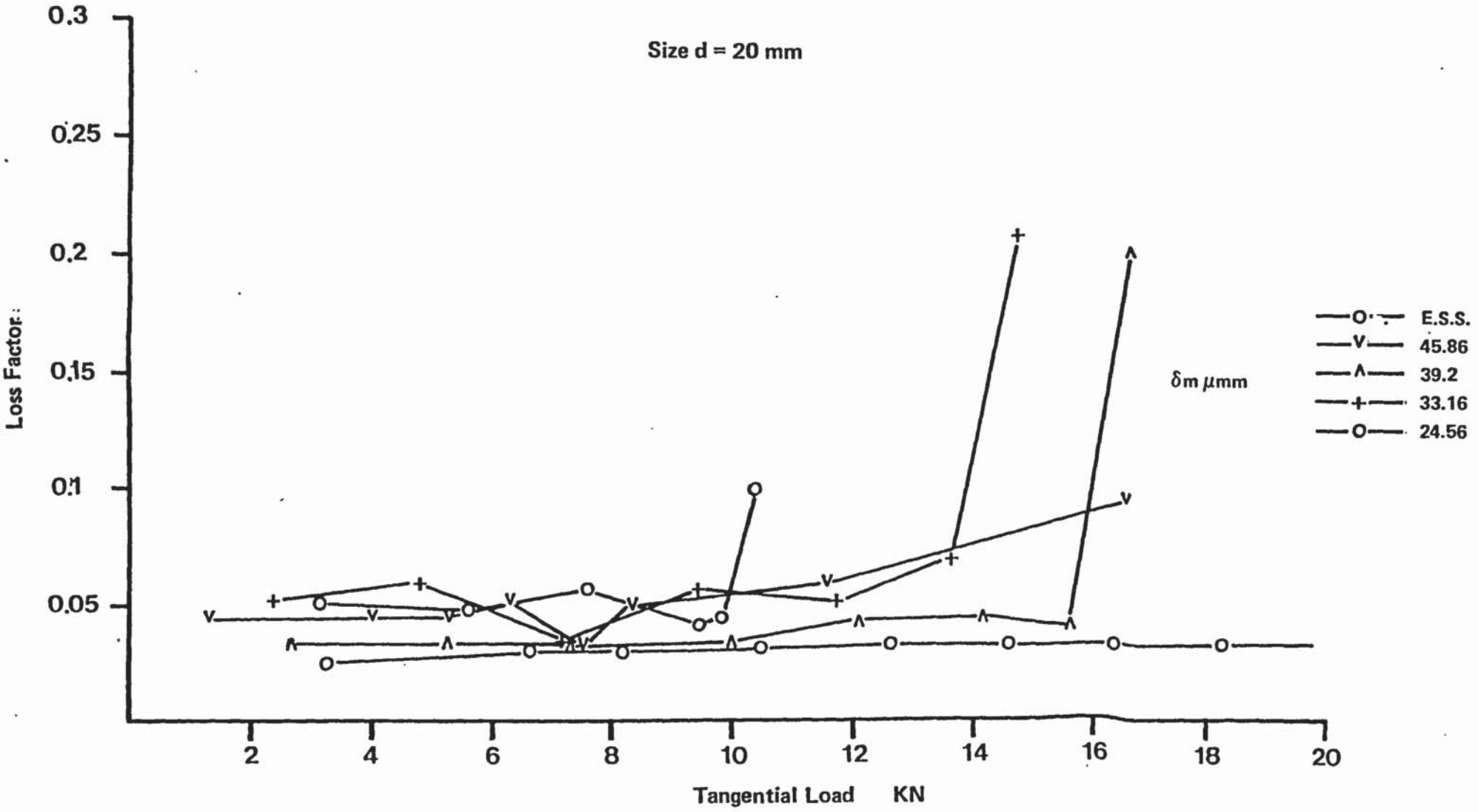

Fig 131 Loss Factor of D52 joints

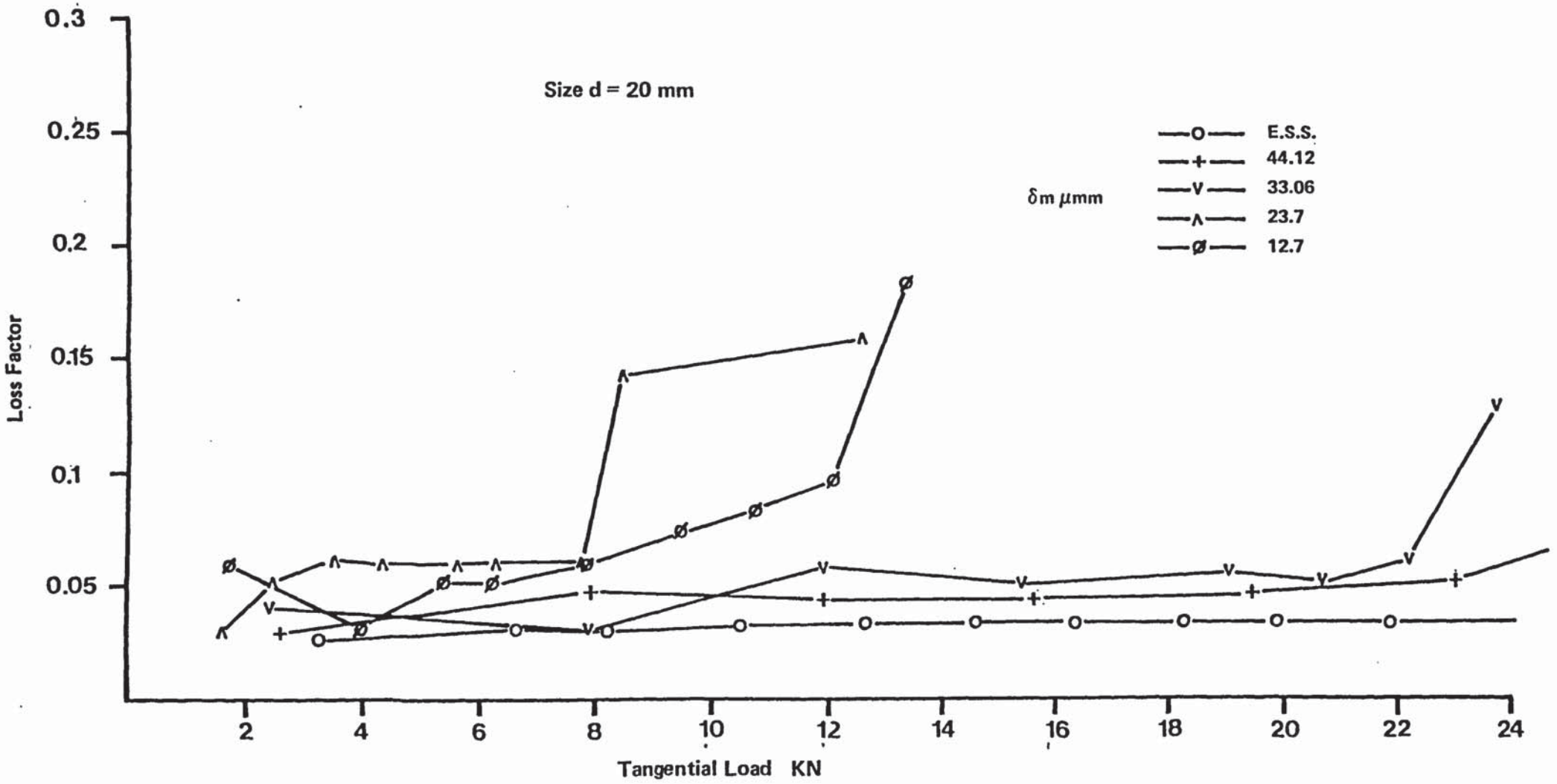

Fig 132 Loss Factor od D61 joints

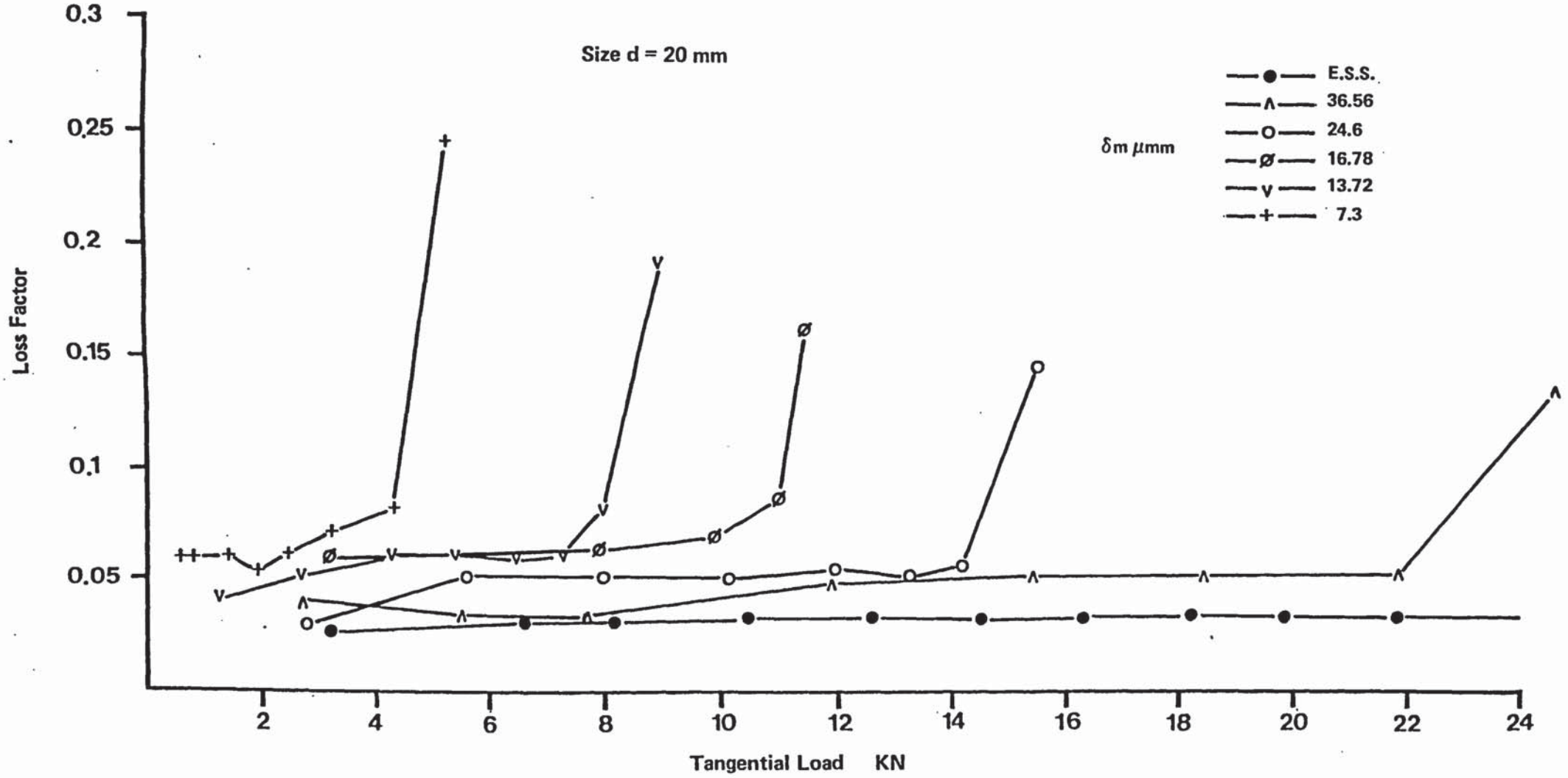

Fig 133 Loss Factor of D62 joints

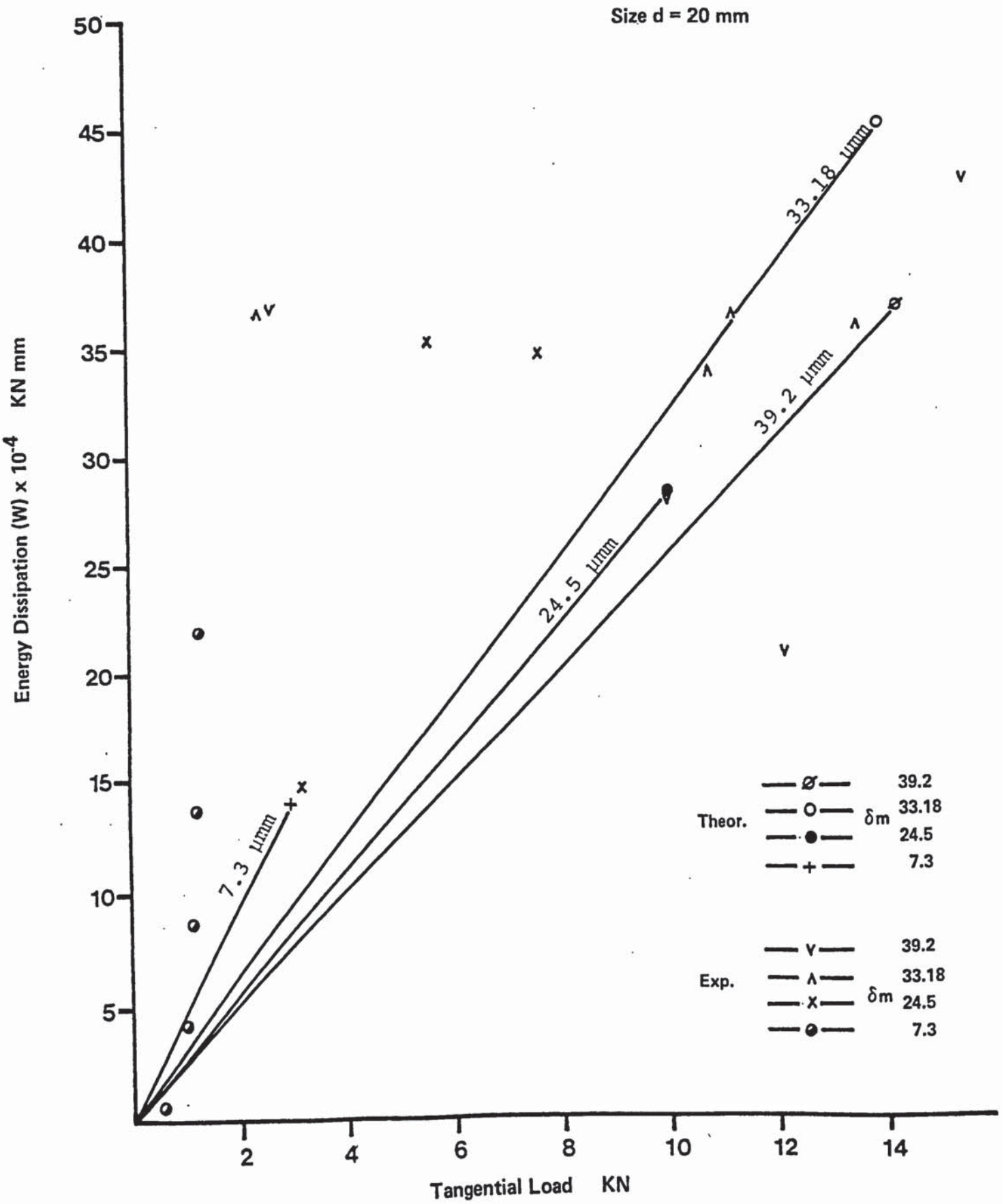

Fig 134 Energy Dissipation of D52 joints

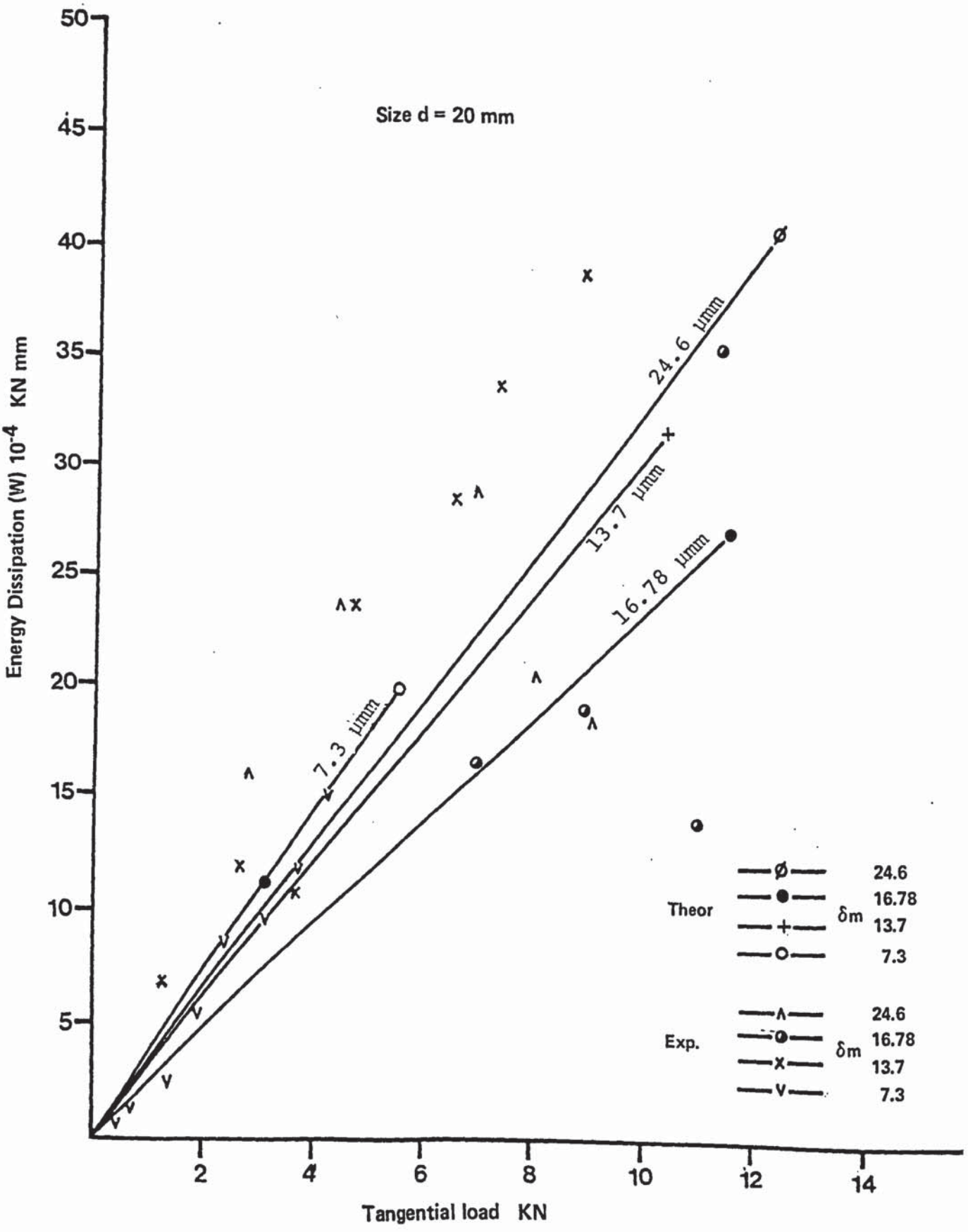

Fig 135 Energy Dissipation of D62 joints